

# Time-Dependent Aspects of Fracture in Ice

BY

©MARK B. KAVANAGH  
B.Sc, B.Ed, M.Sc

A THESIS SUBMITTED TO  
SCHOOL OF GRADUATE STUDIES  
IN PARTIAL FULFILMENT OF THE  
REQUIREMENTS FOR THE DEGREE OF  
DOCTORATE OF PHILOSOPHY  
IN  
OCEAN AND NAVAL ARCHITECTURAL ENGINEERING

FACULTY OF ENGINEERING AND APPLIED SCIENCES  
MEMORIAL UNIVERSITY OF NEWFOUNDLAND

MAY 2018

St. John's

Newfoundland

## Abstract

An important aspect of ice fracture that is yet to be fully resolved in determining the loads and pressures during an interaction with ice is the presence and growth of fractures. Practical applications include icebreakers ramming into ice pack or structures operating in ice-prone regions.

Existing models often use a simplified view of ice mechanics, often based on only the elastic properties, which tend to overestimate the strength of the ice. It has long been known that ice exhibits time-dependent properties, including its strength. This is known from ship ramming experience as well as field and laboratory experiments. Accounting for these time-dependent aspects of ice behaviour would allow for a more analytical approach to interaction modelling and complement the empirical data that is used currently in design practice.

The aim of this thesis is to provide a better understanding of ice fracture that occurs during an interaction. To better understand the viscoelastic properties of ice, an extensive review of the literature was performed. In particular, an in-depth review of linear elastic fracture mechanics was performed, as it is critical to the foundations of the viscoelastic fracture theory.

To guide the development of a new viscoelastic fracture model, three sets of experiments were performed. The first was an indentation series, scaled down from similar field experiments, that displayed several fracture properties of ice. These properties were rate-dependent fracture, delayed fracture, and scale effects.

The next two series, designed to study a single crack, used ice samples under 4-point bending. The first of these were constant loading rate test to further study the rate-dependent fracture properties of ice, resulting in ice that is weaker under faster loading in a decreasing power law relationship. The second of these applied constant loads just below the breaking point to show that ice undergoes delayed fracture. The data suggests a decreasing power law between applied load and time to failure for these samples.

Building on previous works in viscoelastic fracture theory, and making use of the insights gained from the experiments, a new model has been developed to predict the fracture properties of ice. The model accounts for the delayed fracture of ice and provides insights into the time-dependent fracture properties of ice, as was seen in the laboratory and field experiments. The model, based on viscoelastic theory, was shown to reasonably model time to failure for ice beams under constant load, as well as the fracture strength of ice beams under different loading rates. The model, besides expanding the old theories to beam bending geometries, was also shown to work for compact tension specimens with a few minor changes.

Keywords: Ice, Fracture Mechanics, Viscoelasticity, Arctic, Simulation, Ice-Structure Interaction, Scale Effects, Time-Dependence.

## Acknowledgements

After so many years, I've done it! I've finally done it! However, I didn't do it alone and I have many accomplices to thank for helping me to achieve my goal of obtaining my Ph.D.

First and Foremost I would like to thank my Supervisor Dr. Ian Jordaan for his support and guidance throughout this project. Through many discussions, new ideas were formed that lead to the creation of the model that became the centrepiece of my thesis. The project that was set upon me seemed daunting at first, but little by little, all the pieces fell into place thanks to Ian's help (and lots of metaphorical elbow grease!). Ian challenged me every step of the way to make every improvement possible to ensure our work was of the highest quality.

I would also like to thank my co-supervisor, Dr. Rocky Taylor, for the support that he provided as a member of my supervisory committee. Rocky provided a lot of support in the beginning of the project, and continued support over the project with insightful discussions and insightful revisions to my work.

Aside from my supervisors, I would like to thank Dr. Entcho Demirov for becoming a member of my supervisor committee. Dr. Demirov and I have known each other for many years, and it has been a pleasure communicating with him and an honour to have him on my committee.

During the project, I got to work along side of two good colleagues and friends, Joshua Turner and Brian O'Rourke. While our projects were vastly different, we had many engaging conversations about the work we were doing. We helped each other with our experiments without question. Having come to a computational physics background, having Brian's experimental engineering knowledge provided a huge boon in the lab and designing the apparatus used in the experiments. Josh and I put in many hours (more than I care to remember!) of crushing and sifting ice. During those times our talks on physics, our work, and everything else under the sun provided a bit humour and entertainment to ease the making process.

I would like to thank all of my friends that have been a big part of my life. All work and no play make Mark a dull boy. Thankfully it is never a dull time when I'm with friends. Whether it's having a drink, lighting a bonfire, or tearing it up at ultimate frisbee, friends are truly one of the best things a guy can have.

Lastly, but certainly not least, I would like to thank my family for the continued love and support. To my siblings: Gordon, Jordan, and Alison, thank you all for helping me in times of need and for the game nights. As always, I am extremely grateful to my parents, Joan and Albert (or Bert, as everyone calls him). They say you can't choose your family, but I don't think I could have chosen a better one myself.

Oh! Thanks to anyone who reads this thesis! You're a trooper!

Cheers,  
Mark

# Contents

	Page
<b>Abstract</b>	<b>i</b>
<b>Acknowledgements</b>	<b>ii</b>
<b>Table of Contents</b>	<b>iii</b>
<b>List of Tables</b>	<b>vii</b>
<b>List of Figures</b>	<b>viii</b>
<b>List of Symbols</b>	<b>xvi</b>
<b>List of Abbreviations</b>	<b>xix</b>
<b>1 Introduction</b>	<b>1</b>
1.1 Motivation . . . . .	1
1.2 Objectives . . . . .	3
1.3 Mathematical Notation . . . . .	4
<b>2 Physical properties and Behaviour of Ice During interactions</b>	<b>7</b>
2.1 Continuum Mechanics . . . . .	7
2.1.1 Elasticity . . . . .	7
2.1.1.1 Hooke’s Law . . . . .	8
2.1.1.2 Lamé’s Constants for Isotropic Materials . . . . .	10
2.1.1.3 Plane Strain and Plane Stress Conditions . . . . .	11
2.1.2 Linear Viscoelasticity . . . . .	14
2.1.2.1 Viscoelastic Strains . . . . .	15
2.1.2.2 Models of Linear Viscoelasticity . . . . .	16
2.1.3 Viscoelastic Beam Bending and the Correspondence Principle	19
2.1.3.1 4-Point Bending . . . . .	20
2.1.3.2 4-Point Bending with Elastic spring . . . . .	23
2.1.4 Nonlinear Viscoelasticity . . . . .	27
2.1.4.1 The Sinha Model and Andrade’s Form . . . . .	27



2.1.4.2	The Schapery, LeClair, and Dempsey Model . . . . .	29
2.2	Atomic Properties of Ice . . . . .	30
2.2.1	Atoms and Molecules . . . . .	30
2.2.1.1	Hydrogen . . . . .	30
2.2.1.2	Oxygen . . . . .	31
2.2.1.3	Water . . . . .	32
2.2.1.4	Ice . . . . .	33
2.2.2	Lattice Defects . . . . .	39
2.2.2.1	Grains . . . . .	39
2.2.2.2	Dislocations . . . . .	41
2.2.2.3	The Bjerrum Effect . . . . .	57
2.3	Interactions with Ice . . . . .	59
2.3.1	Local and Global Loads . . . . .	59
2.3.2	High Pressure Zones . . . . .	61
2.3.3	Damage Layer . . . . .	63
2.3.4	Types of Ice Fractures . . . . .	65
2.3.4.1	Spalling Event . . . . .	65
2.3.4.2	Wing Cracks . . . . .	66
2.3.4.3	Floe Splitting and Radial Cracks . . . . .	68
2.3.4.4	Bending Failure . . . . .	71
2.3.4.5	Load drops and Area Loss . . . . .	72
2.3.5	Scale Effects . . . . .	72
<b>3</b>	<b>Review of Fracture Mechanics</b>	<b>79</b>
3.1	Key Concepts of Fracture Mechanics . . . . .	79
3.1.1	Linear Elastic approximation . . . . .	80
3.1.2	Modes of Crack Formation . . . . .	80
3.1.3	Crack Nucleation and Propagation . . . . .	82
3.1.4	Energy Release Rate . . . . .	83
3.1.5	Weakest Link Theory of Failure . . . . .	87
3.1.6	Fracture Toughness . . . . .	90
3.1.7	Time-dependent Failure . . . . .	94
3.1.8	Summary of Literature Review . . . . .	100
3.2	Critical Analysis of Linear Elastic Fracture Theory . . . . .	101
3.2.1	The Westergaard Model . . . . .	102
3.2.2	The Williams Model . . . . .	109
3.2.3	The Barenblatt Model . . . . .	114
3.2.4	Summary of Critical Analysis . . . . .	117
3.3	Viscoelastic Fracture . . . . .	118

<b>4</b>	<b>Experimental Program: Indentor Series and Analysis</b>	<b>120</b>
4.1	Objectives . . . . .	120
4.2	Methodology . . . . .	121
4.3	Results and Discussion . . . . .	123
4.3.1	Behaviour at Different Normalized Velocities . . . . .	123
4.3.1.1	Slow Loading Rate ( $V_N = 3 \times 10^{-3} s^{-1}$ ) . . . . .	123
4.3.1.2	Medium Loading Rate ( $V_N = 3 \times 10^{-2} s^{-1}$ ) . . . . .	125
4.3.1.3	Fast Loading Rate ( $V_N = 2 \times 10^{-1} s^{-1}$ ) . . . . .	125
4.3.1.4	Fastest Loading Rate ( $V_N = 3 s^{-1}$ ) . . . . .	128
4.3.1.5	Explanation of Different Fracture Observations . . . . .	128
4.3.2	Examples of Delayed Failure . . . . .	140
4.3.3	Observed Scale Effects . . . . .	141
4.3.3.1	Explanation of Scatter Differences . . . . .	142
4.3.3.2	Explanation of Observed Decreasing Power-Law . . . . .	143
<b>5</b>	<b>Experimental Program: 4-Point Bending Series and Analysis</b>	<b>146</b>
5.1	Objectives . . . . .	146
5.2	Facilities . . . . .	147
5.3	Procedure . . . . .	148
5.3.1	First Series . . . . .	148
5.3.2	Second Series . . . . .	151
5.4	Results and Discussion . . . . .	155
5.4.1	Rate-Dependent Fracture Toughness . . . . .	155
5.4.2	Time to Failure Under Constant Load . . . . .	158
<b>6</b>	<b>Viscoelastic Fracture Theory and Model Development</b>	<b>163</b>
6.1	Graham's Correspondence Principle . . . . .	164
6.1.1	Classical Correspondence Principle . . . . .	164
6.1.2	Extended Correspondence Principle . . . . .	167
6.2	The Schapery Model . . . . .	168
6.2.1	Plane Stress and Plane Strain . . . . .	169
6.2.2	The Process Zone . . . . .	169
6.2.2.1	The Process Zone Stress Distribution . . . . .	170
6.2.2.2	Process Zone Size . . . . .	171
6.2.3	Elastic Crack Opening Displacement . . . . .	172
6.2.4	Continuous Crack Growth . . . . .	175
6.2.4.1	Viscoelastic Crack Tip Opening Displacement . . . . .	176
6.2.4.2	The Effective Compliance . . . . .	178
6.2.4.3	Fracture Energy . . . . .	185
6.2.4.4	Crack Growth . . . . .	193
6.2.4.5	Time to Failure . . . . .	195
6.2.5	Intermittent Crack Growth . . . . .	197
6.2.5.1	Crack Opening Displacement . . . . .	197

6.2.5.2	Fracture Energy . . . . .	199
6.2.5.3	More on the Secant Compliance . . . . .	202
6.3	Nonlinear Viscoelastic Fracture Mechanics . . . . .	203
6.4	Continuous Crack Growth . . . . .	208
6.4.1	Fracture Toughness and Stress Intensity . . . . .	209
6.4.2	Process Zone and Crack growth . . . . .	210
6.4.3	Failure Energy and the Process Zone Stress Field . . . . .	211
6.5	Intermittent Crack Growth . . . . .	215
6.5.1	Secant Compliance . . . . .	215
6.5.2	Fracture Initiation . . . . .	215
6.6	Numerical Implementation . . . . .	216
6.6.1	Time-Stepping . . . . .	216
6.6.2	Updating the Force . . . . .	219
6.6.3	Updating the Stress Intensity and Geometric Shape Function . . . . .	220
6.6.4	Updating the Size of the Process Zone . . . . .	220
6.6.5	Continuous Crack Growth . . . . .	221
6.6.6	Intermittent Crack Growth . . . . .	222
6.6.6.1	Secant Compliance . . . . .	222
6.6.6.2	Fracture Initiation . . . . .	222
<b>7</b>	<b>Model Validation and Results</b>	<b>223</b>
7.1	Underlying Assumptions of the Schapery Model . . . . .	223
7.1.1	Datasets Used for Validation . . . . .	224
7.1.2	Effective Compliance Validation . . . . .	227
7.1.3	Validation of Small Process Zone Size . . . . .	233
7.2	Validation of Linear Model . . . . .	234
7.2.1	Primary Creep . . . . .	236
7.2.2	Secondary Creep . . . . .	238
7.3	Beam Geometry . . . . .	241
7.4	Model Fits Using Brill and Camp Parameters . . . . .	242
7.5	Independent Model Fits . . . . .	245
7.5.1	Rate-Dependent Fracture Results . . . . .	246
7.5.2	Time to Failure Predictions . . . . .	246
7.5.3	Discussion . . . . .	250
7.6	Combined Model Fits . . . . .	250
7.6.1	Rate-Dependent Fracture Results . . . . .	252
7.6.1.1	Baseline Model Results . . . . .	252
7.6.1.2	Sensitivity Analysis of Model to Rheological Parameters . . . . .	252
7.6.2	Time to Failure Predictions . . . . .	256
7.6.2.1	Baseline Model Results . . . . .	256
7.6.2.2	Sensitivity Analysis . . . . .	258
7.6.3	Discussion and Summary . . . . .	261
7.7	Model Fits of Liu and Miller (1979) . . . . .	264

7.8	Time to Failure Approximation . . . . .	268
<b>8</b>	<b>Conclusion</b>	<b>271</b>
8.1	Summary . . . . .	271
8.1.1	A Brief overview . . . . .	271
8.1.2	Time-Dependent Properties of Ice . . . . .	273
8.1.3	The Underlying Theory . . . . .	275
8.1.4	The Viscoelastic Fracture Model . . . . .	276
8.2	Practical Implications . . . . .	278
8.3	Future Work . . . . .	279
8.3.1	New Geometries . . . . .	280
8.3.2	The Process Zone . . . . .	280
8.3.3	Combining with Finite Analysis . . . . .	280
8.3.4	Converting to a Nonlinear Viscoelastic Fracture Model . . . . .	281
8.3.5	More Experimental Data . . . . .	281
	<b>Bibliography</b>	<b>283</b>
	<b>Appendix A CAD Specification Sheets for Dead Weight Apparatus</b>	<b>295</b>

# List of Tables

2.1	Properties of dislocations. $b$ is Burgers vector, $d$ is the direction along the width. $v$ is direction of motion. . . . .	47
2.2	Test matrix of indentation experiments performed in Barrette et al. (2003). . . . .	77
4.1	The various spherical indentors used during the experiments, along with some of the test speeds at different normalized velocities. . . . .	122
7.1	Summary of model coefficients of the compliances from Sinha (1978) and Brill and Camp (1961). . . . .	232
7.2	Model parameter used in fitting LeClair et al. (1999) in Figure 7.8. . . . .	234
7.3	Parameter values used to generate creep values from equations 7.6 and 7.15. . . . .	239
7.4	Geometric dimensions of the ice beam for the ramp series. . . . .	242
7.5	Geometric dimensions of the ice beam for the constant load series. . . . .	242
7.6	Rheological Parameters from uniaxial fit to (Brill and Camp, 1961). . . . .	242
7.7	Rheological ice model parameters from experimental fitting. . . . .	246
7.8	Rheological ice model parameters from experimental fitting. . . . .	247
7.9	Rheological ice model parameters from experimental fitting of both beam series. . . . .	252
7.10	Values of the parameters used in the sensitivity analysis for the ramp loading. . . . .	252
7.11	Values of the parameters used in the sensitivity analysis for the constant applied load tests. . . . .	258
7.12	Rheological ice model parameters from experimental fitting CT-specimens from Liu and Miller (1979). . . . .	266

# List of Figures

2.1	Illustration of the lateral expansion of a cylindrical sample under uni-axial compression caused by the Poisson's effect. Aside from Poisson's effect, "barelling" occurs because the ends are often confined by the end platens of a system (e.g., ice frozen to a steel plate at its ends). . . . .	9
2.2	Example of a hydro dam under stress from the retained water. . . . .	11
2.3	Example of a thin plate under planar stress. . . . .	13
2.4	Conceptual models of viscoelasticity. . . . .	17
2.5	a) 4-Point Bending. b) Shear diagram. c) Moment diagram. d) Elastic beam profile (initial viscoelastic response). e) Changing compliance with time. f) Displacement of the midpoint of the beam over time. . . . .	21
2.6	Superposition of 4-point bending with spring into 4-point bending problem (like above), and problem with a concentrated force due to the spring alone . . . . .	23
2.7	a) Setup for 4-point bending with spring. b) Shear diagram. c) Moment diagram. d) Beam profile with centre bump due to spring. e) The Maxwell compliance (linear in time and no primary creep). f) Change in spring reaction force over time . . . . .	26
2.8	The water molecule. Oxygen coloured in red, hydrogen coloured in yellow. . . . .	31
2.9	Hydrogen bonding between water molecules. . . . .	34
2.10	The ice crystal lattice . . . . .	35
2.11	Water molecules bonding in a tetrahedral formation. There are 6 variations to this bond that allow them to combine to form a hexagonal lattice. . . . .	36
2.12	Various views showing how stacking tetrahedral elements leads to the hexagonal lattice structure in ice. . . . .	37
2.13	Electron bonding orbitals in a water molecule. . . . .	39
2.14	A typical Cross-sectional cut of ice. Solid lines show grain boundaries, arrows and colours indicate c-axis of grain (all in-plane for simplicity). . . . .	40
2.15	Edge dislocation . . . . .	43
2.16	Screw Dislocation . . . . .	46

2.17	Dislocation loop with marked edge and screw dislocations. Mixed dislocations occur between the two types, acting as a transition between them. . . . .	48
2.18	. . . . .	49
2.18	plots a–h show the formation of an edge dislocation (denoted by $\perp$ ) and sliding across a plane of atoms under an applied shear force, the width ( $w$ ) of the dislocation is shown in light gray. Plot i shows the change in force and energy as the dislocation glides through the lattice (distance normalized by the Burgers vector). . . . .	50
2.19	Dislocation Climb. Starting with Figure 2.18e, the lattice has two impurities introduced: A larger atom and a vacancy. . . . .	52
2.20	Dislocation kink caused by the presence of a large atom acting as a barrier. . . . .	54
2.21	Slip and cross-slip of a screw dislocation. . . . .	55
2.22	Generation of dislocations via the Frank-Read Mechanism. a) shows a non-basal, kinked edge dislocation pinned at both ends of the kink. As shear is applied to the basal plane, the dislocation grows outward, eventually annihilating in f) resulting in a new dislocation and the original dislocation in g). . . . .	56
2.23	Bjerrum Effect due to dislocation glide. . . . .	58
2.24	Global vs local loads. From Taylor (2010). . . . .	59
2.25	The Molikpaq drilling caisson surrounded by ice. After Timco et al. (2006). . . . .	60
2.26	High Pressure Zones. . . . .	62
2.27	Thin sections of ice samples showing the underlying grain structure of the damaged layers of fast and slow indentation loading (O’Rourke et al., 2015). . . . .	64
2.28	Cross-section of an ice-structure interaction showing the formation of a spall fracture event. a–c show a pre-existing crack grow under load, reach the edge of the ice, and break off as a discrete piece of ice (spall). . . . .	65
2.29	The formation of wing cracks. a) sorts the stress field into three zones based on the relative strength of the vertical, horizontal, and shear stress components. b) shows the formation of a wing crack under stress. . . . .	66
2.30	a) Photoelastic fringe pattern from Hoek and Bieniawski (1965) for a thin plate of annealed glass. Modified to highlight the presence of a wing crack. b) Wing crack dimensions for a crack oriented 30 degrees to the direction of loading. . . . .	67
2.31	Floe-splitting observed at Hans Island. Light gray represents the island and dark grey shows the tensile zones near the contact area between the ice floe and Hans Island. . . . .	69
2.32	Bending failure of ice due to interaction with structure and vessel. . . . .	71

2.33	Each before/after shows the pressure distribution during an ice-structure interaction from a pressure sensor. a) shows the pressure and area change from a crushing/extrusion event. The crushing event shows very little change in the contact area. b) shows the pressure and area change from a spalling event. The arrows point to various spalls that occurred and lead to localized loss of contact area. The Data is from Nakazawa et al. (1999) for a medium-scale flat indenter. Figure is modified from Taylor et al. (2008). . . . .	74
2.34	Indentation data from a variety of sources from laboratory-scale indentation to island-sized indentation in the field. Taken from Jordaan et al. (2005), modified from Sanderson (1988). . . . .	76
2.35	Observed scale effects for various indentors at different loading rates from Barrette et al. (2003). Units are in MPa and mm <sup>2</sup> . . . . .	77
3.1	Modes of cracking opening. . . . .	80
3.2	Energy release rate due to crack extension. . . . .	84
3.3	Two chains of different strengths. The strength of a chain is determined by its weakest link. . . . .	88
3.4	Sample recommended testing from ASTM for $K_I$ fracture. a)Single Edge Notched Tension (SENT) b) Single Edge Notched Bent (SE(B)) c) Double Edge Notched Tension (DENT) . . . . .	92
3.5	a) 3-Point beam bending set-up. b) Reverse Tapered ice specimen with steel-walled flatjack along crack wall. c) Compact tension specimen loaded at grips above and below an edge crack. . . . .	93
3.6	Delayed fracture during creep test at Hobsons Choice medium-scale indentation test (Frederking et al., 1990). . . . .	95
3.7	Time to Failure for peak loads, taken from Timco (2011). Trendlines added to original plot to show decreasing power law relationship discussed in text. . . . .	96
3.8	Images and data collected during the Rae Point indentation series by Sandwell/GEOTECH in 1984-85 . . . . .	97
3.9	a)Experimental set-up from Urabe et al. (1980). Bottom rollers are adjusted to cancel the buoyancy of the ice, causing it to be weightless. b) Results of Urabe et al. (1980), showing the relationship between apparent fracture toughness and strain rate of sea ice under 3-point bending tests. . . . .	99
3.10	Westergaard setup of a centrally located crack in an infinite plate under biaxial tension . . . . .	102
3.11	Westergaard stress solution at multiple points . . . . .	108
3.12	Williams wedge-shaped geometry. As $\alpha$ tends to zero, the wedge becomes a crack. . . . .	110
3.13	a) Physical setup of ideal crack on the x-axis. b) Stress distribution inside the process zone, and in front of the crack. . . . .	114



4.1	Test T140_2B_V0P06-T10_R20.035. a) Force diagram for a damage-enhanced creep. b) Top view photo showing distributed damage along the surface with no spalling. c) Thin-section photo showing a recrystallized damage zone with a lot of microcracking along the edges of the contact zone. . . . .	124
4.2	a) T122. Load plot for 10 mm indenter with “outside the zone” spalls forming in d). b) T139. Load plot for 20 mm indenter showing crushing behaviour and subsequent OTZ Spalls in e). c) T125. Load plot for 40 mm indenter showing a delayed spalling event within the <i>hpz</i> in f) . .	126
4.3	a) T109. Load plot for 10 mm indenter with a large spall forming from the event at $t = 6.6$ seconds in d). b) and c) are loading plots of tests T115 and T119 for the 40 mm indenter. e) shows the spalling event from T115, which produced a tiny spall. This spall resulted in a drop in the area shown by the Tekscan sensor in f). . . . .	127
4.4	Comparison of two 40 mm indentors. T119 (a-c) has a rate of $V_N = 2 \times 10^{-1} s^{-1}$ and T121 (d-f) has a rate of $V_N = 3 s^{-1}$ . The results of both tests show that they behave similarly in the loading plot, but T121 has more energetic expulsions of ice. . . . .	129
4.5	a) FE model of cylindrical ice sample under indentation inside a rigid mould. The mould completely surrounds the ice, including the bottom. b) Cauchy stress cube showing positive stress components. . . . .	130
4.6	Elastic Stress field of ice under indentation. The $x_1$ -axis is out of page.	133
4.7	Location of compressive, shear, and tensile zones in ice under indentation.	134
4.8	Potential radial crack growth following a path of maximum energy release, perpendicular to the contours of strain energy density. For an unconfined specimen, the indentation would be analogous to the Hans Island experiments. . . . .	135
4.9	Potential spalling following a path of (elastically modelled) maximum energy release from the shear zone. . . . .	136
4.10	Strain Energy Field with possible crack growth for Hobsons Choice Medium-Scale test done at slow speed. . . . .	138
4.11	a) T110 used the 10 mm indenter at $N_V = 0.1$ . b) Final results of T110 displays many large pieces of ice. c) T113 ( $V_N = 0.03 s^{-1}$ ) resulted in a large section of the surface breaking off (10 mm indenter imprint can be seen at the bottom of the piece). . . . .	139
4.12	Pressure vs Area scatter plot of the data from the laboratory-scale indentation series. Data shows a decreasing power-law relationship. .	141
4.13	Samples cut from an ice block will contain random distribution of cracks and flaws. Large samples are likely to be weak due to containing a large flaw. Smaller samples will exhibit more scatter as they may or may not have a large flaw. . . . .	142
4.14	Von Mises elastic stress field for ice underneath the 10- and 40-mm indentors. . . . .	144

5.1	a) 4-point bending experimental setup with dimensions. b) shear-moment diagram for 4-point bending. . . . .	148
5.2	a) 3-Point bending set-up. b) 4-Point bending set-up. c) Bending moment diagram comparison of 3- and 4-point bending. 4-Point bending has a more uniform bending moment near the crack than in a 3-point bending set-up. . . . .	150
5.3	4-Point beam bending dead-weight apparatus. Elevated reservoir filled with fluid not shown. . . . .	153
5.4	a) Experimental results of failure load due to changing loading rates. b) The same results plotted as an apparent fracture toughness. . . . .	156
5.5	Experimentally observed delayed failure in the large ice beams from the first series. Both samples were under a load of 180 N. . . . .	159
5.6	Experimentally observed delayed failure in the small ice beams from the second series. All samples were held under constant load after the initial ramp up phase. . . . .	160
5.7	Experimental results for the dead-weight 4-point bending experiments. Samples that did not break are displayed with an arrow pointing to the right. . . . .	161
6.1	Effective Compliance Normalized by Elastic Compliance. . . . .	178
6.2	First-term effective compliance weighting function . . . . .	181
6.3	Sensitivity of the weighting function, $w_k$ , to $k$ . . . . .	182
6.4	Sensitivity of $\ell_{nk}$ and $\ell_{nk}^{\frac{1}{n}}$ to $k$ . . . . .	184
6.5	Figure showing the relationship between $\Gamma_A$ and $\Gamma_B$ , normalized by the size of the process zone, $R_P$ . . . . .	189
6.6	Contour plot showing anti-symmetry of $\frac{s+s'}{s-s'}$ over the process zone. . . . .	192
6.7	The J-integral is defined by a contour around the process zone. The contour has to be inside the material and contain no cracks, so that continuum mechanics applies within the contour. . . . .	204
6.8	Schematic of 4-Point Bending Specimen showing geometry definitions. Depth of the beam into the page is denoted by $d$ . . . . .	209
6.9	a) Exponentially decreasing normalized process zone stress fields with different steepness parameter, $A$ . b) The value of the $I_1$ for varying steepness parameter . . . . .	213
6.10	Flow chart of how the model numerically simulates continuous crack growth. . . . .	218
7.1	Data (represented by circles) of ice specimens under uniaxial tension from Schapery (1997); LeClair et al. (1999). Nonlinear optimization of the parameters from equation 2.45. . . . .	225
7.2	Left: Comparison of experimental data Sinha (1978) (-41°C, columnar ice) to an effective linear compliance of the form in equation 7.1 by nonlinear optimization of the model parameters. . . . .	226

7.3	Left: Comparison of experimental data Sinha (1978) (-30°C, columnar ice) to an effective linear compliance of the form in equation 7.1 by nonlinear optimization of the model parameters. . . . .	226
7.4	Left: Comparison of experimental data Brill and Camp (1961) (-5°C, isotropic ice) to an effective linear compliance of the form in equation 7.1 by nonlinear optimization of the model parameters. . . . .	227
7.5	Log-log plots showing the creep response of the nine cycles applied to the ice sample from Schapery (1997); LeClair et al. (1999). . . . .	228
7.6	Log-log plots showing the creep response of the nine cycles applied to the ice sample from Schapery (1997); LeClair et al. (1999). . . . .	230
7.7	a-c) Linear profile and process zone size. b-d) Quadratic profile and process zone size. . . . .	232
7.8	Linear and nonlinear parameter optimization fits of LeClair et al. (1999) using equations 7.5 and 7.4. . . . .	235
7.9	Normalized creep for experiments performed by Sinha (1978) presented in Figure 7.3. . . . .	239
7.10	Nonlinear parameter optimization fit of the creep curve from Brill and Camp (1961). . . . .	240
7.11	Normalized creep curves for the experiments of Brill and Camp (1961). . . . .	241
7.12	Model Results of 4-Point bending under constant ramping using parameters from Table 7.6. . . . .	243
7.13	Model Results of 4-Point bending under constant applied load using parameters from Table 7.6. . . . .	244
7.14	Rate dependence of $I_1$ with loading rate, due to the change in the distribution of the process zone stress field under different loading rates. . . . .	247
7.15	Results of model simulation for the ramp up to failure experiments. a) shows the data plot on a normal scale and b) shows the data plotted in the log-log domain. . . . .	248
7.16	Model results for time to failure for the small ice beams used in the second series. a) shows the results the results using normal space, whereas b) shows the results in log-log space. . . . .	249
7.17	Results of model simulation for the ramp up to failure experiments. a) shows the data plot on a normal scale and b) shows the data plotted in the log-log domain. The rheological ice parameters used are in Table 7.9. . . . .	251
7.18	Sensitivity analysis of rheological ice parameters for ramp up to failure simulations. . . . .	255
7.19	Model Results for time to failure for the small ice beams used in the second series. a) shows the results the results using normal space, whereas b) shows the results in log-log space. These results use the parameter set from Table 7.9. . . . .	257
7.20	Sensitivity analysis of rheological ice parameters for time to failure simulations. . . . .	261

---

7.21	Comparison of results from Liu and Miller (1979) (dots) to viscoelastic model with parameters used in Table 7.12 . . . . .	265
7.22	Static loading finite element analysis of a) In-house 4-point beam bending and b) compact tension specimen of Liu and Miller (1979). . . . .	267
7.23	Optimized fit of constant load series using the crack growth approximation from Jordaan and Xiao (1992). . . . .	270
A.1	Complete Assembly with component labels. . . . .	296
A.2	Specifications for wooden table at the base of the apparatus. . . . .	297
A.3	Specifications for table stiffener . . . . .	298
A.4	Specifications for flange at the base of the pulley system. . . . .	299
A.5	Specifications for the bar that holds up the pulley. . . . .	300
A.6	Specifications for the table guide that aligns the top plate. . . . .	301
A.7	Specifications for the supports that hold up the lever. . . . .	302
A.8	Specification for the lever arm. . . . .	303
A.9	Specifications for the rod that the lever pivots about. . . . .	304
A.10	Specifications for the hollowed cylinder part of the rollers. . . . .	305
A.11	Specifications for the steel core of the rollers. . . . .	306
A.12	Specifications for the holders that connect the rollers to the table or top plate. . . . .	307
A.13	Specifications for the top plate. . . . .	308
A.14	Specifications for the bucket portion of the hanging mass. . . . .	309
A.15	Specifications for the brackets that connect the bucket to the pulley (via string). . . . .	310
A.16	Diagram illustrating the construction of the lever arm and its supports. . . . .	311
A.17	Diagram illustrating the construction of the pulley, its support, and the stiffening flange. . . . .	312
A.18	Diagram illustrating the assembly of a roller from its constituent parts. . . . .	313
A.19	Diagram illustrating the assembly of the components that apply and measure the load on the ice sample. . . . .	314
A.20	Diagram of the hanging mass assembled from the bucket and its brackets. . . . .	315

# List of Symbols

Symbol	Meaning(s)
$\sigma$	Stress
$\epsilon$	Strain
$E$	Young's Modulus
$\nu$	Poisson's ratio
$\delta_{ij}$	Kronecker's Delta
$\lambda$	Lamé's Constant
$\mu$	Lamé's Constant
$\lambda^*$	Modified Lamé's Constant
$\kappa$	Alternative Lamé's Constant
$x$	dimensional direction; distance along beam
$y$	dimensional direction; beam deflection
$z$	dimensional direction; Complex variable
$L$	Length
$\beta$	Andrade's flow parameter
$n$	Andrade's flow exponent; Primary creep exponent
$A\{T\}$	Temperature-dependent Arrhenius factor
$q$	Glen's flow law exponent; Secondary creep exponent
$\mu_d, \mu_1, \mu_2$	Dashpot viscosity
$w$	beam width
$b, h$	beam thickness
$F$	Force
$x_1, x_2$	Position of top rollers along beam
$J\{t\}$	Viscoelastic creep compliance
$t$	time
$\delta_c$	Central beam deflection
$R$	Force exerted on beam from spring; ideal gas constant; Material resistance
$V$	Shear force in beam; Volume
$M$	Beam bending moment

---

Symbol	Meaning(s)
$I$	Beam area moment of inertia
$k$	spring constant; Boltzmann's constant; generic constant
$T$	Temperature; Beam thickness
$Q$	Activation Energy
$S_{1,2}$	Shift function
$d$	Grain diameter; Indenter diameter
$K_{gbs}$	Constant related to grain boundary sliding
$p$	Laplace transform variable; Primary creep nonlinearity
$C_0, C_e$	Elastic compliance
$C_1$	Primary creep compliance
$C_2$	Secondary creep compliance
$K_I$	Stress intensity factor
$K_{IC}, K_G$	Fracture toughness
$P$	Pressure
$A$	Area
$\gamma_s$	Surface energy
$U$	Strain energy
$B$	Thin plate thickness
$a$	crack length
$G$	Energy release rate
$R_p$	Size of the process zone
$Y\{a\}$	Geometric shape function
$\phi$	Airy's stress function; polar coordinate
$\Omega, \Phi$	Complex functions
$v$	velocity; vertical displacement
$u$	horizontal displacement
$\theta$	angle
$r$	distance from crack tip
$\ell$	Williams variable
$s$	Distance variable in process zone
$V_N$	Normalized velocity
$\alpha$	crack length / Beam thickness
$\mathcal{B}$	The complete boundary
$\mathcal{B}_1$	the growing boundary
$\mathcal{B}_2$	The boundary that is not $\mathcal{B}_1$
$K_b$	Bulk modulus
$a_b, b_b, c_b, A_b, B_b, C_b$	Graham's boundary conditions

---

Symbol	Meaning(s)
$f$	Normalized process zone stress
$\sigma_m$	Maximum process zone stress
$\eta$	Normalized distance along process zone
$I_1$	Integral of process zone distribution
$I_2$	Integral related o the rate of change in the stress field inside the process zone
$C_\nu$	Viscoelastic creep compliance
$\rho, \tau$	Integrands related to time
$C_{ef}$	Effective compliance
$w$	Weighting function
$A_k$	Displacement coefficients
$\Gamma$	The Gamma function (gives factorials)
$\Gamma_G$	The fracture energy
$\Gamma_A, \Gamma_B, \Gamma_Z$	Fracture energy components
$\ell_n k, \ell_n$	A constant (see equation 6.64); $\ell_n \approx 0.3$
$t_R$	Time for crack to growth the length of the process zone
$\tilde{t}_s$	Time for crack to grow some length $s$
$C_s$	Secant compliance
$T^R$	Traction force
$J_F, J_V$	J-Integral
$S_1, S_2$	Top and bottom roller separation

# List of Abbreviations

Abbreviation	Meaning
<i>hpz</i>	High pressure zone
FE(A)	Finite element (analysis)
LEFM	Linear elastic fracture mechanics
NRC	National Research Council of Canada
MTS	Materials Testing System®
OTZ	Outside the (contact) zone
HSV	High speed video (camera)
LVDT	Linear variable displacement transducer
SERR	Strain energy release rate
CT	Compact tension (specimen)



# Chapter 1

## Introduction

### 1.1 Motivation

The Arctic is an important part of Canada, both culturally and economically. This region presents a new frontier for development but poses many hurdles to overcome for safe and economic development. The question of how to deal with ice in this region is a vital question for Canadians, with safety to personnel and the environment being of paramount concern.

The north is home to many Canadians who require goods and services and are eager for meaningful, economic progress. The area can be developed with respect to community access, tourism, and the transportation of goods and resources. With the highest population growth rate and a high proportion of young people, there is an opportunity to get input from the local communities on how to better serve them and provide opportunities for the young population with new careers in science and engineering that can enhance their way of life.

The North also contains many resources such as gold, diamonds, uranium, oil and gas, and other resources to boost the Canadian economy (Croasdale et al., 2016).

These sites account for roughly 10% of Canada's total mineral production. There are many more mining sites in the north, some of which are in the planning phase of becoming operational. Development of these mines could lead up to the creation of 5000 jobs related to operation and development. For many of the northern mines, the minerals extracted are often stored on site and shipped during the warmer seasons when there is less ice present, though ice-breaking capabilities are still necessary. Future endeavours in Arctic research will aim to increase the shipping season through better ship design, infrastructure, and logistics (e.g., better navigational routes).

Local infrastructure in the Arctic is also important for the communities as many of their goods are delivered by ships. Since there are few wharves in the Arctic, goods are often transferred over beaches and ships are refuelled by fuel lines floating in the water. Both of these problems pose risks to people and the environment, as well as being time-consuming. The design of new docks, that take into consideration the effects of ice loads on the structure and docked vessels, would greatly alleviate these issues.

An important aspect that is yet to be solved in determining the loads and pressures during an interaction with ice is the presence and growth of fractures. One practical application relates to icebreakers ramming into ice packs or ships operating in ice. In some cases, an icebreaker will fracture the ice immediately, but the ice may also undergo a delayed fracture under load from the icebreaker. The type of loading will also affect the type of fracture that occurs in ice from small, localized fractures to large fractures that can span an entire ice floe. It is known from large and medium scale indentation tests that the loads and pressures exerted from the ice onto a structure are dependent on the rate of interaction (i.e., loading or strain rate). One such test was done at the Hobson's Choice ice island (Frederking et al., 1990), that shows that the ice behaves more creep-like at slow rates, more brittle at fast rates, and a mix of

both at medium rates.

Due to many factors, including the presence of pack ice, the cost of living and doing business in the north can be costly, but a better understanding of the physical properties of ice can greatly alleviate these costs.

## 1.2 Objectives

The aim of this project is to provide better insights into the fracture processes in ice that occur during an interaction. This new knowledge can be used in the design process to build more economical structures that meet the safety requirements for Arctic environments. To achieve these goals, an extensive review of previous experiments, along with theories has been investigated to provide guidance as to the issues that need to be addressed.

The first objective is to study the effects that loading rate has on the type of fractures that occur in ice. Following the indentation series of tests done by Frederking et al. (1990), a series of small-scale tests were done in the laboratory to simulate similar results. From these experiments, a pattern between the observed fracturing and loading rates can be addressed.

Another objective of the indentation series is related to the scaling of the data. It would be useful if there was a way to scale the results of small-scale tests to larger scales. Previous experiments (to be discussed) have shown that there is a clear scaling effect between the small and large scale data. These scale effects are explored in the indentation series by the use of various indentors of different sizes to explore how the indentor size affects the fracture behaviour.

The final objective is to develop a fracture model for crack growth using standard geometries, primarily loading under 4-point bending. The model will attempt to

explain two phenomena observed in ice failure. The first observation is the dependence of the strength of ice in relation to loading rate. Various experiments, discussed in the literature review, show that ice behaves as brittle material under fast loading and becomes stronger and more creep-like under slower loading. The second property of ice is the observance of delayed failure under load. This property is often employed by icebreakers ramming up onto an ice floe and waiting for it to split if it does not break immediately. These properties will be achieved in the model by treating ice as a viscoelastic material, as this type of material displays these behaviours.

Two series of 4-point bending experiments (focusing on the different behaviours of ice) provide the model with data that can be used to fit the model parameters. The first series focused on loading the ice at different rates to observe the failure strength dependence on loading rate. The second series held the ice beams under a constant load that does not lead to instantaneous failure, with the aim of observing delayed failure over time.

### 1.3 Mathematical Notation

Given the amount of mathematics in the following chapters, a brief note on the mathematical notation used in this thesis may be warranted. One key difference in mathematical notation is the use of braces (“{””) to denote “function of” instead of the more commonly used parentheses (“(”). For example, the statement “F is a function of x and t” would be written as

$$F \{x, t\}$$

instead of

$$F(x, t)$$

Secondly, derivatives with respect to time will be written as either

$$\frac{\partial a}{\partial t} = F \{x, t\}$$

or by using the dot notation

$$\dot{a} = F \{x, t\}$$

For derivatives of other variables, either the standard notation or a shorthand notation is used, such as

$$\frac{\partial F}{\partial x} = \partial_x F$$

for a derivative, or the second derivative as

$$\frac{\partial^2 F}{\partial x^2} = \partial_{xx} F \tag{1.1}$$

$\Delta$  has two distinct uses in this thesis. The first is as a fractional change, such as

$$\frac{\partial a}{\partial t} \approx \frac{\Delta a}{\Delta t}$$

or  $\Delta a = a \{t + 1\} - a \{t\}$  in numerical approximations. The second use for  $\Delta$  is as the Heaviside-step function, where

$$\Delta \{x - x_0\} = \begin{cases} 1 & \text{if } x > x_0 \\ 0 & \text{if } x < x_0 \end{cases}$$

and are easily distinguished by where it is a function (followed with braces) or not (not followed by braces).

When performing series expansions, generally one will cut off the series at some point at which the terms quickly become negligible. These terms are denoted by  $\mathcal{O}$ .

For example, a series approximation of  $\exp \{x\}$  is given by

$$\begin{aligned}\exp \{x\} &\approx \sum_{n=0}^{\infty} \frac{x^n}{n!} \\ &\approx 1 + x + \frac{x^2}{2} + \frac{x^3}{6} + \frac{x^4}{24} + \dots\end{aligned}$$

For  $x \approx 0$ , a linear approximation may suffice, giving

$$\exp \{x\} \approx 1 + x + \mathcal{O} \{x^2\} \quad (1.2)$$

where the  $\mathcal{O}$  states that all terms of  $x^2$  or higher have been considered negligible.

Complex analysis of variables will make use of the real ( $\mathbf{Re}\{z\}$ ) and imaginary ( $\mathbf{Im}\{z\}$ ) parts of a function/variable so that

$$\begin{aligned}z &= 3 + 4i \\ \mathbf{Re}\{z\} &= 3 \\ \mathbf{Im}\{z\} &= 4\end{aligned} \quad (1.3)$$

As a part of some analysis, the Laplace transform is used. The Laplace transform,  $\mathcal{L} \{F \{x\}\}$ , is defined by

$$\mathcal{L} \{F \{x\}\} = \int_0^{\infty} F \{x\} \exp \{-px\} \, dx \quad (1.4)$$

and the inverse transform is noted by  $\mathcal{L}^{-1} \{F \{p\}\}$ , and is often found from lookup tables, but has an equation of the form

$$\mathcal{L}^{-1} \{F \{p\}\} = \frac{1}{2\pi i} \lim_{P \rightarrow \infty} \int_{c-iP}^{c+iP} \exp \{sp\} F \{p\} \, dp \quad (1.5)$$

for some real-valued  $c$ .

# Chapter 2

## Physical properties and Behaviour of Ice During interactions

### 2.1 Continuum Mechanics

#### 2.1.1 Elasticity

All solids exhibit an elastic response upon loading. When a material behaves elastically, it returns to its undeformed shape when the load is removed. Elasticity is caused by the resistance of atoms of an object to being pushed or pulled apart from their equilibrium separation. Provided no new equilibrium has been established (as is the case with permanent deformation), then the atoms will simply return to their original separation distance upon unloading.

Elasticity is a fundamental response of all materials, so a brief overview is given in this section. Since the model developed in this thesis assumes isotropic, polycrystalline ice, the discussion of elasticity will be limited to linear elasticity (Hooke's Law and Lamé's constants) to cover some notation used in later sections.

Lastly, it is important to discuss elasticity in the context of viscoelasticity since

there is a mapping between the solution of an elastic material under load and a viscoelastic material under the same conditions. This will be discussed in sections about viscoelasticity (In particular, Section 2.1.3).

#### 2.1.1.1 Hooke's Law

Many materials exhibit a linear elastic response that relates the applied load,  $\sigma$ , to the observed strain ( $\epsilon$ ) or vice versa. The relationship for a uniaxial load (in the x-direction) is often written as

$$\sigma_{xx} = E\epsilon_{xx} \quad (2.1)$$

where  $E$  is the constant of proportionality, called the Young's Modulus (or Modulus of Rigidity).

When dealing with multiaxial loading, one has to include the Poisson's effect. The Poisson's effect is an objects lateral response to an applied load. For example, Figure 2.1 shows a cylindrical sample under uniaxial compression. The sides of the sample will bulge outwards (in the y-direction) proportionally to the applied uniaxial load, typically written as

$$\epsilon_{yy} = -\frac{\nu}{E}\sigma_{xx} \quad (2.2)$$

where the strain in the y-direction is related to the applied load in the x-direction. This results in the original cylindrical sample to become compressed down into a barrel-shaped sample.

In general, the elastic strain under a multiaxial loading can be written using summation notation as

$$\epsilon_{ij} = \frac{1}{E} [(1 + \nu)\sigma_{ij} - \nu\delta_{ij}\sigma_{kk}] \quad (2.3)$$

where the subscripts  $i$  and  $j$  loop over the  $x$ ,  $y$ , and  $z$  directions.  $\delta_{ij}$  is the Kronecker



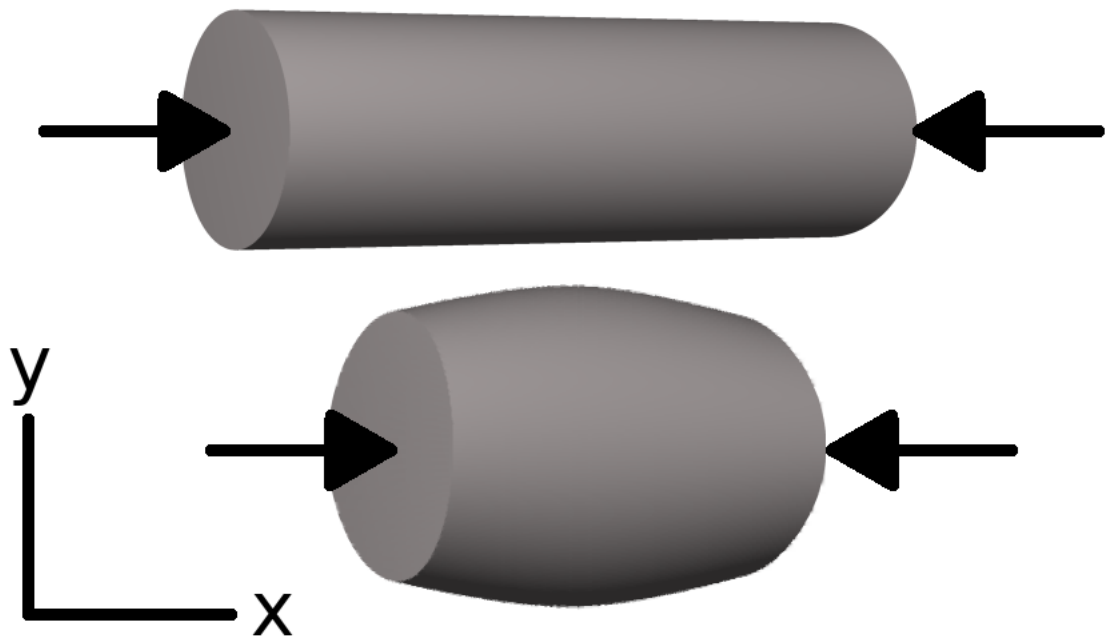


Figure 2.1: Illustration of the lateral expansion of a cylindrical sample under uniaxial compression caused by the Poisson's effect. Aside from Poisson's effect, "barrelling" occurs because the ends are often confined by the end platens of a system (e.g., ice frozen to a steel plate at its ends).

delta defined as

$$\delta_{ij} = \begin{cases} 1 & \text{for } i = j \\ 0 & \text{for } i \neq j \end{cases} \quad (2.4)$$

and  $\sigma_{kk} = \sigma_{xx} + \sigma_{yy} + \sigma_{zz}$ .

### 2.1.1.2 Lamé's Constants for Isotropic Materials

Equation 2.3 can be cast into matrix form and inverted to get

$$\sigma_{ij} = \frac{E}{(1 + \nu)(1 - 2\nu)} [(1 - 2\nu)\epsilon_{ij} + \delta_{ij}\epsilon_{kk}] \quad (2.5)$$

For a generalized isotropic material the compliance tensor,  $C_{ijkl}$ , has the form

$$C_{ijkl} = \lambda\delta_{ij}\delta_{kl} + \mu(\delta_{ik}\delta_{jl} + \delta_{il}\delta_{jk}) \quad (2.6)$$

Noting that stress and strain are related through the generalized, anisotropic compliance tensor,

$$\sigma_{ij} = C_{ijkl}\epsilon_{kl} \quad (2.7)$$

gives the isotropic elastic stress-strain relationship as

$$\sigma_{ij} = \mu(\epsilon_{ij} + \epsilon_{ji}) + \lambda\delta_{ij}\epsilon_{kk} \quad (2.8)$$

Comparing equations 2.5 and 2.8 (and noting  $\epsilon_{ij} = \epsilon_{ji}$ )

$$\begin{aligned} \lambda &= \frac{E\nu}{(1 + \nu)(1 - 2\nu)} \\ \mu &= \frac{E}{2(1 + \nu)} \end{aligned} \quad (2.9)$$

which are known as Lamé's constants.

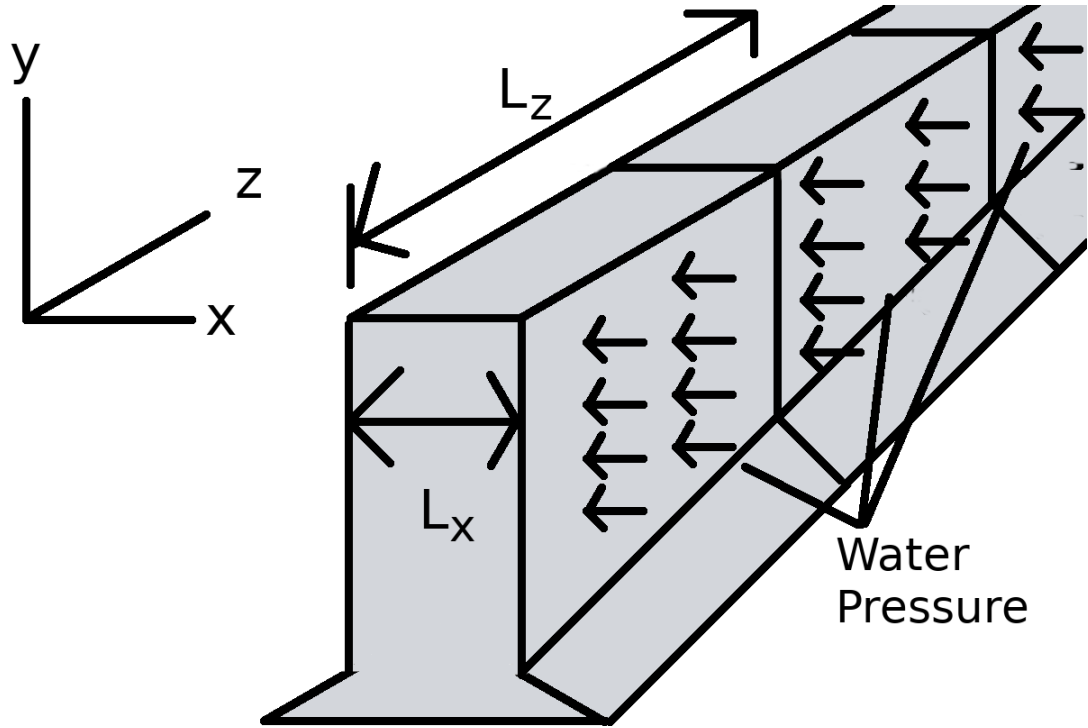


Figure 2.2: Example of a hydro dam under stress from the retained water.

### 2.1.1.3 Plane Strain and Plane Stress Conditions

Two frequently considered situations in engineering are the plane strain and plane stress conditions. These conditions occur in many engineering applications. These two conditions are also applicable to the state of stress and strain near a crack tip, which will be discussed in Section 6.2.1.

#### 2.1.1.3.1 Hookean Equation For Plane Strain

Plane strain conditions exist when the out of plane strain ( $\epsilon_{zz}$ ) are sufficiently small so that they can be assumed negligible. One common example given is the stresses and strains associated with a hydro dam or retaining wall (Figure 2.2). Typically, the dam or wall are much longer than they are tall. Given that the force from the water acts mainly on the plane of the dam/wall, and that the strain along the z-direction is inversely proportional to the length of the wall in the z-direction. The strain in the z-

direction will be considerably smaller than in the x- or y-directions. In mathematical notation

$$\begin{aligned}\frac{\Delta x}{L_x} &\gg \frac{\Delta z}{L_z} \\ \epsilon_{xx} &\gg \epsilon_{zz}\end{aligned}\tag{2.10}$$

with  $\Delta x$  and  $\Delta z$  representing changes in the length of the wall in the x- or z-directions, as well as  $L_x$  and  $L_z$  representing the original lengths. This relationship also the case for  $\epsilon_{yy} \gg \epsilon_{zz}$  since  $L_z \gg L_x, L_y$ .

Without any significant loss to accuracy. i.e.,

$$\begin{aligned}\epsilon_{zz} &\approx 0 \\ \epsilon_{xz} &\approx 0 \\ \epsilon_{yz} &\approx 0\end{aligned}\tag{2.11}$$

for plane strain conditions.

For plane strain, equation 2.8 simplifies to give

$$\begin{aligned}\sigma_{ij} &= \lambda \delta_{ij} \epsilon_{kk} + 2\mu \epsilon_{ij} \\ \sigma_{xx} &= \lambda(\epsilon_{xx} + \epsilon_{yy}) + 2\mu \epsilon_{xx} \\ \sigma_{yy} &= \lambda(\epsilon_{xx} + \epsilon_{yy}) + 2\mu \epsilon_{yy} \\ \sigma_{zz} &= \lambda(\epsilon_{xx} + \epsilon_{yy}) \\ \sigma_{xy} &= 2\mu \epsilon_{xy}\end{aligned}\tag{2.12}$$

#### 2.1.1.3.2 Hookean Equation For Plane Stress

For plane stress to occur, there has to be no significant out-of-plane stress ( $\sigma_{zz}$ ). One example of this, shown in Figure 2.3, is a thin plate under planar stresses. Due to the thinness of the the plate there will be no significant stress acting along the z-direction

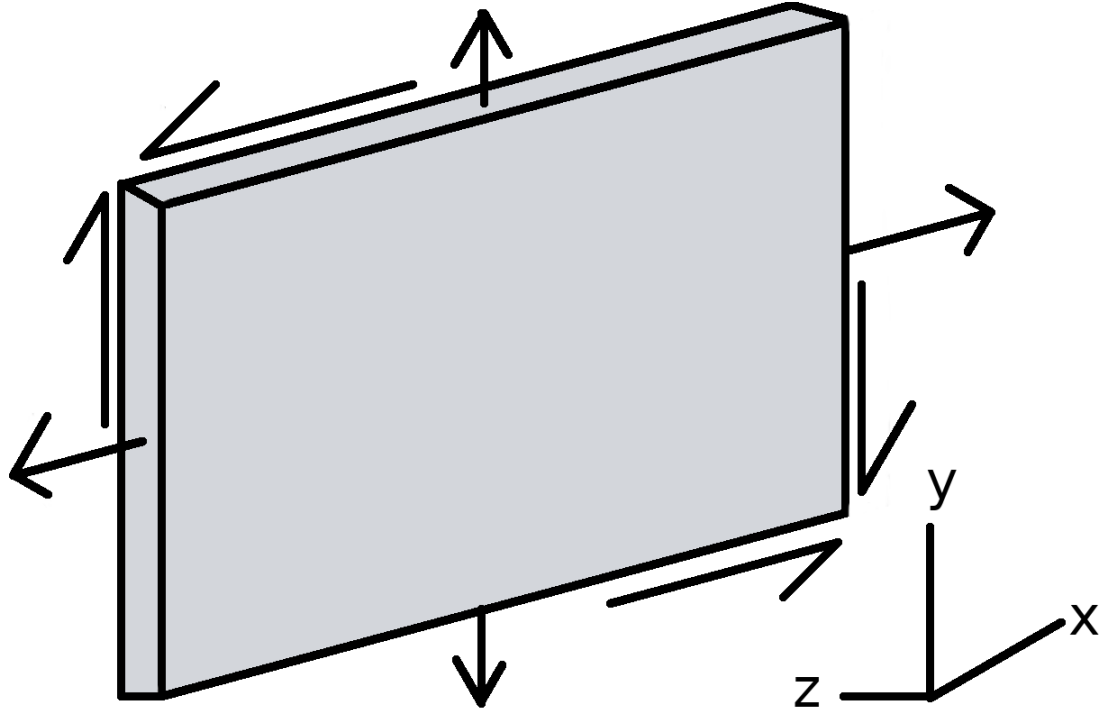


Figure 2.3: Example of a thin plate under planar stress.

of the plate.

Writing out the stress-strain relationships explicitly gives

$$\begin{aligned}
 \sigma_{ij} &= \lambda \delta_{ij} \epsilon_{kk} + 2\mu \epsilon_{ij} \\
 \sigma_{xx} &= \lambda(\epsilon_{xx} + \epsilon_{yy} + \epsilon_{zz}) + 2\mu \epsilon_{xx} \\
 \sigma_{yy} &= \lambda(\epsilon_{xx} + \epsilon_{yy} + \epsilon_{zz}) + 2\mu \epsilon_{yy} \\
 \sigma_{zz} &= \lambda(\epsilon_{xx} + \epsilon_{yy} + \epsilon_{zz}) + 2\mu \epsilon_{zz} \\
 \sigma_{xy} &= 2\mu \epsilon_{xy}
 \end{aligned} \tag{2.13}$$

but since  $\sigma_{zz} = 0$ , then the strain in the z-direction must be

$$\begin{aligned}
 0 &= \lambda(\epsilon_{xx} + \epsilon_{yy} + \epsilon_{zz}) + 2\mu \epsilon_{zz} \\
 \epsilon_{zz} &= -\frac{\lambda}{\lambda + 2\mu}(\epsilon_{xx} + \epsilon_{yy})
 \end{aligned} \tag{2.14}$$

Substituting  $\epsilon_{zz}$  back into the stress-strain relationship defines a different Lamé's constant  $\lambda^*$  for plane stress that is different than plane strain,

$$\begin{aligned}\sigma_{ij} &= \lambda^* \delta_{ij} \epsilon_{kk} + 2\mu \epsilon_{ij} \\ \sigma_{xx} &= \lambda^* (\epsilon_{xx} + \epsilon_{yy}) + 2\mu \epsilon_{xx} \\ \sigma_{yy} &= \lambda^* (\epsilon_{xx} + \epsilon_{yy}) + 2\mu \epsilon_{yy} \\ \lambda^* &= \frac{2\lambda\mu}{\lambda + 2\mu}\end{aligned}\tag{2.15}$$

which allows one to quickly change answers between plane strain and plane stress by using  $\lambda$  or  $\lambda^*$  as needed.

One can also define

$$\lambda = \frac{3 - \kappa}{\kappa - 1} \mu \tag{2.16}$$

where

$$\kappa = \begin{cases} 3 - 4\nu & \text{Plane Strain} \\ \frac{3-\nu}{1+\nu} & \text{Plane Stress} \end{cases} \tag{2.17}$$

instead of switching between  $\lambda$  and  $\lambda^*$ . While switching the value of  $\kappa$  has no real notational advantage over switching  $\lambda$  with  $\lambda^*$ , the  $\kappa$ -notation is the notation used by the underlying theory leading up to the model developed in this project.

### 2.1.2 Linear Viscoelasticity

Ice is found near its melting point under normal conditions in nature. Under fast loading conditions, ice can act like a brittle material. However, under slower loading conditions it behaves as a more ductile material. To study the effects that loading rate has on ice, it can be treated as a viscoelastic material.

### 2.1.2.1 Viscoelastic Strains

The overall strain of viscoelastic materials can be divided into four components: elasticity, primary (or delayed elastic) creep, secondary (or viscous) creep, and tertiary creep.

The elastic strain is the instantaneous<sup>1</sup> strain any object feels under stress and is caused by the stretching or compression of atomic/molecular bonding. Upon the removal of stress, this strain will be completely recovered. The instantaneous elastic response of a material is due to the atoms being displaced from, or returning, to their equilibrium positions.

Creep (primary, secondary, and tertiary) is caused by the sliding of grain boundaries (see Section 2.2.2.1) in the ice, as well as the pile up of dislocations (see Section 2.2.2.2.4). Dislocations are imperfections in the ice caused by different materials or the addition or removal of atoms in the lattice structure usually caused by quick, imperfect crystal growth.

Primary creep, also known as delayed elastic creep, is caused by grain boundary sliding. With primary creep, the grains will return to their original locations upon removal of any applied loads, but they require some (non-instantaneous) time to return to their original positions. One model for primary creep, proposed by Andrade (1910), models primary creep as

$$\epsilon_d = \beta t^n \quad (2.18)$$

which compares well with data for time lengths on the order of decades.  $\epsilon_d$  is the delayed strain component,  $t$  is time, and  $\beta$  and  $n$  are material constants ( $n \approx 1/3$ ). Since the grains will eventually return to their original location, primary creep is an

---

<sup>1</sup>note that “instantaneous” in the context of this thesis means “in a really short period of time” - nothing is truly instant and is limited by the speed that information travels in the material (often the related to the speed of sound in the material).

elastic process that is not instantaneous (hence delayed).

Secondary creep, also known as viscous creep, is also caused by grain boundary sliding, as well as dislocation pile-up within grains. Unlike primary creep, the grains and dislocations are unable to return to their original location. This means that the strain from this component is irrecoverable/inelastic, leading to a build up of strain in the ice. Secondary creep follows the well-known Glen's flow law Glen (1955)

$$\dot{\epsilon}_\nu = A \{T\} \sigma \{t\}^q \quad (2.19)$$

where  $\dot{\epsilon}_\nu$  is the strain rate,  $A \{T\}$  is the temperature dependent Arrhenius factor,  $\sigma$  is the stress, and  $q = 3 - 5$  (typically) is the Glen's flow law exponent.

Tertiary creep is caused by the inability of the material to continue building up dislocations and the stoppage of grain boundary sliding. This leads to a build up of stresses that cause the crystal structure to change (damage and grain restructuring), that allow the new grains and dislocations to continue sliding and gliding. Eventually, these changes of the structure will lead to failure of the material, which needs to be explained by fracture mechanics.

### 2.1.2.2 Models of Linear Viscoelasticity

A simple way to model these processes is to represent the material as a combination of elastic springs and viscous dashpots. These springs and dashpots can be combined in many ways to capture the behaviour of a viscous material. Figure 2.4 presents three basic models of viscoelasticity. Figure 2.4a shows a Maxwell unit, which contains a spring and a dashpot in series. The spring of the Maxwell unit represents an elastic component given by

$$\epsilon = \frac{\sigma}{E} \quad (2.20)$$



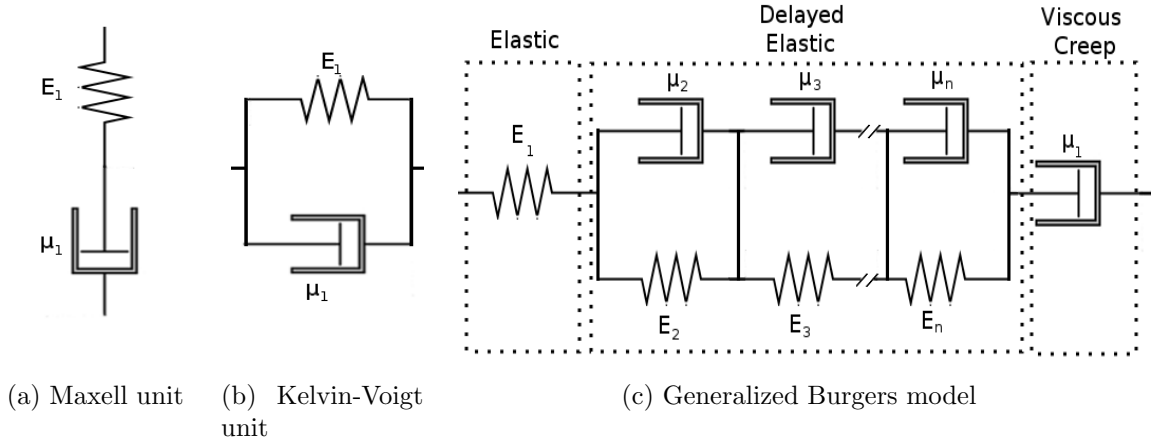


Figure 2.4: Conceptual models of viscoelasticity.

and the dashpot represents the viscous (time-dependent) component, given as

$$\dot{\epsilon} = \frac{\sigma}{\mu_d} \quad (2.21)$$

The spring, represented by  $E_1$  in all three models, is the initial elastic response. The dashpot,  $\mu_1$ , represents the viscous, irrecoverable (secondary) creep. In the case of a constant stress,  $\sigma_0$ , applied from  $t = 0$  to  $t = t_1$  the Maxwell unit can be solved

$$\begin{aligned} \int_0^{t_1} \dot{\epsilon} \{t\} dt &= \int_0^{t_1} \frac{\dot{\sigma} \{t\}}{E_1} dt + \int_0^{t_1} \frac{\sigma \{t\}}{\mu_1} dt \\ \epsilon \{t_1\} &= \left( \frac{1}{E_1} + \frac{1}{\mu_1} t_1 \right) \sigma_0 \end{aligned} \quad (2.22)$$

Equation 2.22 shows that the Maxwell unit has a linear creep response that captures the initial elastic response and a linear viscous term. If the load was removed, the Maxwell unit would show an instantaneous elastic recovery, but some permanent deformation would remain due to the dashpot.

Figure 2.4b shows the Kelvin-Voigt model, which has the spring and dashpot in

parallel. The stress-strain relation for this model can be written as

$$\sigma \{t\} = E_2 \epsilon \{t\} + \mu_2 \dot{\epsilon} \{t\} \quad (2.23)$$

If placed under a constant stress, then the strain in the Kelvin-Voigt model is given by

$$\begin{aligned} \epsilon &= \frac{\int e^{\int \frac{E_2}{\mu_2} dt} \frac{\sigma_0}{\mu_2} dt + c}{e^{\int \frac{E_2}{\mu_2} dt}} \\ \epsilon &= \frac{\sigma_0}{E_2} + ce^{-\frac{E_2}{\mu_2} t} \end{aligned} \quad (2.24)$$

Since the the initial strain in this model is zero then the strain at time  $t = t_1$  is

$$\begin{aligned} 0 &= \frac{\sigma_0}{E_2} + ce^0 \\ c &= -\frac{\sigma_0}{E_2} \\ \epsilon_{t_1} &= \frac{\sigma_0}{E_2} \left(1 - e^{-\frac{E_2}{\mu_2} t_1}\right) \end{aligned} \quad (2.25)$$

If this is followed up by removal of the stress, then the relaxation can be found by setting the initial strain to the value of the strain at  $t_1$ . By solving the ODE

$$\epsilon \{t\} = ce^{-\frac{E_2}{\mu_2} t} \quad (2.26)$$

Using equation 2.25

$$\begin{aligned} \epsilon \{t_1\} &= \frac{\sigma_0}{E_2} \left(1 - e^{-\frac{E_2}{\mu_2} t_1}\right) = ce^{-\frac{E_2}{\mu_2} t_1} \\ c &= \frac{\sigma_0}{E_2} \left(e^{\frac{E_2}{\mu_2} t_1} - 1\right) \end{aligned}$$

which gives the relaxation of strain at time  $t_2$  as

$$\epsilon\{t\} = \frac{\sigma_0}{E_2} \left( e^{\frac{E_2}{\mu_2} t_1} - 1 \right) e^{-\frac{E_2}{\mu_2} t} \quad (2.27)$$

From equation 2.27, the model is able to capture the primary creep response of a viscous material, but due to the dashpot being in series with the spring, equation 2.25 shows that the material has no initial elastic response.

The Generalized Burgers model, shown in Figure 2.4c, is a combination of a Maxwell unit connected in series with one or more Kelvin-Voigt units. In the Burgers model, the Maxwell spring idealizes the instantaneous elastic deformation. The Kelvin-Voigt models represent the primary creep. Having more than one Kelvin-Voigt unit allows for a broad spectrum of creep relaxation times, and providing better fits to experimental data. The Maxwell dashpot represents the secondary creep, which is also dependent on time but is not recoverable upon stress removal.

In linear viscoelasticity, the coefficients  $E_i$  and  $\mu_i$  are independent of stress, they are usually constants for many problems but may depend on other factors such as temperature and ageing effects.

### 2.1.3 Viscoelastic Beam Bending and the Correspondence Principle

To illustrate the properties of viscoelasticity (without fracture), two simple scenarios are discussed below. These scenarios involve an ice beam under 4-point bending, which has a well-known elastic solution. The key concept from these examples is the application of the correspondence principle.

The correspondence principle is the technique that maps an elastic solution to a viscoelastic one. In the first scenario, under static loading, the viscoelastic solution is

found by a quick change of Young's modulus with the inverse creep compliance. In the second case, under non-static loads, a convolution integral is performed to give the viscoelastic solution.

### 2.1.3.1 4-Point Bending

Consider the case of a Burgers model (with one Kelvin unit) ice beam under a 4-point bend (Figure 2.5a) with the following properties

$$\begin{aligned} E_1 = E_2 &= 9 \times 10^9 \text{ Pa} & w &= 0.06 \text{ m} \\ \mu_1 = \mu_2 &= 1 \times 10^{13} \text{ Pa/s} & b &= 0.04 \text{ m} & L &= 0.3 \text{ m} \end{aligned} \tag{2.28}$$

where  $b$  is the thickness,  $w$  is the width,  $L$  is the length, and  $E_1$ ,  $E_2$ ,  $\mu_1$ , and  $\mu_2$  are the viscoelastic parameters. The sign convention shall be positive force and deflection are upwards, positive shear rotates the element clockwise, and positive moment rotates clockwise on the left and counter clockwise on the right (positive moment causes the beam to 'smile' and negative moment causes the beam to 'frown').

The beam is loaded with a force of 2000 N split among two points at  $x_1 = 0.1$  m and  $x_2 = 0.2$  m. The shear and moment diagrams, along with the elastic beam

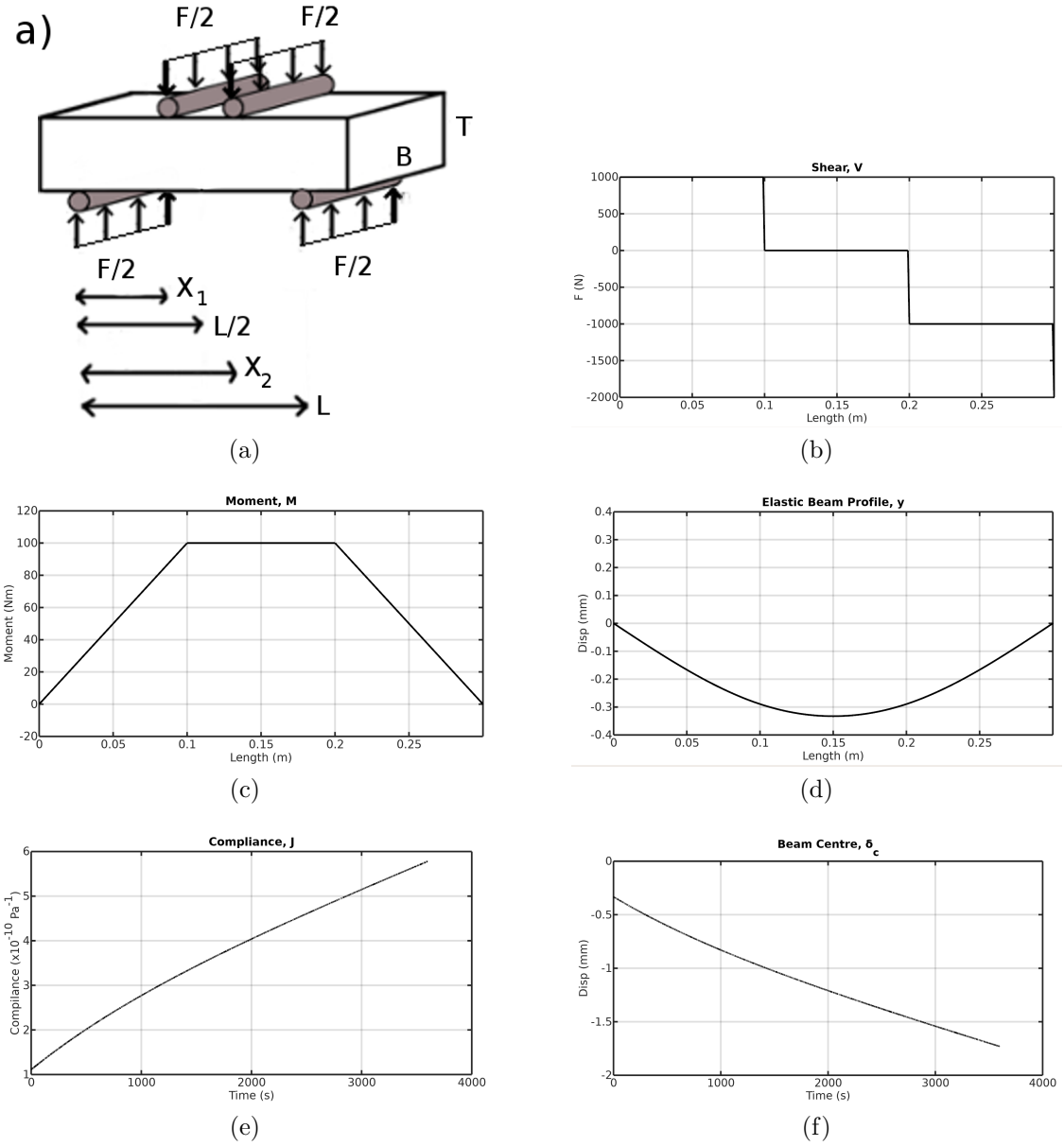


Figure 2.5: a) 4-Point Bending. b) Shear diagram. c) Moment diagram. d) Elastic beam profile (initial viscoelastic response). e) Changing compliance with time. f) Displacement of the midpoint of the beam over time.

solution, are shown in Figures 2.5b—d. For reference, the elastic solution is

$$\begin{aligned}
\frac{\partial^2}{\partial x^2} \left( EI \frac{\partial^2 y}{\partial x^2} \right) &= \frac{F}{2} (\delta\{x\} + \delta\{x - L\}) - \frac{F}{2} (\delta\{x - x_1\} + \delta\{x - x_2\}) \\
V\{x\} &= \frac{F}{2} \Delta\{x\} - \frac{F}{2} \Delta\{x - x_1\} - \frac{F}{2} \Delta\{x - x_2\} + \frac{F}{2} \Delta\{x - L\} \\
M\{x\} &= \frac{F}{2} x \Delta\{x\} - \frac{F}{2} (x - x_1) \Delta\{x - x_1\} - \frac{F}{2} (x - x_2) \Delta\{x - x_2\} \\
&\quad + \frac{F}{2} (x - L) \Delta\{x - L\} \\
y\{x\} &= \left( \frac{F}{12EI} \right) \left( x^3 \Delta\{x\} - (x - x_1)^3 \Delta\{x - x_1\} - (x - x_2)^3 \Delta\{x - x_2\} \right. \\
&\quad \left. + \frac{x}{L} (-L^3 + (L - x_1)^3 + (L - x_2)^3) \right)
\end{aligned} \tag{2.29}$$

where

$$\Delta\{x\} = \begin{cases} 0 & x < 0 \\ 1 & x \geq 0 \end{cases} \tag{2.30}$$

is the Heaviside step function.

Combining equations 2.22 and 2.25 gives the creep compliance of the Burgers model (for a model with only one Kelvin-Voigt unit) as

$$J\{t\} = \frac{1}{E_1} + \frac{1}{E_2} \left( 1 - e^{\left(-\frac{E_2 t}{\mu_2}\right)} \right) + \frac{t}{\mu_1} \tag{2.31}$$

which has been plotted in Figure 2.5e.

For this problem, since the forces and do not change over time, the Correspondence Principle states allows the Young's modulus from equation 2.29 to be replaced with  $1/J\{t\}$  as the effective modulus to get the viscoelastic solution. For the centre

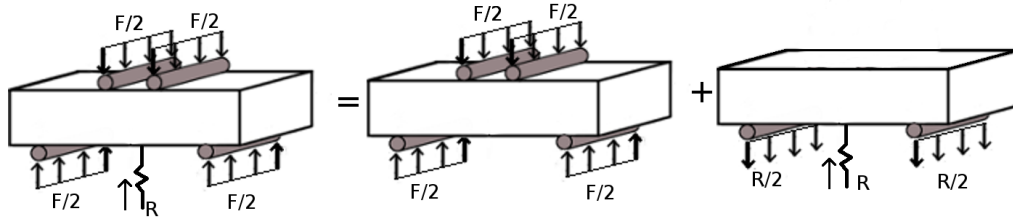


Figure 2.6: Superposition of 4-point bending with spring into 4-point bending problem (like above), and problem with a concentrated force due to the spring alone

displacement,  $\delta_c = y \{L/2\}$ ,

$$\delta_c = \left( \frac{FJ\{t\}}{12I} \right) \left( \frac{L^3}{8} - \left( \frac{L}{2} - x_1 \right)^3 + \frac{1}{2} (-L^3 + (L - x_1)^3 + (L - x_2)^3) \right) \quad (2.32)$$

which is plotted in Figure 2.5f.

From Figure 2.5e, the creep compliance has an initial elastic response, then increases exponentially under primary creep, and becomes linear over longer periods of time as the viscous component becomes dominant. Figure 2.5f shows a similar effect for the centre deflection of the beam - starting at an initial value, slight exponential increase, followed by a linear increase over the long term.

In this case, since the stresses in the beam do not change over time, one could simply replace the elastic compliance with an effective compliance. In the cases where the stresses in the material are changing over time, this will not work as will be shown in the following example.

### 2.1.3.2 4-Point Bending with Elastic spring

When fracture mechanics are considered, the growth of cracks will cause a redistribution of stresses/forces in the material. As an illustrative example of how viscoelastic theory handles changes stresses and forces, consider a beam under 4-point bending as before, but connected to an elastic spring at the centre of the beam, as shown in Fig-

ure 2.6. As the beam deflects downward, the force of the spring will increase, creating a system that has a time-varying force. For this example, consider a Maxwell type material, since a Burgers model would not have an analytical solution - otherwise, using the same parameters as the beam above.

First, the problem is solved for the elastic case by simplifying the problem down into two problems by using the superposition principle. Figure 2.6 shows that the first set up is the same 4-point bending problem solved above (see equations 2.29). The second problem has a concentrated force in the centre caused by the spring as the beam bends downward and has an elastic solution given as

$$\begin{aligned}
\frac{\partial^2}{\partial x^2} \left( EI \frac{\partial^2 y_s}{\partial x^2} \right) &= -\frac{R}{2} \delta\{x\} + R \delta\left\{x - \frac{L}{2}\right\} - \frac{R}{2} \delta\{x - L\} \\
V_s\{x\} &= \frac{R}{2} \Delta\{x\} - R \Delta\left\{x - \frac{L}{2}\right\} + \frac{R}{2} \Delta\{x - L\} \\
M_s\{x\} &= \frac{R}{2} x \Delta\{x\} - R \left(x - \frac{L}{2}\right) \Delta\left\{x - \frac{L}{2}\right\} + \frac{R}{2} (x - L) \Delta\{x - L\} \\
y_s\{x\} &= \frac{1}{6EI} \left( -\frac{R}{2} x^3 \Delta\{x\} + R \left(x - \frac{L}{2}\right)^3 \Delta\left\{x - \frac{L}{2}\right\} \right. \\
&\quad \left. - \frac{R}{2} (x - L)^3 \Delta\{x - L\} \right) + \frac{1}{16EI} R L^2 x
\end{aligned} \tag{2.33}$$

For a given spring constant,  $k$ , the final (elastic) displacement at the centre is given by  $\delta_c = -R/k$ . Using this, with equations 2.29 and 2.33 gives

$$\begin{aligned}
-\frac{R}{k} &= y \left\{ \frac{L}{2} \right\} + y_s \left\{ \frac{L}{2} \right\} \\
-\frac{R}{k} &= -\frac{23FL^3}{1296EI} + \frac{RL^3}{48EI} \\
R &= \frac{23}{27} \left( \frac{FkL^3}{48EI + kL^3} \right)
\end{aligned} \tag{2.34}$$

Replacing  $1/E$  with  $J\{t\}$  will not work since the force from the centre spring,  $R$  becomes  $R\{t\}$  (not constant like  $F$  from the previous example). To solve this problem,



apply the Correspondence Principle to the middle equation from equation 2.34

$$-\frac{R\{t\}}{k} = -\frac{23FL^3}{1296I}J\{t\} + \frac{L^3}{48I} \left[ \int_0^t R\{t'\} \frac{\partial J\{t-t'\}}{\partial t'} dt' + RJ\{0\} \right] \quad (2.35)$$

where the first term is a simple change like before (since  $F$  is constant), but the second term becomes a convolution integral since  $R$  varies in time. Letting

$$J\{t\} = \frac{1}{E_1} + \frac{t}{\mu_1} \quad (2.36)$$

and performing the Laplace transform

$$\begin{aligned} -\frac{1}{k}\mathcal{L}\{R\} &= -\frac{23FL^3}{1296I}\mathcal{L}\{J\} + \frac{L^3}{48I} [\mathcal{L}\{R\}(s\mathcal{L}\{J\} - J\{0\}) + \mathcal{L}\{R\}J\{0\}] \\ \mathcal{L}\{R\} &= \frac{23\mathcal{L}\{J\}FL^3k}{27(48I + \mathcal{L}\{J\}kL^3s)} \end{aligned} \quad (2.37)$$

and converting back into time dimension gives

$$\begin{aligned} A &= \frac{E_1kL^3}{\mu_1(48E_1I + kL^3)} \\ R\{t\} &= \frac{23F}{27} - \frac{368e^{-At}FE_1I}{9(48E_1I + kL^3)} \end{aligned} \quad (2.38)$$

which has the results plotted in Figure 2.7 for a spring constant of  $k = 1 \times 10^8$  N/m.

As before, as time advances, the beam will bend down beyond the initial elastic result plotted in Figure 2.7d. As the bending increases, the elastic spring will apply more force as it is compressed. Figure 2.7f show how the spring reacts changes over time in blue with the elastic solution plotted in red for comparison. Initially, these have the same value, but the Maxwell beam increases the load until it reaches a new equilibrium.

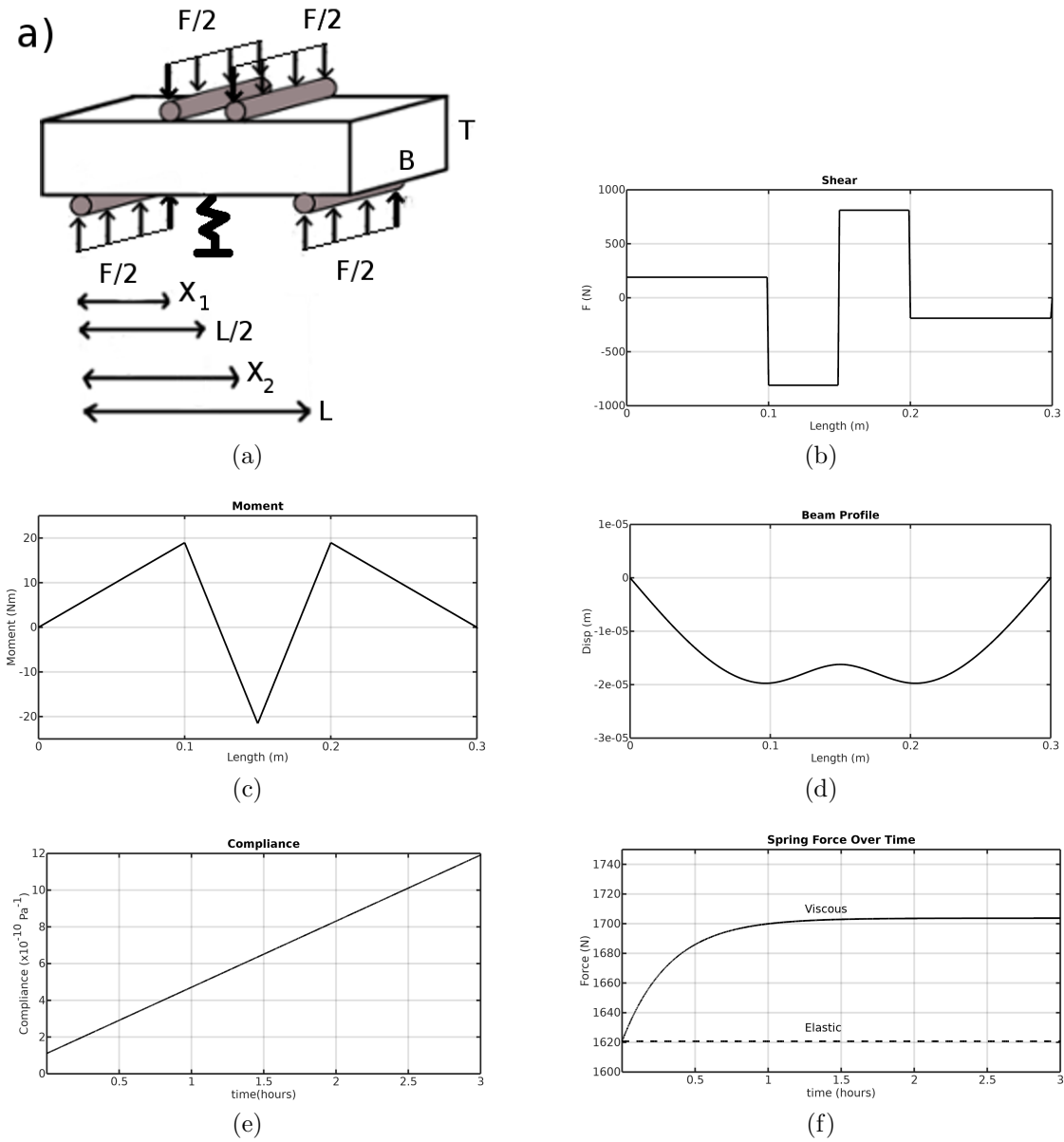


Figure 2.7: a) Setup for 4-point bending with spring. b) Shear diagram. c) Moment diagram. d) Beam profile with centre bump due to spring. e) The Maxwell compliance (linear in time and no primary creep). f) Change in spring reaction force over time

### 2.1.4 Nonlinear Viscoelasticity

For nonlinear viscoelasticity, the three components of strain: elastic, primary creep, and secondary creep are conceptually the same as the linear case. As mentioned previously, the coefficients  $E_i$  and  $\mu_i$  will be functions of stress for a nonlinear viscoelastic material. These functions are often separated into a constant part and a stress-dependent part. These equations will have a similar form to the linear versions, but with stress raised to some power.

#### 2.1.4.1 The Sinha Model and Andrade's Form

One of the earliest models of nonlinear viscoelasticity for ice comes from the works of Sinha (1978, 1979, 1983, 1988) and Glen (1955). In these papers, Sinha performs uniaxial compression tests on a variety of ice samples (usually S2 ice with loading perpendicular to the length of the grains). For constant applied stress,  $\sigma$ , the strain is calculated

$$\begin{aligned}\epsilon_T &= \epsilon_E + \epsilon_d + \epsilon_\nu \\ \epsilon_T &= \frac{\sigma}{E} + c_0 \left( \frac{\sigma}{E} \right)^p (1 - e^{-At^n}) + \dot{\epsilon}_{\nu_1} t \left( \frac{\sigma}{\sigma_1} \right)^q\end{aligned}\tag{2.39}$$

where  $\dot{\epsilon}_{\nu_1}$  is the viscous strain rate for unit stress (e.g., 1 MPa). Sinha noted that both  $A$  and  $\dot{\epsilon}_{\nu_1}$  are temperature-dependent, can be adjusted for other temperatures by using a shift function

$$\begin{aligned}\dot{\epsilon}_{\nu_1} \{T_1\} &= \frac{\dot{\epsilon}_{\nu_1} \{T_2\}}{S_{1,2}} \\ A \{T_1\} &= \frac{A \{T_2\}}{S_{1,2}} \\ S_{1,2} &= \exp \left\{ \frac{Q}{R} \left( \frac{1}{T_1} - \frac{1}{T_2} \right) \right\}\end{aligned}\tag{2.40}$$

where  $Q = 65$  kJ/mol is the activation energy for ice,  $R=8.314$  J/K·Mol is the ideal gas constant, and the temperatures are given in Kelvin units.

Sinha proposes that primary creep is caused by grain boundary sliding, meaning that it will be affected by the size of the grains in the ice sample. Sinha starts with the strain due to grain boundary sliding as

$$\epsilon_{gbs} = K_{gbs} \bar{x} d^{-1} \quad (2.41)$$

where  $\bar{x}$  is the mean boundary displacement,  $d$  is the average grain diameter, and  $K_{gbs}$  is a constant. As a first approximation, one can assume that  $\epsilon_d = \epsilon_{gbs}$ . Following the work of Langdon (1973),

$$\frac{\epsilon_{gbs}}{\epsilon_T - \epsilon_E} = \frac{\epsilon_d}{\epsilon_T - \epsilon_E} = \left[ 1 + \eta \frac{d}{d_1} \left( \frac{\sigma}{\sigma_1} \right)^p \right]^{-1} \quad (2.42)$$

Sinha develops a grain-dependent primary creep as

$$\epsilon_d = \frac{c_1 d_1}{d} \left( \frac{\sigma}{E} \right)^p (1 - e^{-At^n}) \quad (2.43)$$

where  $d_1$  is the unit grain size, and  $c_1$  is a constant (such that  $c_1 d_1 = c_0 d$ ).

The Sinha model of primary creep, based on grain boundary sliding, provides a physical basis for the delayed elastic response in viscoelastic materials. In practice, the model does not completely predict the delayed elastic response. This can be attributed to the model being represented by a single Kelvin-Voigt unit in the Burgers model representation.

Many viscoelastic materials require more than one Kelvin-Voigt unit in the Burgers model to capture the full delayed elastic response of the material. The  $\beta$ -flow

approximation of Andrade (1910) is given by

$$\epsilon_d \approx \beta t^n \quad (2.44)$$

as mentioned in Section 2.1.2.1 and shown in Section 7.2.1. This form of the delayed elastic considerably easier to implement for solving viscoelastic problem than employing a multitude of Kelvin-Voigt units, and is found to be accurate for several decades. The one drawback is that, unlike the Sinha model, there is no upper bound on the maximum delayed elastic strain. While this one drawback is unrealistic as grains can only slide so much (e.g., becoming locked at a triple point), provided the problem works within the limits of the  $\beta$ -flow approximation, then it is expected to give better results than the Sinha model of delayed elastic strain.

#### 2.1.4.2 The Schapery, LeClair, and Dempsey Model

The model developed in Schapery (1997) and LeClair et al. (1999), is generalized nonlinear model. Unlike Sinha's model, which was developed using step loading applied stress, the Schapery, LeClair, and Dempsey model can be applied to any time-dependent stress loading (albeit numerically). The model is of the form

$$\begin{aligned} \epsilon_T &= \epsilon_E + \epsilon_d + \epsilon_\nu \\ \epsilon_T &= C_0 \sigma \{t\} + C_1 \int_0^t (t - t')^b \partial_{t'} \sigma^p \{t'\} dt' + C_2 \int_0^t \sigma^q \{t'\} dt' \end{aligned} \quad (2.45)$$

where the  $\beta$ -flow is modified into hereditary integral since the stress does not have to be a constant anymore. For an applied step loading, equation 2.45 takes the form of Sinha's model (equation 2.43), with the  $\beta$ -flow approximation for primary creep.

For non-constant loading scenarios, such as ramping until failure, this model provides good estimation to the expected viscoelastic response under uniaxial loading

without failure. This model has been incorporated into the fracture model developed in this thesis.

## 2.2 Atomic Properties of Ice

While the typical approach to modelling materials tends to use continuum mechanics (as will the theory presented in this thesis), looking closer at the atomic properties of materials provides insights into the behaviour of the material. Due to the continuum nature of the proposed model, many of the underlying mechanisms presented in this section are only briefly mentioned throughout the remainder of the text.

While these topics discussing the underlying physical mechanisms of viscoelastic behaviour will not be referred to much beyond this chapter, knowledge of these concepts provided many insights into the developed theory, and provides a physical basis as to the assumptions used in the proposed model.

The macroscopic properties of materials are a consequence of the underlying properties of the complex interactions of atoms and molecules. Understanding the motions and interactions of atoms and molecules provides an explanation of many of the rheological properties of materials such as elasticity, plasticity, and viscoelasticity. The temperature-related properties of materials (including the rheological ones) are related to the kinematic energy of the particles, as well as the bonding between those particles.

In particular to ice, looking at the properties of oxygen and hydrogen, primarily their bonding properties, reveals many of the properties of water and ice that make it a unique material.

## 2.2.1 Atoms and Molecules

### 2.2.1.1 Hydrogen

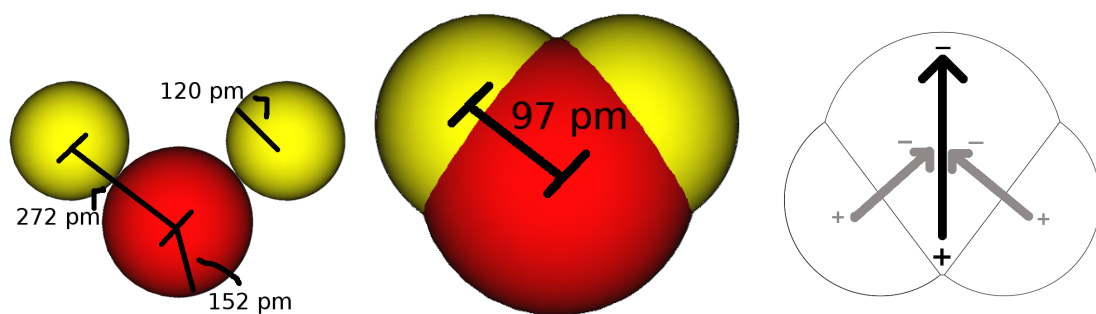
Hydrogen is a colourless, odourless, highly combustible, diatomic gas (under normal conditions) with an atomic mass of 1. Its most common form consists of a proton with a single electron orbiting in the  $1s^1$  shell. The single electron is the hydrogen's valence shell electron used in bonding with other atoms, by either accepting an electron to fill the shell (the  $1s$ -shell can only have two electrons due to the Pauli-exclusion Principle) or donating the electron to empty the shell. It has a covalent bonding radius of  $31 \pm 5$  pm and a Van der Waals radius of 120 pm.

### 2.2.1.2 Oxygen

Similar to hydrogen, oxygen is a colourless, odourless, highly reactive diatomic gas under normal conditions. By Mass, Oxygen is the 3<sup>rd</sup> most abundant element in the universe after hydrogen and helium. Oxygen has an atomic mass of 15.999 and an electron configuration of  $1s^2 2s^2 2p^4$ . The two s-shells of Oxygen are full, but the 2p-shell can hold up to 6 electrons, meaning that oxygen can accept two electrons to fill its valence electron orbital. Oxygen has a covalent bonding radius of  $66 \pm 2$  pm and a Van der Waals radius of 152 pm.

### 2.2.1.3 Water

Water, chemically known as dihydrogen monoxide, is formed from the covalent bonding of oxygen and two hydrogen atoms. In a covalent bond, electrons are shared between two atoms. From the sections above, hydrogen can be seen as having an extra electron to share and oxygen can be seen as needing two electrons to complete its valence electron shell (atoms are more stable when they have full valence shells,



(a) Water molecule at Van der Waals distance, representing atoms by the size of their covalent bonding size (size of valence shell); Black is oxygen, grey is hydrogen.  
 (b) Water molecule at the covalent bonding distance, showing the water molecule's actual shape as less V-shaped and a bit more rotund  
 (c) 2D water molecule showing the polarization of the water molecule due to the electronegativity differences in the oxygen and hydrogen atoms.

Figure 2.8: The water molecule. Oxygen coloured in red, hydrogen coloured in yellow.

like helium and other noble gases). From a classical perspective, it can be said that two hydrogen atoms each give their electron to the oxygen when they bond with it. From a quantum mechanical perspective, it can be said that the electron probability cloud, that was originally centred on the nucleus of the hydrogen atom, is now elongated towards the oxygen atom. This means that the shared electron is orbiting both atoms, but is more likely to be near the oxygen atom than the hydrogen atom, but it is not separated from the hydrogen atom in a covalent bond.

The O-H bonds in a water molecule are about 97 pm in length, and have an angle of roughly  $106^\circ$  between them (Petrenko and Whitworth, 1999). Comparing the bond length to the covalent radii and Van der Waal radii shows that the bond length is equal to the sum of the covalent radii, indicating that the electron shells overlap (as stated above and shown in figure 2.8).

Electronegativity refers to an atom's ability to accept electrons, and electropositivity refers to an atom's ability to donate electrons. These properties are essentially the opposite of each other and simply put: the more electronegative an atom determines which atom will receive the electron during a covalent bond. Since oxygen is



more electronegative than hydrogen (3.44 vs. 2.20 on the Pauling scale), then a single O-H bond will have an electric dipole with a positive terminal on the hydrogen, and a negative terminal on the oxygen, this is shown in figure 2.8c as a grey arrow. In water, due to the symmetry of the placement of the atoms, the two grey dipoles in figure 2.8 combine to give a single strong dipole for water. The dipole for water is shown by a black arrow in figure 2.8 with a strong negatively charged oxygen atom and two positively charged hydrogen atoms. This dipole will become important as the water cools down and becomes ice.

#### 2.2.1.4 Ice

For materials in a gaseous state, the kinetic energy of an atom or molecule can be calculated by

$$K_E \{T\} = \frac{3}{2}kT \quad (2.46)$$

where  $T$  is the temperature in Kelvins, and  $k = 1.38 \times 10^{-23}$  is the Boltzmann constant. For gases, this energy would allow the molecules to move around with velocities close to those given by

$$K_E \{v\} = \frac{1}{2}mv^2 \quad (2.47)$$

since there are minimal forces acting on a gas molecule.

For liquid water, there will be attractive forces between the molecules due to electric dipoles in the water molecules. Normally, this force is called the dipole-dipole interaction, but due to the particularly strong dipoles of O-H bonds, it is given the special name of hydrogen bonding. Unlike gases, due to the intermolecular attractive forces, there is no simple theory to relate the velocity of the molecules to the temperature (Born and Green, 1946). The energy of the molecules will still be related to the temperature as above, but the velocity will be lessened due to the potential

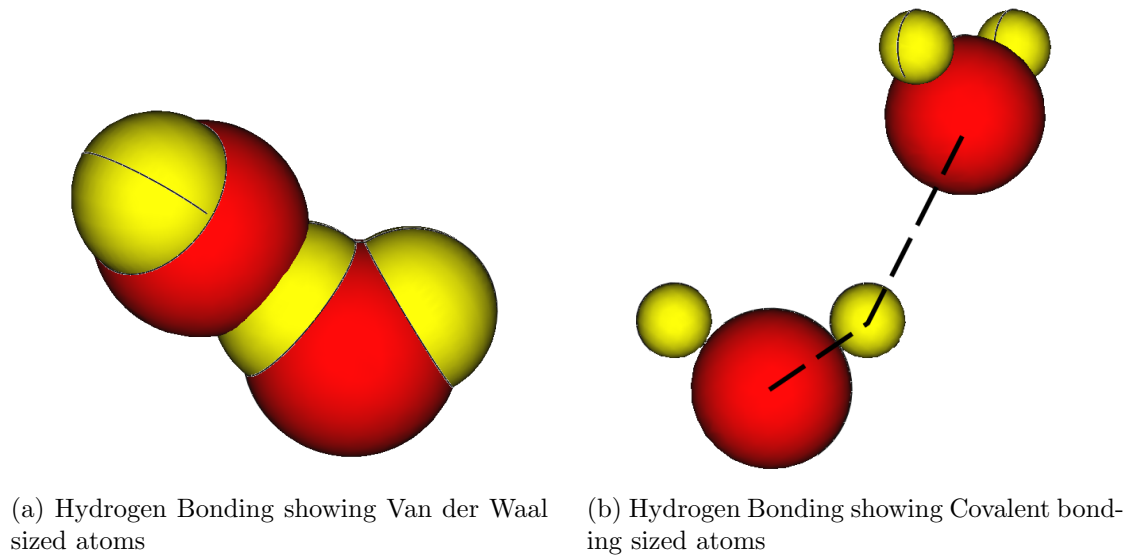


Figure 2.9: Hydrogen bonding between water molecules.

energy of the dipole bonds (there is another force call the London-dispersion force, but it much weaker than covalent and hydrogen bonding).

As a liquid, the water molecules are more confined than as a gas, but do have relative free motion to move within the bounds of the liquid, even allowing oxygen and hydrogen atoms to swap partners. In water, the molecules will bond to three other molecules and will have a hydrogen bonding distance of roughly 178 pm between the oxygen atoms.

As the liquid is cooled, the kinetic energy of the molecules continues to decrease, while the hydrogen bonding strength remains relatively constant. As the water undergoes its phase transition into ice, the molecules start to form solid bonds with each other due to hydrogen bonding becoming more dominant as the molecules slow down. As the molecules are locking into their final positions in ice, they form hydrogen bonds to a fourth molecule. Due to the increased number of interactions caused by more and more molecules moving into closer proximity, the molecule's angle becomes a little wider, about  $109.5^\circ$ , and the oxygen atoms settle around 275 pm apart

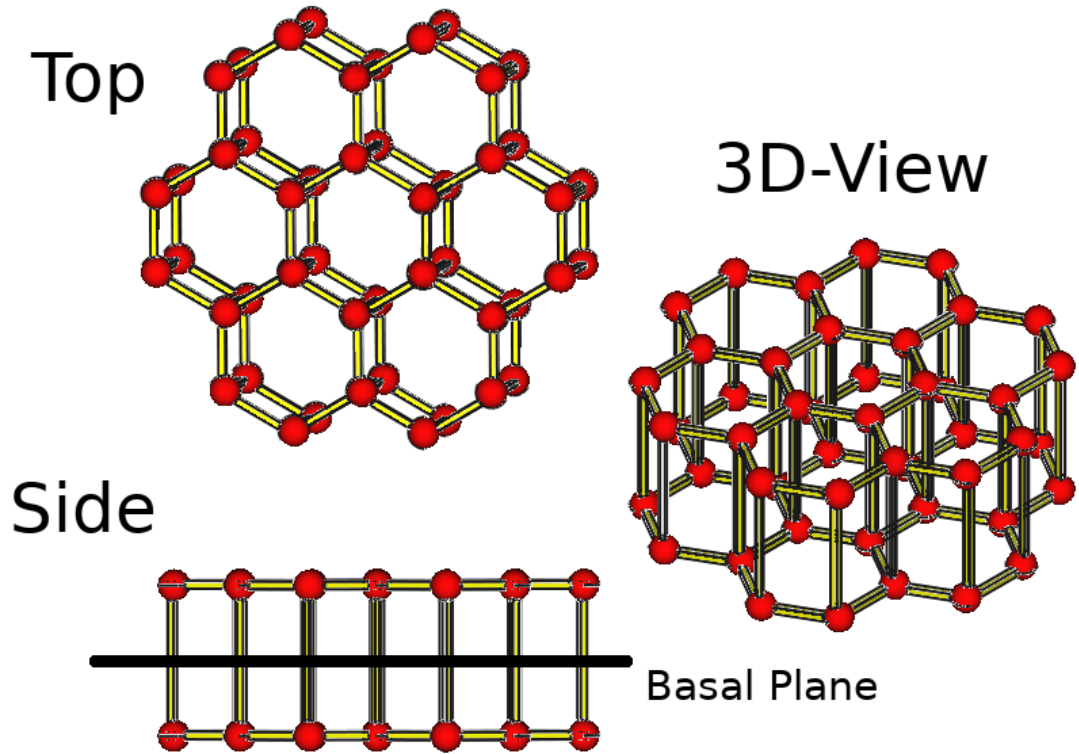
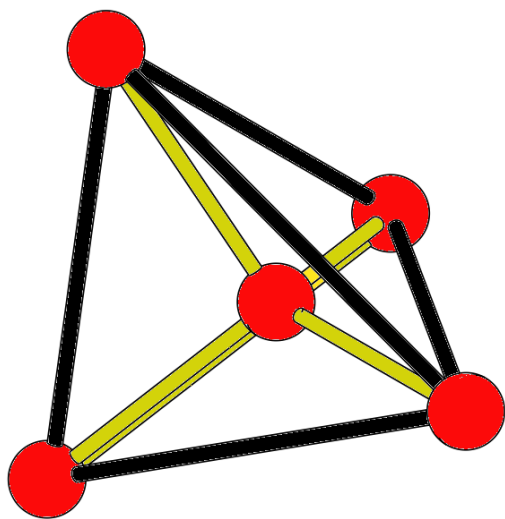


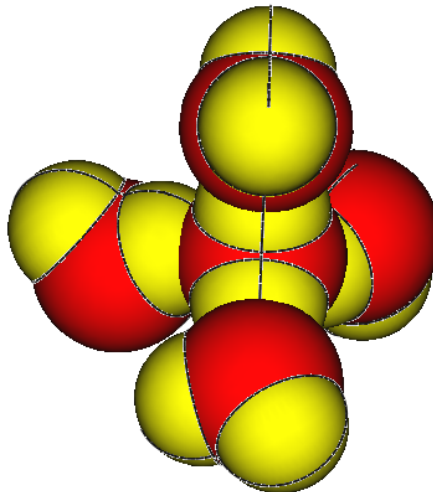
Figure 2.10: The ice crystal lattice

(Petrenko and Whitworth, 1999; Fanourgakis and Xantheas, 2006), which is close to the Van der Waals distance for the atoms in the water molecule from figure 2.8a . Figure 2.9 shows the bonding between two water molecules in ice. Figure 2.9a shows the atoms at Van der Waals sizes to show a true shape of the molecules and that both oxygen atoms are bonded to the hydrogen atom. Figure 2.9b shows the atoms at their covalent bonding sizes to show that one oxygen atom is in a covalent bond with the shared hydrogen atom and the other oxygen is bonded to the hydrogen by hydrogen bonding. The bonding path (path along the covalent and hydrogen bonding) is not actually straight, as often depicted for simplicity (as is done in figure 2.10).

Figure 2.10 shows a simplified view the final position of the water in an ice lattice. The top view looks down on the crystallographic c-axis of ice. The red circles are the



(a) Simplified tetrahedral water/ice bonding arrangement. Yellow lines show atomic bonds; Black lines show tetrahedral shape.



(b) tetrahedral bonding arrangement using Van der Waals sizes for atoms

Figure 2.11: Water molecules bonding in a tetrahedral formation. There are 6 variations to this bond that allow them to combine to form a hexagonal lattice.

oxygen atoms and the bonds between the oxygen atoms, where each bond is the sum of the covalent bond and the hydrogen bond. The two simplifications in this model are the hydrogen atoms are not shown, but it is implied that each bond contains one hydrogen atom covalently bonded to one oxygen and hydrogen bonding to the other. Secondly, the plane of oxygen atoms is not quite planar, but some oxygen atoms are elevated above the others, due to the tetrahedral bonding depicted in figure 2.11

To see why ice forms a hexagonal lattice (as shown in the 3D view of Figure 2.10), consider the basic tetrahedral shape that the bonds form in Figure 2.11a. In Figure 2.11a, the yellow connections are the actual hydrogen-oxygen bonds (these are physical bonds; consisting of the covalent- and OH- bonds that existed between any two oxygen atoms) and the black connections outline the basic tetrahedral shape (they are not physical bonds; purely illustrative).

Figure 2.12a stacks these tetrahedral elements on top of each other. This figure

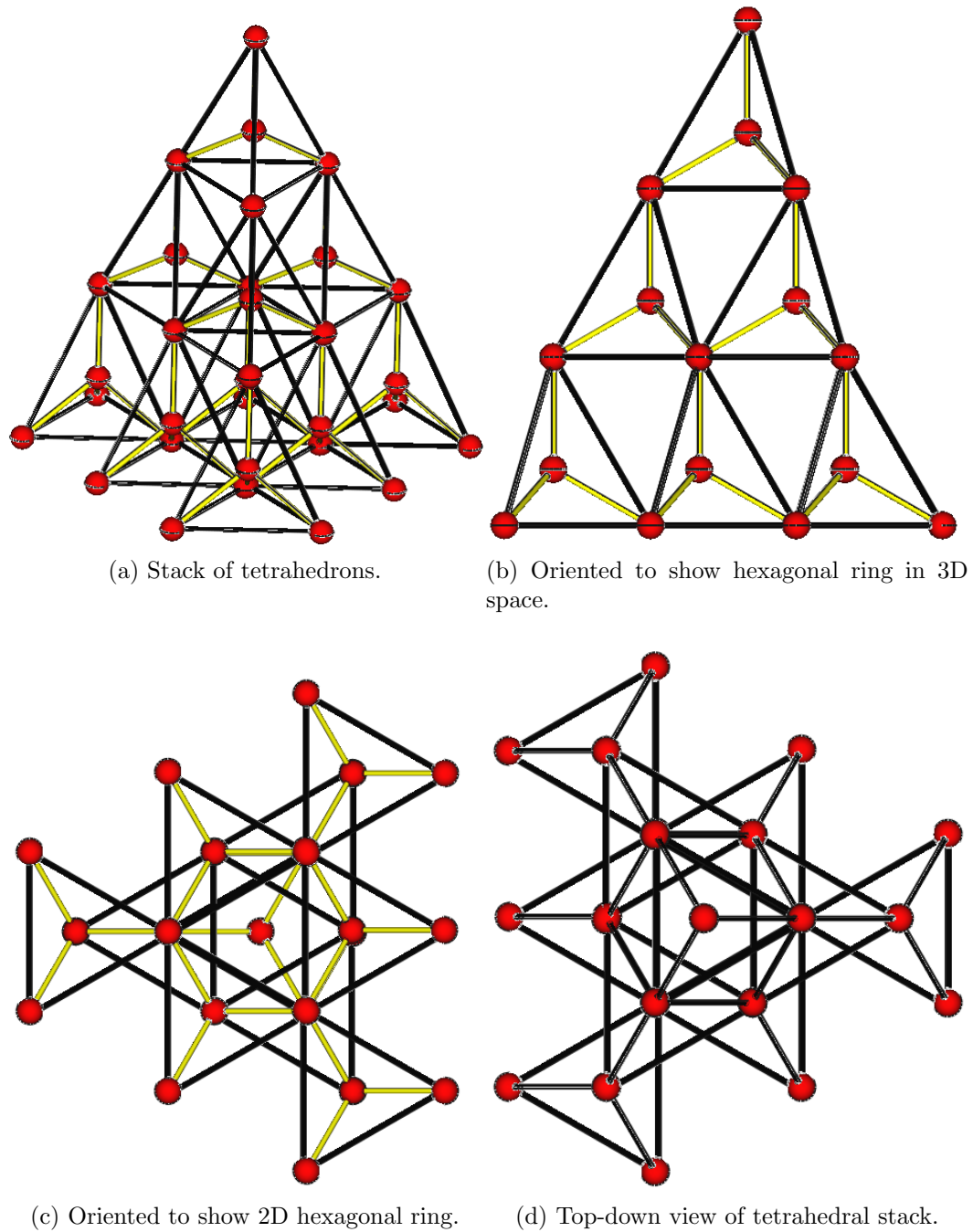


Figure 2.12: Various views showing how stacking tetrahedral elements leads to the hexagonal lattice structure in ice.

was generated by starting with a single element at the top, and placing other elements, such that the top atom of the new elements coincide with the bottom atoms of the first element at the top. The bottom layer was formed in the same manner by making the top atoms of the bottom elements coincide with the bottom atoms in the middle layer.

While the hexagonal pattern is somewhat visible in Figure 2.12a, Figure 2.12b shows the hexagonal rings a little clearer (it is simply a rotation of Figure 2.12a). Figure 2.12b shows how the 3D nature of the tetrahedron gives rise to the formation of hexagonal rings that appear in the (yellow) physical bonds of the atoms. In this view, it is clear that the hexagonal rings are not flat (as simplified in Figure 2.10), but are twisted in 3D space.

Figure 2.12c shows a more 2D-like view of the hexagonal ring formed by the tetrahedrons. Aside from the central hexagon, one can see the beginnings of the neighbouring hexagons and provides a similar view as the one depicted in the top view of Figure 2.10.

While the black connecting lines are not physical, a top-down view of the stack of tetrahedrons (Figure 2.12d) shows that they also exhibit a repeating, hexagonal shape, similar to Figure 2.12c. What Figures 2.12c and 2.12d show is that the (non-physical) black connections are directly above the (physical) yellow connections. This eludes to the typical alternating stacking pattern seen in hexagonal lattices (often called A-B-A-B stacking). In the case of ice, this amounts to saying that every oxygen atom in the top layer is directly above the center of a hexagon formed by six oxygen atoms in the layer below (unless near the edge of a lattice).

The tetrahedral-shaped bonding in ice is due to the positioning of the electron orbitals in the water molecule (Hobbs, 1974). Of the ten electrons in a water molecule, two orbit the 1s shell near the oxygen; four of the electrons lie in the bonding pair

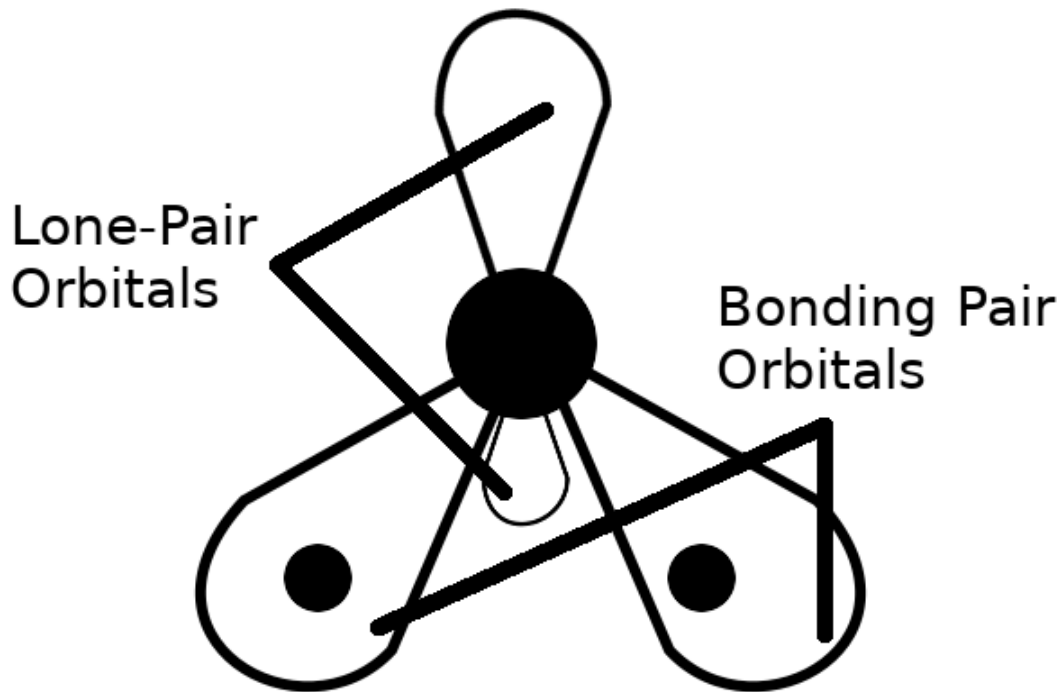


Figure 2.13: Electron bonding orbitals in a water molecule.

orbitals connecting the atoms; and four lie in two lone-pair orbitals. These orbitals are depicted in Figure 2.13. The top lone pair orbital defines the top of the tetrahedron, and the bottom lone pair defines the back corner of the tetrahedron (it is drawn smaller to indicate into the page), and the hydrogen atoms are placed in the remaining two corners (these would be coming out of the page).

What is interesting with the hydrogen bonding in ice is that once it dominates the positioning of the molecules, the molecules are further apart than they were as a liquid since the kinetic energy of the atoms is no longer able to overcome the hydrogen bonding. Combined with the increased angle between the hydrogen atoms, increases the distance between any two water molecules. This is the reason why ice is less dense than water.

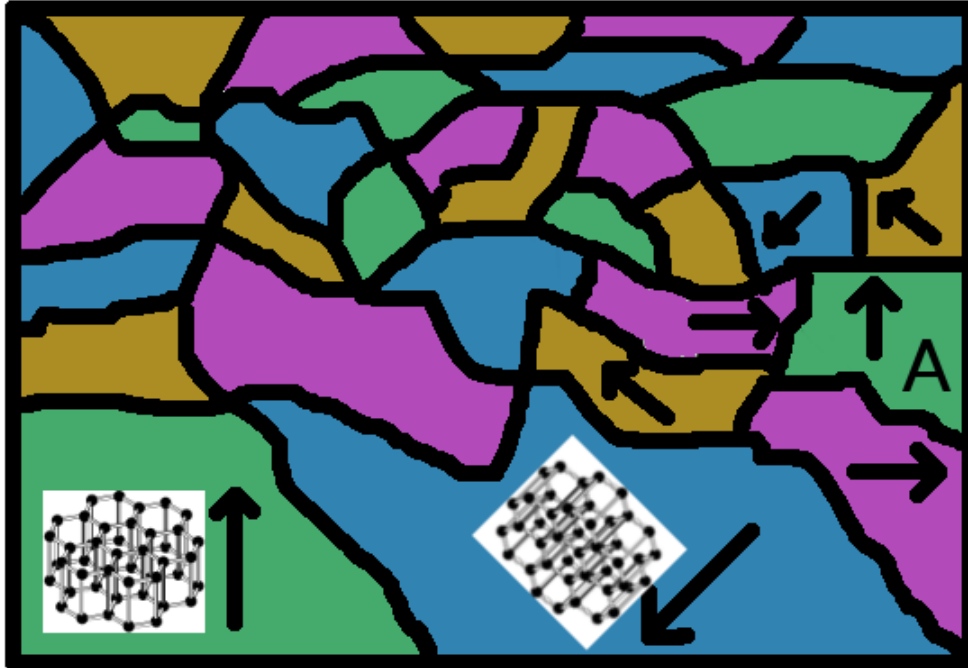


Figure 2.14: A typical Cross-sectional cut of ice. Solid lines show grain boundaries, arrows and colours indicate c-axis of grain (all in-plane for simplicity).

## 2.2.2 Lattice Defects

### 2.2.2.1 Grains

While it is possible for ice to grow from water into a single, perfect lattice, this is not very likely and only occurs under careful laboratory control. For freezing to occur in water, there have to be nucleation sites - sites in the water that the molecules join together. Often this will be at an impurity such as another molecule or air bubbles but can also be a place with a higher concentration of water molecules. Naturally, there will be many nucleation sites for ice to grow from (such as snowflakes landing on a river about to freeze over). This means that a block of ice will have many different lattices growing that will have different orientations and sizes. Due to the solidification process, once molecules are locked into place, there is little movement and re-arrangement allowed. The end result will be that the ice block will be made



up of many lattices that meet up and are unable to change. These lattices are called grains, Figure 2.14 shows how grains of different sizes and orientations meet up in a material such as ice.

Grains play an important role both the viscoelastic and fracture properties of ice. When grains are placed under load, they will slide across one another - called grain boundary sliding (Raj and Ashby, 1971). The sliding of the grains allows the ice to relieve stress and is related to the delayed elastic response of ice since the grains can return to their original locations over time, provided no other mechanism prevents them from doing so.

Due to the discontinuity of the material at the grain boundary, grain boundaries are also sites of stress concentrations (especially if it a triple-point intersection of three grains). Once a grain cannot slide any further (typically on the order of Angstroms), stress can build up along the boundary, leading to the formation of cracks due to inability to relieve stress. Conversely, the build up of stress may attract dislocations leading to a change in the shape of the grains, which may allow more sliding if the surfaces of the grains become more compatible.

#### **2.2.2.2 Dislocations**

Dislocations are curvilinear defects in the crystal lattice structure of a material. These can occur because of missing or extra molecules, dislocated molecules from applied forces, or missing bonds between molecules.

Dislocations are caused by the imperfect growth of a crystal lattice. In the case of ice, a perfect lattice will have a hexagonal shape with oxygen atoms at the vertices. The hexagonal shape is a product of the strong, directional forcing from the hydrogen bonding between the water molecules. For a slow, controlled freezing, the water molecules will be able to place themselves in the perfect positions that minimize the

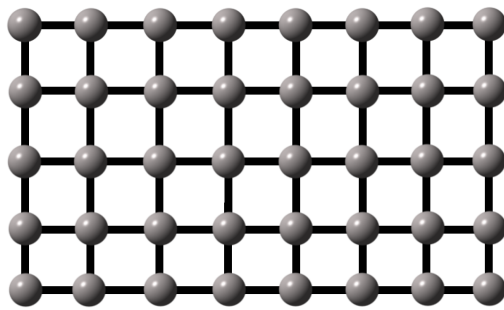
potential energy (i.e., the perfect lattice). Under most freezing, molecules do not have the time to reach the minimum energy configuration before they are locked into place as a solid. Impurities in the water, such as air bubbles and trace amounts of other molecules, will also affect the water's ability to form perfect lattices since the ice will likely have to incorporate those into its final solidified form.

Dislocations play an important role in the non-recoverable strain of materials, as they are the physical mechanisms that cause creep in ice (Taylor, 1934). As will be discussed, dislocations are able to move around in the material, changing the local stress and strain fields in non-recoverable ways.

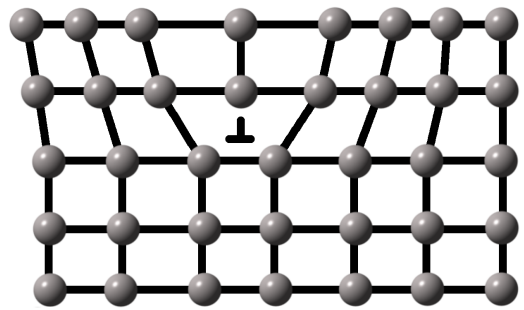
There are two main types of dislocations that have a variety of ways that they can move and get past obstacles. These motions, described in the following sections, lead to the creep behaviour of ice. Eventually, the dislocations will no longer be able to move via their methods of motion. This will lead to a build up of stress in the ice that can lead to tertiary creep and fracture in ice.

#### **2.2.2.2.1 Edge Dislocations**

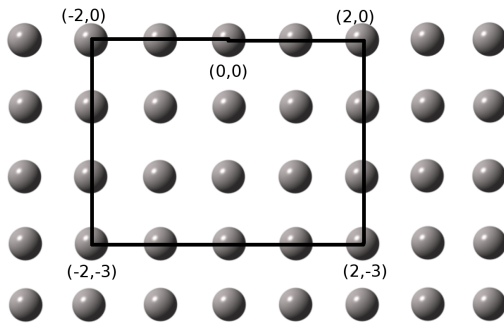
Edge dislocations are caused by the insertion or lack of a partial row/column of atoms that interrupts the normal, perfect arrangement of atoms of a perfect lattice. In ice, edge dislocations tend to form on the non-basal plane (Petrenko and Whitworth, 1999). Figure 2.15a shows a perfect 2-D lattice of atoms as a simple example. In the perfect lattice, all the atoms are bonded to their neighbours forming a square crystal lattice (cubic in 3-D). Figure 2.15b shows the same crystal, but with an edge dislocation occurring in the fourth column of atoms. In this case, the atoms that would have normally occupied the bottom of the third and fifth columns are able to move inward and fill the gap. This causes their bonds to be longer than the ideal condition, causing tension in the bottom of the lattice. At the top, the atoms in columns three



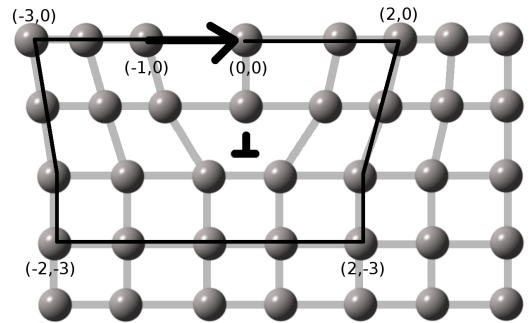
(a) A perfect lattice



(b) An edge dislocation caused by missing atoms in the fourth column



(c) Burgers Vector of a perfect lattice



(d) Burgers Vector of an edge dislocation

Figure 2.15: Edge dislocation

and five will be placed a bit closer to their neighbouring atoms along the sides of the dislocation, putting the top part of the material in a state of compression. Figure 2.15b also shows how the atoms near the dislocation are displaced a fair amount, but the atoms further away are less affected (column 8 in the figure has not moved from the ideal, which will be true of atoms even further away).

A useful property of dislocations that is used in many theoretical calculations is the Burgers vector. To determine the Burgers vector of a dislocation, a path is drawn around the dislocation using the atoms as grid points on a coordinate axis. Each atom counts as one step, steps are only allowed across bonds, and the number steps along a direction must cancel (e.g, if you move left two atoms, then you must move right two atoms later). For example, consider the perfect crystal in Figure 2.15c. Set the origin at the top atom in column three. Move two right, three down, four left, three up, and two right. From the coordinate movements

$$\begin{array}{lll}
 x & : & 2 - 4 + 2 = 0 \\
 y & : & -3 + 3 = 0 \\
 \textit{Start} & : & (0, 0) \\
 \textit{Finish} & : & (0, 0) \\
 \textit{Burgers} & : & \textit{Start} - \textit{Finish} = (0, 0)
 \end{array}$$

the distances moved along x (left/right) and y (up/down) directions cancel out. For the perfect lattice, this path ended at the starting point giving a Burgers vector of (0,0). Now consider the same path in Figure 2.15, due to the rearrangement of the

atoms and new bonds formed

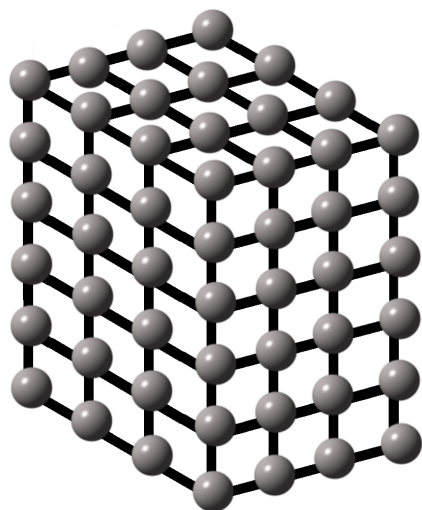
$$\begin{aligned}
 x & : & 2 - 4 + 2 & = 0 \\
 y & : & -2 + 3 & = 0 \\
 Start & : & (0, 0) \\
 Finish & : & (-1, 0) \\
 Burgers & : & (0, 0) - (-1, 0) & = (1, 0)
 \end{aligned}$$

the end point does not return to the starting point. This can be achieved by moving one more atom to the right, giving the Burgers vector as (1,0).

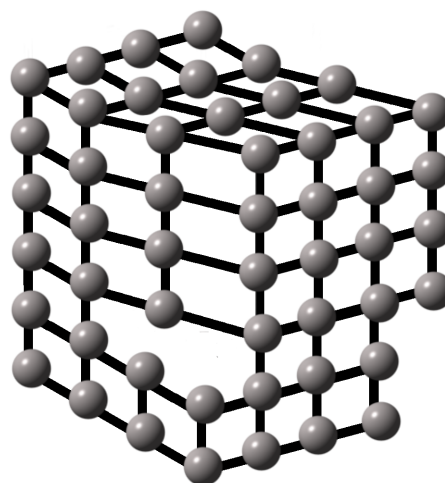
#### 2.2.2.2.2 Screw Dislocations

The second type of dislocation is the screw dislocation. This type of dislocation is a bit harder to visualize than an edge dislocation. While conceptually more difficult, the screw dislocation is the most common dislocation type in ice as its Burgers vector lies parallel to the hexagonal symmetry of ice and glides across the basal plane.(Hobbs, 1974; Petrenko and Whitworth, 1999).

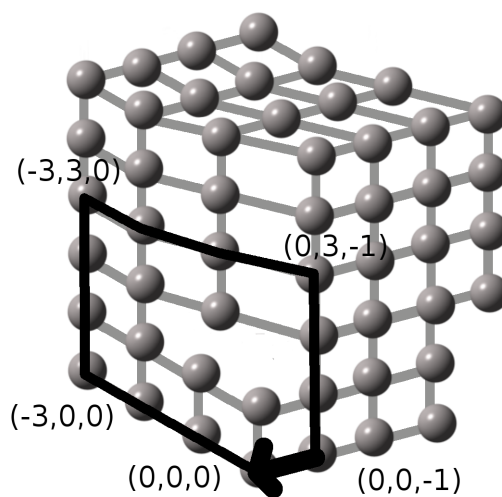
In a screw dislocation, a plane of atoms has been split into two planes. Figure 2.16a shows a perfect arrangement of atoms in a cubic lattice. Figure 2.16b shows a screw dislocation in the lattice. As an analogy, it is as if the first column of atoms were split as if tearing a piece of paper. One of those edges bonds with the next column of atoms while the other will bond into the previous column of atoms that have moved up (not shown). This provides a means to walk along a path of atoms from one plane to another, much like a parking garage. The name screw dislocation comes from the fact that the Burgers vector is found by defining a path that winds down the axis of the dislocation, like the inclined plane that wraps around the core



(a) A perfect 3-D lattice



(b) A screw dislocation



(c) Burgers vector for a screw dislocation

Figure 2.16: Screw Dislocation

	Edge	Screw
Dislocation width, $d$	$\perp$ to $b$	$\parallel$ to $b$
Dislocation motion, $v$	$\parallel$ to shear	$\perp$ to shear

Table 2.1: Properties of dislocations.  $b$  is Burgers vector,  $d$  is the direction along the width.  $v$  is direction of motion.

of the screw.

In the same fashion as the edge dislocation, a Burgers vector can be defined for a screw dislocation by walking along a surface. Figure 2.16c follows a path along the bonds that goes: 3 left, 3 up, 3 right, 3 down giving

$$\begin{aligned}
 x &: 3 - 3 = 0 \\
 y &: -3 + 3 = 0 \\
 Start &: (0, 0, 0) \\
 Finish &: (0, 0, -1) \\
 Burgers &: (0, 0, 0) - (0, 0, -1) = (0, 0, 1)
 \end{aligned}$$

unlike the edge dislocation, the Burgers vector for a screw dislocation will be perpendicular to the plane of atoms.

### 2.2.2.2.3 Dislocation Loops and Mixed Dislocations

Table 2.1 shows the properties of pure edge and screw dislocations discussed so far. For both types, it was assumed that the dislocation went all the way through the lattice. Considering that dislocations define the slip plane of a lattice, it makes sense that a dislocation cannot go only part way through a lattice. For example, in thinking of the screw dislocation as a parking garage, one can travel down through the entire lattice by driving around the screw dislocation line. It cannot be the case for a lattice that driving down the screw dislocation only gets one halfway down before being stuck

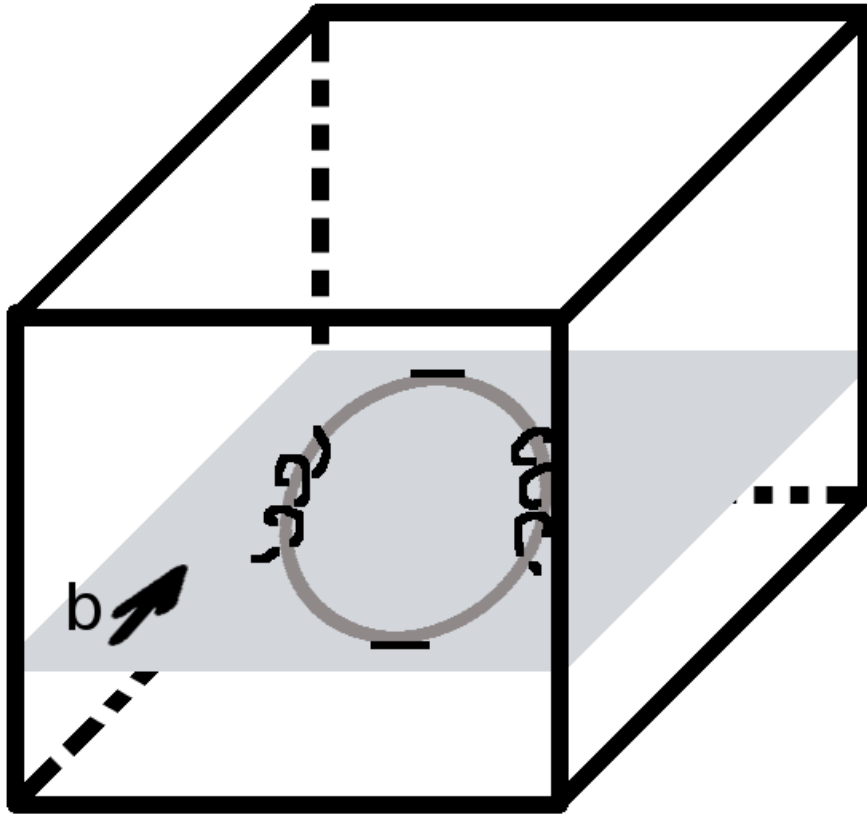


Figure 2.17: Dislocation loop with marked edge and screw dislocations. Mixed dislocations occur between the two types, acting as a transition between them.

in a plane of atoms. For a dislocation to exist in a lattice its ends must either reach the end of a lattice or connect both of its ends to form a dislocations loop, as shown in Figure 2.17.

#### 2.2.2.2.4 Dislocation Glide

Dislocation glide is one of the mechanisms for the motion of dislocations. Figure 2.18 shows the formation of an edge dislocation in a perfect lattice. Due to the applied shear, a slip plane develops around the center of the atoms, where the dislocation forms. The shear causes the top atoms to slide relative to the bottom atoms, causing them to break and form new bonds with new partners. The minimum shear required



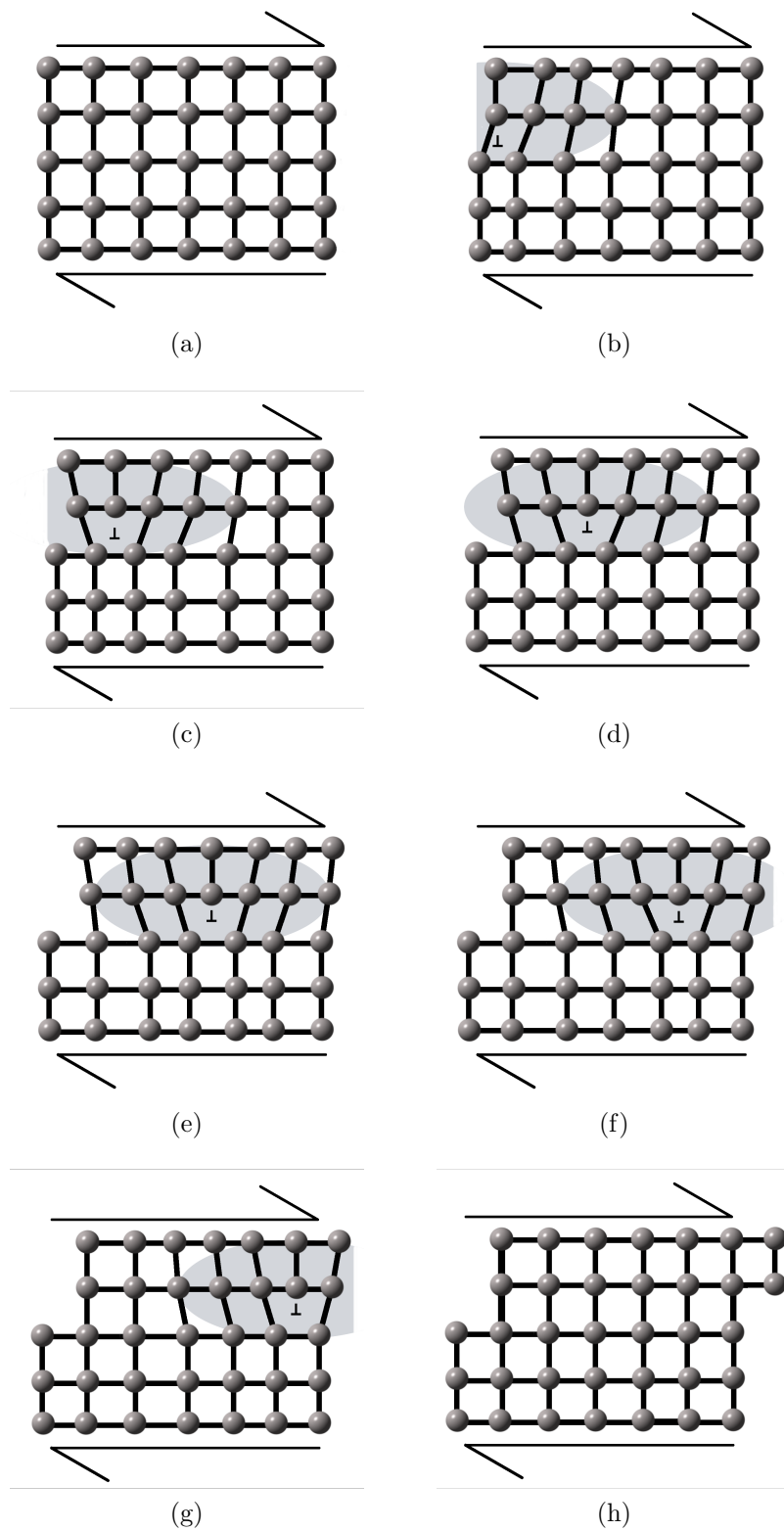


Figure 2.18

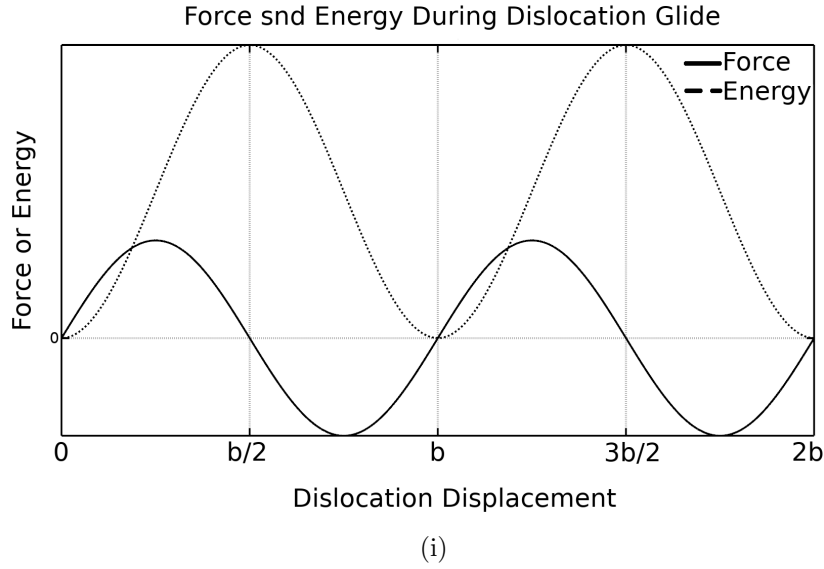


Figure 2.18: plots a–h show the formation of an edge dislocation (denoted by  $\perp$ ) and sliding across a plane of atoms under an applied shear force, the width ( $w$ ) of the dislocation is shown in light gray. Plot i shows the change in force and energy as the dislocation glides through the lattice (distance normalized by the Burgers vector).

to cause dislocation glide is called the Peierls Stress (Peierls, 1940; Nabarro, 1947) given by

$$\sigma_p = \mu \exp \left\{ \frac{2\pi w}{b} \right\} \quad (2.48)$$

$$w = \frac{d}{1 - \nu} \quad (2.49)$$

where  $b$  is the Burgers vector (also the atomic distance),  $\mu$  is the shear modulus, and  $w$  is the width of the dislocation. Here width means how far from the dislocation core are the atoms displaced from the ideal, whereas the dislocation length would refer to the distance the dislocation extends into the third dimension (i.e., out of the page for the edge dislocation in Figure 2.18).

This process is irreversible as the atoms will not return to the original lattice upon unloading. This can be seen from the plot in Figure 2.18i, since the dislocation would

experience sinusoidally-varying energy levels, it would chose to remain in the local minimal energy configuration that it would currently be in. When a dislocation is located at a multiple of  $b/2$  (sitting halfway between where atoms would be in the ideal lattice), there is an unstable equilibrium since there is no force on the dislocation, but the energy configuration is at a maximum. When the dislocation has completed a glide displacement in integer multiples of  $b$ , the forces and energy configuration will be the same as the ideal lattice.

While the final configuration is not the ideal structure, it is in a minimum energy configuration (the same as the ideal lattice). The atoms would require a new source of energy to return to their original positions, such as applying the stress in the opposite direction or by annealing the material with a heat source (though that will do more than just fix those atoms).

Even though the energy configuration and forces are the same as the ideal lattice, the new lattice will have changed the properties of the material. Dislocation glide is the underlying mechanism for strain hardening. The amount of gliding a lattice can do is limited, leading to dislocation pile-up at the boundaries of grains. This leads to greater resistance to ductile flow in materials, making them stronger but more brittle. Dislocation glide is also the cause of slip planes in materials that often lead to specimens under uni- and tri-axial splitting along planes approximately  $45^\circ$  to the primary loading, since the greatest shearing stress happens along this plane leading to the highest Peierls stresses.

#### **2.2.2.2.5 Dislocation Climb and Kinking**

as seen in Figure 2.18, the dislocation ( $\perp$ ) moves horizontally across the page, never leaving the plane of atoms it is between. Under normal circumstances, the edge dislocation is not allowed to change its plane (e.g., go up or down in Figure 2.18). This

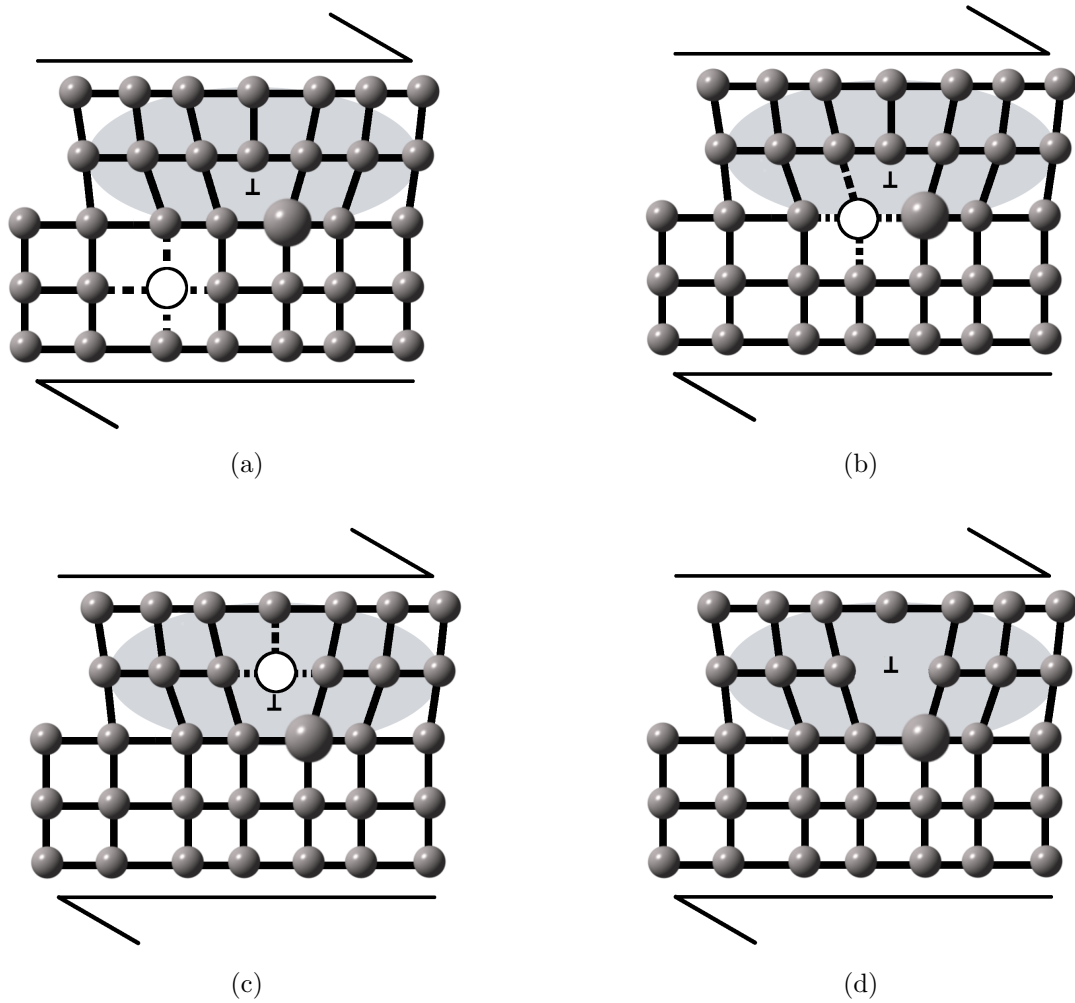


Figure 2.19: Dislocation Climb. Starting with Figure 2.18e, the lattice has two impurities introduced: A larger atom and a vacancy.

means that an edge dislocation can become stuck at a barrier, such as an interstitial atom (e.g., an impurity), and be no longer able to move and relieve stress. A mechanism that allows the edge dislocation to move around the barrier is climb (and anti-climb).

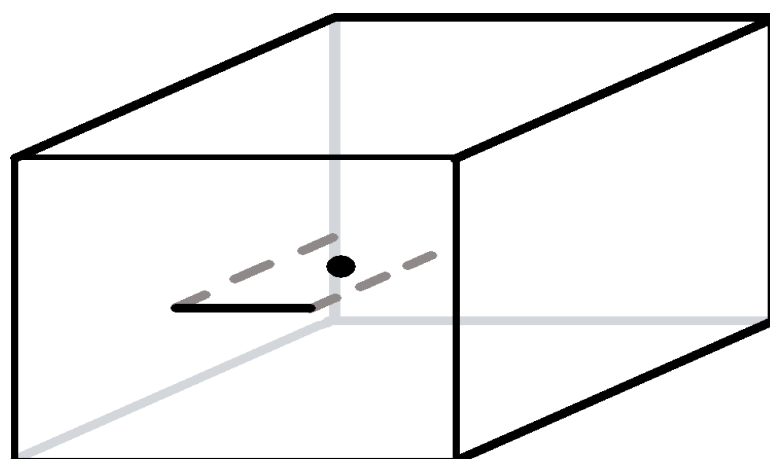
Starting with Figure 2.18, two impurities are introduced: a larger atom and a vacancy (missing atom from the lattice). Similar to before, the dislocation moves to the left along the plane, but this time is unable to advance further due to the larger

atom preventing slip (since this atom cannot move and edge dislocations cannot leave the plane to go around the large atom). As shown in Figure 2.19b–c, the vacancy diffuses towards the dislocation (which is to say the atoms are diffusing away from the dislocation). The vacancy diffuses to the dislocation, removing an atom from the end of the dislocated (or extra) half-plane of atoms. This causes the dislocation to move up (since it has to be just under the last atom in the half-plane, and pass over the barrier. Anti-climb is a similar process that adds atoms to the half-plane, causing the dislocation to move down to another plane instead of up.

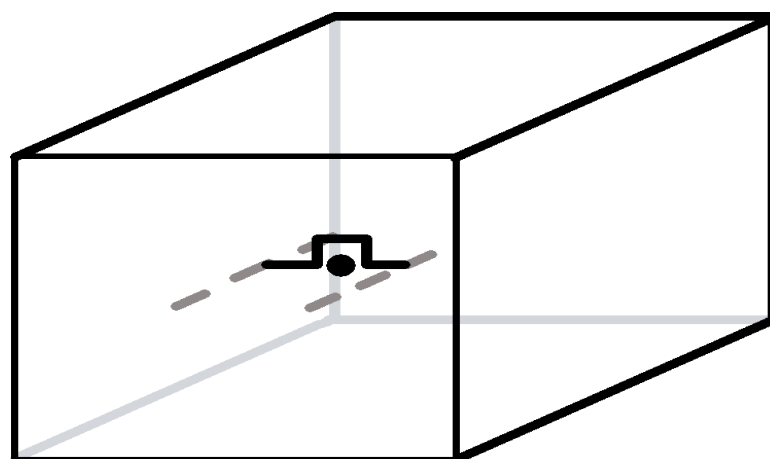
The previous discussion looked at the edge location in 2-D. In 3-D, the edge dislocation is a line, but one does not expect a line of barriers (like the large atoms) to appear in the lattice. This means that the climbing of the edge dislocation is only local to the barriers blocking its motion. The reshaping of the dislocation from a straight line to a bent line is called kinking. Figure 2.20 shows a straight dislocation (in black) travelling along a horizontal plane (denoted with dash, gray lines). Along the path is a barrier (the black dot). When the dislocation reaches the barrier (Figure 2.20b), if possible, it will climb over the barrier. Since edge dislocations are confined to their (in this case - horizontal) plane, the dislocation will continue to travel through the lattice as a bent line provided nothing else causes this to change (such as more kinking around other barriers).

#### **2.2.2.2.6 Slip and Cross-slip of Screw Dislocations**

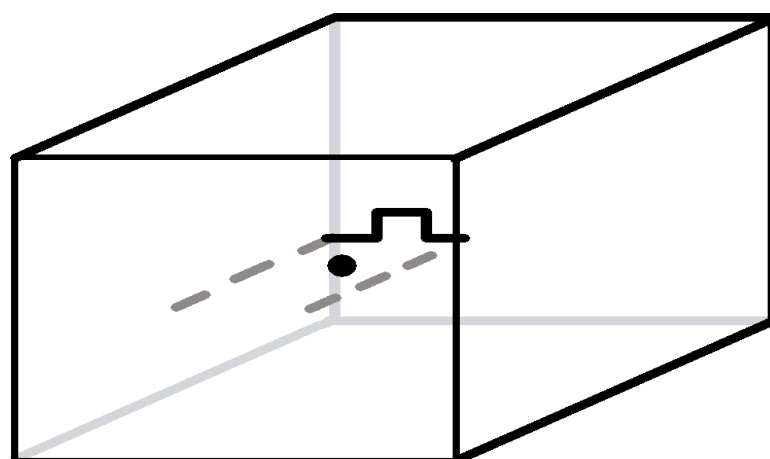
Like edge dislocations, screw dislocations move under load. Due to the shear stress on the lattice, the screw will undergo a motion perpendicular to to the direction of the shear. Figure 2.21a–b show a screw dislocation line (the thicker line) move along a plane of atoms. This (in this case, horizontal) motion of the screw is called slip. Unlike edge dislocations, screw dislocations are able to jump from one plane of



(a)



(b)



(c)

Figure 2.20: Dislocation kink caused by the presence of a large atom acting as a barrier.

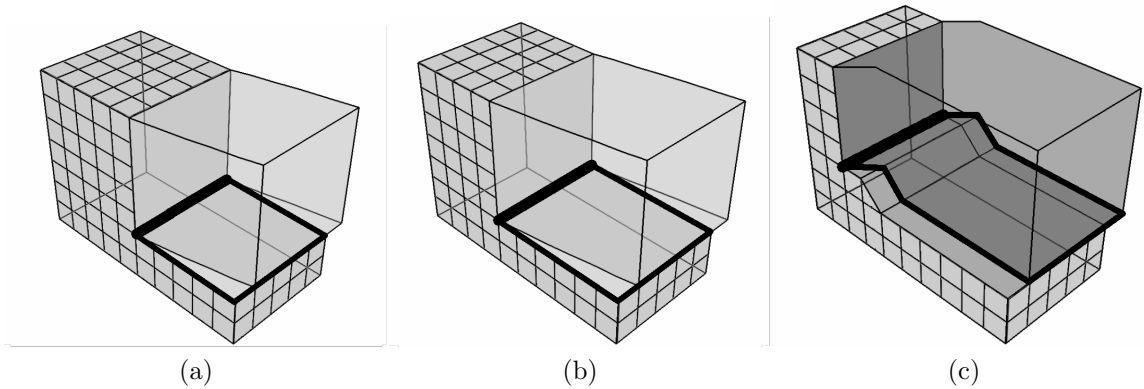


Figure 2.21: Slip and cross-slip of a screw dislocation.

atoms to another, provided the motion is still perpendicular to the shear. The screw dislocation's ability to change its plane is called cross-slip. Figure 2.21b–c, shows a screw that cross-slipped up one plane of atoms. Like edge dislocations, this may be due to getting around barriers like larger atoms, only the screw dislocation does not need any vacancies to do this.

#### 2.2.2.2.7 Frank-Read Mechanism

Since dislocations are the primary cause for creep in materials, dislocations have to form in the material. While many dislocations will be formed just by chance, such as atoms and molecules being unable to reach their ideal positions before locking into place during freezing, dislocations can be formed during the loading of a material. One of the most important sources for dislocation generation is the Frank-Read Mechanism (Read, 1953).

The Frank-Read Mechanism begins with a part of a dislocation pinned on both ends, such as the kinked edge dislocation shown in Figure 2.22. The kink is located in the basal slip plane and is pinned at both ends by some barrier. For low stress, the dislocation bows outward to relieve some stress. As the stress is increased, the edge will bow outward further. The dislocation will bow stably until it reaches a

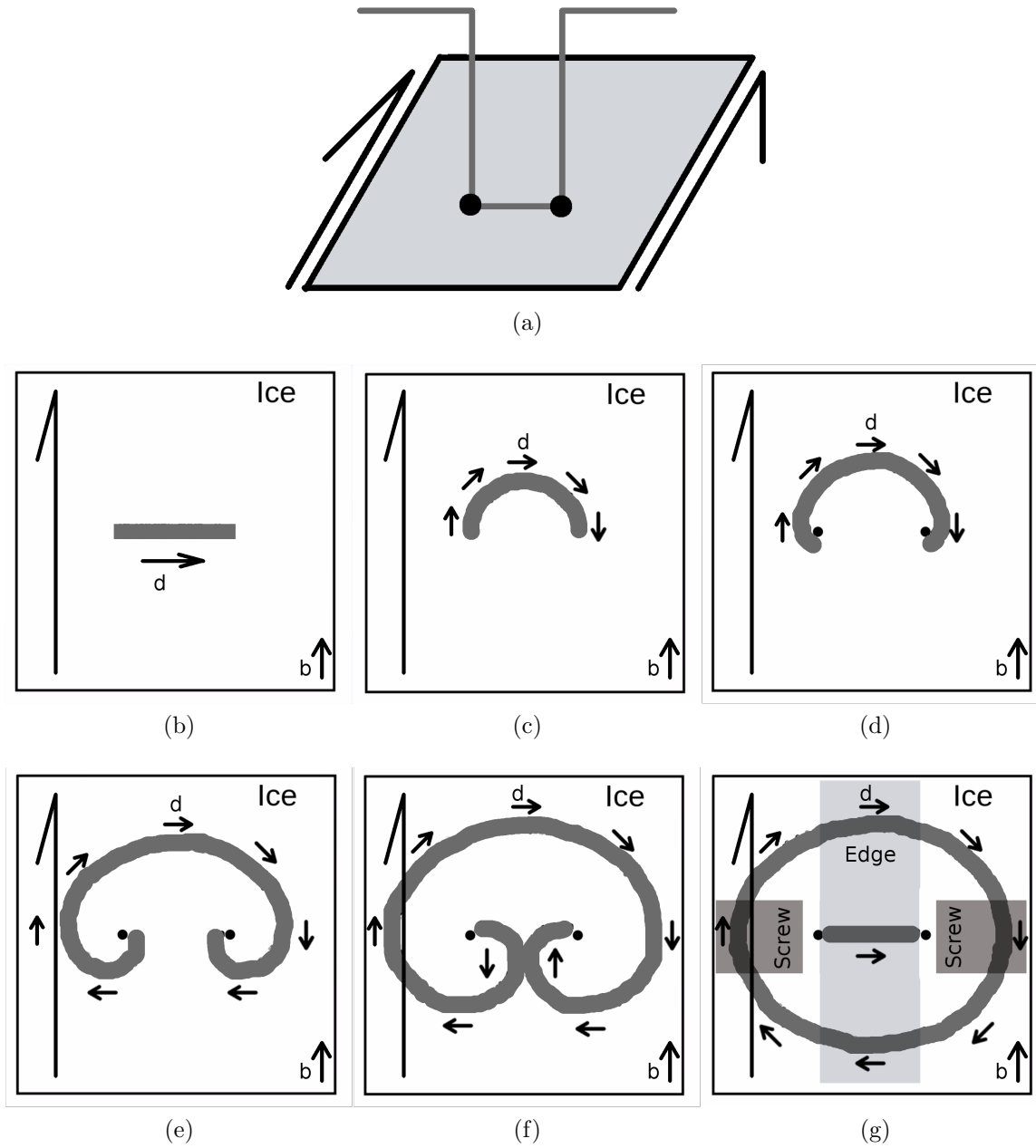


Figure 2.22: Generation of dislocations via the Frank-Read Mechanism. a) shows a non-basal, kinked edge dislocation pinned at both ends of the kink. As shear is applied to the basal plane, the dislocation grows outward, eventually annihilating in f) resulting in a new dislocation and the original dislocation in g).



semi-circular shape, as shown in Figure 2.22c. The critical stress for stable growth is given as

$$\sigma_c = \frac{2\mu b}{x} \quad (2.50)$$

where  $\mu$  is the shear modulus,  $b$  is the Burgers vector, and  $x$  is the distance between the two pinning points (Hobbs, 1974).

Figure 2.22d-f show the unstable growth of the dislocation. The dislocation continues to grow outward and curls around the pinning points. The curling around the bottom of the two sides meets up in Figure 2.22f. Since the dislocations are pointing in the opposite direction, they will annihilate, causing one piece to snap back to the original edge dislocation and one to snap back into a dislocation loop. The final result is shown in Figure 2.22g, showing the original dislocation and dislocation loop. Superimposed is the location of the edge and screw dislocations portion of the dislocation loop, and mixed dislocations elsewhere along the loop.

### 2.2.2.3 The Bjerrum Effect

A common defect in ice is related to defects in the hydrogen-bonding between water molecules. The Bjerrum defect (Bjerrum, 1952) is a defect in the lattice of ice that causes ice to have electrically conductive properties. In a perfect lattice, all the oxygen atoms are bonded in a hexagonal shape with a hydrogen atom along each bond. Similar to how oxygen can be caught out of place during freezing or through dislocations, hydrogen can also be misplaced. The L-type defect is when there is no hydrogen atom between two oxygen atoms and a D-type defect is when there are two hydrogen atoms between two oxygen atoms. The bonding energy for each type of defect is around 0.64 electron-volts (Raj and Ashby, 1971; Frost and Ashby, 1982).

Alternatively, the various mechanisms leading to dislocation motion, discussed above, can cause this effect to occur (Hobbs, 1974). The motions of dislocations

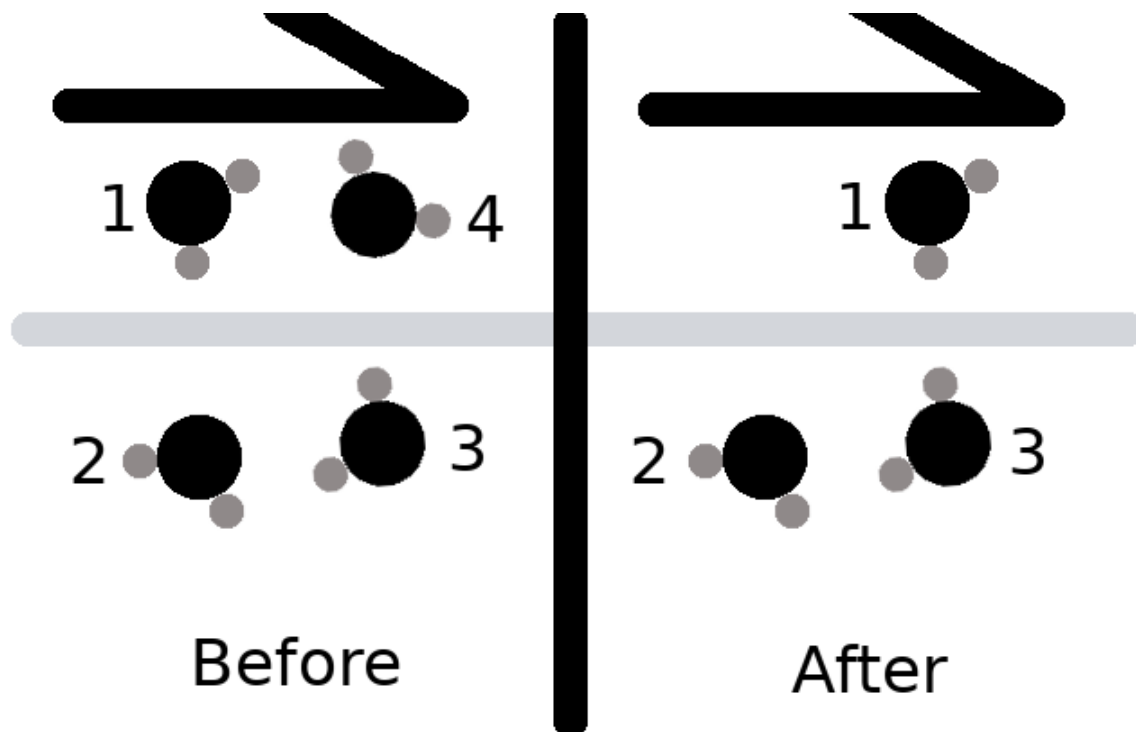


Figure 2.23: Bjerrum Effect due to dislocation glide.

cause the atoms to move in unit length Burgers vector jumps. Figure 2.23 shows the process by which dislocation glide can cause the Bjerrum effect. The “Before” image shows three water molecules that make up a part of an ice lattice. Molecule 1 is above the slip plane and will move relative to molecules 2 and 3 below the slip plane in the direction of stress indicated by the arrow. The motion of dislocations will move molecule 1 one Burgers vector to the right, placing it above molecule 3. In this example, molecule 1 was hydrogen bonding to molecule 2 below the slip plane and molecule 3 was hydrogen bonding to molecule 4 above the slip plane. In the new configuration, molecules 1 and 3 are now bonded to each other, but they both have hydrogen atoms forced to be on the same bond (D-type effect).

The Bjerrum effect acts to weaken the strength of ice. In both the L-type and D-type Bjerrum effects, the bond strength is reduced due to atoms of similar charge (two negative oxygen atoms or two positive hydrogen atoms) being closer to each

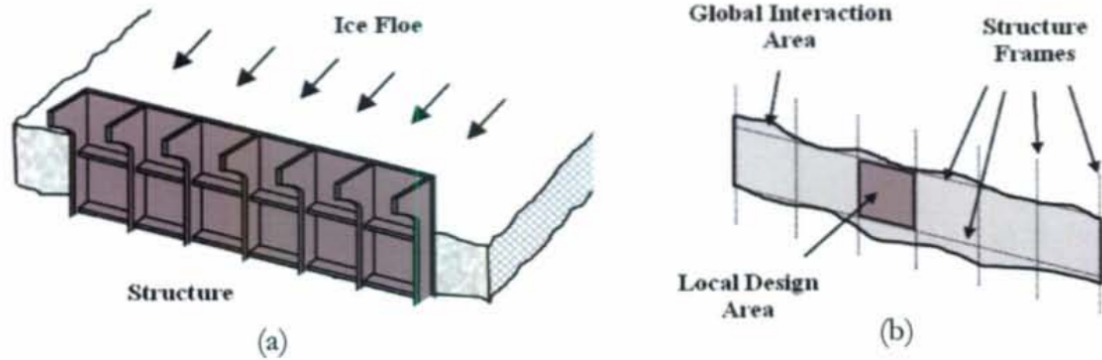


Figure 2.24: Global vs local loads. From Taylor (2010).

other. These atoms will have a stronger repulsion to each other than they would in the perfect lattice configuration. This will cause greater ductility in the ice as these atoms will be more readily available to move to find a more favourable position.

## 2.3 Interactions with Ice

### 2.3.1 Local and Global Loads

Two important aspects of ship and structure design relate to designing it to withstand the global and local loads. During an interaction between ice and structure/vessel (see Figure 2.24a), a global (or nominal) contact area can be defined as a projection of the structure on the ice. For the case depicted in Figure 2.24, the nominal area would be the rectangular cross-section of the structure matching the height of the ice, depicted in light grey in Figure 2.24b). Global load refers to the load exerted over the entire contact area. Similarly, the global pressure can be defined as the global load divided by the global area.

Structures and vessels are built using frames and panels. The frames are the support of the vessel whereas weaker points will exist on the panels between the frames. Thus when it comes to design, one must ensure that the panels are strong



Figure 2.25: The Molikpaq drilling caisson surrounded by ice. After Timco et al. (2006).

enough to withstand the interactions with ice, meaning one should consider the loads and pressures on these panels. The loads and pressures that act on the panel-sized area of the structure/vessel are referred to as the local loads and pressures.

Figure 2.24b shows the distinction between the global and local interaction areas from which the global and local loads/pressures are defined. The local loads need to be considered for every individual panel in the contact area, and the global load is the sum of the local loads from the panels. The local pressure are the local loads divided by the local area and the global pressure is the global load divided by the global area.

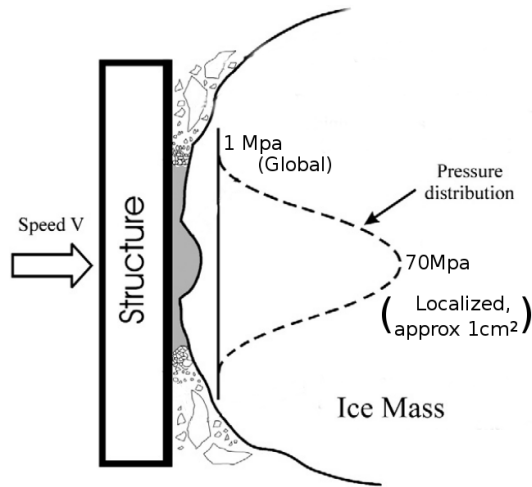
These are two important concepts, because they produce remarkably different results in terms of loads and pressures. The typical global pressures at medium-scale (up to  $3 \text{ m}^2$ ) are around 2–4 MPa and less than 1 MPa for full-scale tests which include

ship ramming and the Molikpaq drilling caisson (See Figure 2.25). Local pressures, at the centre of high pressure zones (discussed in the next section) can reach pressures of 70 MPa (Jordaan et al., 2005). Thus, the design engineer has to consider two strikingly different pressure regimes when designing for Arctic environments.

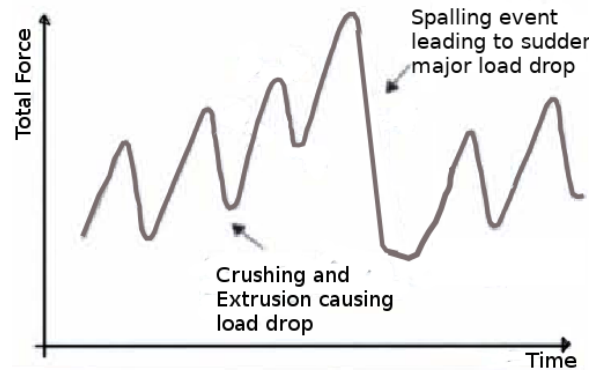
### 2.3.2 High Pressure Zones

When ships or structures come into contact with ice, the applied loads and pressures are generally not evenly distributed, due to irregular shape of ice contact, non-uniformities in the ice (e.g., distribution of pre-existing cracks, dislocations, grain size, and grain boundary effects), and increased confinement near the centre of the contact area. The portions of the contact area that undergo higher-than-normal pressures are known as high pressure zones (*hpzs*) (Jordaan, 2001; Wells et al., 2011), as illustrated in Figure 2.26a. These zones are the primary means by which loads are transmitted to the structure, and understanding their properties and evolution over time are a key aspect in designing safe structures in icy environments. Typical compressive pressures in the field tend to range from 0.1–1.0 MPa (Sanderson, 1988) while the pressures at the centre of a *hpz* (localized to areas on the order of 10 cm<sup>2</sup>) can attain pressures of 70 MPa or greater (Jordaan, 2001).

Jordaan (2001) provides details and insights into the formation of *hpzs*. They detail the *hpz* to have three zones: Zone 1 is near the edge and is the zone where spalling typically occurs due to less confinement, Zone 2 is the area of pulverized ice deeper in the contact zone, and Zone 3 is the pulverized and sintered ice that forms in the contact area closer to the structure. The main processes in the *hpz* are recrystallization and microcracking. Both of these processes causes a change in the compliance of the ice, making it more compliant than undamaged ice, as well as lowering the density in the region. The damaged layer can be deceptive since it tends to maintain a bluish colour



(a) Ice-structure impact cross section



(b) Typical load profile during an interaction



(c) Thin-section displaying microcracking during a slow indentation test

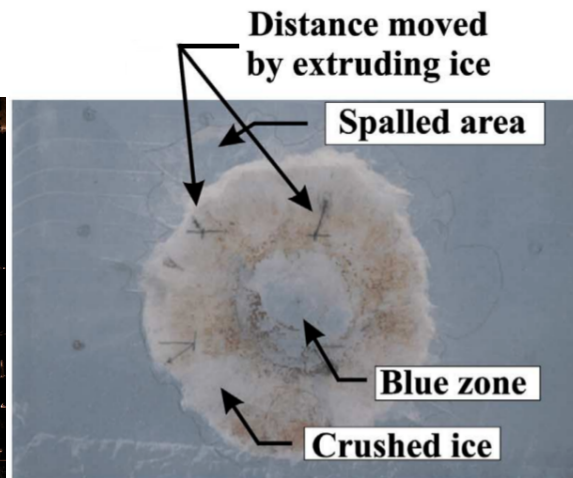
(d) Remains of a *hpz* after an indentation test at Hobsons Choice.

Figure 2.26: High Pressure Zones.

to the eye (see Figure 2.26d), giving an appearance of being undamaged, but thin-sections of this area do show highly damaged and recrystallized grains. High-stress creep tests done under triaxial loading have shown that the inelastic component of creep can greatly exceed the elastic component. There are high shear stresses near the edge of the *hpz* that is the cause of the material flowing out as extrusions.

The *hpz* is under a triaxial state of stress. This is due to confinement from the structure and the rest of the ice that surrounds it. Due to the high confinement near the centre of the *hpz*, the ice tends to undergo dynamic recrystallization. The state of stress in this region acts to suppress crack formation, leading to a thin layer of recrystallized ice. This damaged layer is much softer while under stress than the parent ice (Wells et al., 2011). Outside the centre of the *hpz*, where there is less confinement, the stress field changes to one with more shearing stress, which leads to more frequent microcracking (see Figure 2.26c). As the ice and structure continue to interact, the reformed ice in the *hpz* will gradually undergo viscous flow towards the edge of the *hpz*. As the ice reaches the edge, it will squeeze out (much like toothpaste) as fine particulate, referred to as extrusion. As ice extrudes, the load will undergo a load drop and ramp up as new contact is made, as seen in Figure 2.26b.

### 2.3.3 Damage Layer

Beneath the high pressure zone is a layer of highly damaged ice. The ice beneath the *hpz* will undergo damage in the form of recrystallization or microcracking. Under high confining pressure, the grains near the contact area will undergo pressure melting or softening. During the process of pressure melting, the ice will be softer than undamaged ice, but will harden once the the pressure is removed. Since the grains are pressure melting, they will undergo changes due to the movement of atoms/molecules having sufficient energy to rearrange bonds (similar to how annealing of metals works).



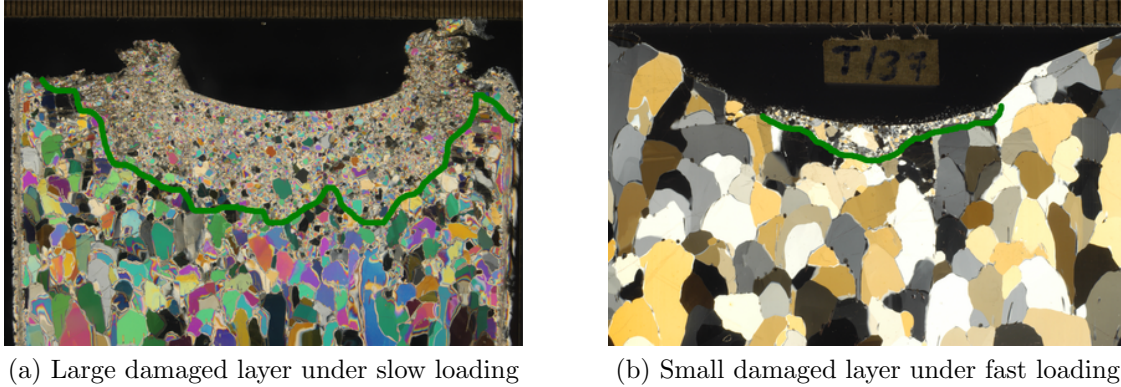


Figure 2.27: Thin sections of ice samples showing the underlying grain structure of the damaged layers of fast and slow indentation loading (O'Rourke et al., 2015).

Upon the removal of the stresses, the atoms/molecules will freeze into place, forming new grains. These new grains can be considerably smaller than the grains from the parent ice. The mechanics and theory of how this damaged layer affects the behaviour of ice during an interaction are discussed in much greater detail by Turner (2018).

For a *hpz* (or parts of a *hpz*) under less confinement, the likelihood of recrystallization decreases due to the lack of pressure melting. In this scenario, microcracking is likely to occur. While technically microcracking is a discontinuity in the material and could be discussed in terms of fracture mechanics, it is typically not done this way. Typically, there will be many microcracks that it is often easier to treat them as weaker continuous material than as distinct cracks. As some of these cracks become larger, they may require consideration of using fracture mechanics, but typically can be discussed in the realm of damage/continuum mechanics.

Barrette et al. (2003) discusses many aspects of laboratory indentation of ice. The experimental program involved isotropic, polycrystalline ice tested at various temperatures and indentation velocities. Much of the data and numerical modelling are focused on the development of the damaged layer of recrystallized grains and microcracks beneath the contact zone. In general, slower tests were shown to have



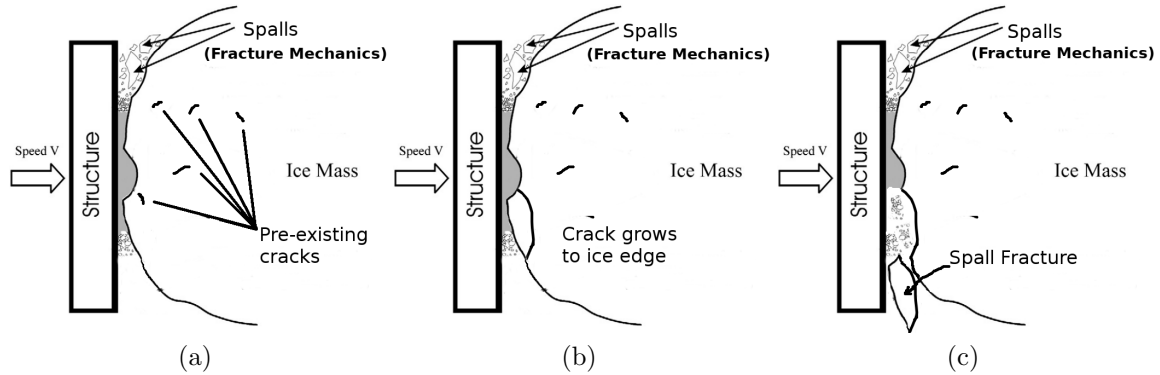


Figure 2.28: Cross-section of an ice-structure interaction showing the formation of a spall fracture event. a–c show a pre-existing crack grow under load, reach the edge of the ice, and break off as a discrete piece of ice (spall).

larger damage layers than faster tests (see Figure 2.27), and warmer temperatures were more likely to be dominated by recrystallization whereas colder temperatures favoured microcracking.

## 2.3.4 Types of Ice Fractures

### 2.3.4.1 Spalling Event

Figure 2.28 shows a spalling event, where a discrete piece of ice (a spall) breaks off. Often, there will be a pre-existing crack in the ice behind a *hpz*. As the load on the ice is increased, the crack will grow as the stress increases. Initially, the crack grows stably, as the energy release upon crack growth will relieve the build up of potential energy (or stresses in terms of loads and pressures). Eventually, the rate of energy going into the crack will be greater than the energy release rate, causing the crack to undergo unstable growth. When the crack grows to the edge of the ice, a piece of the ice will break off as a spall.

As seen in Figure 2.28c, the spall takes away a part of the *hpz*, causing a change in the contact area of the ice and structure. This may result in the destruction of

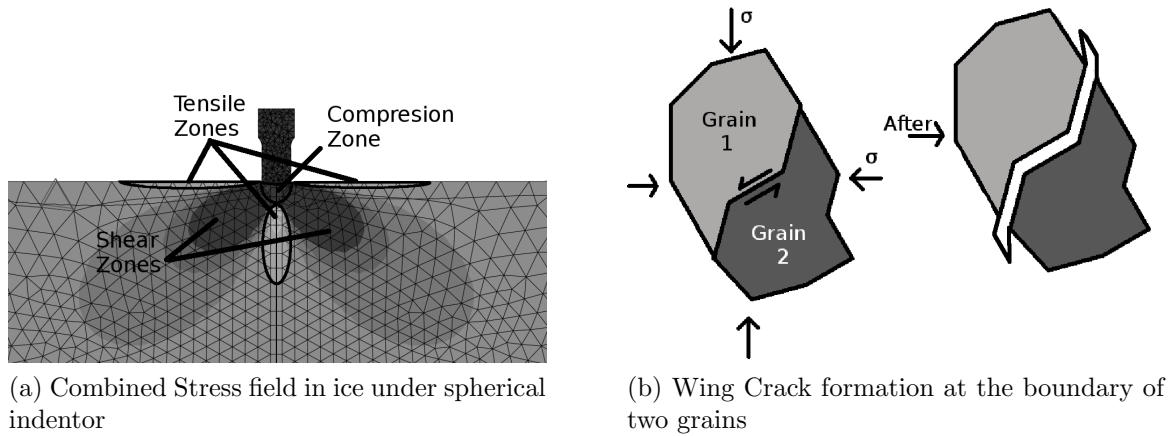


Figure 2.29: The formation of wing cracks. a) sorts the stress field into three zones based on the relative strength of the vertical, horizontal, and shear stress components. b) shows the formation of a wing crack under stress.

the *hpz*. With the removal of the *hpz*, the pressures will redistribute over the contact area, which will give rise to the growth of a new *hpz*.

#### 2.3.4.2 Wing Cracks

Many fractures will occur from pre-existing cracks in the ice. One such crack, known as a wing crack, is caused by sliding along grain boundaries or the faces of an inclined pre-cursor crack (Cannon et al., 1990). In the scenario of depicted in Figure 2.29a, ice is in contact with an indenter (this can be viewed as a top-down view of an ice floe colliding into a structure, such as the leg of a platform). In Figure 2.29a, there is a shear zone that forms beneath the surface of the contact zone. Wing cracks, also known as shear cracks, often start at the boundary between two grains, as depicted in Figure 2.29b. As the pressure increases on the grains, they will begin to slide relative to each other. This causes the crack to grow wings (or kinks) that are roughly  $70^\circ$  to the pre-existing boundary crack. Wing Cracks can grow stably under load, making them a valid candidate for time-dependent fractures in ice discussed in Section 3.1.7.

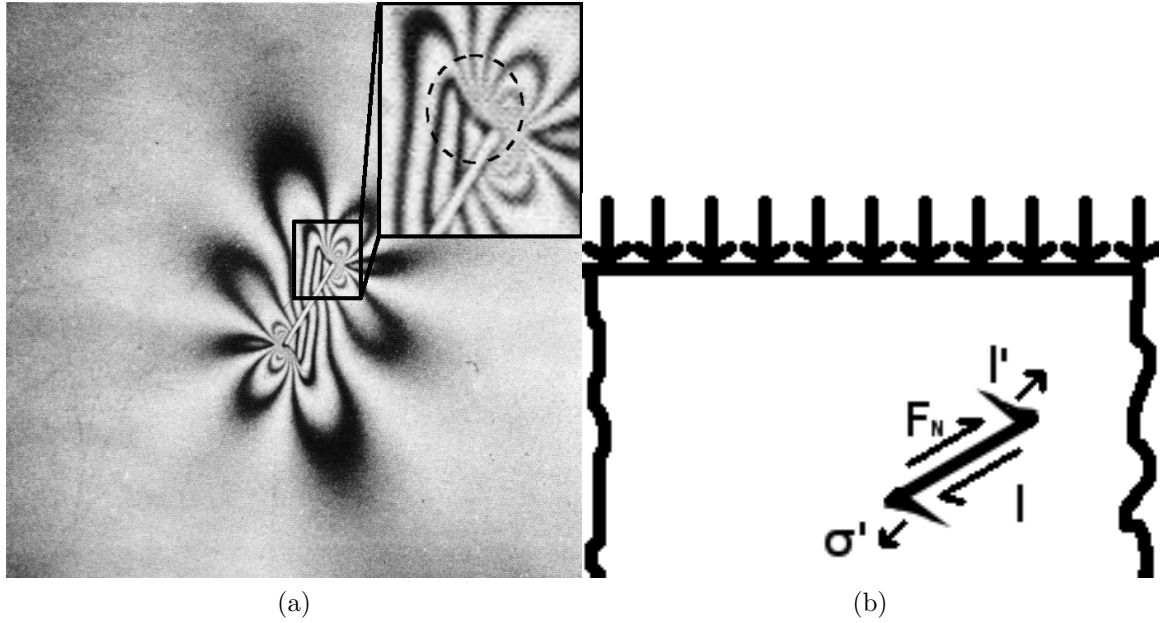


Figure 2.30: a) Photoelastic fringe pattern from Hoek and Bieniawski (1965) for a thin plate of annealed glass. Modified to highlight the presence of a wing crack. b) Wing crack dimensions for a crack oriented 30 degrees to the direction of loading.

Kachanov (1982a,b) provides an analytical solution to the initiation growth of wing cracks in the preferred growing direction (between 30 and 45 degrees to the normal load). The model starts with a pre-existing penny-shaped crack. The model assumes that the wings (kinks) start growing at roughly 70 degrees to the body of the crack. Assuming that the main factor for wing growth is the stress on the wings gives

$$K_I = \kappa F_N \sqrt{\frac{1}{2}l} - \sigma' \sqrt{\frac{\pi}{2}l i} \quad (2.51)$$

where  $F_N$  is the shear stress on the main body of the cracks,  $l$  is the length of the crack body,  $l'$  is the length of the wing, and  $\sigma' = \mathbf{n} \cdot \boldsymbol{\sigma} \cdot \mathbf{n}$  is the stress normal to the wing, as shown in Figure 2.30b.

Hoek and Bieniawski (1965) performed experiments using 6x6x0.5 inch annealed glass plates. In their analysis, they noted that crack growth initiation was near the crack tip (and not at it), but it is of this author's opinion that what they saw was

a wing crack, as seen in Figure 2.30a. Hoek and Bieniawski (1965) also noted a significant time-dependent the fracture of ice, but declined to commit to the idea due to a lack of data.

Following the work of Cannon et al. (1990), E. M. Schulson and colleagues continued to study the properties of wing cracks introduced into thin plates of ice. Batto and Schulson (1993) performed uni-axial compression tests on thin plates of columnar ice at  $-10^{\circ}\text{C}$ . The grain size ranged from 1.5–15 mm and cracks were introduced via 15 mm Teflon strips placed at angles approximately  $45^{\circ}$  to the loading axis, or from naturally occurring wing cracks. The ice was loaded at various rates to study how the cracks behave as the ice properties vary over the ductile-to-brittle transition. Under both ductile and brittle regimes, wing cracks did nucleate after some time. However, they found that the wing cracks did not grow under the ductile (low strain rate) ice, but did grow when the ice transitioned to brittle behaviour. Schulson (1997) provides a summary of the properties of wing cracks from experiments done by the author and his colleagues. Wing cracks are harder to form in granular ice than columnar ice, due to the decreased grain boundary lengths. The growth of wing cracks differs from ductile/brittle regimes due to stress build up and relief near the crack tip. Axial splitting of ice samples in uniform loading experiments are caused by wing crack growth either by a single wing crack (columnar ice) or by the linking up of many smaller wing cracks (granular ice). The stress required to cause wing crack failure is higher in tri-axial experiments due to increased confinement of the crack, leading to greater dissipative forces.

#### **2.3.4.3 Floe Splitting and Radial Cracks**

In a series of experiments done by Canadian Marine Drilling Ltd. (Danielewicz and Metge, 1981), loads exerted on Hans Island (located between Ellesmere Island and

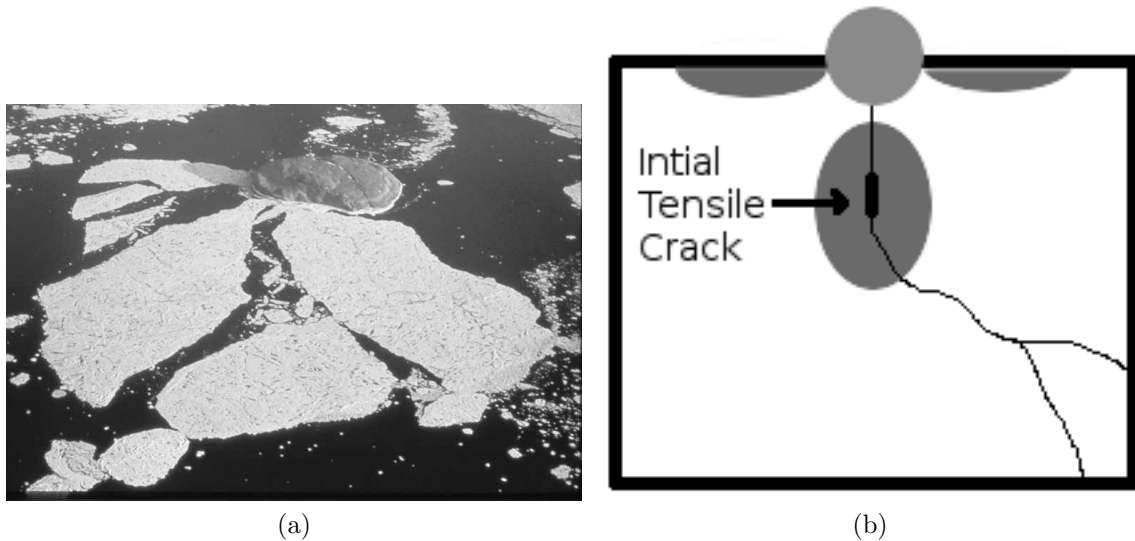


Figure 2.31: Floe-splitting observed at Hans Island. Light gray represents the island and dark grey shows the tensile zones near the contact area between the ice floe and Hans Island.

Greenland) by ice floes colliding with the island were recorded. Danielewicz and Metge (1981) notes that the lowest loads occurred during the test in which floe splitting happened, as seen in Figure 2.31a.

Floe splits originate as cracks that form in the tensile zone beneath the contact zone (the central zone in Figure 2.31b). As the load increases, the tensile stresses on the crack become greater due to Poisson's effect. This will cause the crack to grow in the direction of maximum energy release rate. As crack growth becomes unstable it will begin to grow rapidly.

The crack growth rate is limited by the maximum speed that a crack can grow in ice - roughly 200–400 m/s depending on ice type (Mackay, 1993). Early experiments by Parsons et al. (1987) suggested that the crack velocity in ice was 22 m/s. This was based on the assumption that the crack had time to reach its maximum velocity over the length of their 50 cm specimens, as would be the case for glass. Experiments

done by Dempsey et al. (1999) studied the crack growth in first-year sea ice and saw that the small-scale growth of cracks (e.g., growth between grains) were on the order of 400 m/s, but the large-scale velocity was on the order of 10 m/s. In other words, the cracks did not have continuous growth, which gave an apparent slower velocity than the actual crack velocity would be.

Once a crack reaches its maximum speed limit, its energy release will be capped, but since it must release all the required energy, then the crack will split in two so that the second branch can release the remaining amount. The crack may continue to branch into more segments if needed, until it reaches the surface and fractures the ice.

Tests done by Kendall (1978) on plates with a single crack that would mimic a floe split, suggests that a crack can be modelled by a double cantilever with each half taking half the force. Using elastic beam theory, Kendall developed an expression for the splitting force of the crack for both centre and off-centre cracks. His analysis concluded that off-centre cracks would require more force and thus cracks would prefer to travel along the centre plane.

Kendall's original theory neglected the lateral forces at the end of the beam from when the two cantilevers bend in and touch each other (effectively allowing the two beams to pass through each other). The theory was modified by DeFranco and Dempsey (1990) that constrained the ends of the cantilevers. This eliminated the problem of Kendall (1978) and gave forces nearly three times larger.

Zou et al. (1996) performed numerical simulations in Abaqus FEA for an ice sheet with a central crack loaded by an indenter. They showed that the results of crack energy release approach the modified cantilever theory when the ratio to crack length to ice thickness is 0.8 but doesn't match until the ratio is about 9. This theory can be applied to cases of axial splitting in ice but does not provide much insight into

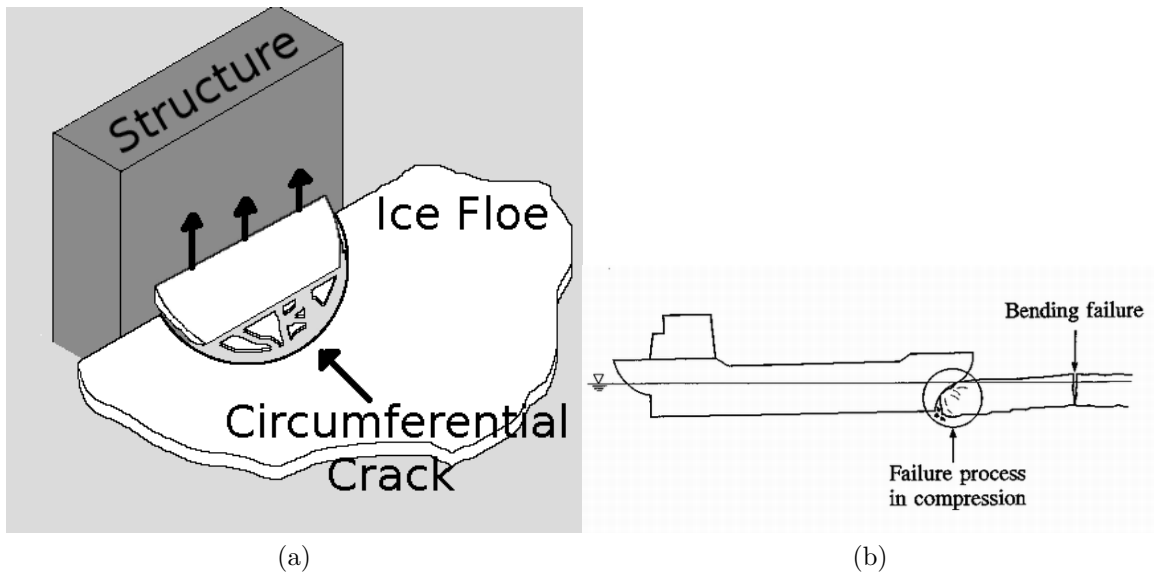


Figure 2.32: Bending failure of ice due to interaction with structure and vessel.

spalling fracture seen during indentation tests, as the cracks need to be sufficiently large for the theory to apply.

Radial cracking can also occur for out-of-plane loads, such as the case of ship ramming. Radial cracking will tend to occur in ice floes that are narrow (meaning their width is roughly equal or greater than their length) and not too small. Long ice floes will likely undergo bending failure (discussed below), whereas a small ice floe may move out of the way or rotate and flip over (Lu et al., 2016).

#### 2.3.4.4 Bending Failure

Bending failure is caused by the creation of circumferential cracks in the ice. As an ice floe collides with a structure, as depicted in Figure 2.32a, cracks can grow circumferentially under flexural failure. This typically requires the ice floe to be long and narrow (much like a beam). Otherwise, other fracture mechanisms are likely to take place. In Figure 2.32b, a bending failure under load from a ship ram is depicted. Ship ramming is likely to cause either floe splitting or bending failure for long, thin

floes. In both cases, icebreakers often ram into the ice and wait for the ice to undergo delayed failure under the weight of the ship.

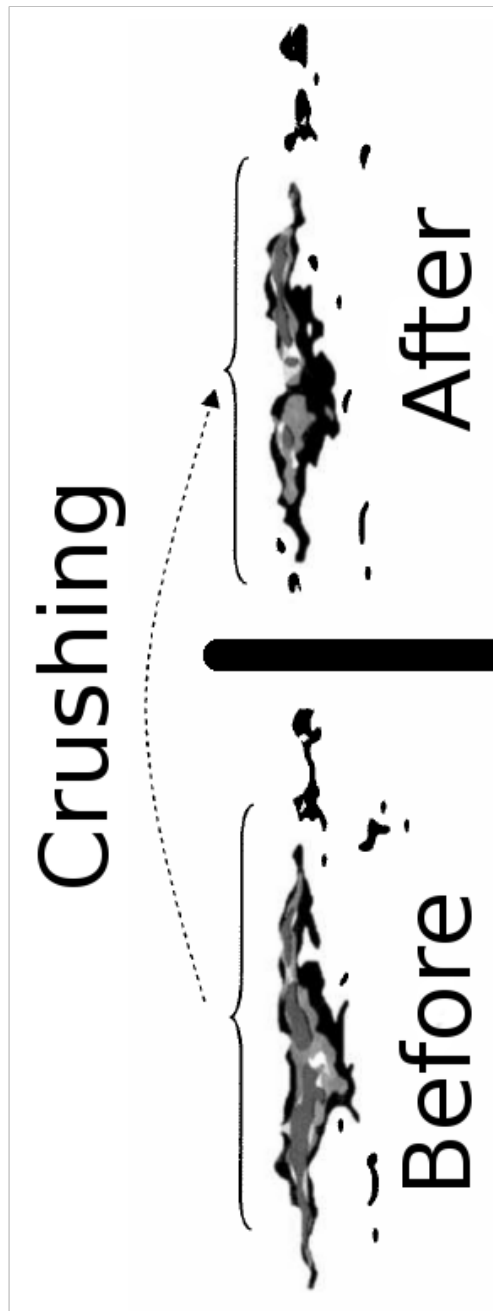
Timco and Cornett (1997) tested how ice sheets of uniform and non-uniform thickness would interact with a sloped structure via a small-scale set-up at NRC-CHC in Ottawa. Experiments were done in a 21x7x1.2 m tank at -20°C. The structure could slope 30° from the vertical to produce either upward-breaking (structure lifted ice up) or downward-breaking (pushed ice down into the water) ice interaction, and had a width of either 0.6 or 1.2 m. They suggest that the effective thickness of the non-uniform sheet can be represented by  $h_{eff} = h_{avg} + kh_{\sigma}$  where  $k$  is a constant,  $h_{avg}$  is the mean, and  $h_{\sigma}$  is the standard deviation. The results from the experiment and the model developed by Croasdale (1980); Croasdale et al. (1994) match up well and show that downward-breaking ice has smaller loads associated with it due to the buoyancy of the ice in water.

#### 2.3.4.5 Load drops and Area Loss

Figure 2.33 shows how the area and loads change under crushing and spalling. For crushing, Figure 2.33a shows that there is a load drop, but minimal area change. This is because crushing causes the material to be extruded relatively slowly as small flakes. Since only fine particulate is extruding at the top of the damaged layer, there is little change in the area since the layer behind is unchanged. Like spalling, there is a load drop since extruding removes energy from the system, providing temporary relief of loading as new contact is established.

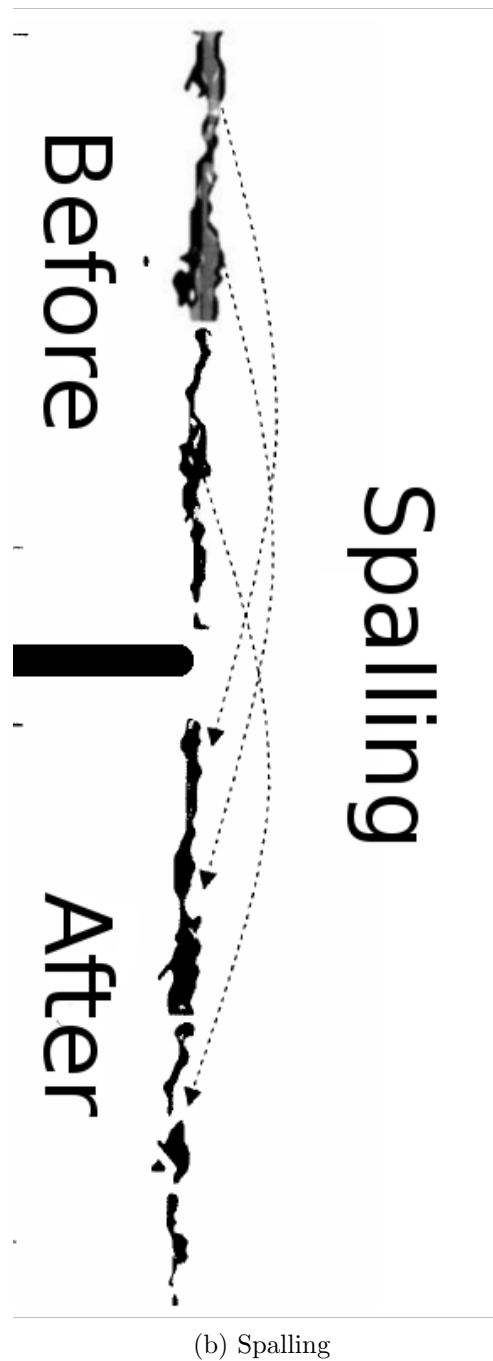
Figure 2.33b shows that there is load drop under spalling, which is usually greater than the load drop under crushing. More notably, there is a significant change in contact area due to the spall removing a large part of the damaged layer. Since spalls start as cracks deeper in the layer, when they break, they remove deeper parts of the





(a) Crushing

Figure 2.33



(b) Spalling

Figure 2.33: Each before/after shows the pressure distribution during an ice-structure interaction from a pressure sensor. a) shows the pressure and area change from a crushing/extrusion event. The crushing event shows very little change in the contact area. b) shows the pressure and area change from a spalling event. The arrows point to various spalls that occurred and lead to localized loss of contact area. The Data is from Nakazawa et al. (1999) for a medium-scale flat indenter. Figure is modified from Taylor et al. (2008).

layer that extrusions do not. This causes a change in the area that will lead to the formation of new *hpz* as the contact area between the indenter and ice has changed.

### 2.3.5 Scale Effects

The experiments performed in Dempsey et al. (1995) investigated the size effect law. This law simply states that material's strength is related to its size. In a comparative sense, the size effect theory postulates that large samples are weaker (break under lower stress) than smaller samples based on the ratio of their sizes. They investigated several size effect laws and determined that they were "rather fickle" in predicting results outside the sample ranges.

Section 2.2 discusses the underlying physics of materials. To briefly summarize a key point: materials are composed of atoms/molecules that are bonded to each other. Some bonds are stronger than others (covalent bonds are stronger than hydrogen bonding) and are affected by defects such as dislocations and grain boundaries. To fracture a material, the atomic bonds in this material need to be broken. This Means that a crack grows when the local stresses are on the order of the theoretical limit (variations due to bonding type and defects).

Since the theoretical limit (hence the bond breaking limit) is independent of sample size, then some other effect must be at play that explains why larger samples are weaker than smaller samples. This other effect is known as the scale effect. The scale effect is related to the size of the specimen and to its distribution of cracks.

The scale effect refers to the relationship seen between the pressures exerted on a structure/vessel (and the ice) and the size of the contact area of the interaction with the ice. Often this relationship is discussed in terms of the pressure-area curve.

Figure 2.34 shows a pressure-area curve for ice from laboratory-scale indentation up to island-sized indentation experiments. The figure shows a clear decreasing power-

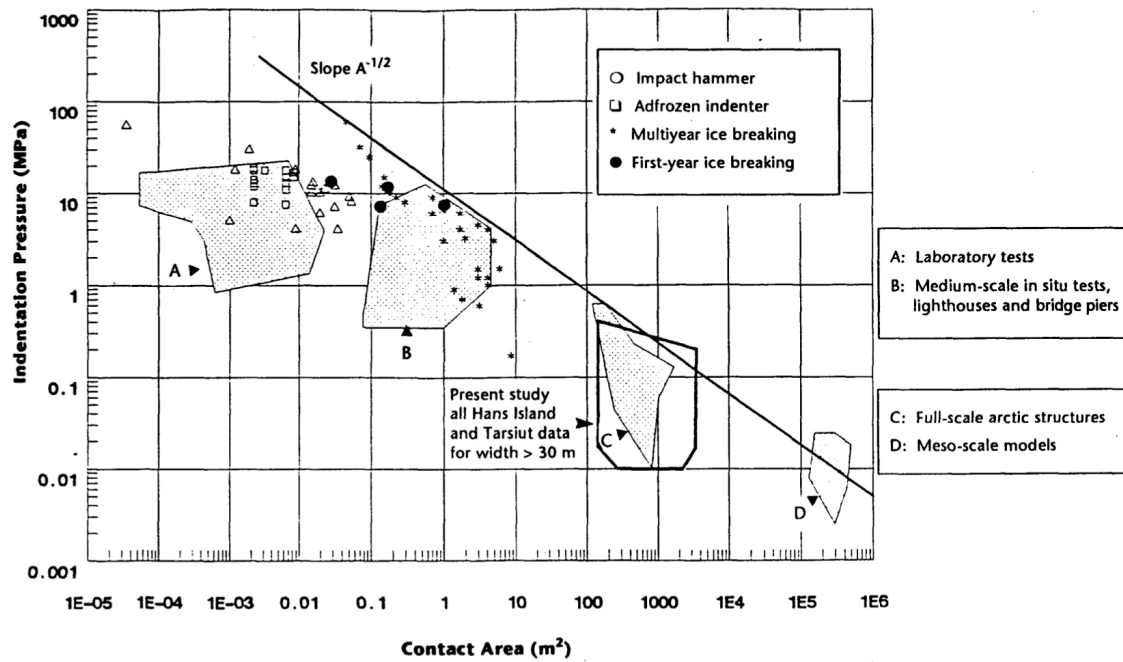


Figure 2.34: Indentation data from a variety of sources from laboratory-scale indentation to island-sized indentation in the field. Taken from Jordaan et al. (2005), modified from Sanderson (1988).

law relationship (linear in a log-log plot) between the measured pressure and the contact area. While there is considerable scatter in the data (which is to be expected since there are a variety of sources), the data shows that laboratory ice typically has pressures on the order of 10 MPa whereas the pressures for the island-size experiments were closer to 0.1 MPa. Much of the field data, such as from ship ramming, resulted in pressures around 0.5–1 MPa. A similar pressure-area curve is also produced from a series of datasets can be found in Timco (2011) that displays the scale effect ranging from full-scale (Island-sized) and medium-scale (offshore structures and bridge).

Barrette et al. (2003) perform a series of indentation tests using four indentors (10-, 20-, 40-, and 100-mm diameters). These indentors were each indented at four different speeds each (the speeds were scaled; for example, the four speeds of the 20-mm indenter were twice the speeds of the 10-mm indenter, and the 100-mm indenter

was 10 times the 10-mm indenter). These experiments were scaled down versions of the experiments done in the field (Frederking et al., 1990; Masterson et al., 1993, 1999). The test matrix for the series is given in Table 2.2.

The results of Barrette et al. (2003) are plotted in Figure 2.35. Series (a) of tests (which was their slowest speeds) produced no noticeable scale effects. Both (b) and (c) displayed scale effects similar to Figure 2.34. The study showed that the pressure followed a decreasing power-law between pressure and contact area given by

$$P = kA^{-n} \quad (2.52)$$

where  $P$  is pressure,  $A$  is area,  $k$  and  $n$  are constants with  $0 < n < 1$ .

To understand why the scale effect occurs, a statistical approach to fracture mechanics is required. Scale effects are well-explained by the theory of ‘weakest-link’ in fracture mechanics (See Section 3.1.5) and is discussed further in Section 4.3.3 (with experimental data).

The basic premise of the scale effect is that it is not the size of the sample that is important, but rather the stress and strain fields. If two samples of the same geometry, where one is a scaled-down version of the other, then a proper scaling of the loads (or loading rate) will lead to similar material strength and behaviour. This is because proper scaling will lead to similar stresses/strains in the material, resulting in similar fracture behaviour from the stresses localized near a crack tip.

One valuable use of the scale effect (as shown in the experiments) is the ability to recreate large-scale experiments in the laboratory. This can be useful for studying a variety of scenarios in the laboratory, which allows for more repeatability, saving on time and resources, and is considerably safer than field experiments.

Indentor Diameter (mm)	Displacement Rate (mm/s)		
	Series a	Series b	Series c
10	0.01	0.1	1
20	0.02	0.2	2
40	0.04	0.4	4
100	0.10	1.0	10

Table 2.2: Test matrix of indentation experiments performed in Barrette et al. (2003).

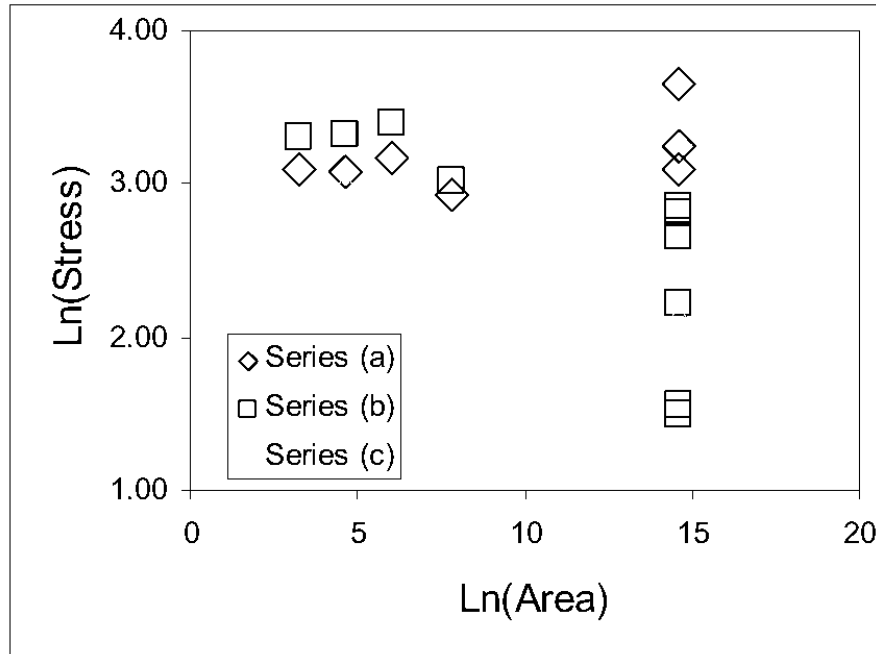


Figure 2.35: Observed scale effects for various indentors at different loading rates from Barrette et al. (2003). Units are in MPa and mm<sup>2</sup>.

# Chapter 3

## Review of Fracture Mechanics

### 3.1 Key Concepts of Fracture Mechanics

Fracture refers to the growth of new or pre-existing cracks in the ice. Cracks nucleate at several stress-raising sites, called nucleation sites. These sites will be related to the atomic and crystal structure of the ice, such as dislocation pile-up and shear causing sliding at grain boundaries, discussed in Section 2.2.2.

This section provides an overview of some key concepts in fracture mechanics. As a crack is loaded, the material in front of the crack will undergo changes in its properties due to the increased stresses caused by the presence of the crack. The energy stored in this region will cause the crack to grow once a critical level is reached, which will be based on the surface energy of the crack as well as of any dissipative processes in the material. The concepts discussed in this section are fundamental to developing any fracture model and outline some of the underlying assumptions used in the development of the proposed model in this thesis.

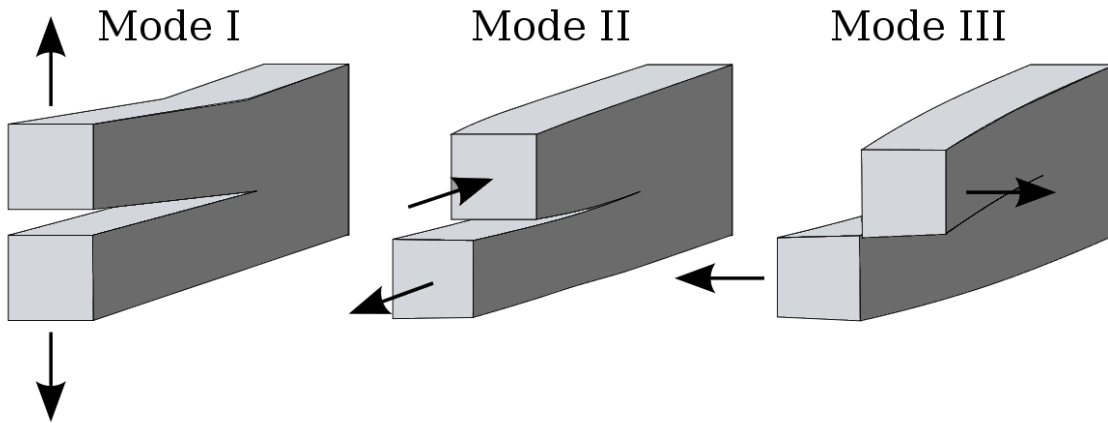


Figure 3.1: Modes of cracking opening.

### 3.1.1 Linear Elastic approximation

Linear elastic fracture mechanics (LEFM) is based on the material being a linear elastic material that eventually undergoes brittle fracture. It relates to the changes in the stress field due to the presence of cracks, and how the cracks will grow and propagate.

Due to the high stresses near the crack tip, the material will have to dissipate energy by either plastic or viscoelastic mechanisms. This will cause a damaged zone near the crack tip, changing the properties inside, while not changing the properties outside (e.g., steel would develop a plastic damaged zone near the crack, but would be elastic elsewhere). Provided that this zone, known as the process zone, is small in comparison to the dimensions of the material, then LEFM can be used as an acceptable approximation. An in-depth analysis of linear elastic fracture theory is discussed in Section 3.2.

### 3.1.2 Modes of Crack Formation

Based on the loading felt by a crack, there are three ways that cracks grow, appropriately called Mode I, Mode II, and Mode III. These modes are shown in Figure



## 3.1.

Mode I is known as the opening mode, where the displacement of the crack surfaces is perpendicular to the plane of the crack. That is, if we say the crack runs in the  $x$  direction, then the surface displacement is in the  $y$ -direction. This mode of fracture is generally considered the most dangerous mode. For ice, a tension crack under Mode I loading conditions is always unstable and will lead to brittle failure once the stress becomes sufficient to break the ice.

Mode II is known as the in-plane shear mode, where the displacement of the crack surfaces are in the same direction as crack growth (the  $x$ -direction). In ice-structure interactions, this mode is considered the second most important type of crack loading. While not as severe as a Mode I type fracture, Mode II plays an important role in ice fracture. For many interactions, Ice is often likely to fail from crack originating in a zone under high shear stresses. These cracks (the wing cracks) are very important cracks that are likely to occur in confined specimens (that limit the Mode I cracks), and can exhibit stable crack growth leading to delayed failure.

Mode III is the out-of-plane shear mode (or tearing). In this mode, the crack surface displacement would be in the  $z$ -direction. This mode is caused by torsion forces causing the separation of the material (i.e; tearing a piece of paper) and is generally considered the least important in ice-structure collisions.

For ice-structure collisions, the cracks are generally going to form via Mode I (under compression), or a mixed mode combining elements of both Modes I and II. A full analysis of ice fracture would need to incorporate all three modes (or at least the first two), but the analysis presented in this project will focus solely on the Mode I type fracture.

### 3.1.3 Crack Nucleation and Propagation

It can be shown (Anderson, 2005) that the cohesive strength of atomic bonds of a material can be approximated by

$$\sigma_c \approx \frac{E}{\pi} \quad (3.1)$$

However, the strength of materials is typically much weaker than the theoretical value. This is due to flaws in the material such as impurities, dislocations, and grain boundaries that lead to stress concentrations. Experiments by Griffith (1921) using glass fibres of varying diameter showed that the fracture strength of the fibre becomes weaker for thicker fibres. For the thinnest fibres, the fracture strength approached the theoretical value of 11 GPa. As the fibres became thicker, the strength approached the bulk glass strength of 175 MPa (about two orders of magnitude less).

The work by Inglis (1913) shows that the stress concentration factor near an elliptical hole with the major axis,  $a$ , and the minor axis,  $b$ , is given by

$$k = \frac{\sigma}{\sigma_a} = 1 + 2\frac{a}{b} \quad (3.2)$$

in the case that  $b$  comes small, on the order of atomic distance  $x_o$ , the hole becomes a crack with a stress concentration given by

$$k = 2\sqrt{\frac{a}{x_o}} \quad (3.3)$$

and the material will crack when the applied stress,  $\sigma_a$ , causes a local stress,  $\sigma$ , to exceed the critical stress,  $\sigma_c$ .

Following the works of Inglis (1913), Griffith (1921) was interested in determining why the strength of materials are significantly less than the strength required to break bonds (Griffith looked at glass, but in terms of ice, the atomic strength of ice should

be on the order of 100-1000 MPa, but many field and laboratory experiments show that ice breaks on the order of 1 MPa).

Griffith, often considered the father of fracture mechanics, was the first to consider the release of strain energy into surface energy as a crack grows. Griffith showed that nucleated cracks can grow when

$$\sigma_f = \left( \frac{2E\gamma_s}{\pi a} \right)^{\frac{1}{2}} \quad (3.4)$$

where  $\gamma_s$  is the surface energy of the material (energy required to create new surfaces).

The explanation why larger samples tend to be weaker than smaller samples had to do with the presence of cracks, where larger samples likely had larger cracks, which would require less energy to break. In other words, all samples break at the theoretical limit, but local energy build up due the presence of cracks significantly reduces the applied stresses needed to fracture the sample.

### 3.1.4 Energy Release Rate

For a linear elastic material under stress, the strain energy is given as

$$U = \frac{1}{2} \int \sigma_{ij} \epsilon_{ij} \, dV \quad (3.5)$$

Consider a situation with two different double-cantilever beams under constant loading  $F$ , but with different crack lengths  $a$  and  $a + \delta a$ , as shown in Figure 3.2a and d. The end displacements of the beams,  $\delta_1$  and  $\delta_2$  (respectively), will differ since the beam with the longer crack will have reduced stiffness, as seen in Figure 3.2c. Then the difference in strain energy of the two systems is

$$\Delta U = \frac{1}{2} F (\delta_2 - \delta_1) \quad (3.6)$$

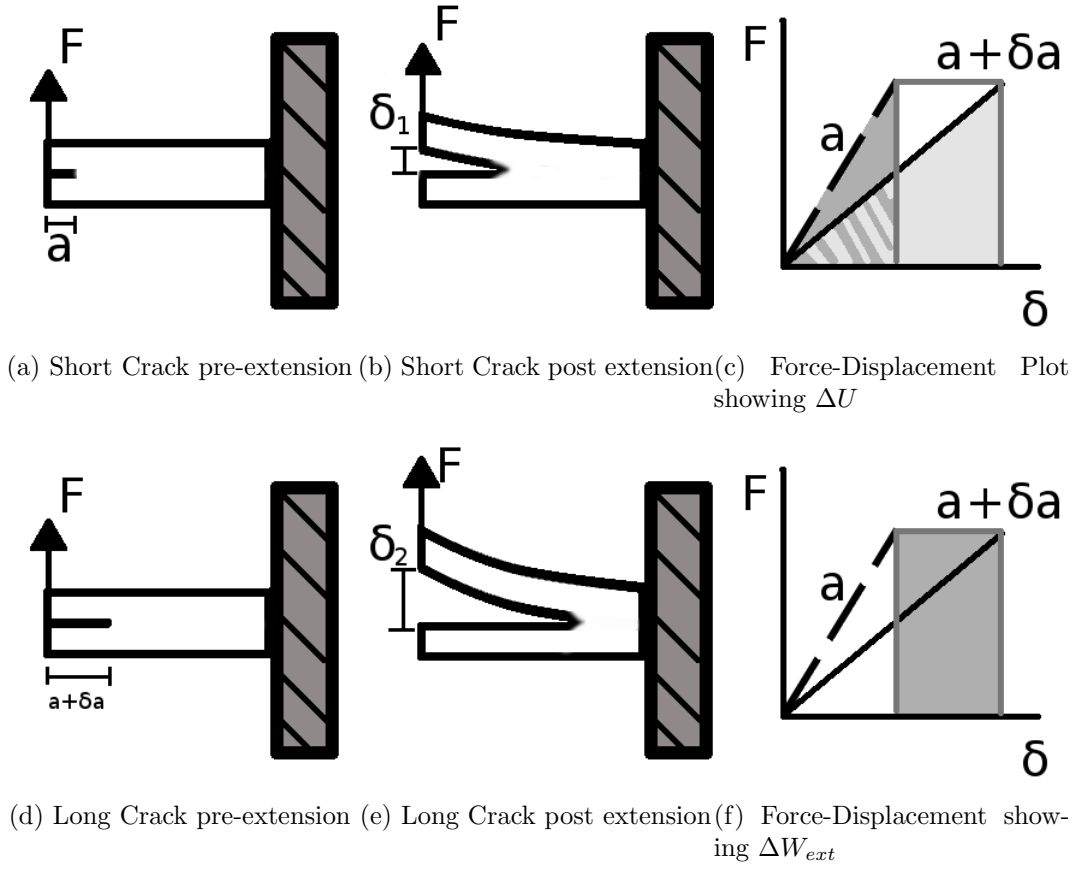


Figure 3.2: Energy release rate due to crack extension.

which is the area under the  $a + \delta a$  line minus the area under the  $a$  line in Figure 3.2c.

Now consider that the two beams are the same beam, just different points in time, then the beam starts with crack  $a$  and undergoes displacement via Hooke's law (the diagonal line). Then a critical point is reached where the crack extends and the  $F - \delta$  plot extends horizontally to the situation of the extended crack beam. Using  $d\delta = \delta_2 - \delta_1$  and calculating the external work done using Figure 3.2f, we get

$$\Delta U = \frac{1}{2} F d\delta \quad (3.7)$$

$$\Delta W_{ext} = F d\delta \quad (3.8)$$

which has an increase in strain energy per crack extension.

The other extreme condition is to force the beam tip under constant displacement. Like before, as the  $\delta$  is increased, the  $F - \delta$  graph increases linearly with a reduced stiffness for a beam with a longer crack. Similar to above, if we allow the crack to extend under constant displacement, then the plot curve would be the diagonal line (as  $\delta$  increases to the extension point), followed by a drop to the point on the second line. In this case, the changes in strain energy and work are

$$\Delta U = \frac{1}{2} \delta \, dF \quad (3.9)$$

$$\Delta W_{ext} = F \, d\delta = 0 \quad (3.10)$$

which shows a decrease in strain energy (since  $dF < 0$ ) when the crack extends.

For a crack in a semi-infinite plate with thickness  $B$ , Griffith (1921) showed that the strain energy of a centre crack (with two tips) is given by

$$U_a = \frac{\pi a^2 \sigma^2}{E} B \quad (3.11)$$

and the energy release from extending the crack is

$$U_s = 2(2a)B\gamma_s = -4aB\gamma_s \quad (3.12)$$

The sum of these two equations gives the total energy at the crack tip

$$U_T = U_a + U_s = \frac{\pi a^2 \sigma^2}{E} B - 4aB\gamma_s \quad (3.13)$$

The derivative of  $U_T$  with respect to  $2a$  gives the slope

$$\frac{\partial U_T}{\partial(2a)} = \frac{\pi a \sigma^2}{E} B - 2B\gamma_s \quad (3.14)$$

Setting the slope equal to zero determines the transition between stable and unstable crack growth. In terms of  $a$ , the critical crack length before unstable growth is

$$a = \frac{2E\gamma_s}{\pi\sigma^2} \quad (3.15)$$

The energy release rate as the crack grows can be written as

$$G = -\frac{\partial \Pi}{\partial A} = -\frac{\partial(U - W_{ext})}{\partial A} = -\frac{1}{B} \frac{\partial \Pi}{\partial a} \quad (3.16)$$

where  $A$  is the change in the area of the crack during extension, where an incremental increase in  $A$  is given by

$$\Delta A = B\Delta a \quad (3.17)$$

In terms of material compliance,  $C$ , for a constant load

$$\delta = CF \quad (3.18)$$

$$G = \frac{F^2}{2B} \frac{\partial C}{\partial a} \quad (3.19)$$

which holds in the case of constant displacement.

The resistance of an elastic material is defined as

$$R = 2\gamma_s \quad (3.20)$$

and is used to determine whether the crack growth is stable or unstable.

For fracture to initiate in an elastic material

$$G \geq R \quad (3.21)$$

meaning that there is enough available energy to create the new crack surfaces.

Stable crack growth occurs when

$$\frac{\partial G}{\partial a} < \frac{\partial R}{\partial a} \quad (3.22)$$

which means the crack would stop growing if the applied load was removed. For the case that

$$\frac{\partial G}{\partial a} \geq \frac{\partial R}{\partial a} \quad (3.23)$$

then the crack growth will be unstable. At this point, the growth of the crack has enough energy to continue its growth without the need of an applied load any more. Removal of the applied load at this point would not cause the crack to stop growing and catastrophic failure will occur.

For 2-D problems (or problems that can be simplified to 2-D), the energy release rate and stress intensity are related by

$$G = \begin{cases} \frac{K_I^2}{E} & \text{Plain Stress} \\ \frac{(1-\nu^2)K_I^2}{E} & \text{Plain Strain} \end{cases} \quad (3.24)$$

### 3.1.5 Weakest Link Theory of Failure

The previous sections outlined the basic theory and terminology for the growth of a single crack. Under normal conditions of interactions with ice, the ice will naturally have a distribution of cracks with many different lengths and orientations. The basic tenant of a weakest link theory is that a linked chain (Figure 3.3) is only as strong as

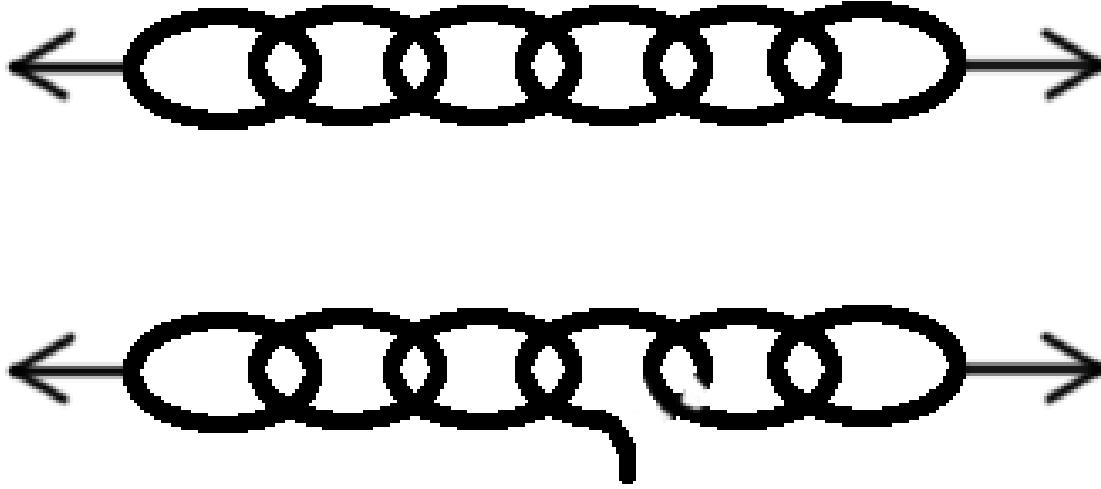


Figure 3.3: Two chains of different strengths. The strength of a chain is determined by its weakest link.

its weakest link, meaning the bottom chain would likely break on the fourth link.

One commonly used theory for describing the weakest link behaviour of materials was proposed by Weibull (1951). For any probability distribution, the following functional form

$$P \{X \leq x\} = F \{x\} = 1 - \exp \{-\psi \{x\}\} \quad (3.25)$$

where  $F$  defines the probability and  $\psi$  is some function that defines the shape of a distribution (such as the classic Gaussian or chi-squared distributions) of finding a value  $X$  less than  $x$ . Conversely,

$$1 - P \{x\} = \exp \{-\psi \{x\}\} \quad (3.26)$$

defines the probability of finding a value  $X$  greater than  $x$ .

Applying this logic to breaking a link in a chain,  $P \{x\}$  would define the probability of the link failing and  $1 - P \{x\}$  would define the probability of non-failure for a given load  $x$ . By definition, a chain is considered broken if any one of the links in the chain



breaks. Assuming there are  $n$  links in the chain, then the probability that the chain survives a forcing is

$$P_{survive} \{x\} = (1 - P \{x\})^n = \exp \{-n\psi \{x\}\} \quad (3.27)$$

which gives the probability that the chain breaks as

$$P_{break} \{x\} = (1 - P \{x\})^n = 1 - \exp \{-n\psi \{x\}\} \quad (3.28)$$

According to Weibull (1951), the shape function  $\psi$ , is only required to be a positive, non-decreasing function. Weibull proposed

$$\psi \{x\} = \frac{(x - x_\mu)^m}{x_0} \quad (3.29)$$

which is an empirical formula. This function has no physical basis, it is simply a basic function that works, but provides exceptional fits to various experimental results (Weibull, 1951).

In the case of ice, the strength of the ice will be affected by the natural distribution of cracks. The strength of an ice sample will be limited by whatever crack has the most favourable length and orientation for failure. A long crack with an orientation along the loading axis will cause an ice sample to fail under smaller loads/pressures than if the crack was shorter or oriented along a different axis (such as perpendicular to the loading axis). Since the distribution of cracks in ice samples will be different from sample to sample, then the strength of any ice sample will follow a statistical distribution. As explored in Hunt and McCartney (1979) and Taylor and Jordaan (2015), the statistical distributions of fracture strengths in ice experiments follow a Weibull-type weakest link theory.

### 3.1.6 Fracture Toughness

The mode I stress intensity factor for an internal crack in a thin, infinite plate is

$$K_I = \sigma\sqrt{\pi a} \quad (3.30)$$

where  $a$  is the half-crack length of an internal crack. Similar definitions for the modes II and III stress intensity can be defined (written as  $K_{II}$  and  $K_{III}$ ), but for notational simplicity, only mode I will be considered here.

The critical stress intensity, otherwise known as fracture toughness is given by

$$K_{IC} = \sigma_f\sqrt{\pi a} = \sqrt{2E\gamma_s} \quad (3.31)$$

The fracture toughness is related to dissipative terms, such as the surface energy release. For ice, this will include any viscoelastic effects giving the fracture toughness as

$$K_{IC} = \sigma_f\sqrt{\pi a} = \sqrt{2E(\gamma_s + \gamma_v)} \quad (3.32)$$

which will also affect  $\sigma_f$ .

In the case of plastic deformation, one can consider an effective crack length which is the actual crack length plus the fracture zone radius (since it cannot support any more stress). The size of the plastic zone is given by

$$R_p = \frac{K_I^2}{2\pi\sigma_y^2} = \frac{\sigma^2 a}{2\sigma_y^2} \quad (3.33)$$

where  $\sigma_p$  is the plastic yield strength. This gives the fracture stress as

$$\sigma_f = \frac{K_{IC}}{\sqrt{\pi(a + R_p)}} = \frac{K_{IC}}{\sqrt{\pi a(1 + K_{IC}^2/(2\pi a\sigma_y^2))}} \quad (3.34)$$

which gives the effective fracture toughness as

$$K_{IC} = \frac{\sigma_f \sqrt{\pi a}}{\sqrt{1 - \frac{1}{2} \left( \frac{\sigma}{\sigma_y} \right)^2}} \quad (3.35)$$

The stress intensity often can be written in a more general form as

$$K_I = Y \sigma \sqrt{\pi a} \quad (3.36)$$

which will lead to fracture when  $K_I \geq K_{IC}$ . This occurs when a critical stress is reached in the presence of a known crack, or when a crack extends to a critical length in the presence of a known stress. The coefficient  $Y$  is known as the geometric shape factor.  $Y$  can be a function of crack shape and size; specimen shape and size; and the loading method (e.g.; loading modes I, II, and III)

To provide a consistent way to measure  $K_I$ , various sets of fracture tests have been defined to guide experimenters in obtaining good results. One such guideline is the ASTM E399 (Anderson, 2005; Zhu and Joyce, 2012) that provide a variety of test scenarios and provides an equation relating  $K_I$  to the applied stress on the specimen in the form of equation 3.36. A few of these specimen geometries are summarized in figure 3.4.

Experiments done by Dempsey (1996) investigated the fracture toughness using naturally grown ice from two lakes in Northern Alberta. A variety of tests were done including 3-point bending, reversed tapered, and specimens with edge cracks split by a flatjack (see figure 3.5). The results of these experiments showed that the fracture toughness nearly tripled over the length scales up to 30 m (covering a ratio of 1:80 from smallest to largest). This increase mostly happened on scales up to 5–10 meters and became nearly constant for larger scales. Unfortunately, the rate of loading on

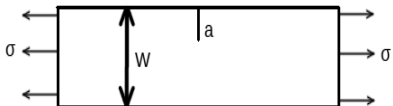
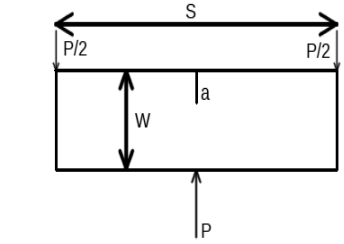
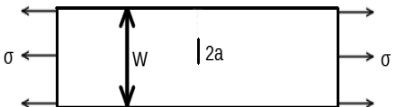
Specimen	Fracture Toughness Equation
<p>a)</p> 	$K = Y\sigma\sqrt{\pi a} = \left( \sqrt{\frac{W}{\pi a}} \frac{2 \tan \frac{\pi a}{2W}}{\cos \frac{\pi a}{2W}} \left[ 0.752 + 2.02 \left( \frac{a}{W} \right) \right] \right) \sigma\sqrt{\pi a}$
<p>b)</p> 	$K = \frac{P}{B\sqrt{W}} \left( \frac{3 \frac{S}{W} \sqrt{\frac{a}{W}}}{2 \left( 1 + 2 \frac{a}{W} \right) \left( 1 - \frac{a}{W} \right)} \left[ 1.99 - \frac{a}{W} \left( 1 - \frac{a}{W} \right) \right. \right. \\ \left. \left. \left( 2.15 - 3.93 \left( \frac{a}{W} \right) + 2.7 \left( \frac{a}{W} \right)^2 \right) \right] \right)$
<p>c)</p> 	$K = Y\sigma\sqrt{\pi a} = \left( \frac{1}{\sqrt{2 \left( 1 - \frac{a}{W} \right)}} \left[ 1.122 - 0.561 \left( \frac{a}{W} \right) - 0.205 \left( \frac{a}{W} \right)^2 + \right. \right. \\ \left. \left. 0.471 \left( \frac{a}{W} \right)^3 + 0.190 \left( \frac{a}{W} \right)^4 \right] \right) \sigma\sqrt{\pi a}$

Figure 3.4: Sample recommended testing from ASTM for  $K_I$  fracture. a) Single Edge Notched Tension (SENT) b) Single Edge Notched Bent (SE(B)) c) Double Edge Notched Tension (DENT)

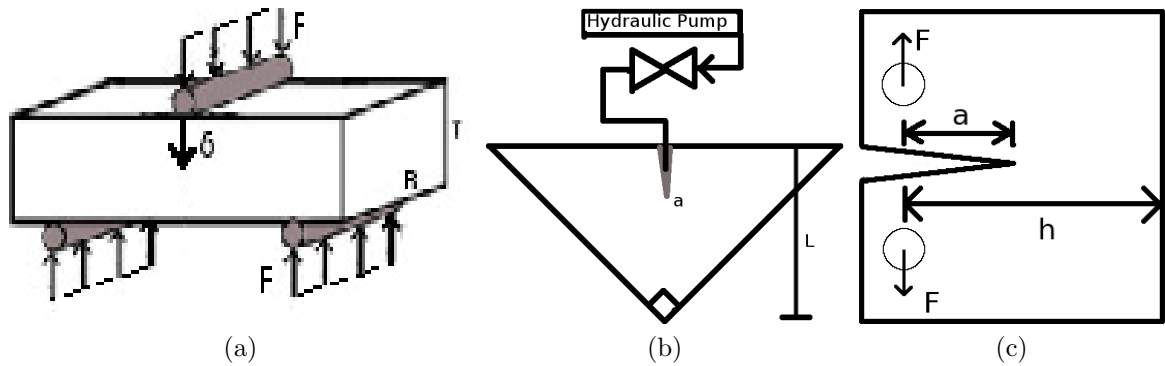


Figure 3.5: a) 3-Point beam bending set-up. b) Reverse Tapered ice specimen with steel-walled flatjack along crack wall. c) Compact tension specimen loaded at grips above and below an edge crack.

the crack faces was not recorded. This hinders the study of any scale effects related to how the strain rate near the crack tip would be changed by the increase in specimen size. The local strain rate at the crack tip is related to the ductile or brittle properties of ice, which would affect the values of the recorded fracture toughness.

Weiss and Schulson (1994) experimented with 155 mm cubic ice samples under multi-axially, proportionally loaded ice at temperatures  $-10^{\circ}\text{C}$ ,  $-20^{\circ}\text{C}$ , and  $-40^{\circ}\text{C}$ . Ice was loaded at a strain rate of  $10^{-3} \text{ s}^{-1}$ , and unloaded at  $10^{-6} \text{ s}^{-1}$  to prevent crack nucleation and growth upon unloading. Their experiment showed that smaller grained ice was more ductile than larger grains.

The work of Goodman and Tabor (1978) also showed that the fracture toughness is dependent on temperature: decreasing with decreasing temperature. This is due to the decreased creep and damage mechanisms at lower temperatures, meaning less energy is dissipated by these mechanisms, reducing the total energy input needed to initiate and propagate cracks.

Gagnon and Gammon (1995) conducted 3-point and 4-point bending tests on ice obtained from Greenland and Labrador. The aim of the study was to explore the effects of bubble density and temperature on the flexural strength of ice. The results

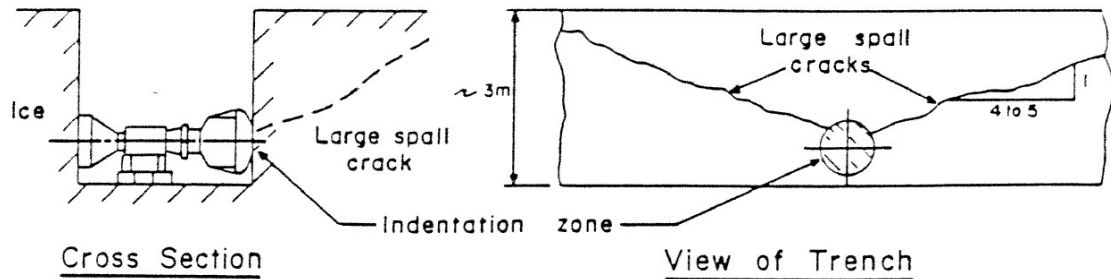
of this study showed the flexural strength of ice increased with increased bubble density (by 27%) and decreased with increased temperature (by 60%). These results show that the flexural strength (and fracture toughness) can vary significantly in ice due to effects such as temperature and bubbles.

Timco and Frederking (1983) studied ice samples from the Beaufort Sea. The samples were granular at the top and become columnar below 30 cm. They performed 4-point bending experiments on the ice to test its flexural strength. Aside from fracture toughness decreasing with increasing loading rate, increasing temperature, and decreasing grain size, Timco and Frederking (1983) also note that fracture toughness decreases with increasing salinity.

### 3.1.7 Time-dependent Failure

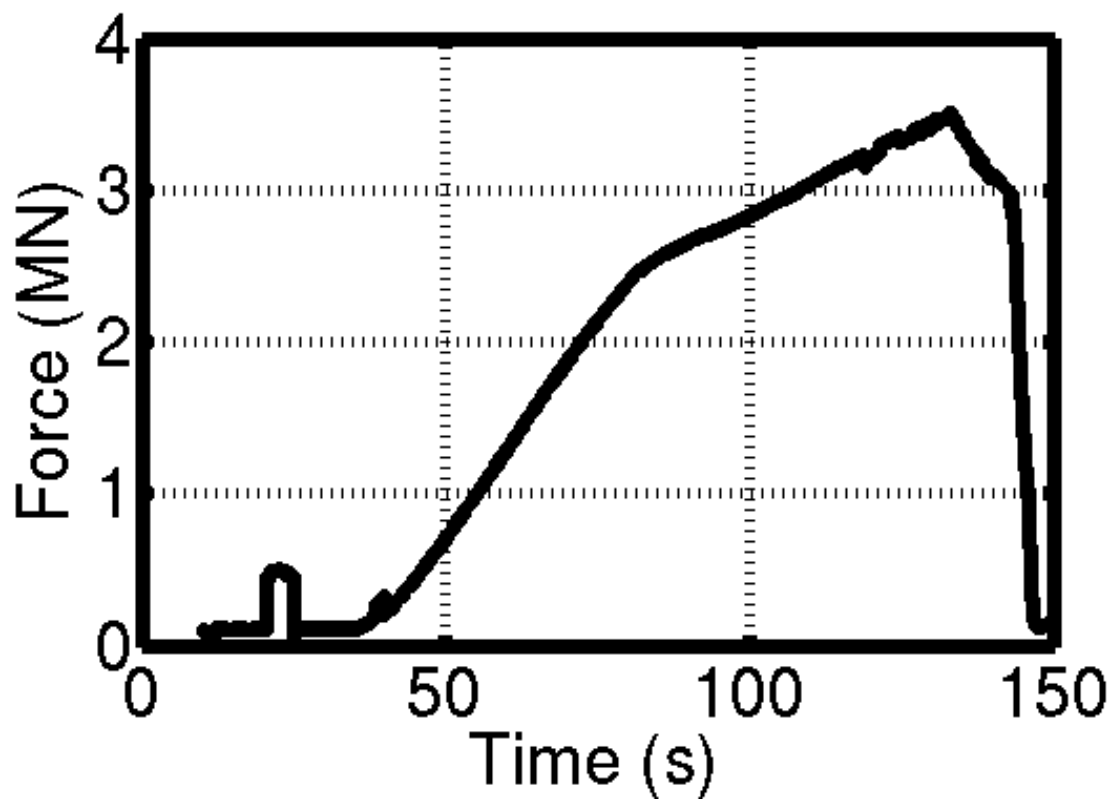
Time-dependent failure in ice is a relatively new development in ice fracture mechanics (though it has been used in other materials), and providing a better understanding of it is the major aspect of this thesis. Studies in the field and the laboratory (discussed later) have shown that the strength of ice is strongly dependent on the loading rate. This relationship is represented as a decreasing power-law curve between the strength of the ice and loading rate (which could be strain-, displacement-, or force-controlled). The strength of ice is highest under slow loading tests and is the weakest under extremely fast loading tests (in which the ice behaves as a brittle elastic). In short, slow loading lead to creep-like behaviour in ice, fast loading lead to brittle behaviour, and intermediate loading rates provide a mix of both.

The second aspect of time-dependent failure is stable cracks growth under load leading to delayed failure. One example of delayed failure occurred during the medium-scale indentation series at Hobson's Choice ice island (Frederking et al., 1990). Many of the experiments done in that series were focused on the loads and pressures exerted



(a)

## Hobsons Choice 1989 Test 1



(b)

Figure 3.6: Delayed fracture during creep test at Hobsons Choice medium-scale indentation test (Frederking et al., 1990).

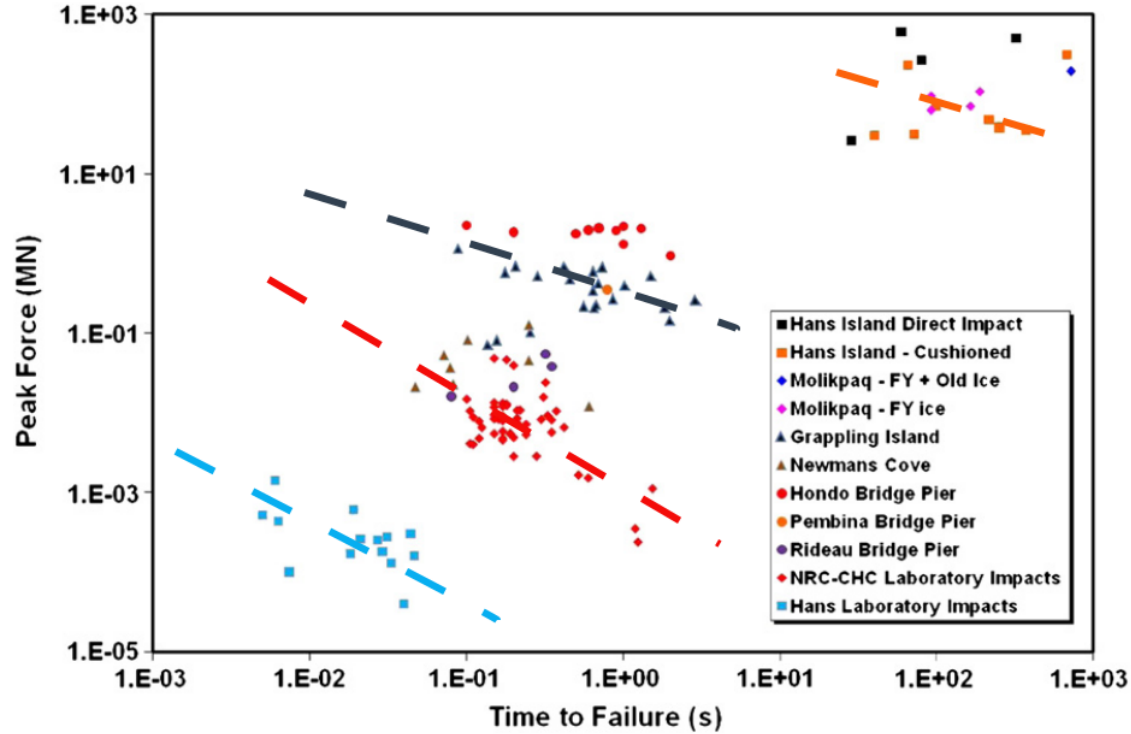


Figure 3.7: Time to Failure for peak loads, taken from Timco (2011). Trendlines added to original plot to show decreasing power law relationship discussed in text.

at the contact zone between the indenter and the ice wall. In one test, a slow speed was used, causing the ice to have a more (damage-enhanced) creep-like response. As shown in figure 3.6, after roughly 1.5 minutes of testing, the ice underwent a large failure that broke off a large section of the ice wall (for comparison, most tests during that series were under 1 second). As will be discussed later, under faster loading, this large-type of failure is less likely to be seen and is replaced by smaller more frequent spalling events.

Timco (2011) provides analysis of a variety of data sources from the Hans Island experiments (Danielewicz and Metge, 1981), the Molikpaq Arctic Caisson (Hardy et al., 1996), and various other bridge and laboratory-scale experiments for a total of 9 data sources. One particularly interesting plot (Figure 3.7), was of peak load versus



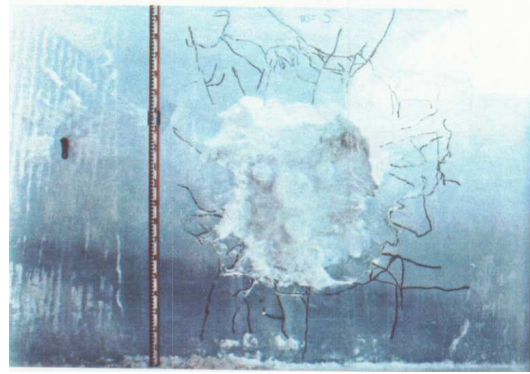
time to failure. In the figure, the data was presented in a way to show that the higher peak loads have a longer time to failure (one can visualize a linear fit with a positive slope connecting the various datasets) and is explained that this is true because the bigger experiments had the bigger loads and would take longer to fail. However, as not mentioned in the paper, there is a decreasing power-law curve relating time to failure with peak load. This can be seen by considering any one dataset, where each data set (e.g., The Hondo Bridge) exhibits increasingly longer time to failure for reduced loads. These all have a power-law decreasing relationship as expected.

A set of medium-scale indentation test were ran in the winter of 1984-85 at Rae Point in Northern Canada. There was a total of 24 indentation test with velocities ranging from 0.1–100mm/s (Masterson et al., 1999). The experiments used flat (surface area= $1m^2$ ) and spherical indentors ( $1m^2$  and  $2m^2$ ) in trenches cut into the ice 50 m long, 2.5 m wide, and 3.5 m deep. Figure 3.8a and b show the results of a slow (1 mm/s) and fast (10 mm/s) loading tests. The slow test displays ice undergoing ductile behaviour with no fracturing and small amounts of crushed ice. The fast test displays brittle behaviour as the ice displays more crushed ice and the formation of cracks radiating from the contact zone. Figure 3.8c shows the data from the  $1m^2$  indenter. This data shows a clear exponentially decreasing pressure with contact area.

Another series of medium-scale indentation experiments were conducted by Memorial University, the National Research Council of Canada (NRC) and Sandwell (formerly GEOTECH) at Hobson's Choice ice island in 1989/1990 (Frederking et al., 1990; Masterson et al., 1993). Trenches were cut into the ice and an indenting apparatus was placed in the trench. The apparatus could be attached by various indentors up to  $3 m^2$  and could load the ice with up to 4.5 MN of force. These experiments showed that the damaged layer was thinner for faster loading rates. The pressure at the centre of the indenter was about three times the average pressures over the



(a) Ductile Indentation



(b) Brittle Indentation

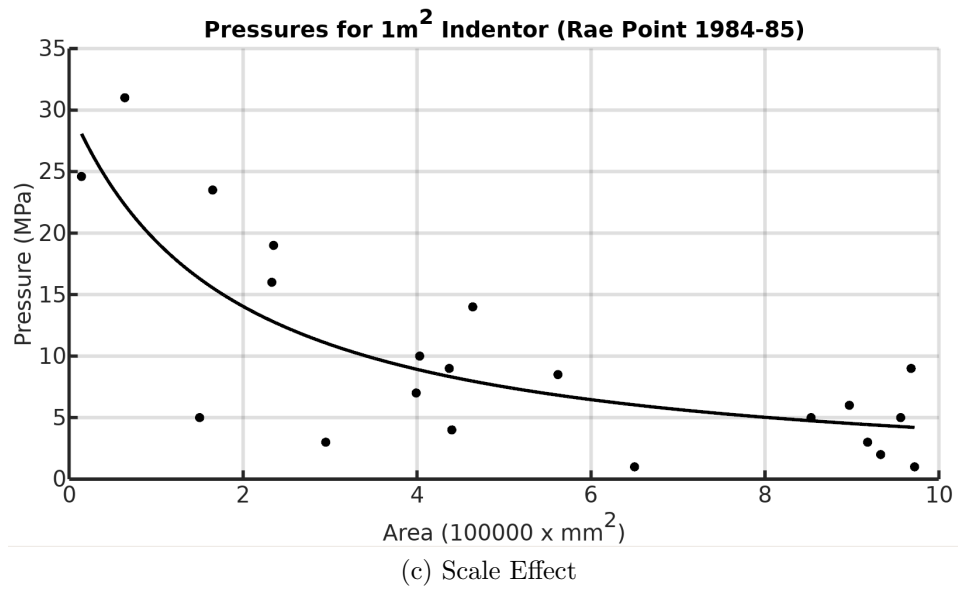


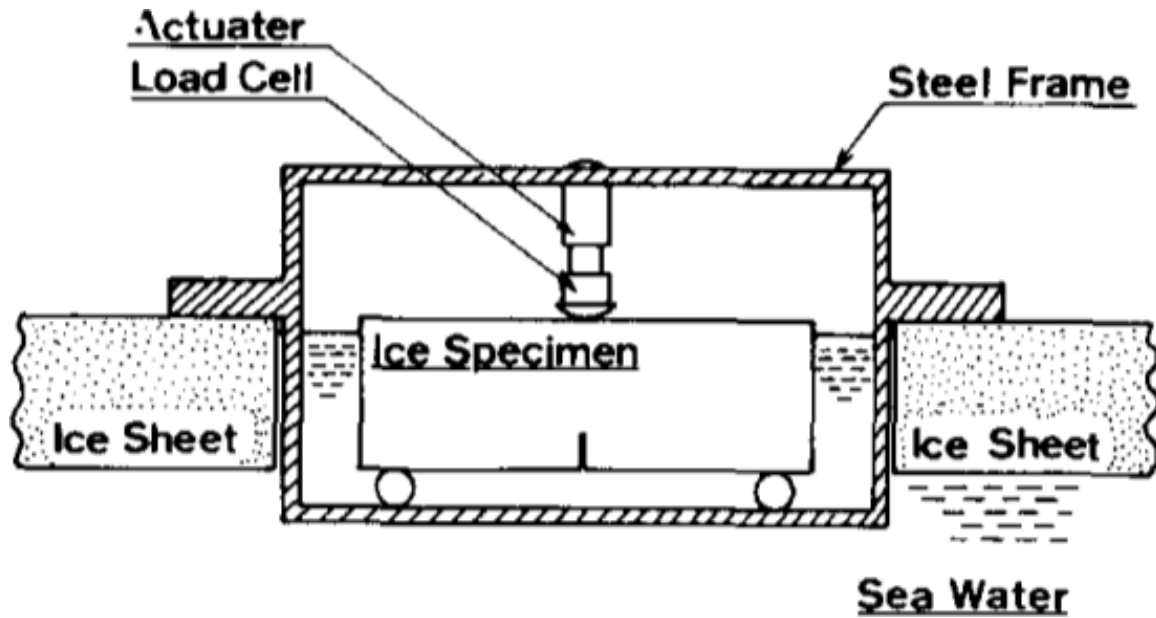
Figure 3.8: Images and data collected during the Rae Point indentation series by Sandwell/GEOTECH in 1984-85

contact area. The results also showed the rate-effect on the ductile-brittle behaviour of ice and a large spalling event that occurred at the end of a slower test (hinting at delayed failure in ice).

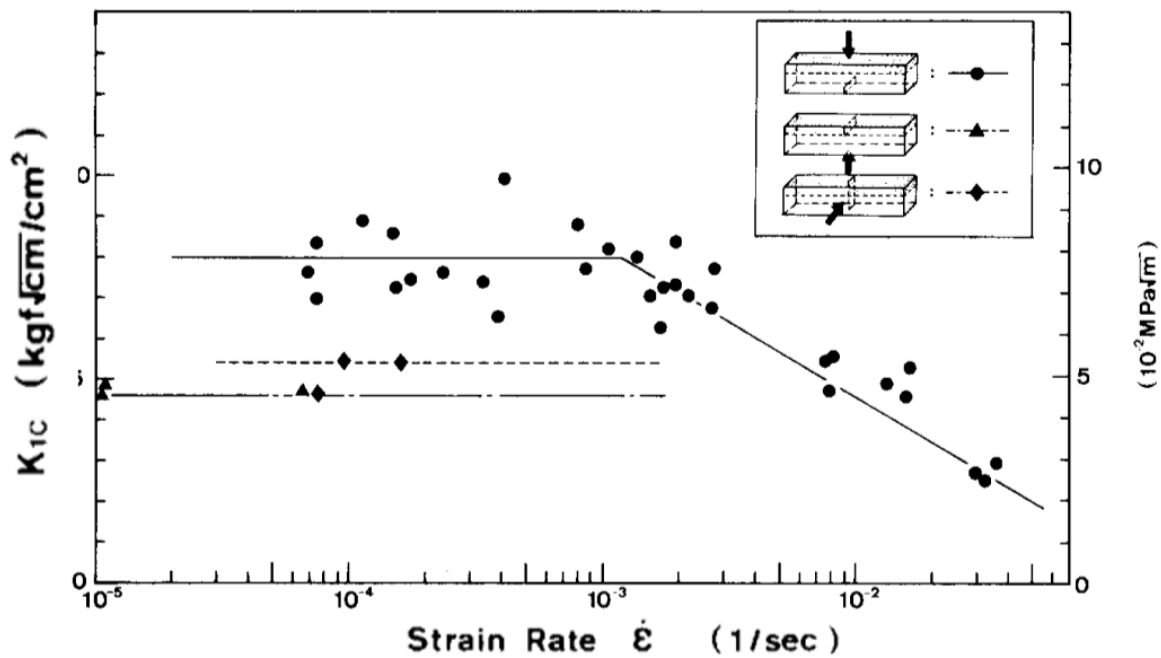
Urabe et al. (1980) did a set of 3-point bending tests using sea ice at  $-2^{\circ}\text{C}$  from an inland sea in Northern Japan. The specimens rested on rollers 160 cm apart in water. The height of the rollers were adjusted so that the weight of the ice from buoyancy was cancelled out, as shown in Figure 3.9a. The experimental results in Figure 3.9b show that the fracture toughness was constant for strain rates less than  $10^{-3}\text{s}^{-1}$  and underwent power-law decay for strain rates above  $10^{-3}\text{s}^{-1}$ .

Fracture toughness testing on compact tension ice specimens, as well as crack-arrest tests, were performed by Liu and Miller (1979). They used fresh-water ice that was distilled and grown from a layer of 4 mm seed placed in the bottom of a tank between  $-8^{\circ}\text{C}$  and  $-10^{\circ}\text{C}$ . Aided by mechanical shaking, this produced bubble-free, columnar ice. Their test speeds ranged from 0.5—480 mm/s for the fracture toughness testing. These experiments showed a decreasing power law with respect to velocity,

Hamza and Muggeridge (1980) performed small-scale experiments on fresh water ice grown at  $-23^{\circ}\text{C}$ . The ice samples were cubes with a side length of 60.96 cm and columnar grain sizes of either 8 or 12 mm. 3-point bending experiments were done with a range of temperatures from  $-40^{\circ}\text{C}$  to  $-3.89^{\circ}\text{C}$ , with velocities that ranged from 0.00167 mm/s to 0.833 m/s. The experiments showed that the faster loading rates resulted in lower fracture toughness, due to viscoelastic effects of the ice. The fracture toughness also increased with decreasing temperature to  $-30^{\circ}\text{C}$  and then lowered at  $-40^{\circ}\text{C}$ . The increasing fracture toughness with decreasing temperature is similar to the results of (Goodman and Tabor, 1978) and (Liu and Miller, 1979), except for the changing trend at  $-30^{\circ}\text{C}$ . The change in the trend at  $-30^{\circ}\text{C}$  may or may not be a real effect as the change is within the errors of the experiment, and more testing could be



(a)



(b)

Figure 3.9: a) Experimental set-up from Urabe et al. (1980). Bottom rollers are adjusted to cancel the buoyancy of the ice, causing it to be weightless. b) Results of Urabe et al. (1980), showing the relationship between apparent fracture toughness and strain rate of sea ice under 3-point bending tests.

done to confirm if this a temperature effect or due to some variability in the ice.

### 3.1.8 Summary of Literature Review

From reviewing previous experiments, there is much work to be done in understanding fracture mechanics and building an appropriate model. The indentation experiments and Rae Point and Hobson's Choice show that there are distinct zones of high pressure that are significantly different from that of the parent ice far from the contact zone. As a result of the high degree of confinement and shear stresses in the centre of these zones, ice becomes highly softened due to processes such as recrystallization, pressure melting, and microcracking.

From a fracture mechanics perspective, the centres of these zones are under high compression, leading to mainly damage processes and microcracking. Just beyond the centre the ice is under less compression but is under a lot of shear stress. This zone of high shear no longer prevents to growth of larger crack formation, leading to spalling events.

The rate of loading on the ice affects its properties (ductile versus brittle), which has an impact on the stability of crack growth and the type of failures - such as small localized spalls or possibly large, global, delayed spalling events.

Given the rate-dependent nature of fracture in ice and the random nature of ice grain formation, experimental results would suggest that a physically-based model using a viscoelastic theory of crack growth would be required to explain the fracture properties of ice.

## 3.2 Critical Analysis of Linear Elastic Fracture Theory

The purpose of this section is to develop the background theories involved in developing the model to be used in this project. The following works provide the physical and mathematical background used in the new model.

As the title of this section suggests, these theories were developed for linear elastic materials, and will be discussed here in such a manner. Field and laboratory experiments on ice have shown that ice does not behave like an elastic (or elastic-plastic) material. As was discussed in the previous sections, the strength of ice has been shown to be highly dependent on how it has been loaded and fails over time. A viscoelastic treatment of ice fracture is discussed in Chapter 6, but is built upon the theories discussed in this section.

Having discussed the key concepts of fracture mechanics (and alluding to the viscoelastic nature of ice), the underlying LEFM model described in Westergaard (1939), Williams (1957), and Alturi et al. (1975) is discussed. The major shortcoming of this theory (to be explained in detail), was an infinite stress at the crack tip. This issue was addressed by the introduction of a cohesive zone in front of the crack tip by Barenblatt (1962). A model developed by Dugdale (1959) using a plastic zone in front of the crack tip has similar results to the work of (Barenblatt, 1962) - leading to what is known as the Dugdale-Barenblatt (DB) model. While the two versions of the cohesive zone (also known as process or failure zones) have similar results, the physical meanings are strikingly different. It is of the opinion of the author that the Barenblatt model lies closer to the reality of the processes in ice, and will explain the Barenblatt model in some detail.

The final step in developing a set of viscoelastic equations for the modelling of

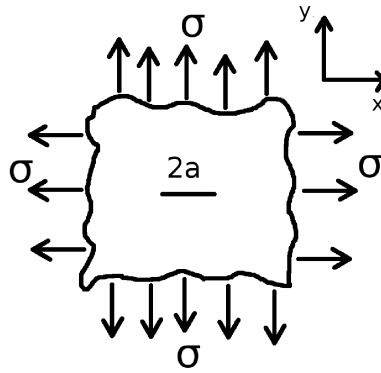


Figure 3.10: Westergaard setup of a centrally located crack in an infinite plate under biaxial tension

ice was developed by Schapery (1975a,b,c). Schapery (1975a) uses the correspondence principle to convert Barenblatt (1962) from a linear elastic material to a linear viscoelastic material. This will be presented in Chapter 6.

### 3.2.1 The Westergaard Model

The model by Westergaard (1939) defines a small crack, of length  $2a$  in a semi-infinite plane of a linear elastic material, as shown in Figure 3.10. This experimental set-up (in either uniaxial or biaxial loading) provides the least complex geometry/mathematics for studying fracture mechanics. Using the approximations of Westergaard (1939), the stress field of the material to be solved analytically near the crack tip, but there will be a stress singularity at the crack tip (which has been resolved). The solution from Westergaard (1939) provides a solid starting point into fracture mechanics and led to many insights.

To begin, the elastic stress field ( $\sigma_x^0$ ,  $\sigma_y^0$ , and  $\sigma_{xy}^0$ ) can be found with the Airy's

Stress Function given by

$$\begin{aligned}
 \nabla^4 \phi &= 0 \\
 \sigma_x^0 &= \partial_{xx}^2 \phi \\
 \sigma_y^0 &= \partial_{yy}^2 \phi \\
 \sigma_{xy}^0 &= \partial_{xy}^2 \phi
 \end{aligned} \tag{3.37}$$

with the boundary conditions

$$\begin{aligned}
 &\text{for } y = 0 \text{ for all } x, \sigma_{xy}^0 = 0 \text{ No shear on crack plane} \\
 &\text{for } -a < x < a \text{ on } y = 0, \sigma_y^0 = \sigma_{xy}^0 = 0 \text{ Stress-free crack face} \\
 &\text{as } z \rightarrow \infty, \sigma_x^0 = \sigma_y^0 = \sigma \text{ and } \sigma_{xy}^0 = 0 \text{ Biaxial tension}
 \end{aligned} \tag{3.38}$$

as defined by the biaxial loading used in Westergaard (1939).

To obtain the Airy's stress function (and hence the Westergaard solution), complex analysis can be used. Starting with the equations from Muskhelishvili (1953b), who developed generalized analytical solutions for the Airy's Stress Function using complex analysis (among other things),

$$\begin{aligned}
 \sigma_x^0 + \sigma_y^0 &= 4\mathbf{Re}\{\partial_z \Omega\{z\}\} \\
 \sigma_y^0 - \sigma_x^0 + 2i\sigma_{xy}^0 &= 2(z^* \partial_{zz} \Omega\{z\} + \partial_{zz} \psi\{z\}) \\
 2\mu(u^0 + iv^0) &= \kappa \Omega\{z\} - z \partial_z \Omega^*\{z\} - \psi\{z\} \\
 \nabla \phi &= \mathbf{Re}\{z^* \Omega\{z\} + \bar{\psi}\{z\}\}
 \end{aligned} \tag{3.39}$$

where  $\Omega\{z\}$  and  $\psi\{z\}$  are complex functions of  $z = x + iy$ . The over bars are integrals with respect to  $z$ , and an asterisk refers to the complex conjugate.  $\kappa$  is defined in equation 2.17.



For the case of biaxial loading,  $\sigma_{xy}^0 = 0$  along  $y = 0$ , from the second expression in equations 3.39

$$\begin{aligned}\mathbf{Im}\{2(z^*\partial_{zz}\Omega\{z\} + \partial_{zz}\psi\{z\})\} &= 0 \\ z^*\partial_{zz}\Omega\{z\} + \partial_{zz}\psi\{z\} + A &= 0 \\ \partial_{zz}\psi\{z\} &= -z^*\partial_{zz}\Omega\{z\} - A\end{aligned}\tag{3.40}$$

where  $A$  is some real constant. In the analysis of Westergaard, he used  $A = 0$ , but it does not have to be. Substituting equation 3.40 back into the equations 3.39 (and setting  $A = 0$ ) gives

$$\begin{aligned}\sigma_x^0 &= 2\mathbf{Re}\{\partial_z\Omega\{z\}\} - 2y\mathbf{Im}\{\partial_{zz}\theta\{z\}\} \\ \sigma_y^0 &= 2\mathbf{Re}\{\Omega\{z\}\} + 2y\mathbf{Im}\{\partial_{zz}\theta\{z\}\} \\ \sigma_{xy}^0 &= -2y\mathbf{Re}\{\partial_{zz}\Omega\{z\}\} \\ 2\mu u^0 &= (\kappa - 1)\mathbf{Re}\{\Omega\{z\}\} - 2y\mathbf{Im}\{\partial_z\Omega\{z\}\} \\ 2\mu v^0 &= (\kappa + 1)\mathbf{Im}\{\Omega\{z\}\} - 2y\mathbf{Re}\{\partial_z\Omega\{z\}\}\end{aligned}\tag{3.41}$$

which provide equations for the stress and displacement fields, provided an Airy's function can be found.

Westergaard showed that the Airy's stress function can be written as

$$\phi = \mathbf{Re}\{\bar{\bar{Z}}\} + y\mathbf{Im}\{\bar{Z}\}\tag{3.42}$$

Where the complex function  $Z$  is subject to the Cauchy-Riemann conditions

$$\begin{aligned}\mathbf{Re}\{\partial_z Z\} &= \frac{\partial \mathbf{Re}\{Z\}}{\partial x} = \frac{\partial \mathbf{Im}\{Z\}}{\partial y} \\ \mathbf{Im}\{\partial_z Z\} &= \frac{\partial \mathbf{Im}\{Z\}}{\partial x} = -\frac{\partial \mathbf{Re}\{Z\}}{\partial y}\end{aligned}\tag{3.43}$$

which are necessary and sufficient conditions for  $Z$  to be complex-differentiable ( $Z$  has real and complex derivatives).

The Airy's stress field defined in equation 3.37 can be rewritten as

$$\begin{aligned}\sigma_x^0 &= \partial_{xx}\phi = \mathbf{Re}\{Z\} - y\mathbf{Im}\{Z\} \\ \sigma_y^0 &= \partial_{yy}\phi = \mathbf{Re}\{Z\} + y\mathbf{Im}\{Z\} \\ \sigma_{xy}^0 &= \partial_{xy}\phi = -y\mathbf{Re}\{Z\}\end{aligned}\tag{3.44}$$

which is the same as equation 3.41 with

$$\Omega\{z\} = \frac{1}{2}Z\tag{3.45}$$

For the case of the crack in a thin, infinite plate under biaxial tension,  $\sigma$ ,

$$Z = \frac{\sigma(z+a)}{\sqrt{(z+a)^2 - a^2}}\tag{3.46}$$

which meets the conditions defined in equation 3.38. Here  $a$  is the half-crack length and  $z$  has its origin at the crack tip. Provided that one is only interested in the area near the crack tip, then  $a \gg z$ , giving

$$Z \approx \frac{\sigma a}{\sqrt{2az}} = \sigma\sqrt{a}(2z)^{-\frac{1}{2}}\tag{3.47}$$

Defining the stress intensity as

$$K_I = \sigma\sqrt{\pi a}\tag{3.48}$$

(by definition,  $Y = 1$  for this geometry), gives

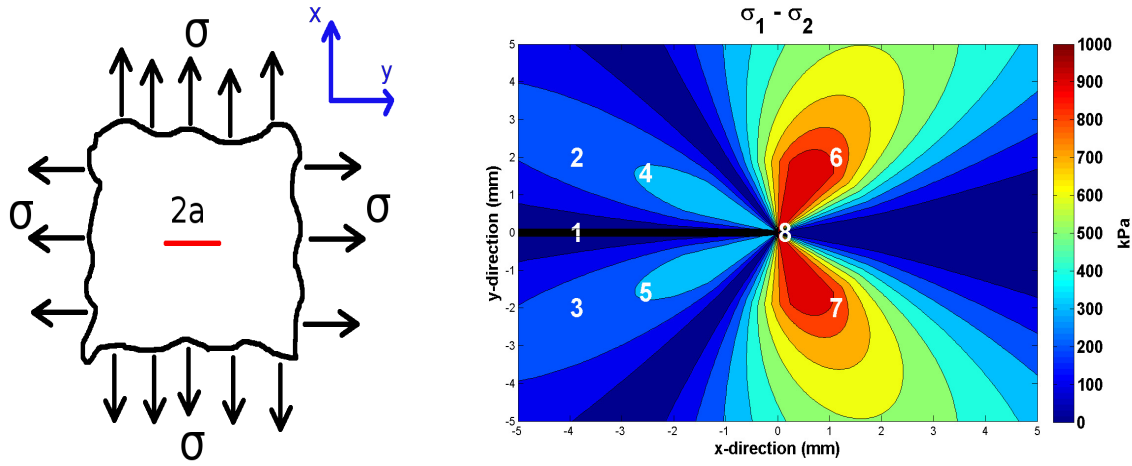
$$Z = \frac{K_I}{\sqrt{2\pi r}} \left( \cos \left\{ \frac{\theta}{2} \right\} - i \sin \left\{ \frac{\theta}{2} \right\} \right) \quad (3.49)$$

to which one can calculate the stress field as

$$\begin{bmatrix} \sigma_x^0 \\ \sigma_y^0 \\ \tau_{xy}^0 \end{bmatrix} = \left( \frac{K_I}{\sqrt{2\pi r}} \right) \left( \cos \left\{ \frac{\theta}{2} \right\} \right) \begin{bmatrix} 1 - \sin \left\{ \frac{\theta}{2} \right\} \sin \left\{ \frac{3\theta}{2} \right\} \\ 1 + \sin \left\{ \frac{\theta}{2} \right\} \sin \left\{ \frac{3\theta}{2} \right\} \\ \sin \left\{ \frac{\theta}{2} \right\} \cos \left\{ \frac{3\theta}{2} \right\} \end{bmatrix} \quad (3.50)$$

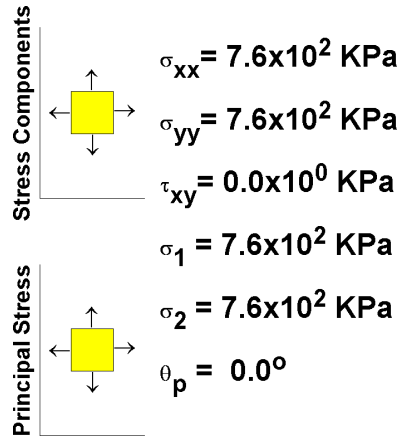
Figure 3.11b—j shows a typical stress field near a crack tip. The first image shows the resulting fringe pattern. The pattern captures most of the properties of a crack in a brittle material, but is missing stresses in front of the crack tip ( $\sigma_1 - \sigma_2$  does not necessarily equal in real materials). The remaining figures show the stress components for the Westergaard solution at various points near the crack. The solution shows that there is no shear stress along the crack or in front of the crack (Points 1 and 8). The other points show that the shear stress (and principal angle) is of the opposite sign for locations above and below (e.g.; Points 2 and 3 differ in shear stress). The Westergaard solution captures much of the pattern observed, but in reality there is a non-zero fringe pattern in front of the crack tip.

The crack opening, for the case of plane strain, can be found by doubling the left-hand side of the last expression in equations 3.41, equations 2.16 and 2.17 for plane

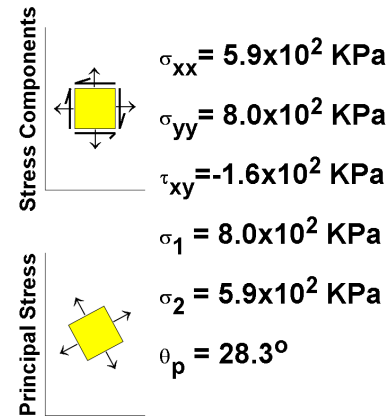


(a) Crack under biaxial tension

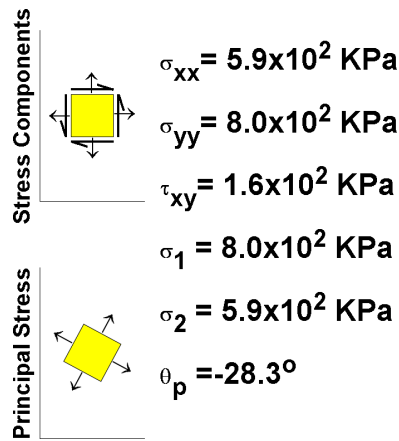
(b) Principal stress fringe pattern near crack tip



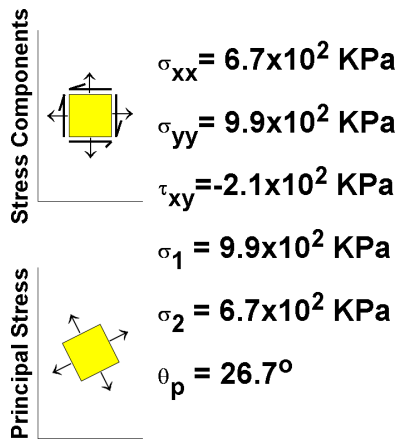
(c) Point 1



(d) Point 2



(e) Point 3



(f) Point 4

Figure 3.11

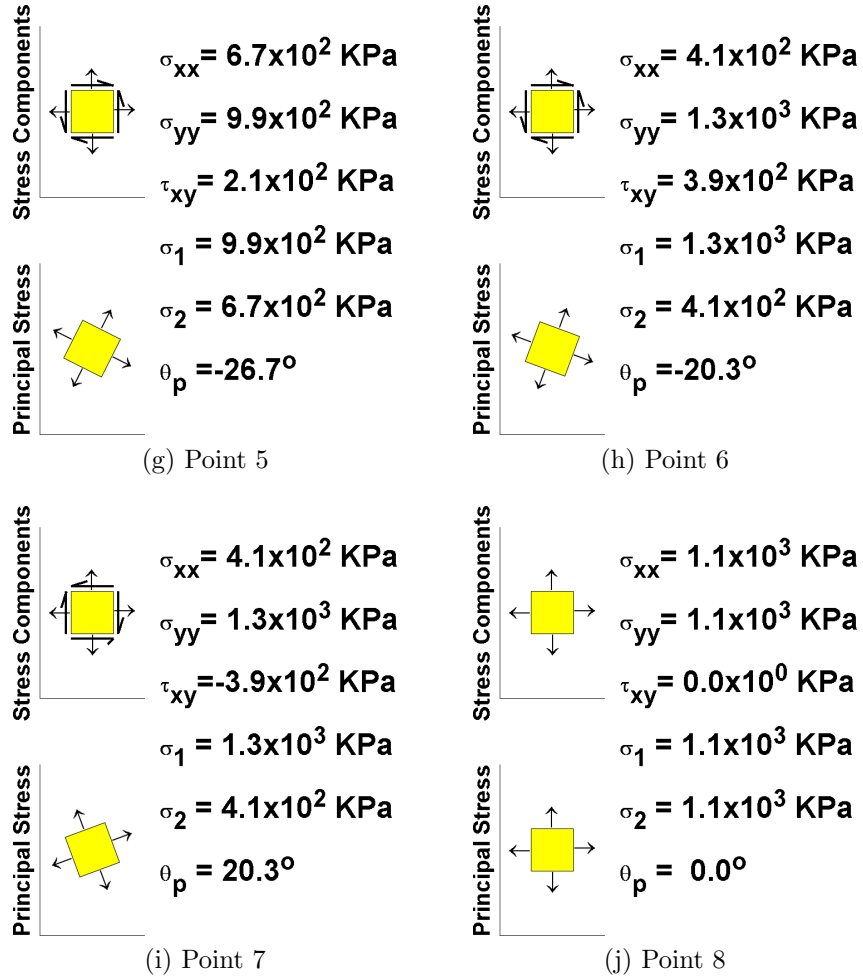


Figure 3.11: Westergaard stress solution at multiple points

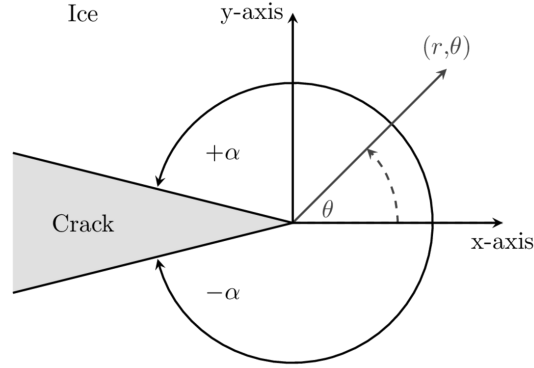


Figure 3.12: Williams wedge-shaped geometry. As  $\alpha$  tends to zero, the wedge becomes a crack.

strain, and using  $y = 0$  along the crack

$$\begin{aligned}
 2\mu v^0 &= 2(\kappa + 1)\mathbf{Im}\{\Omega\{z\}\} - 4y\mathbf{Re}\{\partial_z\Omega\{z\}\} \\
 v^0 &= \frac{1}{\mu}(\kappa + 1)\mathbf{Im}\{\Omega\{z\}\} \\
 v^0 &= 4\frac{1+\nu}{E}(1-\nu)\mathbf{Im}\{Z\} \\
 v^0 &= 4\left(\frac{1-\nu^2}{E}\right)\mathbf{Im}\{Z\}
 \end{aligned} \tag{3.51}$$

### 3.2.2 The Williams Model

The solution of Westergaard (1939) is a first-order approximation of the stress field near the crack tip (but not too close as there exists the singularity at  $r = 0$ ). A more accurate representation of the stress field near the tip can be found in Williams (1957) (but still containing the singularity).

Williams (1957) defines the Airy Stress Function in the form

$$\phi = r^{\ell+1}F\{\theta\} \tag{3.52}$$

from previous works (Williams, 1952), William's approach has two boundary con-

ditions related to the crack being stress free (see Figure 3.12 for crack geometry).

Notably

$$\left. \begin{aligned} \sigma_{\theta\theta} &= 0 \\ \sigma_{r\theta} &= 0 \end{aligned} \right\}_{\theta=\pm\alpha} \quad (3.53)$$

where the stress components, in polar coordinates are

$$\sigma_{rr} = \frac{1}{r} \frac{\partial \phi}{\partial r} + \frac{1}{r^2} \frac{\partial^2 \phi}{\partial \theta^2} = \frac{1}{r} F\{\theta\} (\ell + 1) r^\ell + \frac{1}{r^2} r^{\ell+1} F''\{\theta\} \quad (3.54)$$

$$\sigma_{\theta\theta} = \frac{\partial^2 \phi}{\partial r^2} = \ell(\ell + 1) r^{\ell-1} F\{\theta\} \quad (3.55)$$

$$\sigma_{r\theta} = -\frac{\partial}{\partial r} \left( \frac{1}{r} \frac{\partial \phi}{\partial \theta} \right) = -\frac{\ell}{r^2} r^{\ell+1} F'\{\theta\} \quad (3.56)$$

Using the boundary conditions (equation 3.53), setting  $\sigma_{\theta\theta} = 0$  implies  $F\{\alpha\} = 0$ , and setting  $\sigma_{r\theta} = 0$  implies  $F'\{\alpha\} = 0$  at the crack face. This means  $F\{\theta\}$  is an Eigenfunction, thus for every value of  $\ell$  (the Eigenvalue), there is a corresponding Eigenfunction. William's generalized stress solution is the sum of all the combinations of  $\ell$  and  $F\{\theta\}$  that satisfy the boundary conditions.

Substituting equation 3.52 into the Biharmonic equation gives

$$\nabla^2 \phi = \frac{\partial^4 F}{\partial \theta^4} + 2(\ell + 1) \frac{\partial^2 F}{\partial \theta^2} + (\ell^2 - 1) F = 0 \quad (3.57)$$

resulting in the following family of solutions

$$\begin{aligned} F\{\theta\} &= c_1 \cos\{(\ell - 1)\theta\} + c_2 \sin\{(\ell - 1)\theta\} \\ &+ c_3 \cos\{(\ell + 1)\theta\} + c_4 \sin\{(\ell + 1)\theta\} \end{aligned} \quad (3.58)$$

Now applying the boundary condition  $\sigma_{\theta\theta} = F \{\pm\alpha\} = 0$  gives

$$\begin{aligned} F \{\alpha\} &= c_1 \cos \{(\ell - 1)\alpha\} + c_2 \sin \{(\ell - 1)\alpha\} \\ &+ c_3 \cos \{(\ell + 1)\alpha\} + c_4 \sin \{(\ell + 1)\alpha\} \end{aligned} \quad (3.59)$$

$$\begin{aligned} F \{-\alpha\} &= c_1 \cos \{(\ell - 1)\alpha\} - c_2 \sin \{(\ell - 1)\alpha\} \\ &+ c_3 \cos \{(\ell + 1)\alpha\} - c_4 \sin \{(\ell + 1)\alpha\} \end{aligned} \quad (3.60)$$

and for  $\sigma_{r\theta} = F' \{\pm\alpha\} = 0$

$$\begin{aligned} F' \{\alpha\} &= -c_1(\ell - 1) \sin \{(\ell - 1)\alpha\} + c_2(\ell - 1) \cos \{(\ell - 1)\alpha\} \\ &- c_3(\ell + 1) \sin \{(\ell + 1)\alpha\} + c_4(\ell + 1) \cos \{(\ell + 1)\alpha\} \end{aligned} \quad (3.61)$$

$$\begin{aligned} F' \{-\alpha\} &= c_1(\ell - 1) \sin \{(\ell - 1)\alpha\} + c_2(\ell - 1) \cos \{(\ell - 1)\alpha\} \\ &- c_3(\ell + 1) \sin \{(\ell + 1)\alpha\} - c_4(\ell + 1) \cos \{(\ell + 1)\alpha\} \end{aligned} \quad (3.62)$$

Writing equations 3.59 and 3.61 in matrix form

$$\begin{bmatrix} \cos \{(\ell - 1)\alpha\} & \cos \{(\ell + 1)\alpha\} \\ (\ell - 1) \sin \{(\ell - 1)\alpha\} & (\ell + 1) \sin \{(\ell + 1)\alpha\} \end{bmatrix} \begin{bmatrix} c_1 \\ c_2 \end{bmatrix} = \begin{bmatrix} 0 \\ 0 \end{bmatrix} \quad (3.63)$$

which should give a zero determinant for a non-trivial solution. This gives

$$\begin{aligned} \ell [\cos \{(\ell - 1)\alpha\} \sin \{(\ell + 1)\alpha\} - \cos \{(\ell + 1)\alpha\} \sin \{(\ell - 1)\alpha\}] \\ + \cos \{(\ell - 1)\alpha\} \sin \{(\ell + 1)\alpha\} + \cos \{(\ell + 1)\alpha\} \sin \{(\ell - 1)\alpha\} = 0 \end{aligned} \quad (3.64)$$

which simplifies to

$$\ell \sin \{2\alpha\} + \sin \{2\ell\alpha\} = 0 \quad (3.65)$$



and for a crack ( $\alpha = \pi$ )

$$\sin \{2\pi\ell\} = 0 \quad (3.66)$$

which is valid when

$$\ell = \frac{n}{2} \quad \text{for } n=1,2,3,\dots \quad (3.67)$$

which is the same result when combining equations 3.60 and 3.62.

Now the general form for the Airy Stress Function can be written as

$$\begin{aligned} \phi &= \phi_I + \phi_{II} \\ \phi_I &= \sum_{n=1,3,\dots}^{\infty} c_{1n} \left( \cos \left\{ \frac{n-2}{2} \theta \right\} - \frac{n-2}{n+2} \cos \left\{ \frac{n+2}{2} \theta \right\} \right) \\ &\quad + c_{2n} \left( \sin \left\{ \frac{n-2}{2} \theta \right\} - \sin \left\{ \frac{n+2}{2} \theta \right\} \right) \\ \phi_{II} &= \sum_{n=2,3,\dots}^{\infty} c_{1n} \left( \cos \left\{ \frac{n-2}{2} \theta \right\} - \cos \left\{ \frac{n+2}{2} \theta \right\} \right) \\ &\quad + c_{2n} \left( \sin \left\{ \frac{n-2}{2} \theta \right\} - \frac{n-2}{n+2} \sin \left\{ \frac{n+2}{2} \theta \right\} \right) \end{aligned} \quad (3.68)$$

where  $\phi_I$  and  $\phi_{II}$  are the stress functions for crack opening modes I and II respectively.

The 1st-order approximation for the stress field is

$$\begin{bmatrix} \sigma_{rr} \\ \sigma_{\theta\theta} \\ \sigma_{r\theta} \end{bmatrix} = \frac{K_I}{4\sqrt{2\pi r}} \begin{bmatrix} 5 \cos \left\{ \frac{\theta}{2} \right\} - \cos \left\{ \frac{3\theta}{2} \right\} \\ 3 \cos \left\{ \frac{\theta}{2} \right\} + \cos \left\{ \frac{3\theta}{2} \right\} \\ \sin \left\{ \frac{\theta}{2} \right\} + \sin \left\{ \frac{3\theta}{2} \right\} \end{bmatrix} \quad (3.69)$$

Following the work of Alturi et al. (1975), the William's mode I stress field can be

cast into Cartesian coordinates as

$$\begin{bmatrix} \sigma_{xx} \\ \sigma_{yy} \\ \sigma_{xy} \end{bmatrix} = \sum_{n=1}^{\infty} \frac{n}{2} A_{1n} r^{\frac{n-2}{2}} \begin{bmatrix} \left(2 + (-1)^n + \frac{n}{2}\right) \cos \left\{\frac{n-2}{2}\theta\right\} - \frac{n-2}{2} \cos \left\{\frac{n-6}{2}\theta\right\} \\ \left(2 - (-1)^n - \frac{n}{2}\right) \cos \left\{\frac{n-2}{2}\theta\right\} + \frac{n-2}{2} \cos \left\{\frac{n-6}{2}\theta\right\} \\ - \left((-1)^n + \frac{n}{2}\right) \sin \left\{\frac{n-2}{2}\theta\right\} + \frac{n-2}{2} \sin \left\{\frac{n-6}{2}\theta\right\} \end{bmatrix} \quad (3.70)$$

which provide generalized stress field equations for LEFM. These equations can be fitted to experimental stress fields by choosing appropriate values for  $A_{1n}$ . The 1st-order Cartesian stress field is

$$\begin{bmatrix} \sigma_{xx} \\ \sigma_{yy} \\ \sigma_{xy} \end{bmatrix} = \frac{1}{2} A_{11} r^{-\frac{1}{2}} \begin{bmatrix} \frac{3}{2} \cos \left\{\frac{1}{2}\theta\right\} + \frac{1}{2} \cos \left\{\frac{5}{2}\theta\right\} \\ \frac{5}{2} \cos \left\{\frac{1}{2}\theta\right\} - \frac{1}{2} \cos \left\{\frac{5}{2}\theta\right\} \\ -\frac{1}{2} \sin \left\{\frac{1}{2}\theta\right\} + \frac{1}{2} \sin \left\{\frac{5}{2}\theta\right\} \end{bmatrix} \quad (3.71)$$

setting  $A_{11} = K_I / \sqrt{2\pi}$  gives

$$\begin{bmatrix} \sigma_{xx} \\ \sigma_{yy} \\ \sigma_{xy} \end{bmatrix} = \frac{K_I}{2\sqrt{2\pi r}} \begin{bmatrix} \frac{3}{2} \cos \left\{\frac{1}{2}\theta\right\} + \frac{1}{2} \cos \left\{\frac{5}{2}\theta\right\} \\ \frac{5}{2} \cos \left\{\frac{1}{2}\theta\right\} - \frac{1}{2} \cos \left\{\frac{5}{2}\theta\right\} \\ -\frac{1}{2} \sin \left\{\frac{1}{2}\theta\right\} + \frac{1}{2} \sin \left\{\frac{5}{2}\theta\right\} \end{bmatrix} \quad (3.72)$$

Directly ahead of the crack tip ( $\theta = 0$ ) gives

$$\begin{bmatrix} \sigma_{xx} \\ \sigma_{yy} \\ \sigma_{xy} \end{bmatrix} = \frac{K_I}{\sqrt{2\pi r}} \begin{bmatrix} 1 \\ 1 \\ 0 \end{bmatrix} \quad (3.73)$$

which gives the same stress field as Westergaard (1939) in front of the crack tip, and is used in the development of the viscoelastic theory in Schapery (1975a)

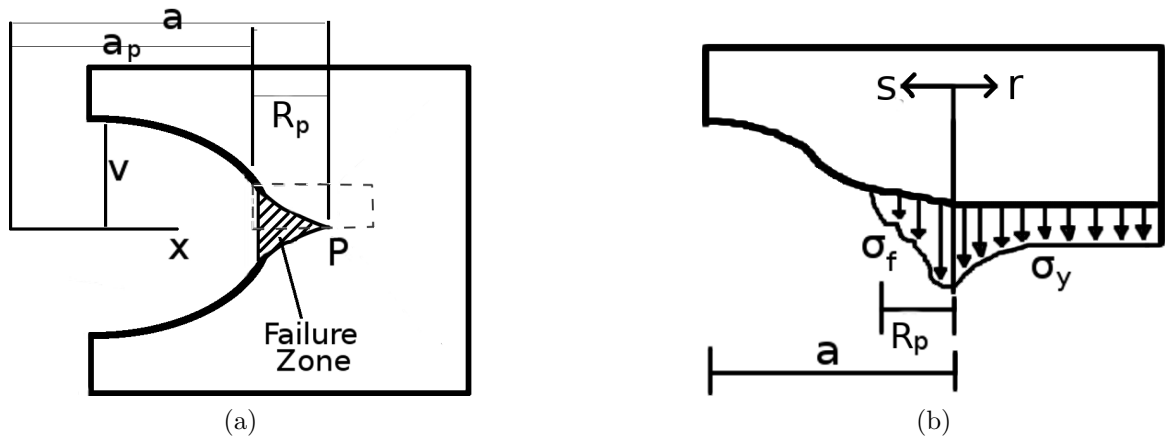


Figure 3.13: a) Physical setup of ideal crack on the x-axis. b) Stress distribution inside the process zone, and in front of the crack.

### 3.2.3 The Barenblatt Model

While Westergaard (1939) and Williams (1957) provide a good start into LEFM, there arises a problem in equation 3.50 as the model approaches the crack tip. Since there is a  $1/r$  term, the stress at the crack tip becomes infinity. Barenblatt (1962) rectified by this using limiting values of Cauchy-type integrals (Muskhelishvili, 1953b).

Figure 3.13a shows an ideal crack in a material, where  $a_p$  is the distance from the centre of the crack to the apparent crack tip. The apparent crack tip is where the crack faces join together - much of the literature refer to this as the crack tip, as it is visually the tip of the crack (i.e., what the eye can tell). For the following discussion, the actual crack tip occurs at  $a = a_p + R_p$ . This crack tip includes the process zone of length  $R_p$ . In the process zone, the forces of cohesion between the molecules of the material act to hold the material together, but the material in this zone may not be continuous or behave the same as the bulk material. It is because of the forces of cohesion that allowed Barenblatt (1962) to develop the theory to remove the stress singularity at the crack tip.

From Figure 3.13b, we define two coordinate systems that originate at the crack

tip. Coordinate  $s$  increases to the left (e.g., the apparent crack tip is at  $s = +R_p$ ), and coordinate  $r$  increases to the right (the same as Westergaard's). The stress field outside the process zone can be solved using Westergaard (1939) or Williams (1957), as before. To deal with the stress field inside the process zone, Barenblatt (1962) considers a superposition of two stress fields. The first stress field is simply the elastic solution of Westergaard (1939) or Williams (1957) (as if there were no cohesive forces in the zone). Due to the presence of the cohesive stresses, the actual stresses acting on the crack (in particular, the process zone) will differ from the elastic solution. The second stress field,  $g\{t\}$ , is defined as the difference between the stress field from the elastic solution and the actual stress field.

As stated by Barenblatt, the actual stress field is unknown, but for now, assume that it is (or can be found). This issue will be addressed using other principles of continuum and fracture mechanics to alleviate this shortcoming. Barenblatt (1962) defines the Airy's stress function of this second stress state as

$$\Phi\{z\} = \frac{1}{2\pi i \sqrt{z}} \int \frac{\sqrt{s'} g\{s'\} ds'}{s' - z} \quad (3.74)$$

which is a complex Cauchy-type integral (Muskhelishvili, 1953a).

Integrating equation 3.74 with respect to  $z = x + iy$  gives

$$\phi_b\{z\} = \frac{1}{2\pi i} \int g\{s'\} \log \left\{ \frac{\sqrt{s'} + \sqrt{z}}{\sqrt{s'} - \sqrt{z}} \right\} ds' \quad (3.75)$$

which allows  $\Phi\{r\}$  can be written as (Muskhelishvili, 1953a)

$$\Phi\{r\} = \frac{1}{2\pi i \sqrt{z}} \int \frac{(\phi\{s'\} - \phi\{r\}) ds'}{s' - r} + \frac{\phi\{r\}}{2\sqrt{z}} \quad (3.76)$$

where  $\phi\{s'\} = \sqrt{s'} g\{s'\}$ .

In the case that  $s \gg r$  (in the process zone) and along the  $y = 0$  axis (giving  $\theta = \pi$  along the crack), the stress field is found using Muskhelishvili (1953a) as

$$\begin{aligned}\sigma_y^{(2)} &= \sigma_x^{(2)} = 2\mathbf{Re}\{\Phi\{z = r\}\} = \Phi\{r\} + \overline{\Phi\{r\}} \\ &= \frac{\phi\{r\}}{\sqrt{r}} - \frac{1}{\pi\sqrt{r}} \int_0^{R_p} \frac{\phi\{s'\}}{s' - r} ds' + \mathcal{O}\{\sqrt{r}\} \\ &= g\{0\} - \frac{1}{\pi\sqrt{r}} \int_0^{R_p} \frac{g\{s'\}}{\sqrt{s'}} ds' + \mathcal{O}\{\sqrt{r}\}\end{aligned}\quad (3.77)$$

where the integral runs over the process zone, from the crack tip (at  $s = 0$ ) to the apparent crack tip (at  $s = R_p$ ).

Superimposing equation 3.77 onto the elastic solution for no cohesive stress gives the actual stress field due to the cohesive stresses as

$$\sigma_y^b = \sigma_f\{0\} - \frac{1}{\pi\sqrt{r}} \int_0^{R_p} \frac{\sigma_f\{s'\}}{\sqrt{s'}} ds' + \mathcal{O}\{\sqrt{r}\} \quad (3.78)$$

where  $\sigma_f$  is the stress field in the process zone, and  $\sigma_y^b$  is the Barenblatt stress in the bulk material.

Equations 3.50 and 3.78 combine to give the complete stress in the material near the crack tip as

$$\begin{aligned}\sigma_y^b + \sigma_y^0 &= \left(\frac{K_I}{\sqrt{2\pi r}}\right) \left(\cos\left\{\frac{\theta}{2}\right\}\right) \left[1 + \sin\left\{\frac{\theta}{2}\right\} \sin\left\{\frac{3\theta}{2}\right\}\right] + \sigma_f\{0\} \\ &\quad - \frac{1}{\pi\sqrt{r}} \int_0^{R_p} \frac{\sigma_f\{s'\}}{\sqrt{s'}} ds' \\ \sigma_y^b + \sigma_y^0 &= \left(\frac{K_I}{\sqrt{2\pi r}}\right) + \sigma_f\{0\} - \frac{1}{\pi\sqrt{r}} \int_0^{R_p} \frac{\sigma_f\{s'\}}{\sqrt{s'}} ds'\end{aligned}\quad (3.79)$$

for  $\theta = 0$ . This can only be finite at the crack tip ( $r = 0$ ) if

$$\begin{aligned} 0 &= \left( \frac{K_I}{\sqrt{2\pi r}} \right) - \frac{1}{\pi\sqrt{r}} \int_0^{R_p} \frac{\sigma_f \{s'\} ds'}{\sqrt{s'}} \\ K_I &= \left( \frac{2}{\pi} \right)^{\frac{1}{2}} \int_0^{R_p} \frac{\sigma_f \{s'\} ds'}{\sqrt{s'}} \end{aligned} \quad (3.80)$$

which relates the stress intensity to the forces of cohesion of the material and removes the singularity (infinite stresses) at the crack tip.

Using similar analysis from Muskhelishvili (1953a,b), the crack opening displacement can be found as

$$v^b = \frac{4(1-\nu^2)}{E} \mathbf{Im}\{\phi_b \{z = s\}\} = -\frac{2(1-\nu^2)}{\pi E} \int_0^{R_p} g \{s'\} \log \left\| \frac{\sqrt{s'} + \sqrt{s}}{\sqrt{s'} - \sqrt{s}} \right\| ds' \quad (3.81)$$

### 3.2.4 Summary of Critical Analysis

The aim of this chapter was to highlight the underlying theories used to develop the new model developed for this thesis. The fundamental theory on fracture mechanics were developed by Westergaard (1939), Williams (1957), and Alturi et al. (1975). Their approach was to look at the stresses near a crack tip and treat the crack as if it were a thin elliptical hole (its semi-major axis was much longer than its semi-minor axis). This led to a formulation that could work near the crack, but led to a singularity (infinite stress) at the crack tip itself.

This theory was enhanced by the addition of cohesive forces by Barenblatt (1962), that act to hold the crack together (and would be related to breaking atomic bonds). Barenblatt's addition, while still elastic, provided a means to remove the singularity at the crack tip, allowing for a better physical approximation.

With the linear elastic fracture theory developed, a viscoelastic fracture theory can now be developed (Chapter 6). While there are field and laboratory experiments

that demonstrate the viscoelastic properties of ice, a set of in-house experiments were also performed. These experiments were able to test the viscoelastic properties of ice and can provide great insight and guidance in expanding the original viscoelastic fracture theory developed in Schapery (1975a,b,c).

### 3.3 Viscoelastic Fracture

As discussed, this time-dependence of the properties of ice have been explored by several other authors. It is in the opinion of the author that ice is best described as a viscoelastic material. This type of material displays all the time-dependent properties of ice that treating ice as an elastic-plastic material could not encompass. There are several components to a viscoelastic material that incorporate elasticity, anelasticity, and viscous flow into the continuum nature of the ice. The growth of cracks also needs to be incorporated into the continuum model in such a way to allow for a crack to grow as a discontinuity in the ice.

Aside from the viscoelastic fracture model discussed in Chapter 6 of this thesis, other models of viscoelastic fracture do exist. One such model was created by Mulmule and Dempsey (1998). This model makes use of cohesive zone in front of the crack tip where LEFM does not apply (this is in agreement with the proposed model in this project), but they seem to treat the process zone as a linear viscoelastic material, which is in disagreement of our proposed model. As (Schapery, 1975a) points out, the process zone may be discontinuous and highly nonlinear.

They make several assumptions about the process zone, such as the use of an empirical stress-separation curve (cohesive stress as a function of atomic separation and rate of separation). The proposed model in Chapter 6 will also make (albeit different) assumptions about the process zone stress. Mulmule and Dempsey (1998)

make no attempt to justify their assumptions, while this is not a direct critique of those assumptions, it is unfortunate that they do not provide any physical basis for their choice.

There certainly may be some merit to their modelling approach, such as being usable for complex geometries (the proposed model here is not as universal), but there are a couple of issues with Mulmule and Dempsey (1998). One issue is that they propose a viscoelastic model, meaning that their model has time-dependence (which the equations do have), but they present several figures, none of which have any mention of time. While this is not directly related to the model, it is certainly an omission of the importance of time in their presented results. The second issue was that the maximum cohesive strength of the ice was 10 MPa in the model. The physical mechanism of the cohesive zone is the atomic bonds of the crystal lattice of ice. It is not reasonable to assume that these atomic bonds are going to break under 10 MPa of stress, that is at least an order of magnitude off, as the stress should be the theoretical stress (note that an applied load at the surface can be considerably less than 100 MPa, but the local stresses near a crack tip will be much higher than at the surface).



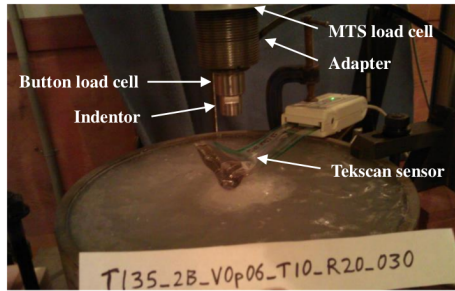
# Chapter 4

## Experimental Program: Indentor Series and Analysis

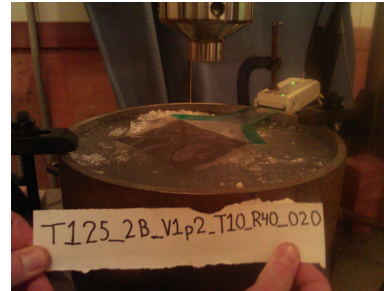
### 4.1 Objectives

The indentation series, explained in greater detail below (also see Kavanagh et al. (2015) and O'Rourke et al. (2015)), comprised of several loading scenarios of a spherical-capped indenter into cylindrical ice samples at varying displacement rates. This series was a laboratory-scale version of the experiments done at Hobsons Choice Ice Island in 1989 (Frederking et al., 1990) and Pond Inlet (Masterson et al., 1992). This series was designed to highlight several key properties of ice.

The first objective was to provide insights to the fracture properties of ice under compressive loads at different rates of loading. As noted in the literature review, several authors (Goodman and Tabor, 1978; Liu and Miller, 1979; Hamza and Muggenridge, 1980; Urabe et al., 1980) provide evidence of time-dependent fracture for a single crack in different testing specimens. As will be discussed, the series demonstrates the brittle and viscoelastic properties of ice that lead to rather diverse fracture



(a) Indenter Setup



(b) Tekscan Pressure Sensor



(c) Large Moulds



(d) Small Moulds

behaviour in the ice samples.

Secondly, the series provides evidence of delayed failure, much like the slow loading test from Frederking et al. (1990). The use of a load transducer, high-speed video, and pressure sensors should provide evidence of delayed failure in the samples under slow loading conditions.

Lastly, the series reproduces the pressure-area relationships seen in medium-scale experiments (Barrette et al., 2003; Taylor, 2010). These relationships describe a decreasing power-law relationship between the pressures exerted on the ice and the contact area during the interaction. This relationship will be tested through the use of indentors of different sizes.

Table 4.1: The various spherical indentors used during the experiments, along with some of the test speeds at different normalized velocities.

Diameter (mm)	Radius of curvature (mm)	Velocity (mm/s)				
10	12.8	0.03	0.3	2	3	30
20	25.6	0.06	0.6	4	N/A	60
40	51.2	0.12	1.2	8	12	120
70	89.6	0.21	2.1	14	21	N/A

## 4.2 Methodology

To simulate the interaction between ice and a structure, a set of indentation tests were done. Ice was grown from bubble-free ice that was chipped down and sieved into ice seed with grain sizes between 2–3.75 mm. Steel moulds (of 154 mm and 300 mm inner diameters) were filled to  $\frac{1}{3}$  of the mould depth with the seed. Water that was cooled to  $0^{\circ}\text{C}$  was poured in the moulds with the seed ice, and allowed to freeze at  $-13^{\circ}\text{C}$ . This procedure produced isotropic, polycrystalline ice which was used in the series of indentation tests.

Each mould was clamped to platens attached to the actuator on a Materials Testing System<sup>®</sup> (MTS) frame beneath various steel indentors (10-, 20-, 40-, and 70-millimetre diameters). The indenter approached the ice with fixed velocities-to-indenter-diameter ratios, here termed the “Normalized Velocity” as

$$V_N = \frac{v}{d} \quad (4.1)$$

for indentation velocity,  $v$ , and indenter diameter,  $d$ . For example, the 10 mm indenter with a velocity of 3 mm/s would have  $V_N = 3/10 = 0.3 \text{ s}^{-1}$ .

For each test, the indenter penetrated into the ice to a depth of 10–15 mm at various normalized velocities (some of which are shown in Table 4.1), at a temperature of  $-10^{\circ}\text{C}$ .

During the experiment, loading and penetration data were recorded using the MTS (load and displacement) transducers and software. A high-speed video-camera (HSV) recorded the event to be played back in slow motion. Lastly, some of the experiments used Tekscan pressure sensors to record the pressure profile. This data was used to identify and distinguish crushing and spalling events that occur during the interaction.

After each test, the sample was stored at  $-13^{\circ}\text{C}$  until it was ready to be thin sectioned. Each sample was then cut into a 10 mm thick vertical section near the contact zone using a band saw. These “thick” sections were then finely scraped down to a thickness less than 0.5 mm using a microtome. Photographs of the thin sections were taken between crossed-polarized sheets with a back light and side-lighting to produce images that show the grain structure and microcracking in the ice. Thin-sectioning of the samples follow the procedure outlined in Sinha (1977).

## 4.3 Results and Discussion

### 4.3.1 Behaviour at Different Normalized Velocities

#### 4.3.1.1 Slow Loading Rate ( $V_N = 3 \times 10^{-3} \text{ s}^{-1}$ )

Test T140 used the 20 mm diameter indenter with a velocity of 0.06 mm/s. The results of this test are given in Figure 4.1, the figure shows that under such low loading rates, the ice undergoes damage-enhanced creep. As the indenter continues into the ice, the slow rate allows the energy to be dissipated via damage processes giving a characteristically large region of recrystallized grains over the contact area and deep into the ice. This recrystallized material remains a part of the ice continuum, as shown in the thin section in Figure 4.1c <sup>1</sup>.

---

<sup>1</sup>Section was slightly damaged during microtoming, causing the top right surface to break off

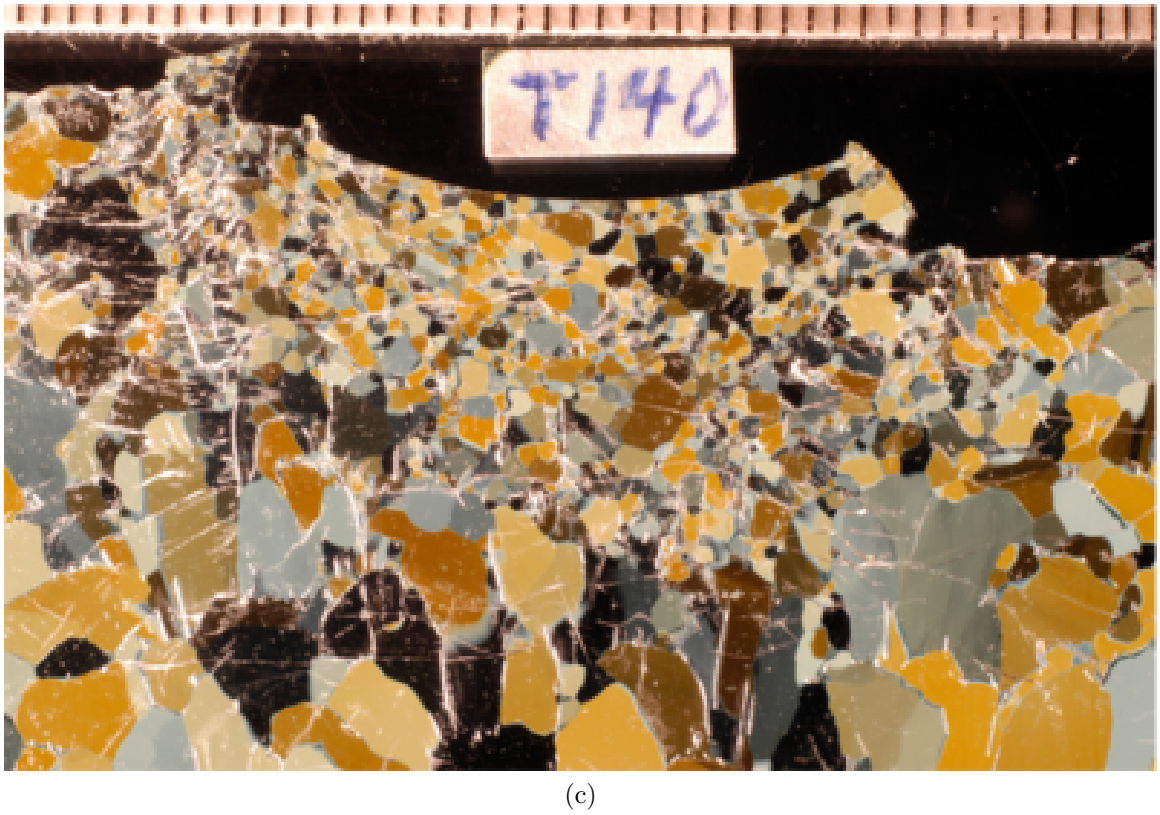
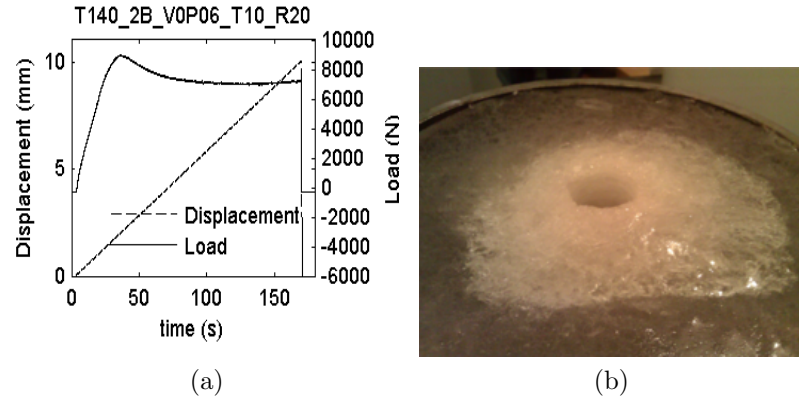


Figure 4.1: Test T140\_2B\_V0P06\_T10\_R20\_035. a) Force diagram for a damage-enhanced creep. b) Top view photo showing distributed damage along the surface with no spalling. c) Thin-section photo showing a recrystallized damage zone with a lot of microcracking along the edges of the contact zone.

Due to the slow loading, the various mechanisms of energy release (such as grain boundary sliding and dislocation glide; see Section 2.2) are able to act. These mechanisms cause a gentle dissipation of energy that spread out the damage deeper into the ice. Jordaan (2001)).

#### 4.3.1.2 Medium Loading Rate ( $V_N = 3 \times 10^{-2} \text{ s}^{-1}$ )

Figure 4.2 shows a set of tests using the 10-, 20-, and 40-mm indentors. The loading plot in Figure 4.2a looks like a creep curve from the slower tests. However, Figure 4.2d shows spalling events that occurred outside the contact zone during this test. These “outside the zone” (OTZ) spalls, dissipate little energy and do not cause any major changes in the load on the ice.

Test T139, shown in Figure 4.2b, displays a behaviour similar to the creep curves, but there is a major load drop in the beginning, caused by crushing and extrusion. After the extrusion event, the ice load plot is similar to the damaged-enhanced creep curve of the slower tests. Visual inspection of Figure 4.2e, shows many OTZ spalls had formed that do not affect the compressive loading behaviour.

Test T125, for the 40 mm indenter, shows a different behaviour than before. The loading curve in Figure 4.2c and HSV in Figure 4.2f show that the test had a lot of small crushing and OTZ spalls that dissipates the energy. Near the end of this test, the energy build up leads to a spall that causes a big drop in the load. The spall can be seen on the left of Figure 4.2f, which had its origin in the contact zone.

#### 4.3.1.3 Fast Loading Rate ( $V_N = 2 \times 10^{-1} \text{ s}^{-1}$ )

At this rate of loading, the ice behaviour has become more brittle than the previously mentioned experiments. The loading plots in Figure 4.3a-c no longer have a dominant creep curve, but rather a cycle of build up and release. As shown in Figure 4.3a, the

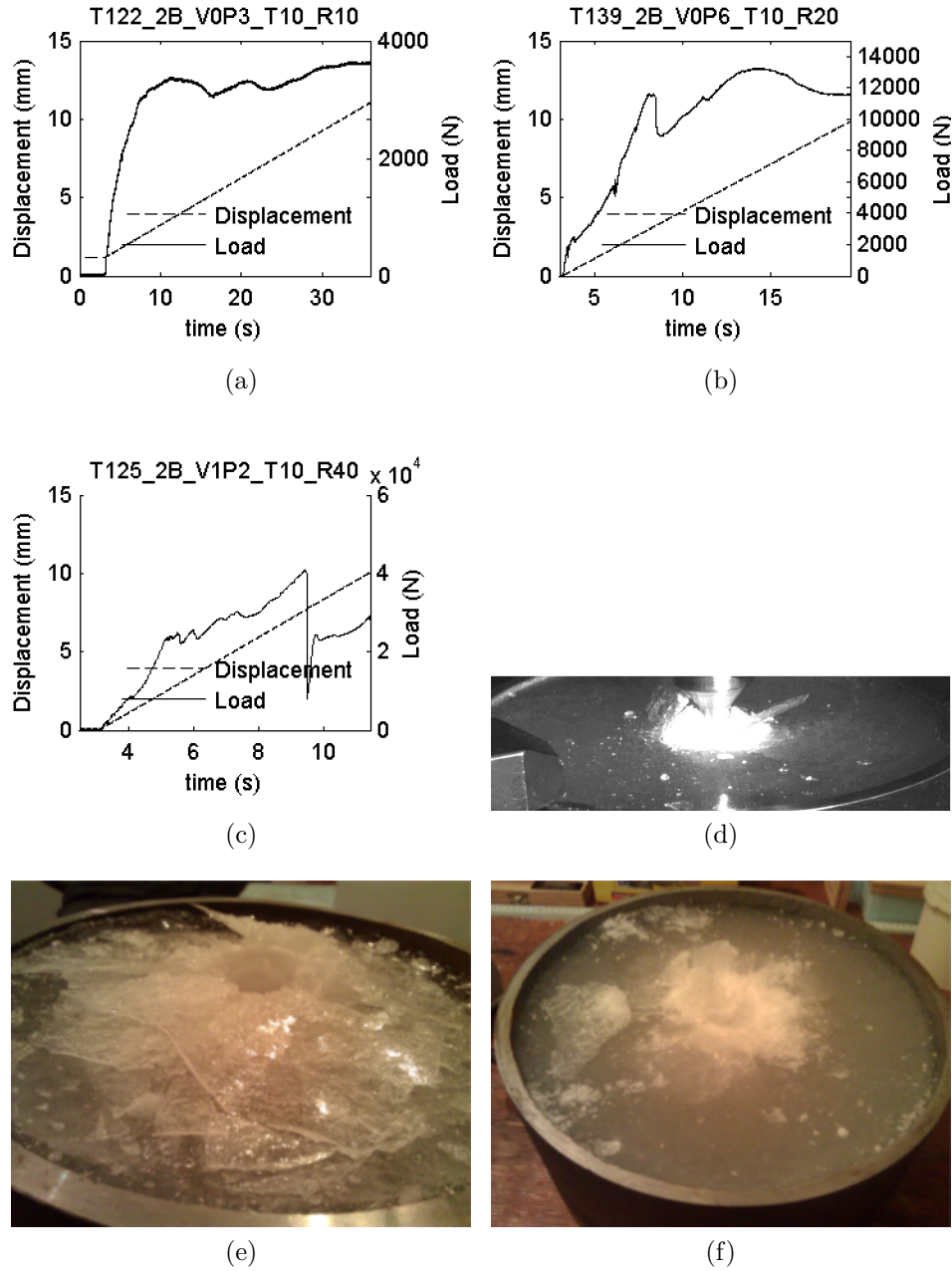


Figure 4.2: a) T122. Load plot for 10 mm indenter with “outside the zone” spalls forming in d). b) T139. Load plot for 20 mm indenter showing crushing behaviour and subsequent OTZ Spalls in e). c) T125. Load plot for 40 mm indenter showing a delayed spalling event within the *hpz* in f)

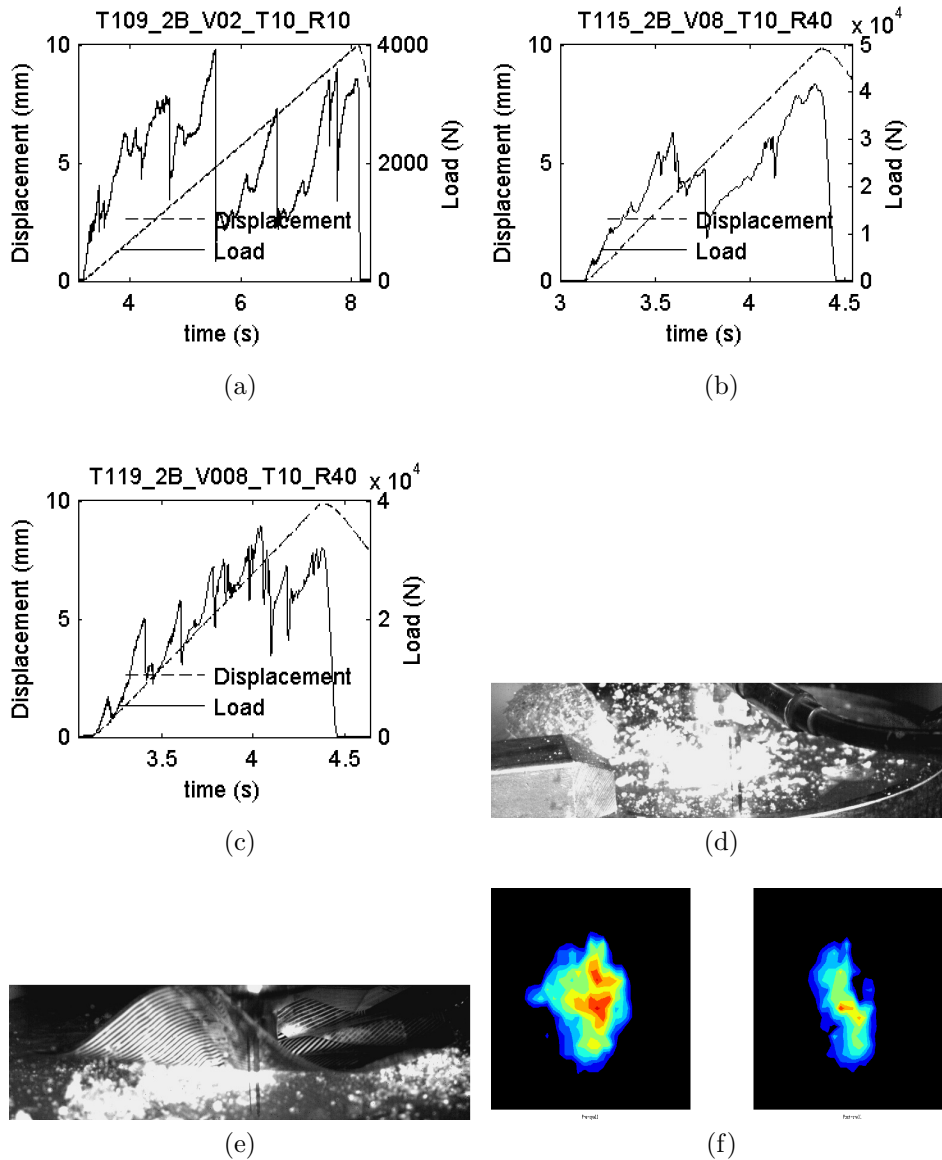


Figure 4.3: a) T109. Load plot for 10 mm indenter with a large spall forming from the event at  $t = 6.6$  seconds in d). b) and c) are loading plots of tests T115 and T119 for the 40 mm indenter. e) shows the spalling event from T115, which produced a tiny spall. This spall resulted in a drop in the area shown by the Tekscan sensor in f).



load builds and undergoes ice crushing and eventually spalls. After both spalling events ( $t = 5.5$  and  $6.6$  seconds), there is a rebound in the load (the high-frequency spikes) as the ice and indenter re-establish contact.

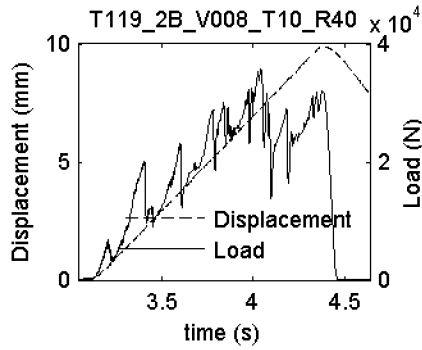
Test T109 in Figure 4.3a shows a typical brittle material with a build up of load with some minor crushing, leading up to several major events. Figure 4.3d shows a large spall that formed from the event at  $t = 6.6$  seconds. The other events in Figure 4.3a do not eject any large spall features (just particulate ice).

The HSV image in Figure 4.3e, for test T115, shows the ice being ejected from underneath the Tekscan sensor. This resulted in a tiny spall piece being ejected, as evidenced by the Tekscan sensor. The loading plot in Figure 4.3b showed that the spall did suddenly lower the load, but not a big drop that is typical for spalling events.

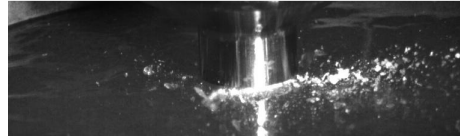
The peak loads of the brittle ice are of similar magnitude to the more ductile ice in the lower rate tests, but the constant crushing and spalling constantly reduce the loads, reducing the mean load and the time that the indenter is under high stress in comparison to the slower speeds.

#### 4.3.1.4 Fastest Loading Rate ( $V_N = 3 \text{ s}^{-1}$ )

The highest indentation rates were done at  $V_N = 3 \text{ s}^{-1}$ . The tests done at this velocity show similar behaviour as the tests done at  $V_N = 2 \times 10^{-1} \text{ s}^{-1}$ . Figure 4.4 compares the result of the 40 mm indenter under these two different rates. The two loading plots exhibit brittle behaviour with build up leading to spalling or crushing. The HSV captures shown in Figure 4.4b and e show the initial contact between the ice and indenter. These images show how different the interaction can behave, even with similar loading behaviour. Along with the post-test photos in Figure 4.4c and f, it can be seen that test T121 had more spalling over a short period of time. The HSV showed the spalls and crushed ice in test T121 ejected from beneath the indenter with



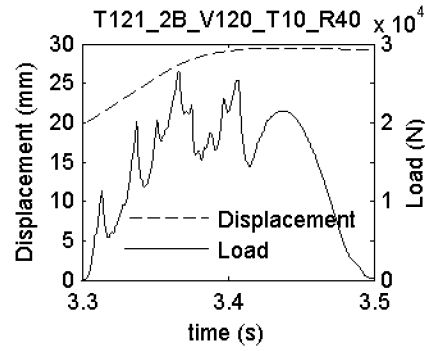
(a)



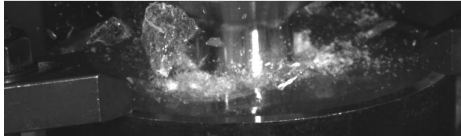
(b)



(c)



(d)



(e)



(f)

Figure 4.4: Comparison of two 40 mm indenters. T119 (a-c) has a rate of  $V_N = 2 \times 10^{-1} \text{ s}^{-1}$  and T121 (d-f) has a rate of  $V_N = 3 \text{ s}^{-1}$ . The results of both tests show that they behave similarly in the loading plot, but T121 has more energetic expulsions of ice.

greater velocity.

#### 4.3.1.5 Explanation of Different Fracture Observations

##### 4.3.1.5.1 Indentation Series

As seen from the previous sections, the indentation series displayed many time-related properties in relation to fracture mechanics. Slow loading tests often resulted in no fracture, fast loading resulted in many localized spalling events, and medium-rate tests resulted in a combination of the two with occasional large fracture events.

To analyse these different behaviours, an elastic FE model (shown in Figure 4.5) was ran to study the stress fields generated in the ice. The model uses an elastic material for the ice, confined in a rigid mould and indented by a rigid indenter. While there could be some stresses on the sides of the mould (due to cohesion between the ice and the mould), this is not modelled here. This analysis is meant to be illustrative, so many of the finer details are left out, in favour of a quick-and-easy means of considering (at least approximately) the stress fields present during an indentation test.

Figure 4.6 shows the equilibrium stress field of the ice under indentation. Figure 4.6a shows the  $\sigma_{11}$  (out of plane) stress<sup>2</sup>. The analysis shows that the ice is mostly confined to the plane with the exception of a large zone beneath the contact area (outside of the *hpx*) and near the edge of the ice. The large tension zone is due to the Poisson's effect of the ice compression and will contain both the shear zone and interior tensile zone, discussed below.

Figure 4.6b shows the stress component in the direction of loading. Not surprisingly, the compression is strongest in the *hpx* and directly beneath the indenter. There is little to no compression near the surface of the ice outside the *hpx*, which will aid

---

<sup>2</sup>it should be noted that  $\sigma_{11}$  and  $\sigma_{33}$  are the same radial stress due to axial symmetry, but are rotated 90 degrees, so that a  $\sigma_{33}$  is tangential view of  $\sigma_{11}$  is plotted

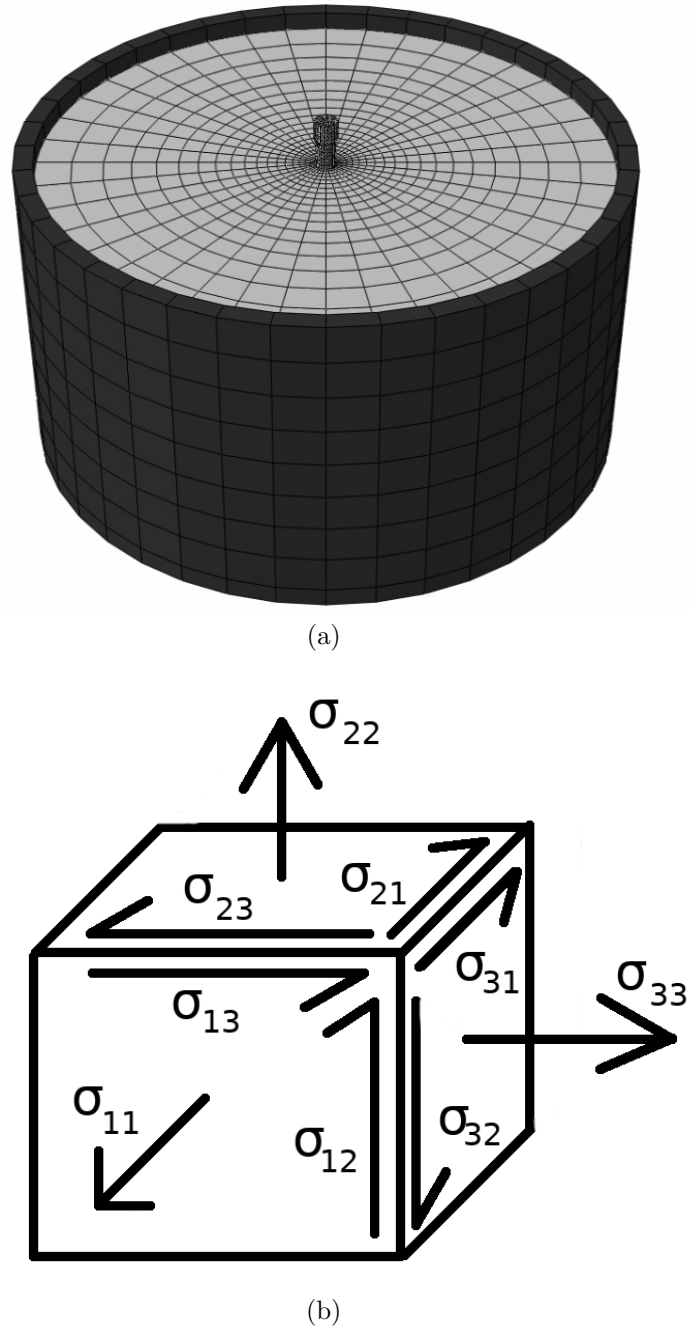
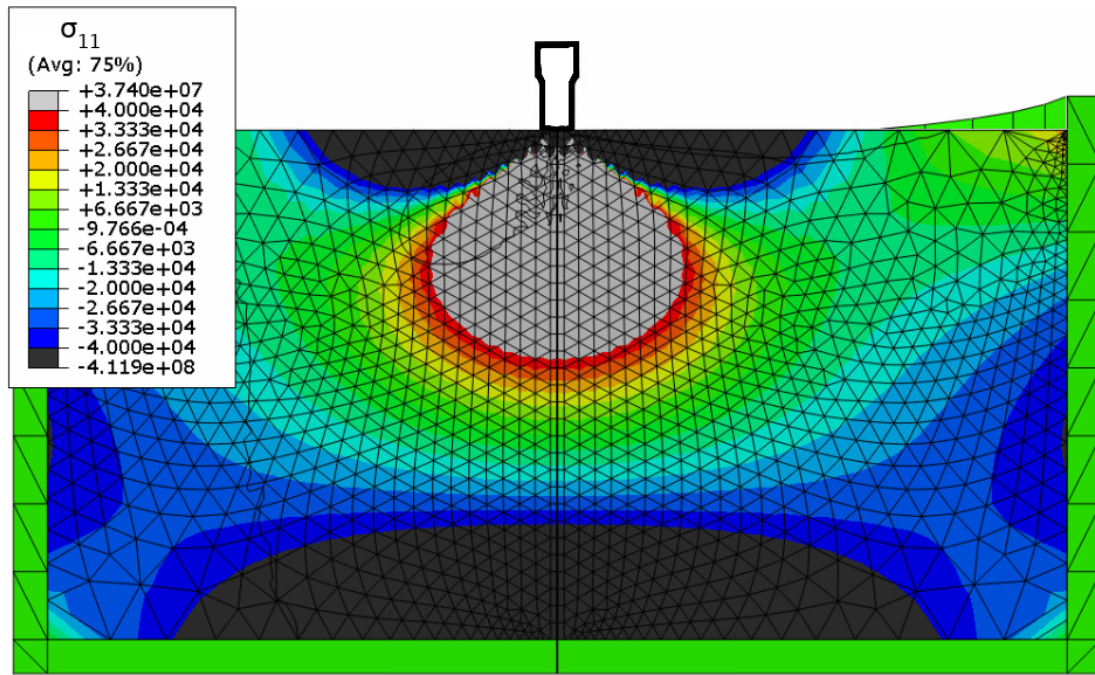
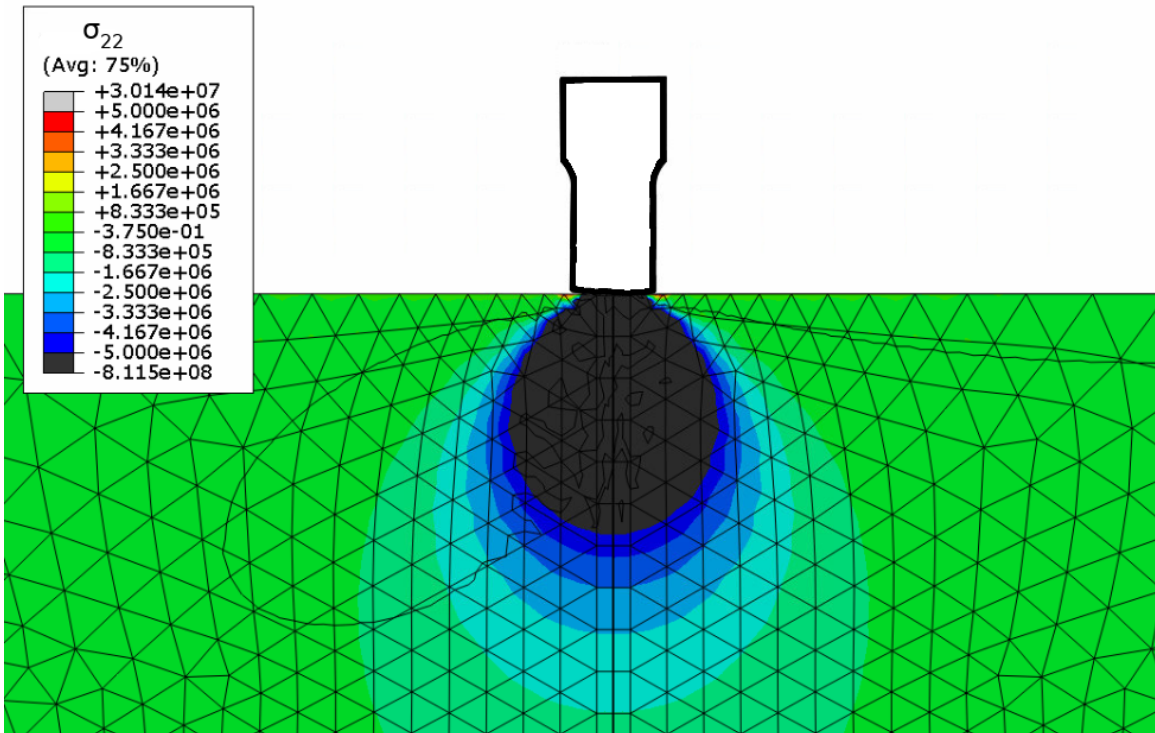


Figure 4.5: a) FE model of cylindrical ice sample under indentation inside a rigid mould. The mould completely surrounds the ice, including the bottom. b) Cauchy stress cube showing positive stress components.



(a)  $\sigma_{11}$  elastic stress field under indentation. Grey shows areas of highest tension and black shows areas of highest compression.



(b) Close-up of contact area for the vertically applied stress,  $\sigma_{22}$ . There is a compressive stress near the indenter, but becomes tensile further down.

Figure 4.6

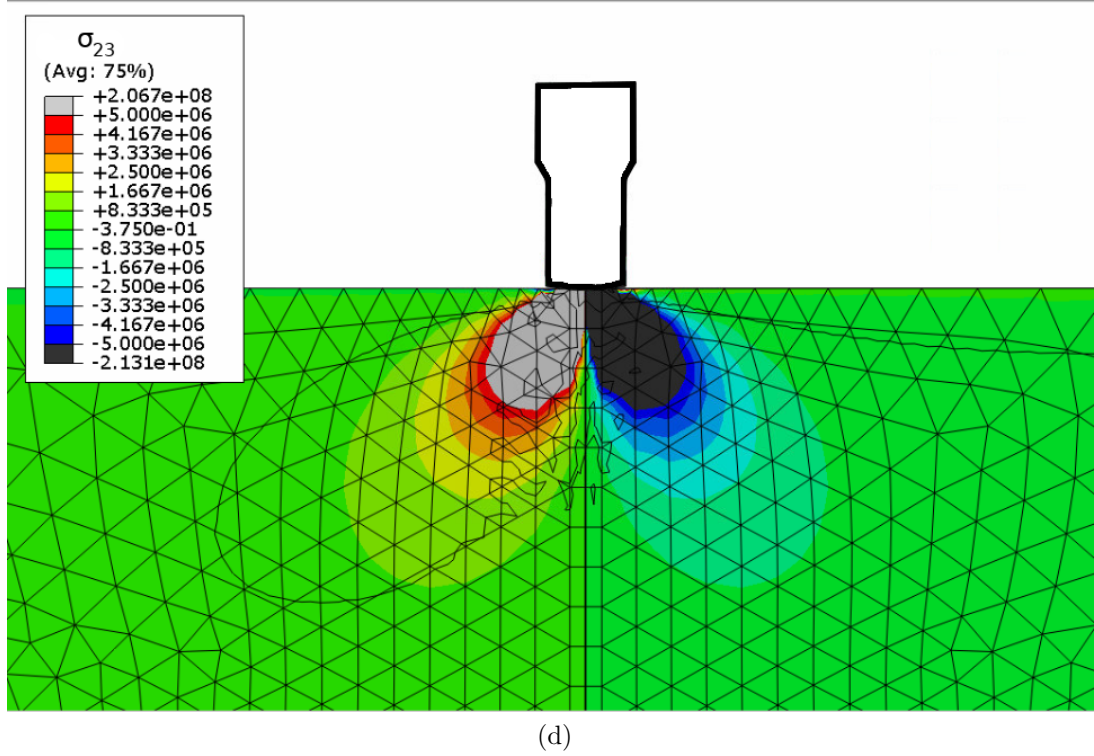
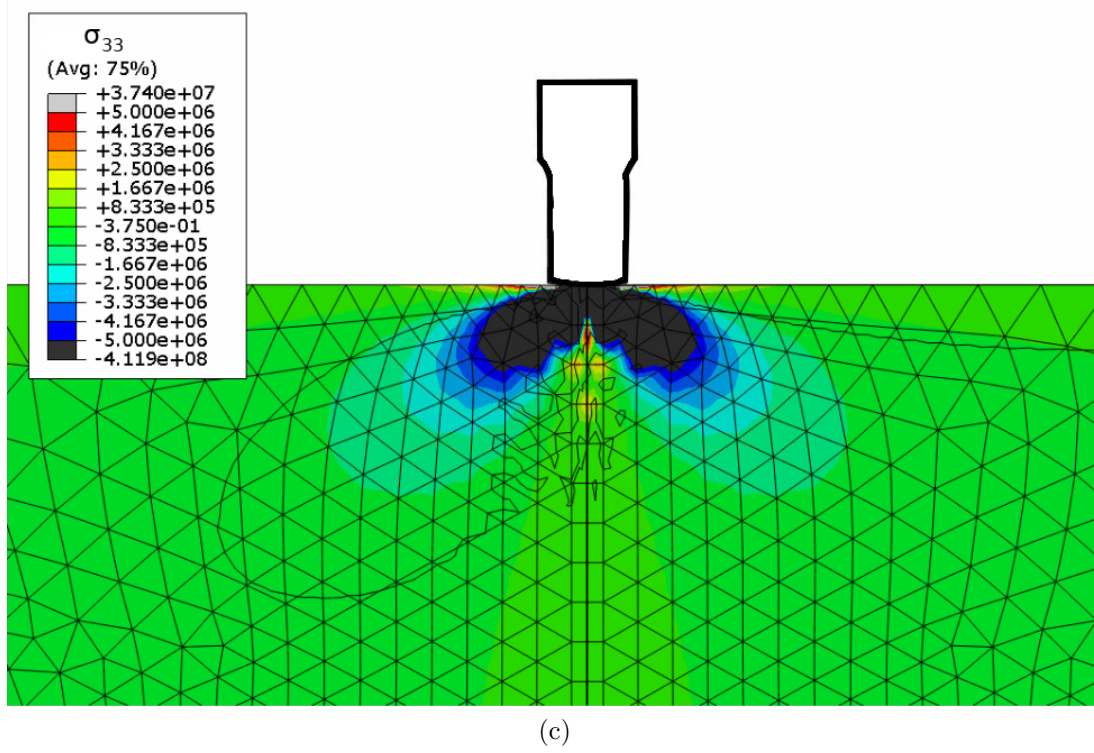


Figure 4.6: Elastic Stress field of ice under indentation. The  $x_1$ -axis is out of page.

in the creation of the surface cracks (the OTZ spalls) that occurred but caused no significant load drops in the experiments.

Figure 4.6c shows the in-plane stress field. As expected, there is a compressive *hpz* beneath the indenter, with a tensile zone beneath that. There are compressive zones that branch out from the *hpz* and angles of  $45^\circ$  to the loading axis. At the surface of the ice, and just outside the *hpz*, are two tensile zones of ice that are the origin of those surface fractures that caused no significant load drops.

Figure 4.6d shows the in-plane shear stresses (the out-of-plane stresses are practically zero). The shear zone has two sections that split  $45^\circ$  to the loading axis and surround the interior tensile zone. This zone will be conducive to the growth of microcracks and wing cracks, as well as grain boundary sliding. These processes lead to the growth of deeper cracks that lead to the spalling events that caused the significant load drops in the experiments.

Figure 4.7 shows the locations of the different stress zones. Near the surface of the ice is the two tensile zones (they are really just one zone that circles around the ice). The state of stress in this region is dominated by tensile stresses parallel to the ice surface. Due to the lower stresses in this region, there is not an appreciable load drop upon removal of a fractured piece of ice, unless the crack extends into the *hpz*, in which case there would be a significant load drop. The OTZ spalls originate in this zone, which explains why the load curves for those fractures show no appreciable load drop.

The compressive zone is the core of the *hpz*. Due to the high confining stresses, cracks are unlikely to originate in this region since any potential crack surfaces would likely be compressed together and healed. This region will likely undergo dynamic recrystallization and extensive damage (not modelled here).

The interior tensile zone is due to the Poisson's effect that would like to split the

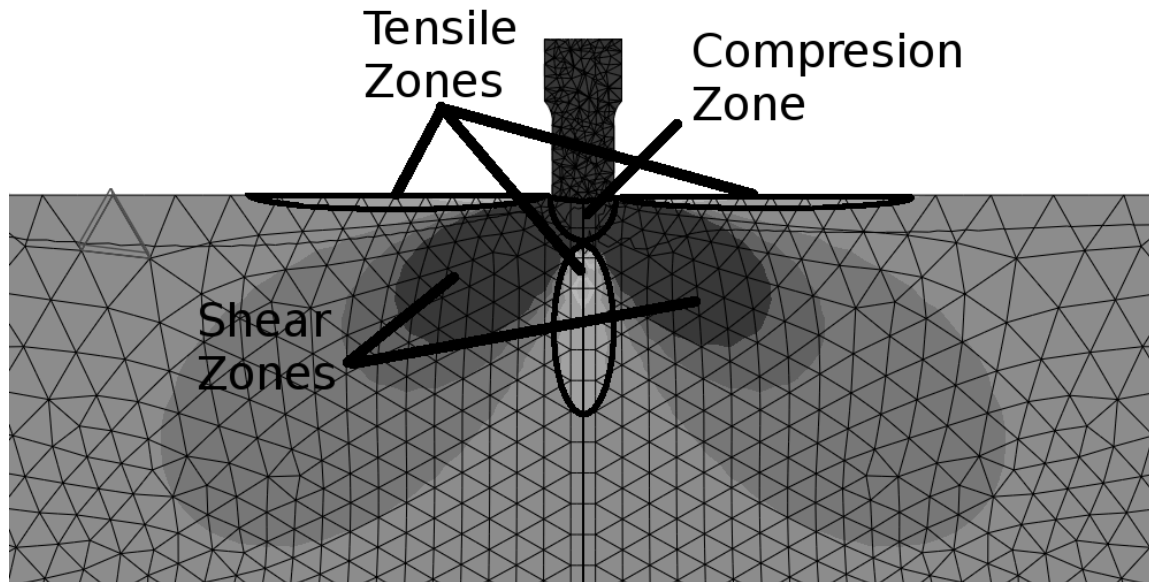


Figure 4.7: Location of compressive, shear, and tensile zones in ice under indentation.

ice in half. Figure 4.8 shows the elastic strain energy stored in the ice. The build up of this energy (or equivalent in stress formulation) is the cause of crack growth. Considering a pre-cursor crack along the centre of the ice, the crack will grow by opening due to the tensile forces pulling the faces apart. Since the crack will follow the path of maximum energy release, for smaller specimens this may split down the middle, but confinement may cause it to tend to the sides, as depicted in Figure 4.8 (or the Hans Island experiments).

The shear zone is arguably the most important region for fracture mechanics in ice. While a central, radial crack (from the tensile zone) would all but remove the loads from the ice (since the ice would have split), these are rare events. The most likely place for fracturing of ice will occur in the shear zones, especially for faster loading. For faster loading rates, stresses in the shear zone will rise quickly. Since stresses



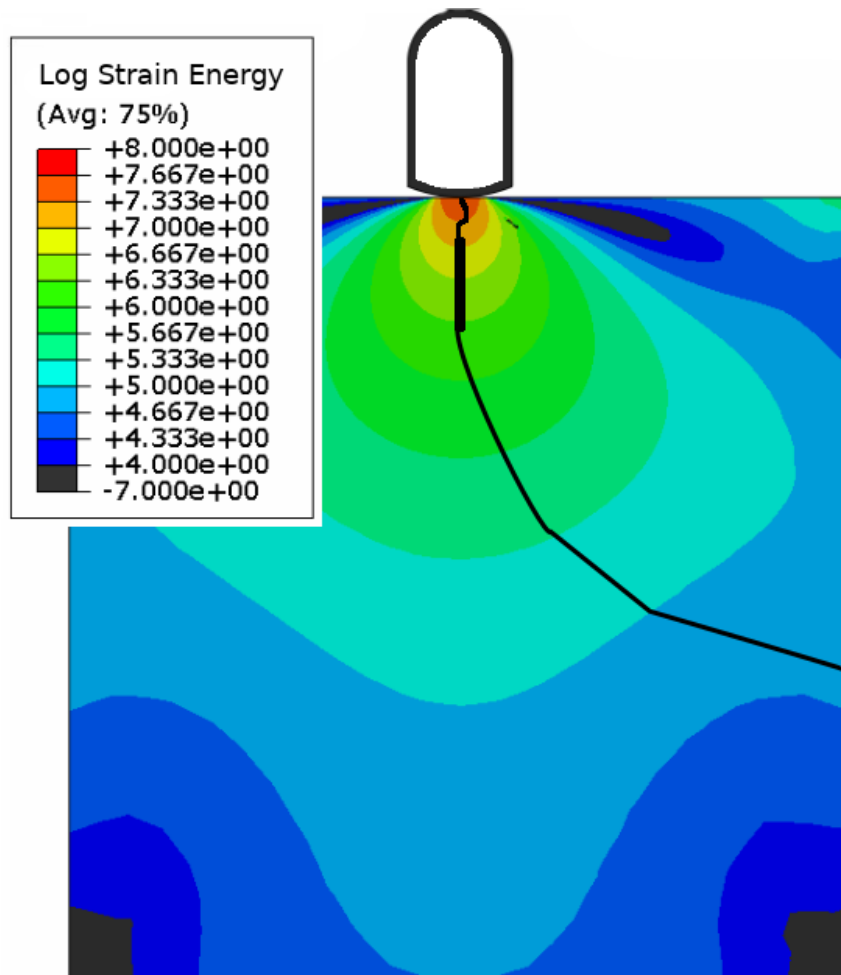


Figure 4.8: Potential radial crack growth following a path of maximum energy release, perpendicular to the contours of strain energy density. For an unconfined specimen, the indentation would be analogous to the Hans Island experiments.

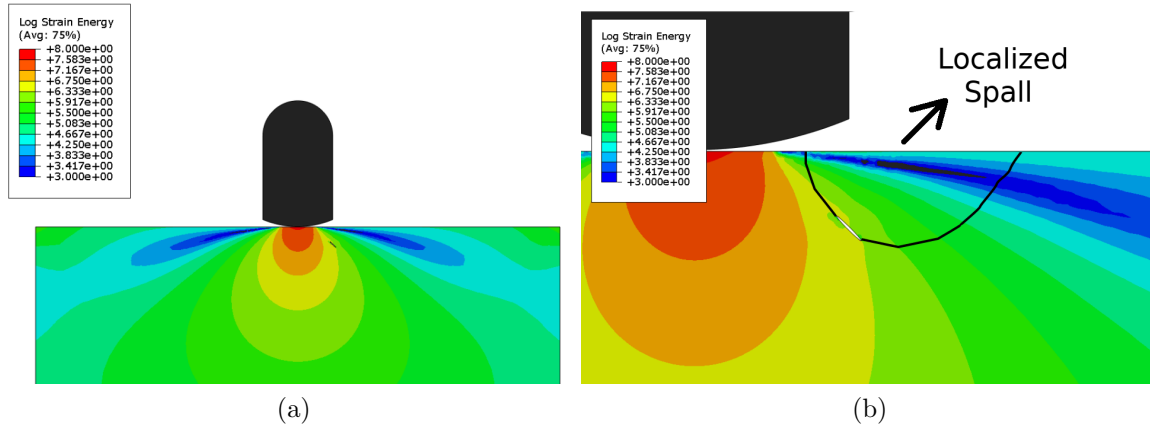


Figure 4.9: Potential spalling following a path of (elastically modelled) maximum energy release from the shear zone.

have to propagate through a material, the stress field under fast loading will not resemble the static stress fields from the FE analysis - there will be high stresses near the indenter and little elsewhere (due to the time-dependent aspect of viscoelastic stresses and strains from the underlying mechanisms). Since stresses will initially build up closer to the contact area, brittle failure is accompanied by fractures that occur near the surface - leading to many localized, small spalling events occurring in rapid succession. For medium loading rates, the stresses near the surface are able to relax, allowing the stress field to more closely resemble the stress field from the analysis. This stress field covers a larger area, so that deeper cracks may form and spall from the shear zone. The medium-rate tests showed fewer spalls than the fast-rate tests since the energy was more distributed, but the medium-rate spalls were larger since they originated deeper in the ice. The medium rate tests were also able to captured delayed failure as small, stable cracks are able to grow until they reach a critical length.

Figure 4.9a shows a close up of the elastic potential energy stored near the indenter with no crack. Figure 4.9b introduces a shear crack near the indenter in the shear zone. The presence of the crack slightly alters the elastic potential energy field as

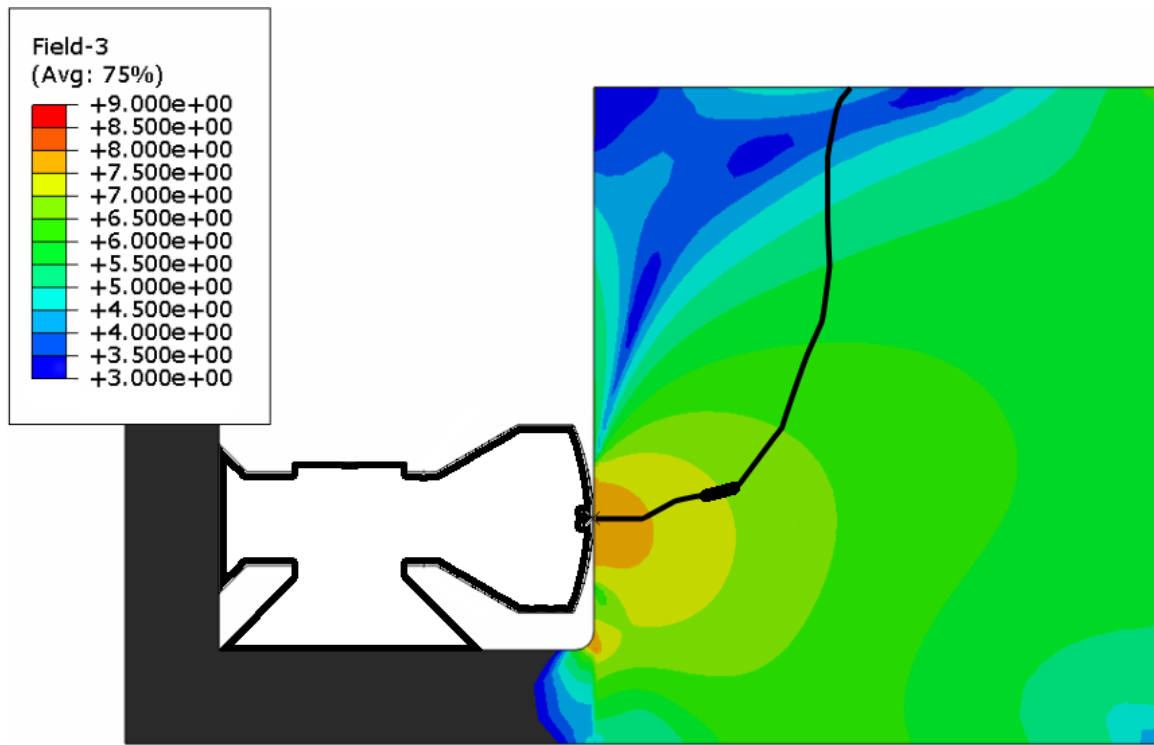


Figure 4.10: Strain Energy Field with possible crack growth for Hobsons Choice Medium-Scale test done at slow speed.

it grows. Figure 4.9b shows a rough estimation of the crack growth that follows the path of maximum energy release. As the spall breaks off, the elastic potential energy (and stresses) in the ice will decrease. This decrease will hinder the growth of other cracks, such as the radial cracks, making the shear zone the dominant area of ice for controlling the loading forces that the ice would exert on a structure or vessel.

#### 4.3.1.5.2 Hobsons Choice Indentation

One of the better known examples of delayed failure was the slow loading test done in Frederking et al. (1990), and discussed in Section 3.1.7. In this slow loading test, a large failure was observed that started ahead of the contact area and broke off a large piece of the ice wall. One possible explanation can be seen in Figure 4.10.

The figure shows an elastic finite analysis <sup>3</sup> of the strain energy for the Hobsons Choice experiment. A crack may have originated in either the interior tensile zone (as depicted in Figure 4.10) or the shear zone in the ice. The strain energy field is such that the maximum energy release would be towards the top of the ice wall due to its lower confinement. Much like the observed crack (see Figure 3.6a), this strain energy field would suggest that the crack grows towards the top, leading to the large spall that was observed.

### 4.3.2 Examples of Delayed Failure

The time-dependence of ice fracture can be seen in how the ice fractures according to different normalized velocities. At the lowest velocities in this experimental series (this would likely be different had the experiments ran for longer than they had), the creep behaviour of ice is dominant and little-to-no fracture occurs. At the highest velocities, the ice is constantly either crushing or undergoing spalling that creates small spall fragments (but larger than fragments from crushing). At medium normalized velocities, where the ice behaviour is a mix of ductile and brittle properties, the spalls that can occur are quite sizeable.

Figure 4.11a and b show that for test T110 (10 mm indenter), had a lot of fracturing at the surface. Many of these were OTZ spalls that had little impact on the loading plot, but two of the spalls did cause a drop in the load (though not down to zero), suggesting that at least some of these spalls originated from the contact zone.

Test T113, shown in Figure 4.11c, was interesting in that it formed a single OTZ spall that covered nearly a quarter the surface of the ice sample. This behaviour is similar to results seen from the medium-scale experiments done at Hobson's Choice

---

<sup>3</sup>All finite analysis uses  $E = 9.5$  GPa, and  $\nu = 0.3$ . These analysis are very simple and are meant for illustrative purposes only.

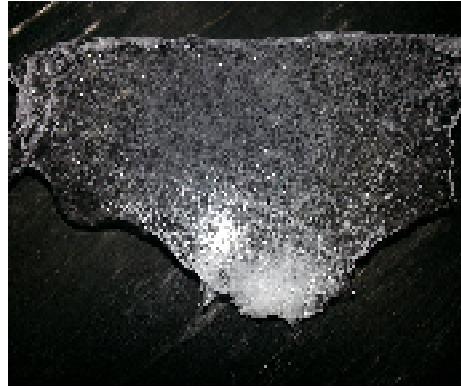
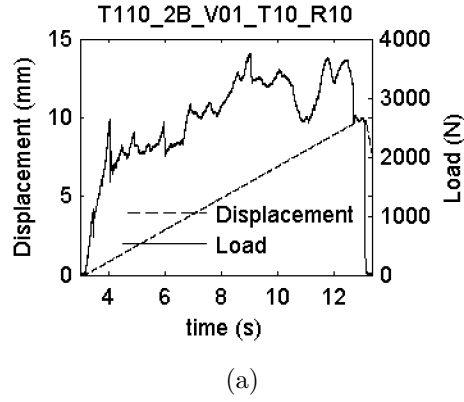


Figure 4.11: a) T110 used the 10 mm indenter at  $N_V = 0.1$ . b) Final results of T110 displays many large pieces of ice. c) T113 ( $V_N = 0.03 s^{-1}$ ) resulted in a large section of the surface breaking off (10 mm indenter imprint can be seen at the bottom of the piece).

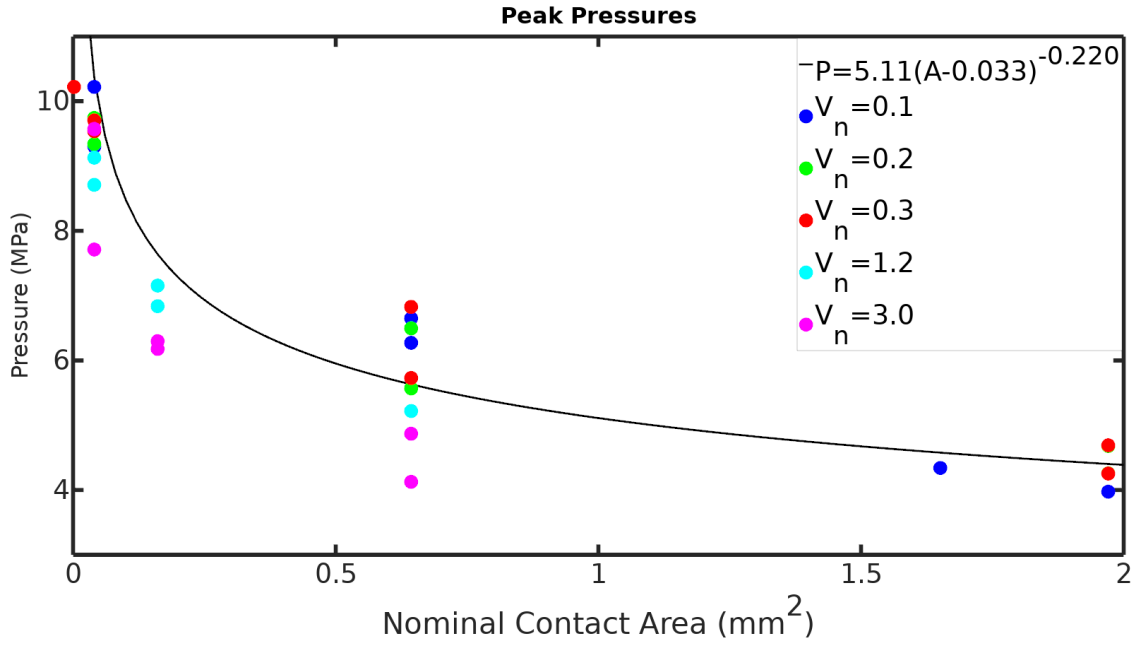


Figure 4.12: Pressure vs Area scatter plot of the data from the laboratory-scale indentation series. Data shows a decreasing power-law relationship.

ice island (Frederking et al., 1990; Jordaan, 2001) and shown in Figure 3.6

Test T125 underwent creep-like behaviour that caused a crack to grow slowly over time until it became unstable leading the spall piece presented in Figure 4.2f. This spall did cause the load to drop significantly (see Figure 4.2c). This can be understood from the works of Schapery (Schapery, 1964, 1981, 1984a), and Schapery's linear viscoelastic crack model (Schapery, 1975a,b,c), discussed in Chapter 6.

### 4.3.3 Observed Scale Effects

Figure 4.12 presents the pressure-area relationship from the indentation series. The figure shows the maximum pressures for all the tests from the series. The area used in this plot is the nominal area of the indenter, resulting in several columns of data points corresponding to each indenter. The data is also sorted into groups of normalized velocities by colour.

Observations of Figure 4.12 clearly shows the expected decreasing power-law relationship that was seen in the medium-scale experiments. The plot also shows a decrease in pressure for higher normalized velocities than the slower normalized velocities. However, for any particular normalized velocity, the decreasing power-law trend is clearly evident. The power-law curve fit is the best fit curve to the data.

A second observation about the data is in the scatter. In general, including the medium-scale data sets, there is more scatter in the smaller contact area experiments/interactions. The scatter decreases for increasing contact area.

Both of these observations can be explained by the weakest link theory of Weibull (1951), as discussed in Section 3.1.5. To begin, the explanation will begin with a simple case of samples cut from a block of ice and put under some applied load. One may assume that these samples in the next sections are thin plates under biaxial loading to ease discussion. The discussion will then relate back to the results of the indentation series.

#### 4.3.3.1 Explanation of Scatter Differences

Figure 4.13 shows an ice block cut into four samples labelled A1, A2, B1, and B2. A1 and A2 are both large samples that contain a large number of cracks of different lengths and orientations. In every sample, there will be a critical crack that fails first, much like the weakest link in a chain, that causes the sample to have failed. Given a large number of cracks that can exist in larger samples, it is more likely that they will have critical cracks that are similar in length and orientation. This suggests that large samples like A1 and A2 will have similar failure loads (less scatter). On the other hand, smaller samples like B1 and B2 are less likely to have similar critical cracks. It can be seen that the crack in B2 is considerably larger than the crack in B1, meaning that B2 will likely be much weaker than B1. This suggests that smaller



Figure 4.13: Samples cut from an ice block will contain random distribution of cracks and flaws. Large samples are likely to be weak due to containing a large flaw. Smaller samples will exhibit more scatter as they may or may not have a large flaw.

samples should have more scatter than the large samples.

#### 4.3.3.2 Explanation of Observed Decreasing Power-Law

Similar to the explanation of the scatter, the decreasing power-law is also a result of the distribution of cracks in a sample. For large samples (A1 and A2), it is very likely that they will contain a large critical crack or one that is favourably oriented. Simply put, it is very likely these samples will be weak because a large, random distribution of cracks will likely contain a critical crack that will cause the ice to fail under smaller loads/pressures.

In the case of small samples (B1 and B2), they will have a smaller number cracks. Since the crack distribution is random, then it is more likely that some small samples will contain a small (or unfavourably oriented) critical crack, requiring larger loads/pressures to break the sample. Griffith (1921) applied axial tension to glass fibres and found that thinner wires were stronger than thicker wires. This is due to the increased likelihood of weaker critical cracks that are found in larger samples and

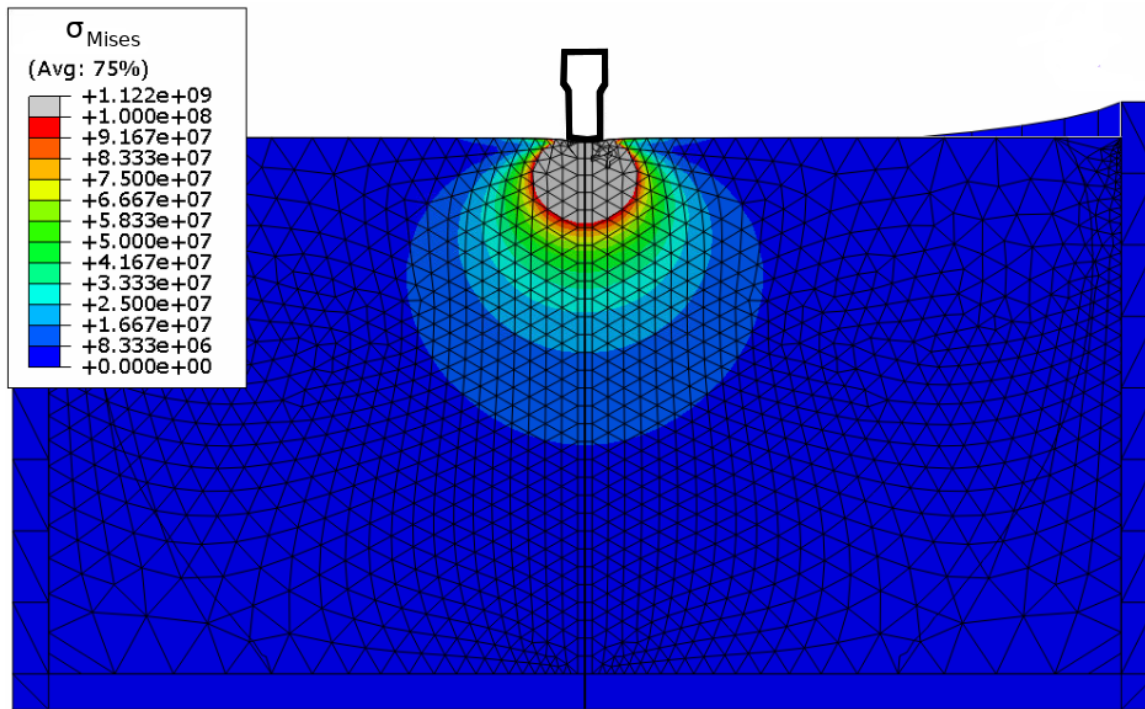


the increased likelihood of less severe cracks in smaller samples.

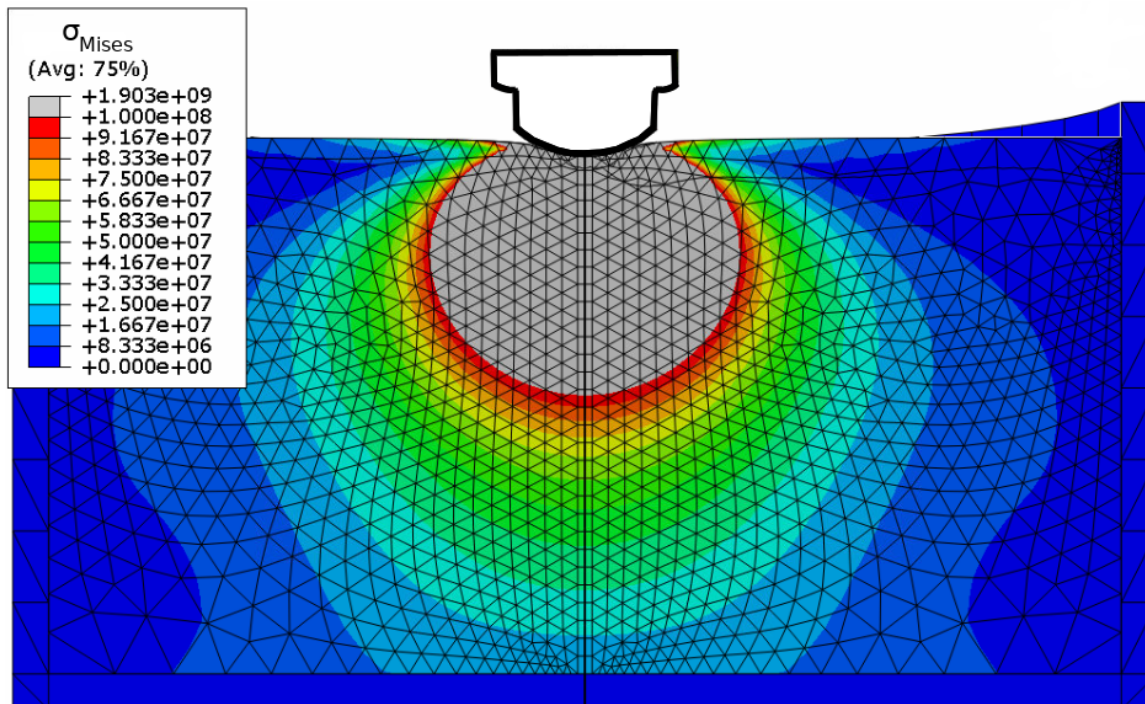
#### **4.3.3.2.1 Application of Theory to the Indentation Scale Effects**

Unlike the previous section, all the indentation experiments listed here were performed on ice samples of one or two different sizes, both of which would be considered large samples. While the sample size here may have some influence, it is not likely the case as most samples were made in the smaller mould. Clearly, the actual size of these samples would not be the main factor, possibly even negligible at this scale.

Figure 4.14 shows the Von Mises stress field in the ice beneath the indenter for both the 10-mm and 40-mm indentors as they are indented 2 mm into the ice sample. As expected, the stress field beneath the larger indenter covers a larger area of the cross-sectional cut. The difference between these two areas under high stress is akin to the sample sizes from the previous section. Essentially, the larger area underneath the 40-mm indenter is more likely to contain weak critical cracks like the A1 and A2 samples above. Due to the smaller area of high stress underneath the 10-mm indenter, much like B1 and B2, this area is more likely to have some samples with less severe critical cracks.



(a) 10-mm Indenter



(b) 40-mm Indenter

Figure 4.14: Von Mises elastic stress field for ice underneath the 10- and 40-mm indentors.

# Chapter 5

## Experimental Program: 4-Point Bending Series and Analysis

### 5.1 Objectives

The aim of the 4-point beam bending series was also to study the fracture properties of ice. The indentation series showcased many of the viscoelastic properties of fracture in ice. Due to the random crystal structure of ice, and the random distribution of pre-existing cracks in natural (and many lab-grown) ice samples, these properties will generally require statistical methods to understand them. That said, the underlying physical properties of crack growth are still crucial as they provide the means in which cracks grow.

More specifically, the aim of the 4-point beam bending series is to study the fracture properties of a single crack. In the following series of experiments, a large crack is cut into the bottom-centre of a beam of ice. Due to the large size of the crack, it will clearly become the critical crack that fractures the ice beam. These experiments will provide insights into crack growth that cannot be obtained from the

indentation series by simplifying the geometry and reducing the randomness that was evident in the indentation series due to the presence of many cracks.

## 5.2 Facilities

Two sets of 4-point beam experiments took place in the Thermal lab of the S. J. Carew building at Memorial University. The lab contains a temperature-controlled cold room that can be maintained to within  $\pm 0.5^\circ\text{C}$ . Within the cold room is a series 311.21 MTS load frame which can be loaded to 500 kN of force.

For the first series of tests, the load on the ice beam was measured using a 10 kN force transducer (MTS series 661.19), located between the MTS crosshead and the top of the beam bending apparatus. This transducer is good for temperatures down to  $-53^\circ\text{C}$  with a reading sensitivity of 0.002% per  $^\circ\text{C}$ . This transducer was chosen because it provides more precise results than the 500 kN force transducer (series 661.23) that was available.

Data was acquired using National Instruments SC-2043-SG Data Acquisition (DAQ) connected to MTS Flextest™ GT 100 (series 793.00) controller with 8 channels for data acquisition with a frequency of 4 kHz. The Controller was connected to a Dell Optiplex 980 computer running the MTS FlexTest™ GT Station Manager software for electronically controlling the MTS frame, designing test programs, and storing data onto the computer.

High-speed video was recorded on a Mega Speed MS55K camera with accompanying software on an IBM Lenovo Thinkpad X60s. Typical frame rates were 1000-1500 fps, as to keep adequate image quality.

The second set of experiments made use of a custom-designed dead-weight apparatus. Force was measured using a 250-lbs button load cell. This load cell is good

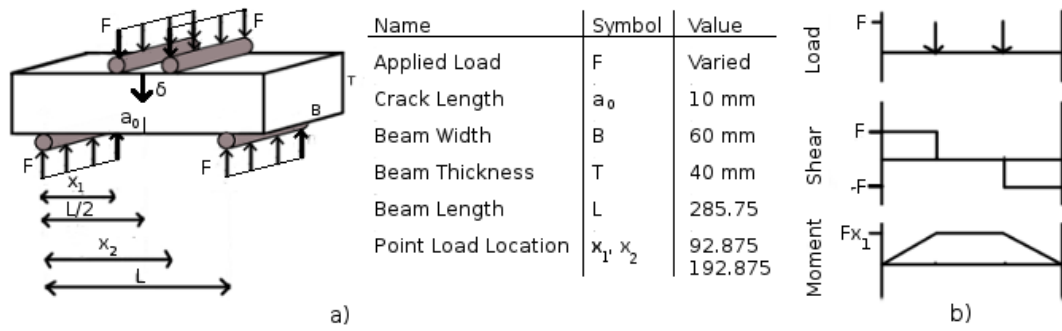


Figure 5.1: a) 4-point bending experimental setup with dimensions. b) shear-moment diagram for 4-point bending.

for temperatures down to  $-40^{\circ}\text{C}$  with a voltage sensitivity of  $2 \text{ mV/V}$ . This load cell was chosen as the only other button load cell available was a 1000-lbs load cell by the same company. A linear variable displacement transducer (LVDT) was used to record deflection of the beam. The LVDT used a Sensotech AC Modulator to modulate its voltage to 0–5 volts and had a sensitivity of  $2 \text{ mv/V}$ .

Data for this series was acquired using a National Instruments NI-6008 DAQ connected to the same Dell Optiplex 980 computer. All the components (including a solenoid valve for load control) were controlled using a program designed in National Instruments Labview software, which would also record data from the DAQ until the ice failed or the experiment was aborted.

## 5.3 Procedure

### 5.3.1 First Series

Bubble-free ice was crushed and sieved to grain sizes between 2–3.35 mm. A plastic container, surrounded by insulation on the bottom and sides, was filled with seed and water and allowed to freeze over 2-3 days at  $-2^{\circ}\text{C}$  to ensure the ice froze slowly (reducing bubbles), creating granular, polycrystalline ice. The ice was then cut down

to the final dimensions in Figure 5.1 using a bandsaw. The ice was then allowed to equilibrate to  $-10^{\circ}\text{C}$  before testing. Each ice sample was notched with a fine-tooth saw to a depth of 10 mm, and a razor blade was used to give the crack a sharp edge. Prior to each test, the razor blade was run through the crack to prevent the cracks from healing and becoming dull.

The experimental setup, shown in Figure 5.1 (and again in Figure 5.2b), used a 4-point bending apparatus to ensure a constant moment was applied at the mouth of the crack between the top rollers. A 4-point bending specimen was chosen over the 3-point bending specimen (see Figure 5.2a) as the 4-point specimen has a constant bending moment between the the top rollers, ensuring that the experiments would not be affected by any slight misalignment from the centring of the beam, which can be compared to the bending moment under 3-point bending from Figure 5.2c.

The beam was installed on a MTS frame that would apply a stress to the beam. As is the case for the second series of tests, the ice was placed by hand on the bottom rollers, using measuring tape to centre the beam as best as possible. The top rollers were slowly brought into contact with the ice. The top portion of the 4-point bending apparatus was connected to a swivel that would allow it some rotation so that the loads would be evenly distributed between the two rollers.

During initial tests, various loading rates were considered during the ramp up phase, but it was subsequently decided to use a constant rate of approximately 1000 N/s. The loading rates were set using the MTS software, but the load-time plot of each test was checked to get the actual loading rate, as the MTS would be slightly off the prescribed value.

The original goal of this series was to apply a stress that was less than the failure stress (i.e.; fracture toughness,  $K_{IC}$ , was greater than the stress intensity factor,  $K$ ). Once the peak load was attained (which varied from specimen to specimen) this

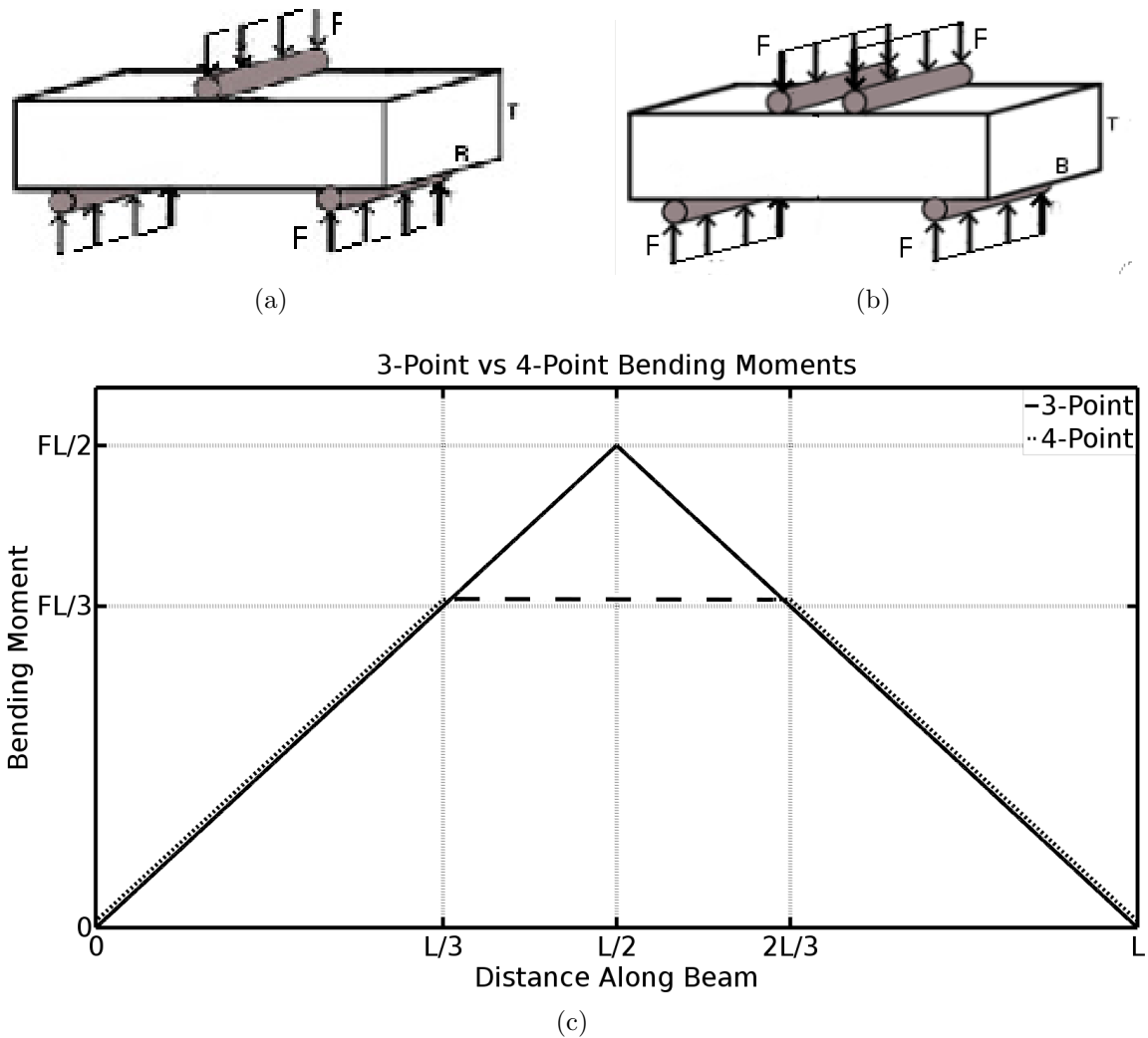


Figure 5.2: a) 3-Point bending set-up. b) 4-Point bending set-up. c) Bending moment diagram comparison of 3- and 4-point bending. 4-Point bending has a more uniform bending moment near the crack than in a 3-point bending set-up.

load level was maintained until either the ice broke or until the test was stopped (intentionally or in some instances due to technical issues with the apparatus).

Due to the varying failure strength in ice (due to both time-dependent aspects and natural variability in flaw distribution), many experiments failed while the load was still ramping up towards a set load. Since many of these experiments were under different loading rates, the experiments also provided data on the relationship between failure load and the applied loading rate.

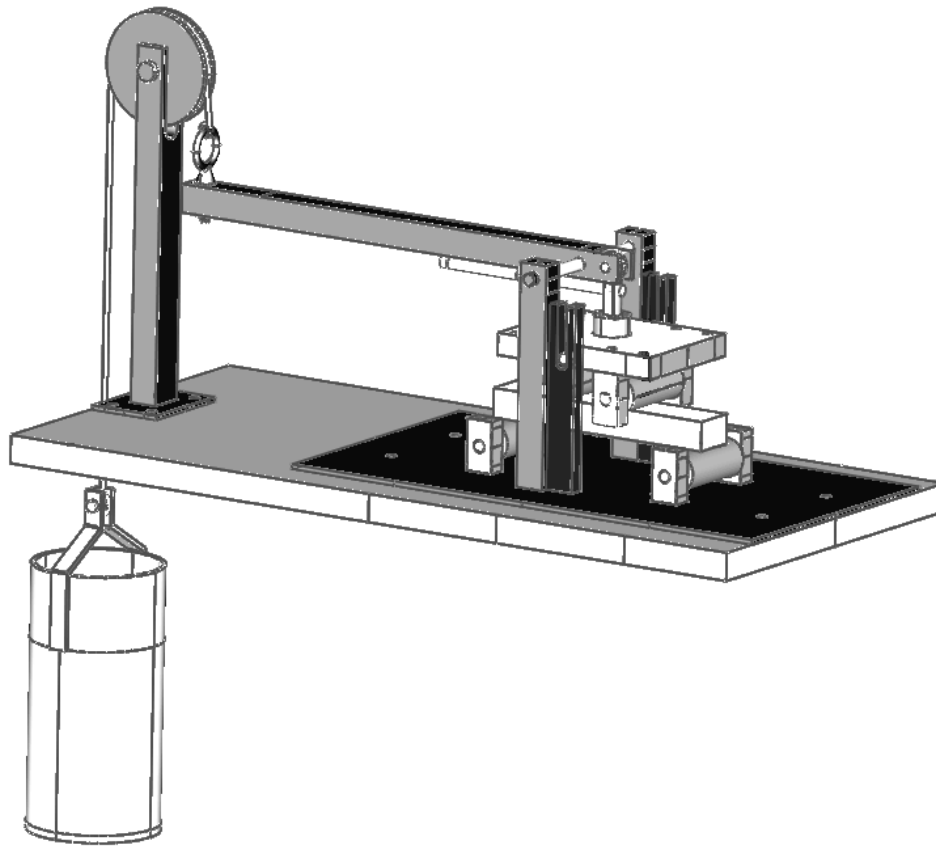
### 5.3.2 Second Series

The method of growing the bubble-free ice remained the same from the first series of beam bending experiments. Likewise, the samples were cut to their final dimensions using a bandsaw and were pre-notched using a razor blade.

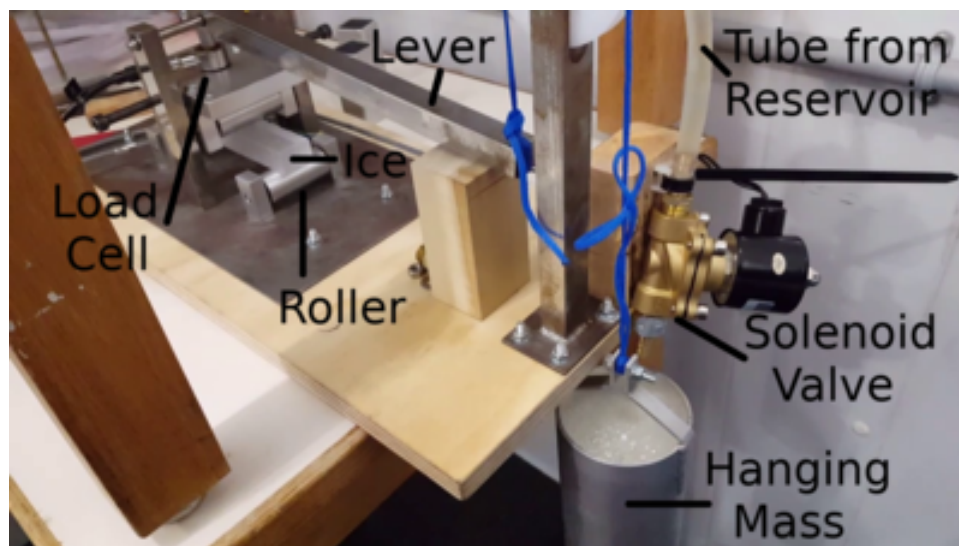
To allow more experiments to be completed, it was decided that the samples for this series of tests were to be made about half the size of the previous ice beams for each dimension. The ice samples were 150 mm in length (technically they were longer, but the bottom roller separation was 150 mm), 30 mm in width, and 20 mm in thickness. The larger beams had a crack that was  $1/4$  of the thickness of the beam, to keep the experiments self-similar, the smaller beams were pre-notched with a crack that was 5-mm in length.

The previous beam bending series only provided a couple of delayed failure examples. Consideration went into determining the best means to capture delayed failure. It was decided that using a dead weight loading apparatus would provide a stable and consistent way to apply a load over long periods of time. The apparatus, shown in Figure 5.3, used a hanging mass and lever to apply a load to the top rollers of the 4-point bending apparatus in contact with the ice. For this experimental series, various loads were tested to see how the the time to failure would change as a function



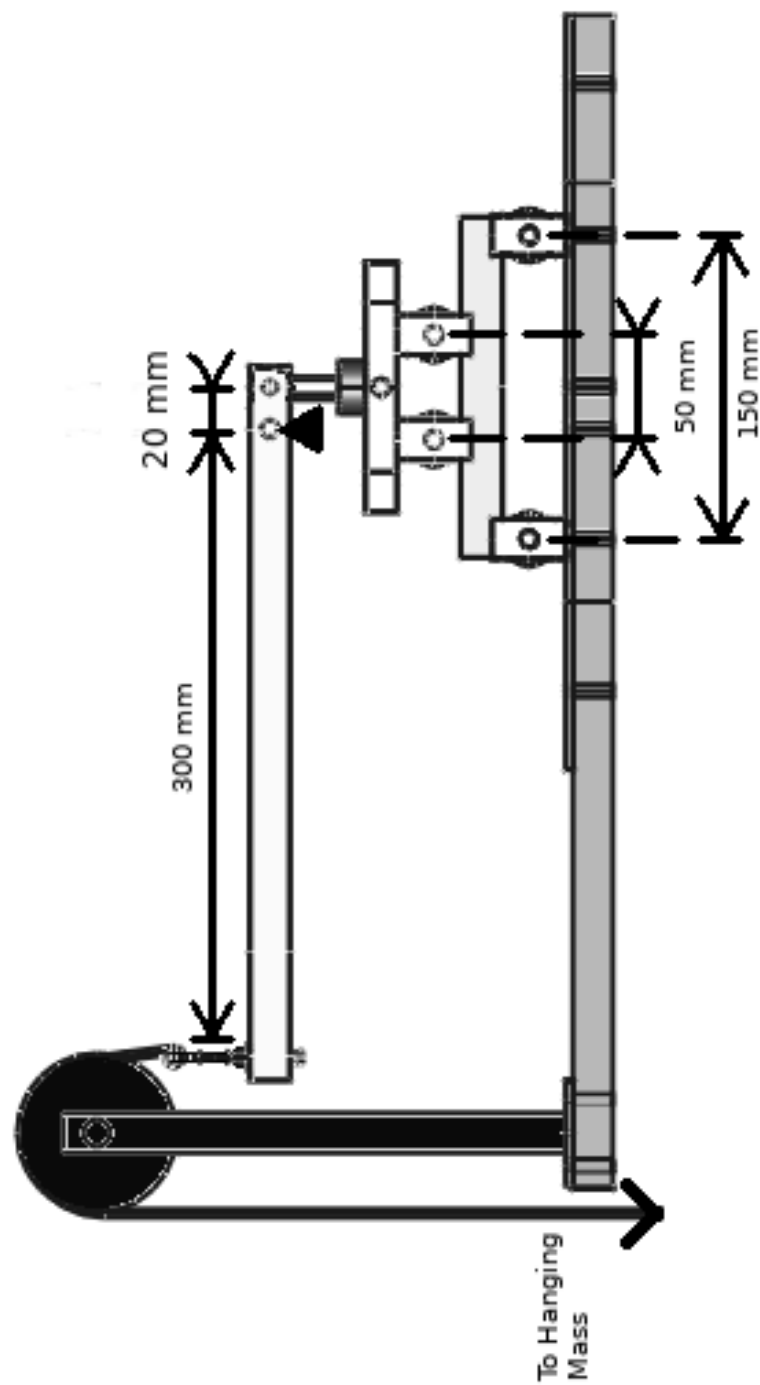


(a)



(b)

Figure 5.3



(c)

Figure 5.3: 4-Point beam bending dead-weight apparatus. Elevated reservoir filled with fluid not shown.

of applied load.

The apparatus sits atop of a wooden table that is supported with steel plates to act as stiffeners, preventing unwanted deformation. A pair of rollers are bolted to the table 150 mm apart. Each roller has a 8 mm steel rod as a core, surrounded by a hollowed 25.4 mm cylinder that constitutes the bulk of the roller. The steel rod core stiffens the roller, minimizing any deformation in the roller. The aluminium shell is used as ice is less likely to freeze to it than it would to steel, reducing any additional stress on the ice due to the rollers.

The ice is placed on top of the rollers that are bolted to the table. On top of the ice is another pair of rollers bolted to an aluminium top plate, spaced 50 mm apart. The purpose of the top plate is to have the top rollers at their proper spacing and to connect them to the lever arm that will apply a downward force to the top plate and the ice. Between the lever arm and the top plate is a 250-lbs button load cell for measuring the applied load. The load cell has two 6.35 mm bolts built into its design. One of the bolts screws into a hole in the centre of the top plate. The other bolt is screwed into 6.35 mm female tie rod end. A 6.35 mm bolt is used to connect the tie rod to the right side of the lever arm, 20 mm from the lever's fulcrum.

On the front and back of the apparatus, there are four supports near the ice sample. One pair, the darker-coloured in Figure 5.3, are steel guides for the top plate. As a force is applied to the top plate, it will move downward into the ice. On either side of the top plate, there are 2 M8 bolts that protrude outward and rest within the prongs of the steel guides. This ensures that the top plate moves straight down and minimizes any twisting of the top plate from the ideal motion.

Next to the steel guides, shown as a lighter colour in Figure 5.3, are the lever supports. At the top of the lever supports there are 8 mm holes for an M8 bolt to connect the two supports to the lever. A threaded steel rod is screwed into the two

lever supports and acts as the lever's fulcrum.

On the left side of Figure 5.3 there is a hanging bucket that fills up from an elevated reservoir (not shown). As the bucket fills up it pulls down on a string. This string is connected to a pulley that causes a lever to be pulled up on its left side. The fulcrum of the lever is 20 mm from the top plate and 300 mm from the left end, providing the hanging mass a mechanical advantage of 15, allowing for the necessary loads while requiring significantly less fluid for the hanging bucket.

As the right side of the levers lowers from the increased mass in the bucket, it pushes the top plate of rollers into the ice sample, causing it to bend. The force that is applied to the ice is measured by the load cell. A program was written in LabVIEW™ that recorded the load data. Prior to each experiment, the desired load was input to the program. Upon starting the program a solenoid valve would open up and fluid from the reservoir would flow into the hanging bucket. When the desired load was reached (or the sample broke on loading), the solenoid valve would shut off. The program would record data to the computer until the ice broke or the experiment was terminated.

## 5.4 Results and Discussion

### 5.4.1 Rate-Dependent Fracture Toughness

Figure 5.4a displays the results from the first series of experiments that involved ramp up to failure for various loading rates. There is a decreasing power-law relationship between the load at failure and the applied loading rate. For faster loading rates, the failure load approached an asymptotic value for failure load. For the curve fitted to the data, this would be around 120 Newtons as the elastic limit of failure. All the samples broke at loads just under 450 Newtons, which provides an upper limit on

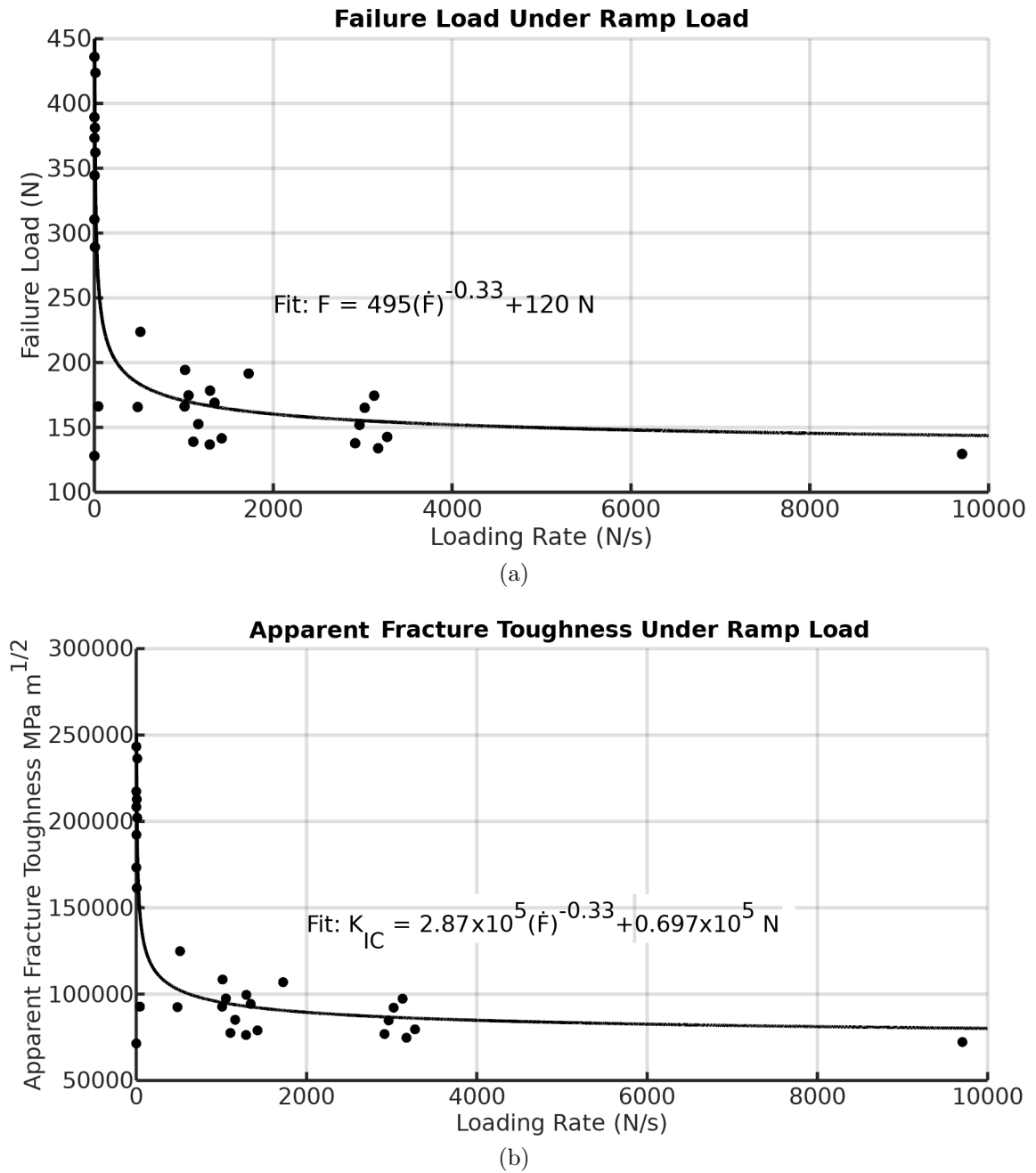


Figure 5.4: a) Experimental results of failure load due to changing loading rates. b) The same results plotted as an apparent fracture toughness.

the failure load of ice (essentially the failure load can be estimated by the smaller of 450 Newtons and the curve fit). A preliminary analysis of this dataset (along with the indentation series) was discussed in Kavanagh et al. (2015) that highlighted these features (There was a slight calculation error in that paper that altered the numerical results, but the trends and ideas from that analysis still hold with the corrections).

The apparent fracture toughness plot (Figure 5.4b) was generated from the load plot (Figure 5.4a) by converting the loads to fracture toughness by using the following 4-point bending stress intensity equations (see Figure 5.1 for values)

$$K_{IC} = Y\{\alpha\} \frac{F(x_2 - x_1)}{BT^{\frac{3}{2}}}$$

$$Y\{\alpha\} = 1.9887 - 1.326\alpha - \frac{(3.49 - 0.68\alpha + 1.35\alpha^2)\alpha(1 - \alpha)}{(1 + \alpha)^2} \quad (5.1)$$

There is roughly a three-fold difference between the maximum and minimum failure loads for these samples. Clearly, the data demonstrates that the fracture properties of ice are time-dependent. Since the behaviour of the crack changes from a brittle to more ductile response, it is clear to see why the range of behaviours was seen in the indentation series.

Under fast loading conditions, the material in front of the crack (in particular, the process zone) have little time to adjust to the sudden increase in stress. This increase in stress near the crack provides the crack with sufficient energy to grow and become unstable more quickly.

As the loading rate decreases, the stress near the crack rises more slowly. As discussed in Section 2.2, there are various ways (such as grain boundary sliding and dislocation glide) that allow the ice to relieve stress by the movement of grains or sub-grain structures. For slower loading, these processes have more time to react to the stress increase, allowing these processes to lower the maximum stress. These

processes are the underlying mechanism for ductility in materials and provide the means for viscoelasticity in materials.

As seen in previous experiments (Urabe et al., 1980), the data shows a clear upper limit that is unaffected by the loading rate. The processes that relieve stress have a limit to how much they can do, for example, grains can only slide so far before becoming locked into place. This provides an upper limit on how strong ice can be as the slower tests all achieve the maximum amount of local stress relief from the dissipative processes, resulting in similar peak failure loads.

#### 5.4.2 Time to Failure Under Constant Load

Two examples of delayed failure were observed in the first beams series using the large ice beams. The loading curves of these samples are plotted in Figure 5.5. Figure 5.5a shows a sample that was held for roughly 12 minutes and 45 seconds before it underwent delayed failure. Figure 5.5b shows a sample that broke just after 0.2 seconds under applied load.

Both samples were loaded to 180 N but gave drastically different failure times. This is likely due to the natural variations in flaws that occur during ice growth as both samples had similar loads (180 N) and loading rates (1055 N/s and 1083 N/s), and should have similar geometries.

Figure 5.6 shows several delayed failure events that occurred in the second series of 4-point beam bending tests using the small ice samples. An initial run on the samples found that they would break during the load up if the load reached 80 Newtons (though given the variation in ice strength, this was more of a rule of thumb than a guarantee). The samples are shown in Figure 5.6 were loaded to values under this 80 Newton threshold and held until failure. The samples broke approximately at 3, 10, 20, and 50 minutes respective to their order in Figure 5.6. The initial spike in the

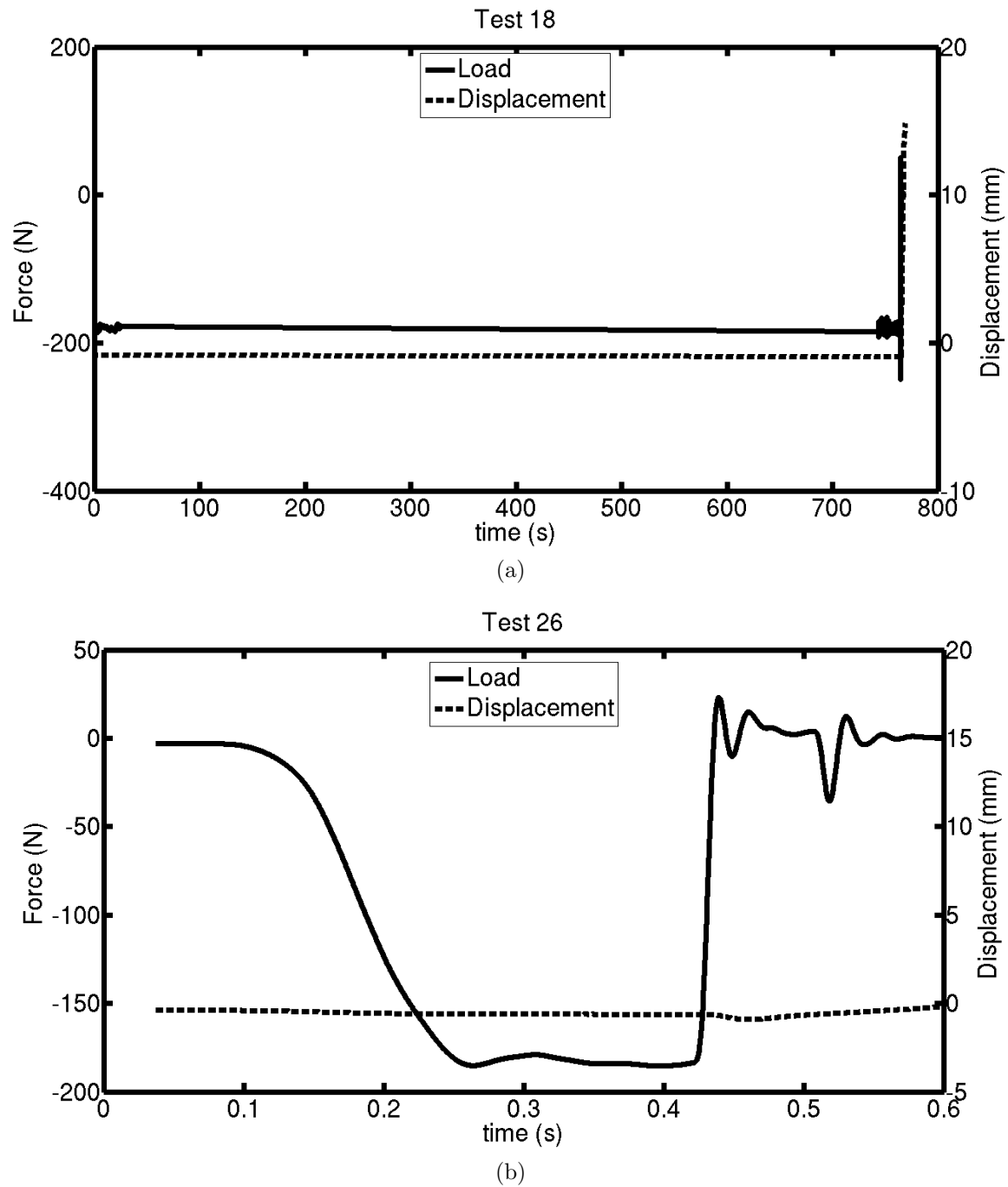


Figure 5.5: Experimentally observed delayed failure in the large ice beams from the first series. Both samples were under a load of 180 N.



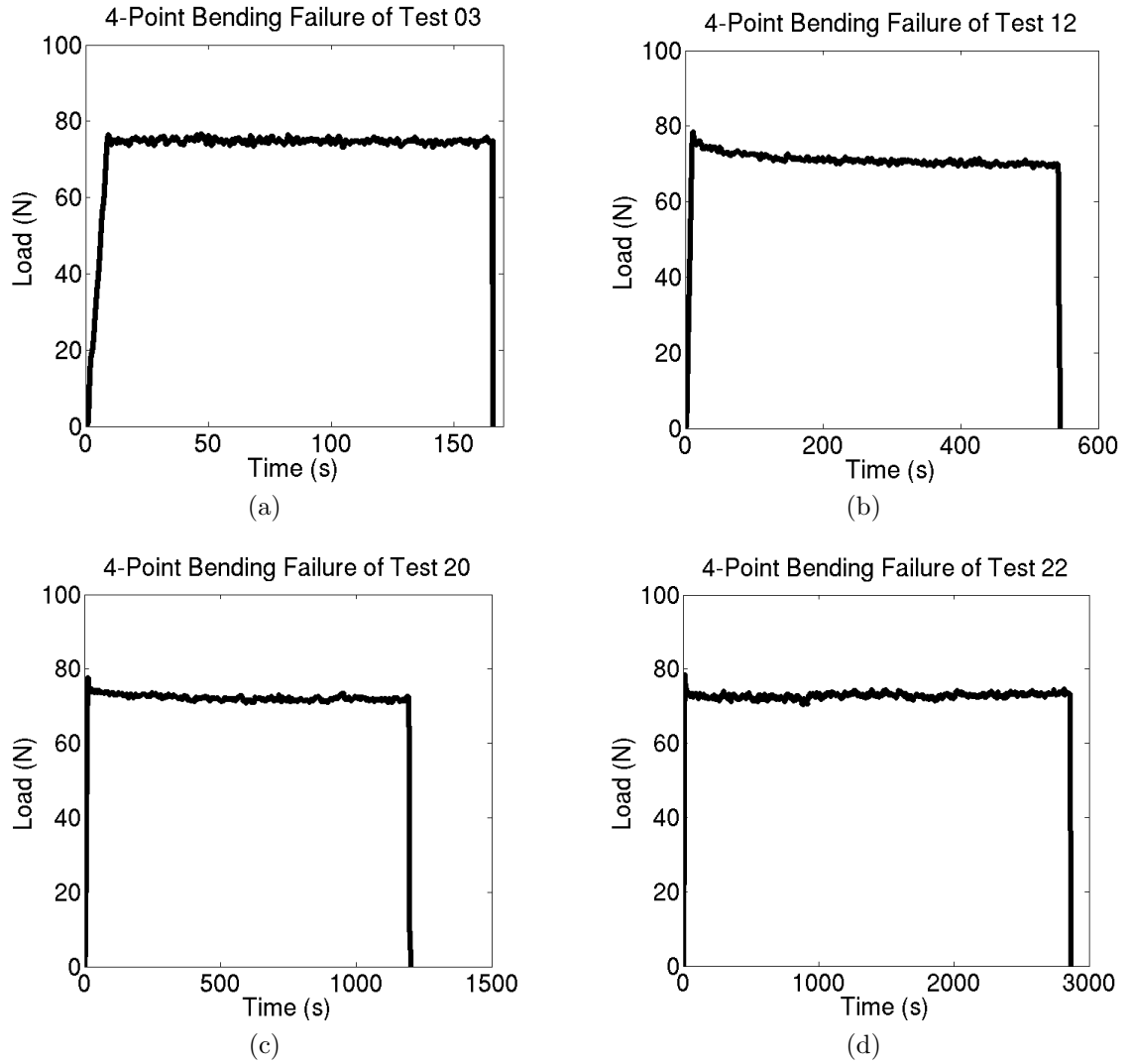


Figure 5.6: Experimentally observed delayed failure in the small ice beams from the second series. All samples were held under constant load after the initial ramp up phase.

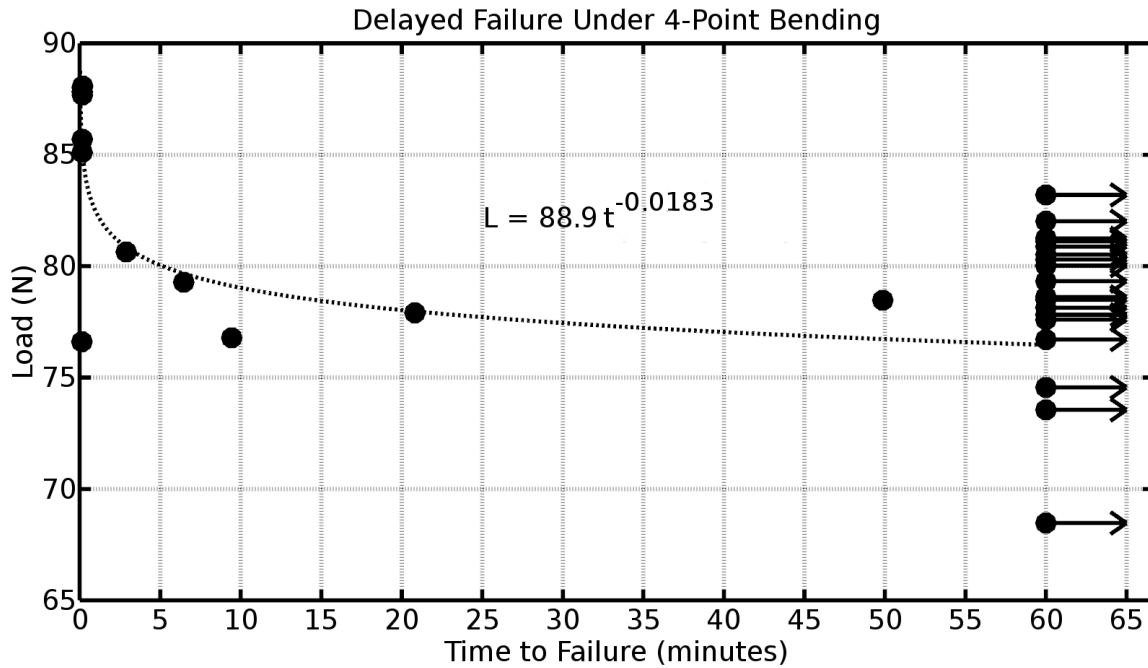


Figure 5.7: Experimental results for the dead-weight 4-point bending experiments. Samples that did not break are displayed with an arrow pointing to the right.

data as the desired load is reached is an artefact of data filtering and not physical in nature.

To better understand the relationship between the time to failure and the constant applied load, consider Figure 5.7 that plots all the experiments from the second series. Due to the random strength of ice, there are many samples that did not break within an hour (or longer), these tests are indicated when an arrow that points to the right. The experiments that lasted for over an hour were either stopped early (within two hours) to do another experiment (to collect as many data points as possible), or were allowed to run over a weekend before termination. While these points do show the variability of ice strength from sample to sample, that is not the focus of this thesis, and these samples will be omitted during the analysis to follow (focusing instead on the time-dependent aspects of the data points from the specimens that broke).

For the samples that did break under delayed failure, there is a clear decreasing

power-law relationship between the applied load and the time to failure. Experiments on solithane 50/50 (Knauss, 1970) under uniaxial tension show a similar power-law relationship between the applied load/stress and the time to failure in the specimen.

To have a better understanding of the physical processes that lead to this result, a numerical model based on the theory of Schapery (1975a,b,c) was designed. This model will be discussed in the following chapter.

## Chapter 6

# Viscoelastic Fracture Theory and Model Development

The aim of this chapter is to provide an in-depth analysis of viscoelastic fracture theory. This analysis, along with new insights, is then used to advance the theory to new geometries and to new loading scenarios. The linear viscoelastic theory presented by Schapery (1975a,b,c) provides a solid physical basis for analysing the behaviour of ice. This chapter provides the author's interpretation of the works of Schapery (1975a,b,c) (providing details left out of the original), and provides a means to expand the theory to both 4-point bending beam bending scenarios considered in Chapter 5.

As briefly discussed in Section 2.1, a viscoelastic material can be thought of as being an elastic material that has a changing compliance over time (an effective compliance), so that one can convert an elastic solution to a viscoelastic solution (should such an effective compliance exist). In Chapter 3, an elastic fracture theory was discussed that provides the basis for the viscoelastic theory in Schapery (1975a,b,c). As with the simplified cases in Section 2.1, the correspondence principle is needed to convert the elastic fracture theory from Section 3.2.3 into a viscoelastic one. As will

be discussed, there are certain conditions required to allow for an effective compliance to be found.

## 6.1 Graham's Correspondence Principle

### 6.1.1 Classical Correspondence Principle

As mentioned in section 2.1.3, the correspondence principle provides a mapping from elastic solution to a viscoelastic solution. The version of the correspondence principle presented there is known as the classical correspondence principle.

The classical correspondence principle is relatively straight forward to implement but has some limitations (Graham, 1968). For the classical correspondence principle to work, the complete history of the boundary conditions must be known and the boundary conditions must be stationary over time (e.g., an applied load may vary in magnitude, but not in the location on the boundary). It is also required that the boundary does not change over time. The indentation series would fail the classical correspondence principle since the boundary conditions change as the region of applied load changes as the indenter penetrates into contact with a sample. Crack growth problems (the core of this project) also fail since the boundary itself changes as the crack grows, adding more surface to the material.

These issues are taken care of by the correspondence principle developed in Graham (1968). This section will highlight the key points of Graham's theory as it relates

to the project. To begin, consider the typical elastic stress conditions given by

$$2\epsilon_{ij} \{x, t\} = \frac{\partial u_i \{x, t\}}{\partial x_j} + \frac{\partial u_j \{x, t\}}{\partial x_i} \quad (6.1)$$

$$\frac{\partial \sigma_{ij} \{x, t\}}{\partial x_j} = 0 \quad (6.2)$$

$$\sigma_{ij} \{x, t\} = \sigma_{ji} \{x, t\} \quad (6.3)$$

then the classical correspondence principle for constant temperature gives

$$\begin{aligned} s_{ij} \{x, t\} &= J_1 \{t\} e_{ij} \{x, 0\} + \int_0^t J_1 \{t - \tau\} \frac{\partial}{\partial \tau} e_{i,j} \{x, \tau\} d\tau \\ \sigma_{kk} \{x, t\} &= J_2 \{t\} \epsilon_{kk} \{x, 0\} + \int_0^t J_2 \{t - \tau\} \frac{\partial}{\partial \tau} \epsilon_{i,j} \{x, \tau\} d\tau \end{aligned} \quad (6.4)$$

where  $J_1$  and  $J_2$  are the viscoelastic moduli for shear and hydrostatic stress components.  $s_{ij}$  and  $e_{ij}$  are the deviatoric stress and strain, respectively.

For the classical correspondence principle, the Laplace transform of previous equations are required, resulting in

$$\begin{aligned} 2\mathcal{L} \{ \epsilon_{ij} \{x, p\} \} &= \mathcal{L} \left\{ \frac{\partial u_i \{x, p\}}{\partial x_j} \right\} + \mathcal{L} \left\{ \frac{\partial u_j \{x, p\}}{\partial x_i} \right\} \\ \mathcal{L} \left\{ \frac{\partial \sigma_{ij} \{x, p\}}{\partial x_j} \right\} &= 0 \\ \mathcal{L} \{ \sigma_{ij} \{x, p\} \} &= \mathcal{L} \{ \sigma_{ji} \{x, p\} \} \\ \mathcal{L} \{ s_{ij} \{x, p\} \} &= p \mathcal{L} \{ J_1 \{p\} \} \mathcal{L} \{ e_{ij} \{x, p\} \} \\ \mathcal{L} \{ \sigma_{kk} \{x, p\} \} &= p \mathcal{L} \{ J_2 \{p\} \} \mathcal{L} \{ \epsilon_{kk} \{x, p\} \} \end{aligned} \quad (6.5)$$

Equation 6.5 defines a set of equations that can be solved in the usual methods of solving elastic problems.

For any problem in elasticity, boundary conditions are typically defined in terms of either stresses/forces or strains/displacements. Both stresses and strains can be

split into components normal to the boundary ( $\sigma_n$  and  $u_n$ ) and tangential to the boundary ( $\sigma_s$  and  $u_s$ ). For the classical correspondence principle, two of the four components need to be defined along the boundary. Three boundary conditions are needed for Graham's extended correspondence principle. These components can be listed in matrix form as (Graham, 1968)

$$\begin{bmatrix} a_b : & \sigma_s & \sigma_s & \sigma_n & \sigma_n & u_s & u_s & u_n & u_n \\ b_b : & u_n & \sigma_n & u_s & \sigma_s & \sigma_n & u_n & \sigma_s & u_s \\ c_b : & \sigma_n & u_n & \sigma_s & u_s & u_n & \sigma_n & u_s & \sigma_n \end{bmatrix} \quad (6.6)$$

where  $a_b$ ,  $b_b$ , and  $c_b$  are the boundary conditions from any one column of the matrix that match the problem to be solved. For example, the problem may be defined by the normal and tangential stresses on the boundary (e.g., biaxial loading), in this case  $a_b$  and  $b_b$  would represent  $\sigma_n$  and  $\sigma_s$  from column four of the matrix.

Having determined two of the four boundary conditions, they can be represented in vector form as

$$\begin{aligned} a_b \{x, t\} &= A_b \{x, t\} \text{ on the boundary } \mathcal{B} \\ b_b \{x, t\} &= B_b \{x, t\} \text{ on the boundary } \mathcal{B} \end{aligned} \quad (6.7)$$

and the Laplace transform as

$$\begin{aligned} \mathcal{L} \{a_b \{x, p\}\} &= \mathcal{L} \{A_b \{x, p\}\} \text{ on the boundary } \mathcal{B} \\ \mathcal{L} \{b_b \{x, p\}\} &= \mathcal{L} \{B_b \{x, p\}\} \text{ on the boundary } \mathcal{B} \end{aligned} \quad (6.8)$$

The equations defined in 6.5 and 6.8 define a complete set of elastic equations that can be solved using typical methods (e.g., Airy's stress function). Upon Laplace inversion, the final solution will be the viscoelastic solution for the classical correspondence

principle

### 6.1.2 Extended Correspondence Principle

For the extended correspondence, the boundary conditions become

$$\begin{aligned} a_b \{x, t\} &= A_b \{x, t\} \text{ on the boundary } \mathcal{B} \\ b_b \{x, t\} &= B_b \{x, t\} \text{ on the boundary } \mathcal{B}_1 \{t\} \\ c_b \{x, t\} &= 0 \text{ on the boundary } \mathcal{B}_2 \{t\} \end{aligned} \tag{6.9}$$

where  $\mathcal{B}_1 \{t\}$  and  $\mathcal{B}_2 \{t\}$  are the changing components of the boundary  $\mathcal{B}$ . That is, the union of  $\mathcal{B}_1 \{t\}$  and  $\mathcal{B}_2 \{t\}$  is  $\mathcal{B}$  ( $\mathcal{B}_1 \{t\} \cup \mathcal{B}_2 \{t\} = \mathcal{B}$ ). Given that the boundary conditions  $b_b$  and  $c_b$  are constantly changing, it is not possible to have a complete history of all the boundary points, meaning that the classical correspondence principle is not applicable. As before, the boundary conditions are chosen from the matrix in equation 6.6, only with an addition condition (c).

Considering a simplified problem with

$$\begin{aligned} s_{ij} \{x, t\} &= 2\mu e_{ij} \\ \sigma_{kk} \{x, t\} &= 3K_b \epsilon_{kk} \{x, t\} \end{aligned} \tag{6.10}$$

where  $\mu$  and  $K_b$  is the elastic shear and bulk moduli. Then elastic solutions for  $c$  can be found as

$$c_b^e \{x, t\} = K_P \{\mu, K_b\} C_b^e \{x, t\} \text{ on boundary } \mathcal{B} \tag{6.11}$$

where  $K_P$  is a function of the elastic shear and bulk moduli, whereas  $C_b^e$  is independent



of the elastic moduli. Taking the Laplace transform of equation 6.11 yields

$$\mathcal{L}\{c_b^e\{x, p\}\} = K_P\{\mu, K_b\} \mathcal{L}\{C_b^e\{x, p\}\} \text{ on boundary } \mathcal{B} \quad (6.12)$$

By making the substitutions

$$\begin{aligned} \mu &= \frac{p}{2} \mathcal{L}\{J_1\{p\}\} \\ K_b &= \frac{p}{3} \mathcal{L}\{J_2\{p\}\} \end{aligned} \quad (6.13)$$

results in converting the simplified problem to the full solution of equations represented in equations 6.5. This results in

$$\begin{aligned} \mathcal{L}\{c_b\{x, p\}\} &= K_P \left\{ \frac{p}{2} \mathcal{L}\{J_1\{p\}\}, \frac{p}{3} \mathcal{L}\{J_2\{p\}\} \right\} \mathcal{L}\{C_b^e\{x, p\}\} \\ c_b\{x, t\} &= J_3\{t\} C_b^e\{x, 0\} + \int_0^t J_3\{t - \tau\} \frac{\partial}{\partial \tau} C_b^e\{x, \tau\} d\tau \end{aligned} \quad (6.14)$$

with the viscoelastic modulus defined as

$$J_3\{t\} = \mathcal{L}^{-1} \left\{ \frac{1}{p} K_P \left\{ \frac{p}{2} \mathcal{L}\{J_1\{p\}\}, \frac{p}{3} \mathcal{L}\{J_2\{p\}\} \right\} \right\} \quad (6.15)$$

under the condition that  $\mathcal{B}_1\{t\}$  is a monotonically increasing function in time.

## 6.2 The Schapery Model

The work of Schapery (1975a,b,c) uses the correspondence principle (Graham, 1968) to convert the works of Westergaard (1939), Williams (1957), and Barenblatt (1962) from a purely elastic material to a viscoelastic material. The addition of the viscoelastic properties provides an explanation of observed phenomena in ice, such as delayed failure and time-dependent fracture properties, that cannot be explained with a time-

independent model.

### 6.2.1 Plane Stress and Plane Strain

For a crack, the local state of stress/strain will be approximately represented by plane strain under the following conditions:

- The crack tip is far from the surface or another crack in comparison to the process zone size,  $R_P$  (see Figure 3.13).
- The radius of curvature of the crack is much greater than  $R_P$ .
- The stress normal to the plane is small in comparison to the in-plane stress. This is the case if  $R_P$  is small in comparison to the plate thickness for a crack in an infinite plate.

These conditions will all be valid in the case that  $R_P$  is exceedingly small. For the case of a crack in a thin plate, if  $R_P$  is large in comparison to the thickness of the plate, then the crack will be under a state of plane stress.

### 6.2.2 The Process Zone

As mentioned in Section 3.2.3, the process zone is the small section of material in front of the apparent crack tip that is vastly different from the bulk of the material. Within this zone, the stress field can be quite different than the rest of the material and the viscoelastic properties of the process zone can change from the bulk material. The process zone may not be continuous as this is the section of material that is fracturing from the breaking of the atomic bonds that hold the ice together in the crystal structure.

While the process zone is a key factor in determining the fracture properties of ice, little is (or possibly - can be) known about it. While this is a shortcoming of any cohesive model, provided the zone is small, it is possible to determine the fracture properties of ice using an averaged model of the process zone, allowing the theory to gloss over the finer details of the process zone. This assumption will be validated in Section 7.1.3.

To begin the discussion of the model presented by Schapery (1975a,b,c), the distribution of the stress field in the process zone is discussed. Aside from normalizing the stress field by its maximum value, an integral that relates to the normalized stress field is formalized. These two terms appear throughout the theory and are pivotal in the discussion of viscoelastic fracture.

#### 6.2.2.1 The Process Zone Stress Distribution

Starting with the cohesive zone stress intensity definition (equation 3.80) from Barenblatt (1962). Making the following substitutions

$$\begin{aligned}\sigma_m &= \max[\sigma \{s'\}] \\ f &= \frac{\sigma \{s'\}}{\sigma_m}\end{aligned}\tag{6.16}$$

gives

$$K_I = \sqrt{\frac{2}{\pi}} \sigma_m \int_0^{R_P} \frac{f\{s'\}}{\sqrt{s'}} ds' \tag{6.17}$$

Next, the limits of integration can be normalized to the size of the process zone using the following substitutions

$$\begin{aligned}\eta &= \frac{s'}{R_P} \\ ds' &= R_P d\eta\end{aligned}\tag{6.18}$$

and changing the limits of integration

$$\begin{aligned} \text{as } s' \rightarrow 0 & \quad \text{then } \eta \rightarrow 0 \\ \text{as } s' \rightarrow R_P & \quad \text{then } \eta \rightarrow 1 \end{aligned} \tag{6.19}$$

resulting in a normalized stress intensity function

$$\begin{aligned} K_I &= \sqrt{\frac{2}{\pi}} \sigma_m \int_0^1 \frac{f\{R_P \eta\}}{\sqrt{R_P \eta}} R_P \, d\eta \\ &= \sqrt{\frac{2}{\pi}} \sigma_m \sqrt{R_P} \int_0^1 \frac{f\{R_P \eta\}}{\sqrt{\eta}} \, d\eta \\ &= \sqrt{\frac{2R_P}{\pi}} \sigma_m I_1 \end{aligned} \tag{6.20}$$

with

$$I_1 = \int_0^1 \frac{f}{\sqrt{\eta}} \, d\eta \tag{6.21}$$

with the arguments of  $f$  dropped for clarity.

$I_1$  defines the shape of the stress distribution. For a constant stress (i.e.,  $f$  is constant),  $I_1$  will have a value of 2, which is the maximum value it can attain.

### 6.2.2.2 Process Zone Size

The size of process zone can be found by rearranging equation 6.20 as

$$R_P = \frac{\pi}{2} \left( \frac{K_I}{\sigma_m I_1} \right)^2 \tag{6.22}$$

In the case that  $\sigma_m I_1$  is constant (e.g., under constant load) then the process zone is proportional to the square of the current stress intensity factor.

### 6.2.3 Elastic Crack Opening Displacement

Starting with the elastic crack opening displacements from Williams (1957) and Barenblatt (1962)

$$v = \frac{C_e}{2\pi} \int_0^{R_P} \sigma\{s'\} \left( 2\sqrt{\frac{s}{s'}} - \text{Ln} \left| \frac{\sqrt{s'} + \sqrt{s}}{\sqrt{s'} - \sqrt{s}} \right| \right) ds' \quad (6.23)$$

and assuming that the stress distribution between the process zone and the rest of the material is continuous, i.e.,

$$\sigma\{s\} = \sigma_0 + \Delta\sigma\{s\} \quad (6.24)$$

the displacement can be split into two components

$$\begin{aligned} v = & \frac{C_e}{2\pi} \int_0^{R_P} \sigma_0 \left( 2\sqrt{\frac{s}{s'}} - \text{Ln} \left| \frac{\sqrt{s'} + \sqrt{s}}{\sqrt{s'} - \sqrt{s}} \right| \right) ds' \\ & + \frac{C_e}{2\pi} \int_0^{R_P} \Delta\sigma\{s'\} \left( 2\sqrt{\frac{s}{s'}} - \text{Ln} \left| \frac{\sqrt{s'} + \sqrt{s}}{\sqrt{s'} - \sqrt{s}} \right| \right) ds' \end{aligned} \quad (6.25)$$

Using the approximation

$$\begin{aligned} \left( 2\sqrt{\frac{s}{s'}} - \text{Ln} \left| \frac{\sqrt{s'} + \sqrt{s}}{\sqrt{s'} - \sqrt{s}} \right| \right) & \approx -\frac{2}{3} \left( \frac{s}{s'} \right)^{\frac{3}{2}} - \frac{2}{5} \left( \frac{s}{s'} \right)^{\frac{5}{2}} \\ & \approx -\frac{2}{3} \left( \frac{s}{s'} \right)^{\frac{3}{2}} + \mathcal{O}\{s^{\frac{5}{2}}\} \end{aligned} \quad (6.26)$$

and subbing into the first term of equation 6.25 gives

$$\begin{aligned} v = & \frac{C_e}{2\pi} \sigma_0 \int_0^{R_P} \left( -\frac{2}{3} \left( \frac{s}{s'} \right)^{\frac{3}{2}} - \frac{2}{5} \left( \frac{s}{s'} \right)^{\frac{5}{2}} \right) ds' \\ & + \frac{C_e}{2\pi} \int_0^{R_P} \Delta\sigma\{s'\} \left( 2\sqrt{\frac{s}{s'}} - \text{Ln} \left| \frac{\sqrt{s'} + \sqrt{s}}{\sqrt{s'} - \sqrt{s}} \right| \right) ds' \end{aligned} \quad (6.27)$$

In the limit of  $s \rightarrow 0$ , higher order terms of  $s$  can be ignored leading to

$$v = -\frac{C_e}{3\pi}\sigma_0(s^{\frac{3}{2}} + \mathcal{O}\{s^{\frac{5}{2}}\}) \int_0^{R_P} (s')^{-\frac{3}{2}} ds' + \frac{C_e}{2\pi} \int_0^{R_P} \Delta\sigma\{s'\} \left( 2\sqrt{\frac{s}{s'}} - \text{Ln} \left| \frac{\sqrt{s'} + \sqrt{s}}{\sqrt{s'} - \sqrt{s}} \right| \right) ds' \quad (6.28)$$

and solving the integral of the first term

$$v = \frac{2C_e}{3\pi} \frac{\sigma_0}{\sqrt{R_P}} (s^{\frac{3}{2}} + \mathcal{O}\{s^{\frac{5}{2}}\}) + \frac{C_e}{2\pi} \int_0^{R_P} \Delta\sigma\{s'\} \left( 2\sqrt{\frac{s}{s'}} - \text{Ln} \left| \frac{\sqrt{s'} + \sqrt{s}}{\sqrt{s'} - \sqrt{s}} \right| \right) ds' \quad (6.29)$$

The second term in equation 6.29 can be split in two as

$$v = \frac{2C_e}{3\pi} \frac{\sigma_0}{\sqrt{R_P}} (s^{\frac{3}{2}} + \mathcal{O}\{s^{\frac{5}{2}}\}) - \frac{C_e}{3\pi} \int_0^{R_P} \Delta\sigma\{s'\} \left( \frac{s}{s'} \right)^{\frac{3}{2}} ds' + \frac{C_e}{2\pi} \int_0^{R_P} \Delta\sigma\{s'\} \left( 2\sqrt{\frac{s}{s'}} - \text{Ln} \left| \frac{\sqrt{s'} + \sqrt{s}}{\sqrt{s'} - \sqrt{s}} \right| + \frac{2}{3} \left( \frac{s}{s'} \right)^{\frac{3}{2}} \right) ds' \quad (6.30)$$

Applying equation 6.26 to the third term gives

$$\begin{aligned} v_{3\text{rd term}} &= \frac{C_e}{2\pi} \int_0^{R_P} \Delta\sigma\{s'\} \left( 2\sqrt{\frac{s}{s'}} - \text{Ln} \left| \frac{\sqrt{s'} + \sqrt{s}}{\sqrt{s'} - \sqrt{s}} \right| + \frac{2}{3} \left( \frac{s}{s'} \right)^{\frac{3}{2}} \right) ds \\ &= \frac{C_e}{2\pi} \int_0^{R_P} \Delta\sigma\{s'\} \left( -\frac{2}{5} \left( \frac{s}{s'} \right)^{\frac{5}{2}} \right) ds' \\ &= \mathcal{O}\{s^{\frac{5}{2}}\} \end{aligned} \quad (6.31)$$

which simplifies the the displacement as

$$v = \frac{2C_e}{3\pi} \frac{\sigma_0}{\sqrt{R_P}} s^{\frac{3}{2}} - \frac{C_e}{3\pi} s^{\frac{3}{2}} \int_0^{R_P} \Delta\sigma\{s'\} (s')^{-\frac{3}{2}} ds' + \mathcal{O}\{s^{\frac{5}{2}}\} \quad (6.32)$$

Performing integration by parts on the second term, and noting that,

$$\begin{aligned} \lim_{s \rightarrow 0} \frac{\Delta\sigma\{s\}}{\sqrt{s}} &= 0 \quad (\text{because of stress continuity}) \\ \frac{\partial\Delta\sigma\{s\}}{\partial s\{s\}} &= \frac{\partial\sigma}{\partial s} \quad (\text{from equation 6.24}) \end{aligned} \tag{6.33}$$

gives

$$\begin{aligned} v &= \frac{2C_e}{3\pi} \frac{\sigma_0}{\sqrt{R_P}} s^{\frac{3}{2}} - \frac{C_e}{3\pi} s^{\frac{3}{2}} \left( - \frac{2\Delta\sigma\{s'\}}{\sqrt{s'}} \Big|_0^{R_P} + 2 \int_0^{R_P} \frac{\partial\Delta\sigma}{\partial s'} \frac{1}{\sqrt{s'}} ds' \right) + \mathcal{O}\{s^{\frac{5}{2}}\} \\ &= \frac{2C_e}{3\pi} \frac{\sigma_0}{\sqrt{R_P}} s^{\frac{3}{2}} - \frac{2C_e}{3\pi} s^{\frac{3}{2}} \left( - \frac{\Delta\sigma\{R_P\}}{\sqrt{R_P}} + \int_0^{R_P} \frac{\partial\sigma}{\partial s'} \frac{1}{\sqrt{s'}} ds' \right) + \mathcal{O}\{s^{\frac{5}{2}}\} \end{aligned} \tag{6.34}$$

where the argument of  $\sigma\{s'\}$  inside the integral have been dropped for clarity.

Replacing  $\Delta\sigma\{R_P\}$  in equation 6.34 with equation 6.24 gives

$$\begin{aligned} v &= \frac{2C_e}{3\pi} \frac{\sigma_0}{\sqrt{R_P}} s^{\frac{3}{2}} - \frac{2C_e}{3\pi} s^{\frac{3}{2}} \left( \frac{\sigma_0 - \sigma\{R_P\}}{\sqrt{R_P}} + \int_0^{R_P} \frac{\partial\sigma}{\partial s'} \frac{1}{\sqrt{s'}} ds' \right) + \mathcal{O}\{s^{\frac{5}{2}}\} \\ &= - \frac{2C_e}{3\pi} s^{\frac{3}{2}} \left( - \frac{\sigma\{R_P\}}{\sqrt{R_P}} + \int_0^{R_P} \frac{\partial\sigma}{\partial s'} \frac{1}{\sqrt{s'}} ds' \right) + \mathcal{O}\{s^{\frac{5}{2}}\} \end{aligned} \tag{6.35}$$

For the case of a stress-free (apparent) crack surface

$$\sigma\{R_P\} = 0 \tag{6.36}$$

giving

$$v = - \frac{2C_e}{3\pi} s^{\frac{3}{2}} \int_0^{R_P} \frac{\partial\sigma}{\partial s'} \frac{1}{\sqrt{s'}} ds' + \mathcal{O}\{s^{\frac{5}{2}}\} \tag{6.37}$$

Applying the substitutions from equations 6.18 and 6.19 changes the displacement

to

$$\begin{aligned}
v &= -\frac{2C_e}{3\pi} \sigma_m s^{\frac{3}{2}} \int_0^1 \frac{1}{R_P} \frac{\partial f}{\partial \eta} \frac{1}{\sqrt{R_P \eta}} R_P d\eta + \mathcal{O}\{s^{\frac{5}{2}}\} \\
&= -\frac{2C_e}{3\pi} \frac{\sigma_m}{\sqrt{R_P}} s^{\frac{3}{2}} \int_0^1 \frac{\partial f}{\partial \eta} \frac{1}{\sqrt{\eta}} d\eta + \mathcal{O}\{s^{\frac{5}{2}}\} \\
&= -\frac{2C_e}{3\pi} \frac{\sigma_m}{\sqrt{R_P}} s^{\frac{3}{2}} I_2 + \mathcal{O}\{s^{\frac{5}{2}}\}
\end{aligned} \tag{6.38}$$

where

$$I_2 = \int_0^1 \frac{\partial f}{\partial \eta} \frac{1}{\sqrt{\eta}} d\eta \tag{6.39}$$

$I_2$  is related to the rate of change in the stress field inside the process zone. Similar to  $I_1$ , it provides a single integral that stores the details of the process zone into a much easier to manipulate form during the development of the theory. Equation 6.38 provides a simplified approximation of the crack opening displacement near the crack tip.

#### 6.2.4 Continuous Crack Growth

There are two phases of crack growth. The first phase is the intermittent phase where the material does not have a fully developed process zone. During this phase, the process zone has to grow before the apparent crack starts to grow.

Once the process zone has grown, and conditions for crack initiation have been met, the second phase begins. This phase is the continuous crack growth phase. Discussion of these two phases will begin (maybe somewhat counter-intuitively) with the continuous crack growth phase. For many constant loading tests (e.g., looking for delayed failure), this is the phase that will be the predominant phase of crack growth. Aside from its greater importance, many viscoelastic principles will be introduced that will be also needed for the intermittent crack growth.



This section breaks down the various components and terminology used in viscoelastic fracture mechanics and culminates to an equation of continuous crack growth from an initial length up to unstable failure.

#### 6.2.4.1 Viscoelastic Crack Tip Opening Displacement

According to the correspondence principle (Graham, 1968; Schapery, 1975a), the elastic solution of the opening displacement defined in equation 6.38, can be cast into a linear viscoelastic solution as

$$v = -\frac{2}{3\pi} \int_{t_1}^t C_\nu\{t - \tau\} \frac{\partial}{\partial \tau} \left\{ \frac{\sigma_m}{\sqrt{R_P}} s^{\frac{3}{2}} I_2 \right\} d\tau \quad (6.40)$$

having dropped the higher-ordered terms.

Using the substitutions

$$\rho = \tau - t_1$$

$$d\rho = d\tau \quad (6.41)$$

$$\Delta t = t - t_1$$

and applying to equation 6.40 gives

$$v = -\frac{2}{3\pi} \int_0^{\Delta t} C_\nu\{\Delta t - \rho\} \frac{\partial}{\partial \rho} \left\{ \frac{\sigma_m}{\sqrt{R_P}} s^{\frac{3}{2}} I_2 \right\} d\rho \quad (6.42)$$

Assuming that the crack growth can be approximated linearly as

$$a = a\{t_0\} + (t - t_1)\dot{a} \quad (6.43)$$

for short time scales, then  $s\{\tau\}$  can be defined as

$$s\{t\} = (\tau - t_1)\dot{a} \quad (6.44)$$

where  $\dot{a}$  is approximately constant over small time scales.

Returning to equation 6.42, and assuming that  $R_P$ ,  $\sigma_m$ , and  $I_2$  are constant, the displacement can now be written as

$$\begin{aligned} v &= -\frac{2\sigma_m I_2}{3\pi\sqrt{R_P}} \int_0^{\Delta t} C_\nu\{\Delta t - \rho\} \frac{\partial}{\partial \rho} \left\{ s^{\frac{3}{2}} \right\} d\rho \\ &= -\frac{2\sigma_m I_2}{3\pi\sqrt{R_P}} \int_0^{\Delta t} C_\nu\{\Delta t - \rho\} \dot{a}^{\frac{3}{2}} \frac{\partial}{\partial \rho} \left\{ (\tau - t_1)^{\frac{3}{2}} \right\} d\rho \end{aligned} \quad (6.45)$$

By definition

$$\dot{a} = \frac{s\{t\}}{t - t_1} = \frac{s\{t\}}{\Delta t} \quad (6.46)$$

then the displacement can be further simplified

$$\begin{aligned} v &= -\frac{2\sigma_m I_2}{3\pi\sqrt{R_P}} \int_0^{\Delta t} C_\nu\{\Delta t - \rho\} (s\{t\}(\Delta t)^{-1})^{\frac{3}{2}} \frac{\partial}{\partial \rho} \left\{ \rho^{\frac{3}{2}} \right\} d\rho \\ &= -\frac{2\sigma_m I_2}{3\pi\sqrt{R_P}} \int_0^{\Delta t} C_\nu\{\Delta t - \rho\} (s\{t\}(\Delta t)^{-1})^{\frac{3}{2}} \left( \frac{3}{2} \rho^{\frac{1}{2}} \right) d\rho \\ &= -\frac{2\sigma_m I_2}{3\pi\sqrt{R_P}} s\{t\}^{\frac{3}{2}} \left( \frac{3}{2} (\Delta t)^{-\frac{3}{2}} \int_0^{\Delta t} C_\nu\{\Delta t - \rho\} \rho^{\frac{1}{2}} d\rho \right) \\ &= -\frac{2\sigma_m I_2}{3\pi\sqrt{R_P}} s\{t\}^{\frac{3}{2}} C_{ef}\{\Delta t\} \end{aligned} \quad (6.47)$$

where the effective compliance has been defined as

$$C_{ef}\{t\} = \frac{3}{2} (t)^{-\frac{3}{2}} \int_0^t C_\nu\{t - \rho\} \rho^{\frac{1}{2}} d\rho \quad (6.48)$$

and equation 6.47 has the same form as the elastic crack opening displacement (equation 6.38), with the elastic compliance replaced by the effective compliance.

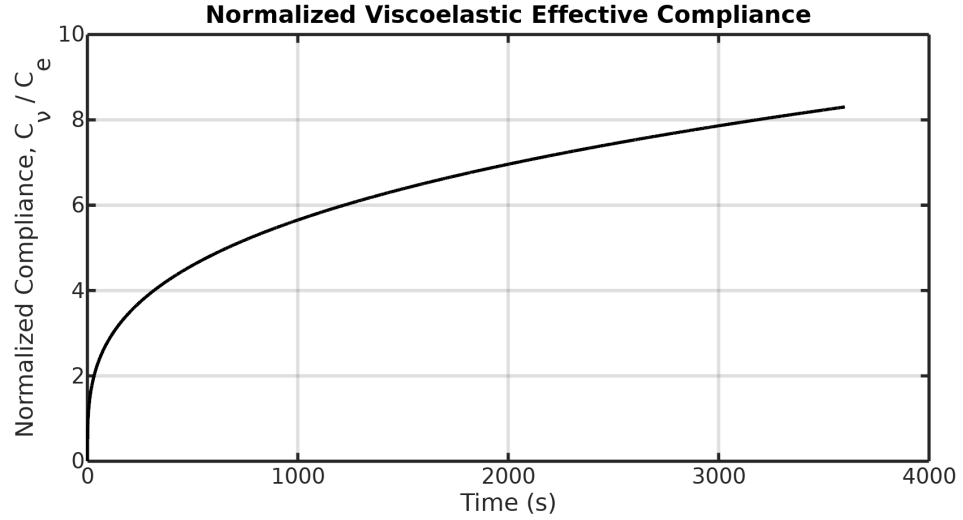


Figure 6.1: Effective Compliance Normalized by Elastic Compliance.

For illustrative purposes, consider a viscoelastic compliance of the form

$$C_\nu = C_e(1 + t^n)$$

so the elastic and viscous coefficients are the same, and  $n = 0.3$ . Figure 6.1 shows how the compliance would change over time (normalized by the elastic compliance). This would also have the same effect on the crack tip opening displacement, as seen from equation 6.47

#### 6.2.4.2 The Effective Compliance

The effective compliance, discussed in Section 6.2.4.1, defines the correspondence between the elastic and viscoelastic solutions. Provided one can derive (or compute) an elastic solution to a problem with a given stress field, then a viscoelastic solution is found by substituting the elastic compliance with the viscoelastic compliance (not accounting for crack growth).

This section will provide insights into the sensitivity of the viscoelastic solution to

the approximated elastic solution from equation 3.70. This section will result in some simplifications to the compliance that is expected to still provide reasonable results to experimental data.

#### 6.2.4.2.1 Sensitivity of Elastic Solution (The k-sensitivity)

The effective compliance can be converted to logarithmic (base 10) time using the following substitutions

$$\begin{aligned}\rho_v &= \frac{\rho}{t} \\ L &= \log\{t\} \\ l &= \log\{1 - \rho_v\} \\ dl &= \frac{-d\rho}{(t - \rho)\text{Ln}\{10\}}\end{aligned}\tag{6.49}$$

noting that  $L + l = t - \rho$  gives the logarithmic compliance ( $\hat{C}_\nu$ ) as

$$C_{ef}\{t\} = \frac{3}{2}t^{-\frac{3}{2}} \int_0^t \hat{C}_\nu\{L + l\} \rho^{\frac{1}{2}} d\rho\tag{6.50}$$

converting from  $d\rho$  to  $dl$  changes the limits of integration:

$$\begin{aligned}\text{as } \rho \rightarrow 0 & \quad \text{then } l \rightarrow 0 \\ \text{as } \rho \rightarrow t & \quad \text{then } l \rightarrow -\infty\end{aligned}\tag{6.51}$$

$$C_{ef}\{t\} = \frac{3}{2}t^{-\frac{3}{2}} \int_0^{-\infty} -\hat{C}_\nu\{L + l\} \rho^{\frac{1}{2}} (t - \rho) \text{Ln}\{10\} dl$$

where Ln is the natural log (base e). Flipping the limits of integration, bringing the  $\text{Ln}\{10\}$  outside the integral, and the  $t^{-\frac{3}{2}}$  inside gives

$$C_{ef}\{t\} = \frac{3}{2}\text{Ln}\{10\} \int_{-\infty}^0 \hat{C}_\nu\{L + l\} \frac{\rho^{\frac{1}{2}}}{t^{\frac{1}{2}}} \frac{(t - \rho)}{t} dl\tag{6.52}$$

from equation 6.49

$$10^l = 1 - \rho_v = \frac{t - \rho}{t} \quad (6.53)$$

giving the effective compliance as

$$C_{ef}\{t\} = \frac{3}{2} \text{Ln}\{10\} \int_{-\infty}^0 \hat{C}_\nu\{L + l\} w_{\frac{3}{2}} \, dl \quad (6.54)$$

with a weighting function defined as

$$w_{\frac{3}{2}} = 10^l (1 - 10^l)^{\frac{1}{2}} \quad (6.55)$$

The analysis of displacements so far have focused on a one-term solution (in much the same way that the Westergaard (1939) solution is the first-term approximation of Williams (1957)). Had the analysis included multiple terms (of the form of equation 3.70), i.e

$$v = \sum_k A_k s^k C_{ef}^{(k)}\{\Delta t\} \quad (6.56)$$

where  $C_{ef}^{(k)}$  is the k-th effective compliance (not a power of k), and is given by

$$C_{ef}^{(k)} = k t^{-k} \int_0^t C_\nu\{t - \rho\} \rho^{k-1} \, d\rho \quad (6.57)$$

Similar to before

$$\begin{aligned} C_{ef}^{(k)} &= k t^{-k} \int_0^t \hat{C}_\nu\{L + l\} \rho^{k-1} \, d\rho \\ C_{ef}^{(k)} &= k t^{-k} \int_{-\infty}^0 \hat{C}_\nu\{L + l\} \rho^{k-1} (t - \rho) \text{Ln}\{10\} \, dl \\ C_{ef}^{(k)} &= k \text{Ln}\{10\} \int_{-\infty}^0 \hat{C}_\nu\{L + l\} \frac{\rho^{k-1}}{t^{k-1}} \frac{(t - \rho)}{t} \, dl \\ C_{ef}^{(k)} &= k \text{Ln}\{10\} \int_{-\infty}^0 \hat{C}_\nu\{L + l\} (1 - 10^l)^{k-1} 10^l \, dl \end{aligned} \quad (6.58)$$

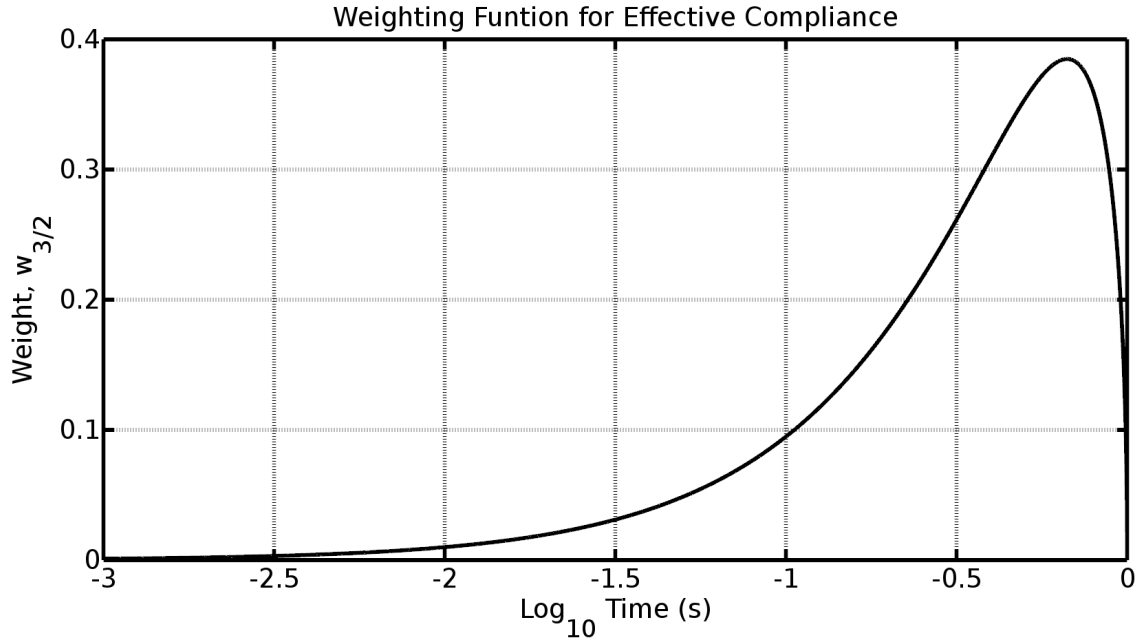


Figure 6.2: First-term effective compliance weighting function

which can be recast as

$$C_{ef}^{(k)} = \frac{3}{2} \text{Ln}\{10\} \int_{-\infty}^0 \hat{C}_\nu\{L+l\} \frac{2}{3} k (1-10^l)^{k-1} 10^l \, dl \quad (6.59)$$

giving the k-th weighting function as

$$w_k = \frac{2}{3} k 10^l (1-10^l)^{k-1} \quad (6.60)$$

Figure 6.2 shows the first-term weighting function,  $w_{\frac{3}{2}}$ , plotted from present time to 1000 seconds in the past. From the figure it can be seen that the weighting function (and by extension, the first-term effective compliance) is only significant during the past 1.2 decades (roughly 15 seconds).

Figure 6.3 shows how the weighting function,  $w_k$  changes with different values of k. As k is increased, the weighting function begins to spread out. By 15–30 seconds, the weighting functions have decreased considerably in value. Given that

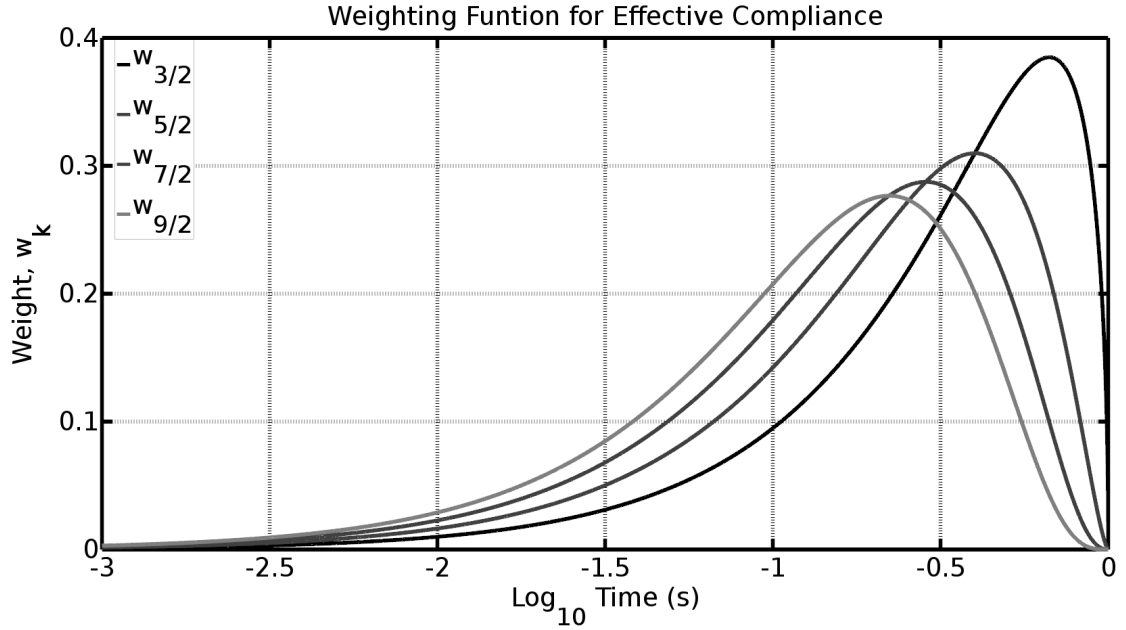


Figure 6.3: Sensitivity of the weighting function,  $w_k$ , to  $k$

the majority of the materials displacement is captured in the first term and that successive displacement terms will affect the resultant displacement in less significant amounts, it is reasonable to approximate the effective compliance of each term by using only the  $w_{\frac{3}{2}}$  weighting function to simplify the analysis.

#### 6.2.4.2.2 Approximation of the Effective Compliance

Schapery (1975b) assumes that the creep compliance,  $C_\nu$ , can be approximated by

$$C_\nu = C_1 t^n \quad (6.61)$$

where the primary and secondary creep components are combined into a single term (which will be validated in Section 7.1.2). Substituting equation 6.61 into equation 6.57 gives

$$C_{ef}^{(k)} = k t^{-k} \int_0^t C_1 (t - \rho)^n \rho^{k-1} d\rho \quad (6.62)$$

and integrating gives

$$\begin{aligned} C_{ef}^{(k)} &= kt^{-k} \left( C_1 \frac{\Gamma\{k\}\Gamma\{n+1\}}{\Gamma\{k+n+1\}} t^{k+n} \right) \\ &= C_1 t^n \left( \frac{k}{n+k} \right) \left( \frac{\Gamma\{k\}\Gamma\{n+1\}}{\Gamma\{k+n\}} \right) \end{aligned} \quad (6.63)$$

Setting

$$\ell_{nk} = \left( \frac{k}{n+k} \right) \left( \frac{\Gamma\{k\}\Gamma\{n+1\}}{\Gamma\{k+n\}} \right) \quad (6.64)$$

and the effective compliance can be written as

$$\begin{aligned} C_{ef}^{(k)} &= \ell_{nk} C_1 t^n \\ &= C_\nu \{ \ell_{nk}^{\frac{1}{n}} t \} \end{aligned} \quad (6.65)$$

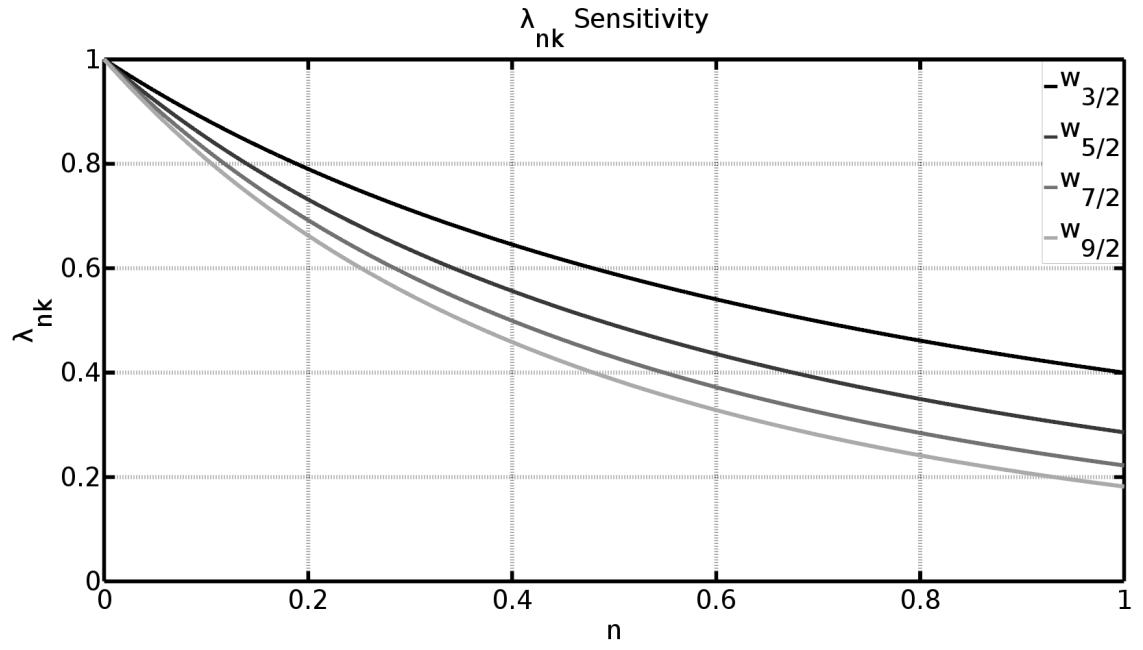
Figure 6.4 shows how  $\ell_{nk}$  and  $\ell_{nk}^{\frac{1}{n}}$  varies over  $n$  for different values of  $k$ . For most materials, including ice, the values of  $n$  are around  $n = 0.3$  or less. For values of  $n$  around 0.3,  $\ell_{nk}$  is relatively insensitive to the value of  $k$ . As expected,  $\ell_{nk}^{\frac{1}{n}}$  is also relatively insensitive to  $k$ . For values of  $n \approx 0.3$ ,  $\ell_{nk}^{\frac{1}{n}}$  can be set to a constant.

Given the relative insensitivity to  $k$ , the effective compliance can be approximated by using only the first-term compliance ( $k = 3/2$ ). Subbing  $k = 3/2$  into equations 6.64 and 6.65 gives the effective compliance as

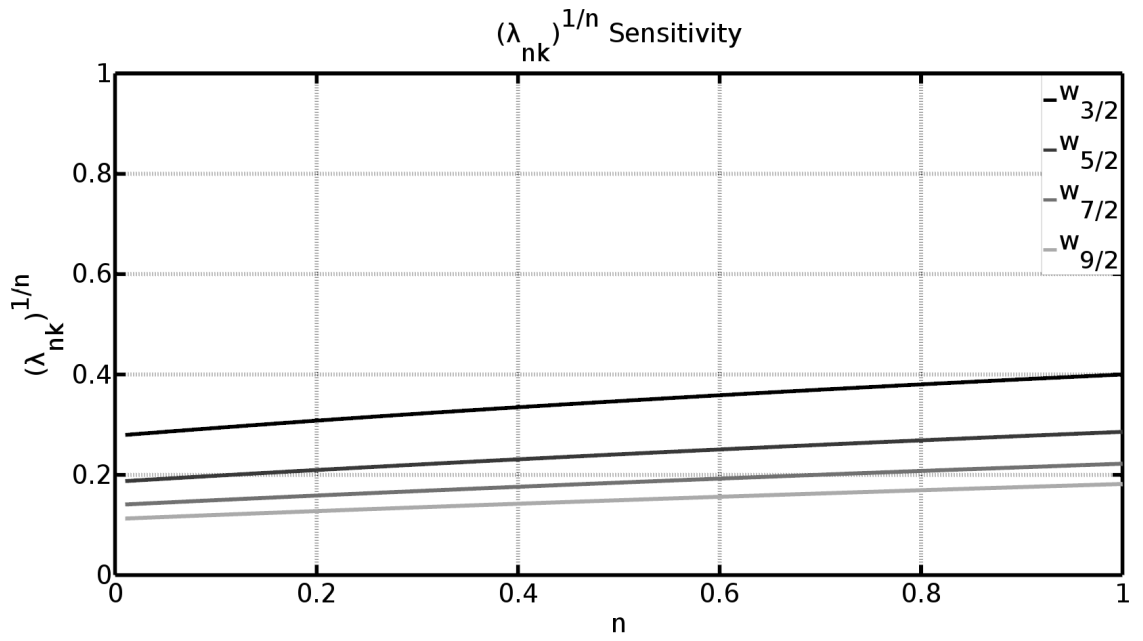
$$\begin{aligned} C_{ef} &= C_\nu \{ \ell_n^{\frac{1}{n}} t \} \\ \ell_n &= \left( \frac{3}{2(n + \frac{3}{2})} \right) \left( \frac{\Gamma\{\frac{3}{2}\}\Gamma\{n+1\}}{\Gamma\{n + \frac{3}{2}\}} \right) \\ &= \left( \frac{3\sqrt{\pi}}{4(n + \frac{3}{2})} \right) \left( \frac{\Gamma\{n+1\}}{\Gamma\{n + \frac{3}{2}\}} \right) \end{aligned} \quad (6.66)$$

where the removal of the  $k$  sub- and super-scripts implies  $k = 3/2$ . For values of  $n$





(a)



(b)

Figure 6.4: Sensitivity of  $\ell_{nk}$  and  $\ell_{nk}^{\frac{1}{n}}$  to  $k$ .

associated with ice,  $\ell_n^{\frac{1}{n}} \approx 0.3$  from Figure 6.4b.

### 6.2.4.3 Fracture Energy

#### 6.2.4.3.1 Definition

As a material is loaded, stress and strain will build up near the crack tip, due to processes such as dislocation glide and grain boundary sliding that cause viscoelastic effects. The amount of force on the process zone would be

$$F_{RP} = \sigma_f dA \quad (6.67)$$

where  $dA$  is the area defined by the height of the process zone along an element length  $ds$  and along the width of the crack,  $\ell_c$  (i.e.,  $dA = \ell_c ds$ ). Thus the work done on the process zone is

$$W_f = \int_0^{v_m} (\sigma_f dA) dv \quad (6.68)$$

Assuming that  $dA = \Delta A$  is approximately constant over the process zone, then the work done per area, known as the fracture energy, is defined as

$$\Gamma_G = \frac{W_f}{\Delta A} = \int_0^{v_m} \sigma_f dv \quad (6.69)$$

If the crack opening displacement is a function of time (as it would be for a viscoelastic material), then the fracture energy is also defined as

$$\Gamma_G = \int_{t_1}^{t_2} \sigma_f \frac{\partial v}{\partial t} dt \quad (6.70)$$

where  $v = 0$  at  $t_1$  and  $v = v_m$  at  $t_2$ .

Equivalently, noting that  $s\{t\} = a\{t\} - x$ , the fracture energy can be expressed as

$$\Gamma_G = \int_0^{R_P} \sigma_f \frac{\partial v}{\partial s'} ds' \quad (6.71)$$

The viscoelastic approximation for the crack opening displacement can now be given by replacing the elastic compliance from equation 6.23 with the effective compliance from equation 6.66 to give

$$v = \frac{C_\nu \{\ell_n^{\frac{1}{n}} t\}}{2\pi} \int_0^{R_P} \sigma\{s'\} \left( 2\sqrt{\frac{s}{s'}} - \text{Ln} \left| \frac{\sqrt{s'} + \sqrt{s}}{\sqrt{s'} - \sqrt{s}} \right| \right) ds' \quad (6.72)$$

Two periods of time can be considered: the time it takes the crack to grow some distance  $s < R_P$ , and the time it takes the crack to grow the length of the process zone. These would be

$$\begin{aligned} t_s &= \frac{s}{\dot{a}} \\ t_R &= \frac{R_P}{\dot{a}} \end{aligned} \quad (6.73)$$

respectively. Combining with the  $\ell_n^{\frac{1}{n}}$  gives

$$\begin{aligned} \tilde{t}_s &= \ell_n^{\frac{1}{n}} \frac{s}{\dot{a}} \\ \tilde{t}_R &= \ell_n^{\frac{1}{n}} \frac{R_P}{\dot{a}} \end{aligned} \quad (6.74)$$

With these time definitions, two displacements can be defined as

$$\begin{aligned} v &= \frac{C_\nu \{\tilde{t}_s\}}{2\pi} \int_0^{R_P} \sigma\{s'\} \left( 2\sqrt{\frac{s}{s'}} - \text{Ln} \left| \frac{\sqrt{s'} + \sqrt{s}}{\sqrt{s'} - \sqrt{s}} \right| \right) ds' \\ v_R &= \frac{C_\nu \{\tilde{t}_R\}}{2\pi} \int_0^{R_P} \sigma\{s'\} \left( 2\sqrt{\frac{s}{s'}} - \text{Ln} \left| \frac{\sqrt{s'} + \sqrt{s}}{\sqrt{s'} - \sqrt{s}} \right| \right) ds' \end{aligned} \quad (6.75)$$

Equation 6.71 can be separated into two terms

$$\begin{aligned}
 \Gamma_G &= \int_0^{R_P} \sigma_f\{s'\} \frac{\partial v}{\partial s'} ds' \\
 &= \int_0^{R_P} \sigma_f\{s'\} \frac{\partial v_R}{\partial s'} ds' + \int_0^{R_P} \sigma_f\{s'\} \frac{\partial(v - v_R)}{\partial s'} ds' \\
 &= \Gamma_A + \Gamma_B
 \end{aligned} \tag{6.76}$$

which defines two parts of the total fracture energy.

#### 6.2.4.3.2 Fracture Energy Term, $\Gamma_A$

The first term of the total fracture energy,  $\Gamma_A$ , can be rearranged by integration by parts

$$\begin{aligned}
 \Gamma_A &= \int_0^{R_P} \sigma_f\{s'\} \frac{\partial v_R}{\partial s'} ds' \\
 &= \sigma_f\{s'\} v_R \Big|_0^{R_P} - \int_0^{R_P} \frac{\partial \sigma\{s'\}}{\partial s'} v_R ds' \\
 &= - \int_0^{R_P} \frac{\partial \sigma\{s'\}}{\partial s'} v_R ds'
 \end{aligned} \tag{6.77}$$

where the first term is zero since

$$\begin{aligned}
 \sigma_f\{R_P\} &= 0 \\
 v_R\{0\} &= 0
 \end{aligned} \tag{6.78}$$

#### 6.2.4.3.3 Fracture Energy Term, $\Gamma_B$

From equation 6.75

$$v - v_R = \left( \frac{C_\nu\{\tilde{t}_s\}}{C_\nu\{\tilde{t}_R\}} - 1 \right) v_R \tag{6.79}$$

and

$$\Gamma_B = \int_0^{R_P} \sigma_f\{s'\} \frac{\partial}{\partial s'} \left\{ \left( \frac{C_\nu\{\tilde{t}_s\}}{C_\nu\{\tilde{t}_R\}} - 1 \right) v_R \right\} ds' \tag{6.80}$$

Using integration by parts with

$$\begin{aligned} u &= \sigma_f\{s'\} & du &= \frac{\partial \sigma\{s'\}}{\partial s'} ds' \\ v &= \left( \frac{C_\nu\{\tilde{t}_s\}}{C_\nu\{\tilde{t}_R\}} - 1 \right) v_R & dv &= \frac{\partial}{\partial s'} \left\{ \left( \frac{C_\nu\{\tilde{t}_s\}}{C_\nu\{\tilde{t}_R\}} - 1 \right) v_R \right\} ds' \end{aligned} \quad (6.81)$$

gives

$$\begin{aligned} \Gamma_B &= \sigma_f\{s'\} \left( \frac{C_\nu\{\tilde{t}_s\}}{C_\nu\{\tilde{t}_R\}} - 1 \right) v_R \Big|_0^{R_P} - \int_0^{R_P} \frac{\partial \sigma_f\{s'\}}{\partial s'} \left( \frac{C_\nu\{\tilde{t}_s\}}{C_\nu\{\tilde{t}_R\}} - 1 \right) v_R ds' \\ &= - \int_0^{R_P} \frac{\partial \sigma_f\{s'\}}{\partial s'} \left( \frac{C_\nu\{\tilde{t}_s\}}{C_\nu\{\tilde{t}_R\}} - 1 \right) v_R ds' \end{aligned} \quad (6.82)$$

#### 6.2.4.3.4 Comparison of $\Gamma_A$ and $\Gamma_B$

Using a one-term solution from equation 6.56

$$v \approx A_{\frac{3}{2}} s^{\frac{3}{2}} C_\nu\{\tilde{t}_s\} \quad (6.83)$$

$$v\{R_P\} \approx A_{\frac{3}{2}} R_P^{\frac{3}{2}} C_\nu\{\tilde{t}_R\} \quad (6.84)$$

gives a normalized displacement for  $v_R$  as

$$\begin{aligned} v_N &= \frac{v_R}{v\{R_P\}} = \frac{A_{\frac{3}{2}} s^{\frac{3}{2}} C_\nu\{\tilde{t}_R\}}{A_{\frac{3}{2}} R_P^{\frac{3}{2}} C_\nu\{\tilde{t}_R\}} \\ &= \left( \frac{s}{R_P} \right)^{\frac{3}{2}} = \eta^{\frac{3}{2}} \end{aligned} \quad (6.85)$$

also the ratio of the compliances in  $\Gamma_B$  is

$$\frac{C_\nu\{\tilde{t}_s\}}{C_\nu\{\tilde{t}_R\}} = \frac{\tilde{t}_s}{\tilde{t}_R} = \left( \frac{s}{R_P} \right)^n = \eta^n \quad (6.86)$$

having used equations 6.18, 6.61, and 6.74.

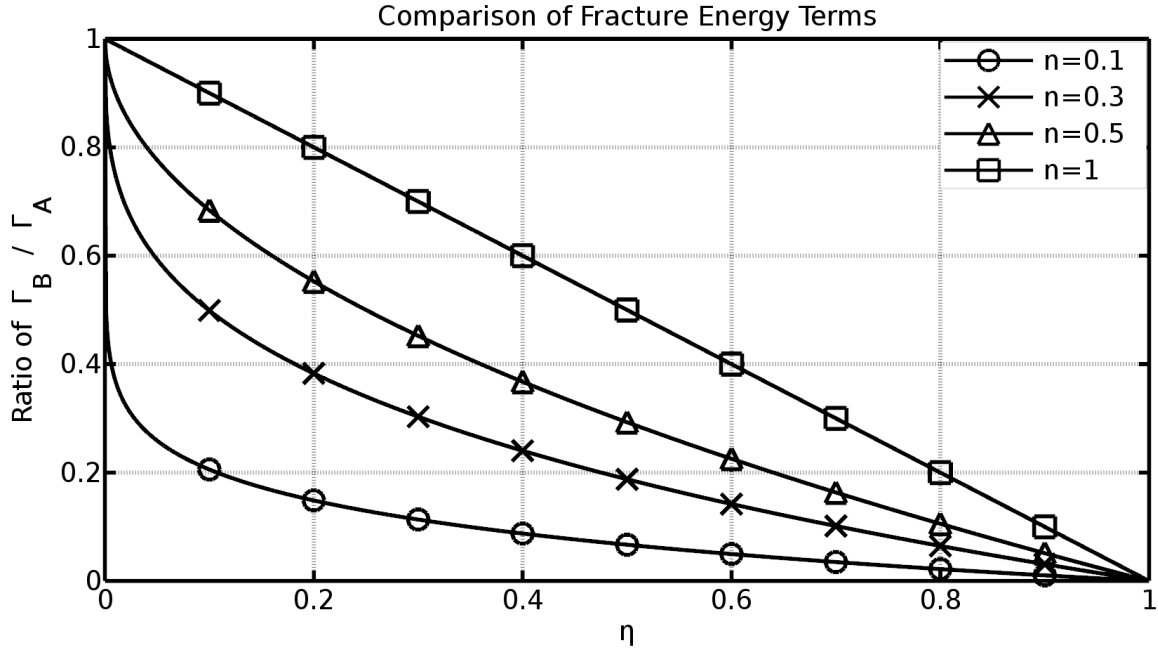


Figure 6.5: Figure showing the relationship between  $\Gamma_A$  and  $\Gamma_B$ , normalized by the size of the process zone,  $R_P$ .

From equation 6.82 and 6.86

$$\begin{aligned}
 \Gamma_B &\propto - \left( \frac{C_\nu \{\tilde{t}_s\}}{C_\nu \{\tilde{t}_R\}} - 1 \right) v_R \\
 &= - (\eta^n - 1) \eta^{\frac{3}{2}} v \{R_P\} \\
 &= (1 - \eta^n) \eta^{\frac{3}{2}} v \{R_P\}
 \end{aligned} \tag{6.87}$$

Likewise, substitution of equation 6.84 into equation 6.77 shows that

$$\Gamma_A \propto -v_R = \eta^{\frac{3}{2}} v \{R_P\} \tag{6.88}$$

The ratio of the two terms energy terms of  $\Gamma_G$  as

$$\left| \frac{\Gamma_B}{\Gamma_A} \right| = 1 - \eta^n \tag{6.89}$$

Figure 6.5 shows the relation of  $\Gamma_A$  and  $\Gamma_B$  (equation 6.89). From the figure, it is seen that  $\Gamma_A \gg \Gamma_B$  as long as the failure stress is not acting primarily in the region of  $\eta = 0$  (near the actual crack tip).

#### 6.2.4.3.5 Defining Fracture Energy in Terms of Stress Intensity

Up to now, the fracture energy has been discussed in terms of the local, and unknown, stress field in the process zone. This section relates the fracture energy to the stress intensity factor. This is an important step since it relates the unknown properties of the model (the process zone stress) to properties that can be measured or calculated by the engineer.

From the previous section

$$\Gamma_G \approx \Gamma_A = \int_0^{R_P} \sigma_f\{s'\} \frac{\partial v_R\{s\}}{\partial s'} ds' \quad (6.90)$$

substituting in equation 6.72 (setting  $t = t_R$  from equation 6.73) gives

$$\begin{aligned} \Gamma_G &= \int_0^{R_P} \sigma_f\{s'\} \frac{\partial}{\partial s'} \left[ \frac{C_\nu\{\tilde{t}_R\}}{2\pi} \int_0^{R_P} \sigma_f\{s\} \left( 2\sqrt{\frac{s}{s'}} - \text{Ln} \left| \frac{\sqrt{s'} + \sqrt{s}}{\sqrt{s'} - \sqrt{s}} \right| \right) ds \right] ds' \\ &= \frac{C_\nu\{\tilde{t}_R\}}{2\pi} \int_0^{R_P} \sigma_f\{s'\} \int_0^{R_P} \sigma_f\{s\} \frac{\partial}{\partial s'} \left( 2\sqrt{\frac{s}{s'}} - \text{Ln} \left| \frac{\sqrt{s'} + \sqrt{s}}{\sqrt{s'} - \sqrt{s}} \right| \right) ds ds' \end{aligned} \quad (6.91)$$

Performing the derivation in the integrand

$$\begin{aligned}
 F\{s, s'\} &= \frac{\partial}{\partial s'} \left( 2\sqrt{\frac{s}{s'}} - \text{Ln} \left| \frac{\sqrt{s'} + \sqrt{s}}{\sqrt{s'} - \sqrt{s}} \right| \right) \\
 &= \left( \frac{1}{s' \sqrt{\frac{s}{s'}}} - \frac{\left( \frac{\sqrt{s} + \sqrt{s'}}{2\sqrt{s}(\sqrt{s'} - \sqrt{s})^2} + \frac{1}{2\sqrt{s}(\sqrt{s'} - \sqrt{s})} \right) (\sqrt{s'} - \sqrt{s})}{\sqrt{s} + \sqrt{s'}} \right) \\
 &= \sqrt{\frac{s}{s'}} \left( \frac{1}{s - s'} \right)
 \end{aligned} \tag{6.92}$$

and returning to equation 6.91 with equation 6.92 yields

$$\begin{aligned}
 \Gamma_G &= \frac{C_\nu\{\tilde{t}_R\}}{2\pi} \int_0^{R_P} \sigma_f\{s'\} \int_0^{R_P} \sigma_f\{s\} \sqrt{\frac{s}{s'}} \left( \frac{1}{s - s'} \right) ds ds' \\
 &= \frac{C_\nu\{\tilde{t}_R\}}{2\pi} \int_0^{R_P} \frac{\sigma_f\{s'\}}{\sqrt{s'}} \int_0^{R_P} \frac{\sigma_f\{s\}}{\sqrt{s}} \left( \frac{s}{s - s'} \right) ds ds'
 \end{aligned} \tag{6.93}$$

Making the substitution

$$\frac{s}{s - s'} = \frac{1}{2} + \frac{1}{2} \left( \frac{s + s'}{s - s'} \right) \tag{6.94}$$

results in

$$\begin{aligned}
 \Gamma_G &= \frac{C_\nu\{\tilde{t}_R\}}{4\pi} \int_0^{R_P} \frac{\sigma_f\{s'\}}{\sqrt{s'}} ds' \int_0^{R_P} \frac{\sigma_f\{s\}}{\sqrt{s}} ds \\
 &\quad + \frac{C_\nu\{\tilde{t}_R\}}{2\pi} \int_0^{R_P} \int_0^{R_P} \frac{\sigma_f\{s'\}}{\sqrt{s'}} \frac{\sigma_f\{s\}}{\sqrt{s}} \left( \frac{s + s'}{s - s'} \right) ds ds' \\
 &= \frac{C_\nu\{\tilde{t}_R\}}{4\pi} \int_0^{R_P} \frac{\sigma_f\{s'\}}{\sqrt{s'}} ds' \int_0^{R_P} \frac{\sigma_f\{s\}}{\sqrt{s}} ds + \Gamma_Z
 \end{aligned} \tag{6.95}$$

with

$$\Gamma_Z = \frac{C_\nu\{\tilde{t}_R\}}{2\pi} \int_0^{R_P} \int_0^{R_P} \frac{\sigma_f\{s'\}}{\sqrt{s'}} \frac{\sigma_f\{s\}}{\sqrt{s}} \left( \frac{s + s'}{s - s'} \right) ds ds' \tag{6.96}$$



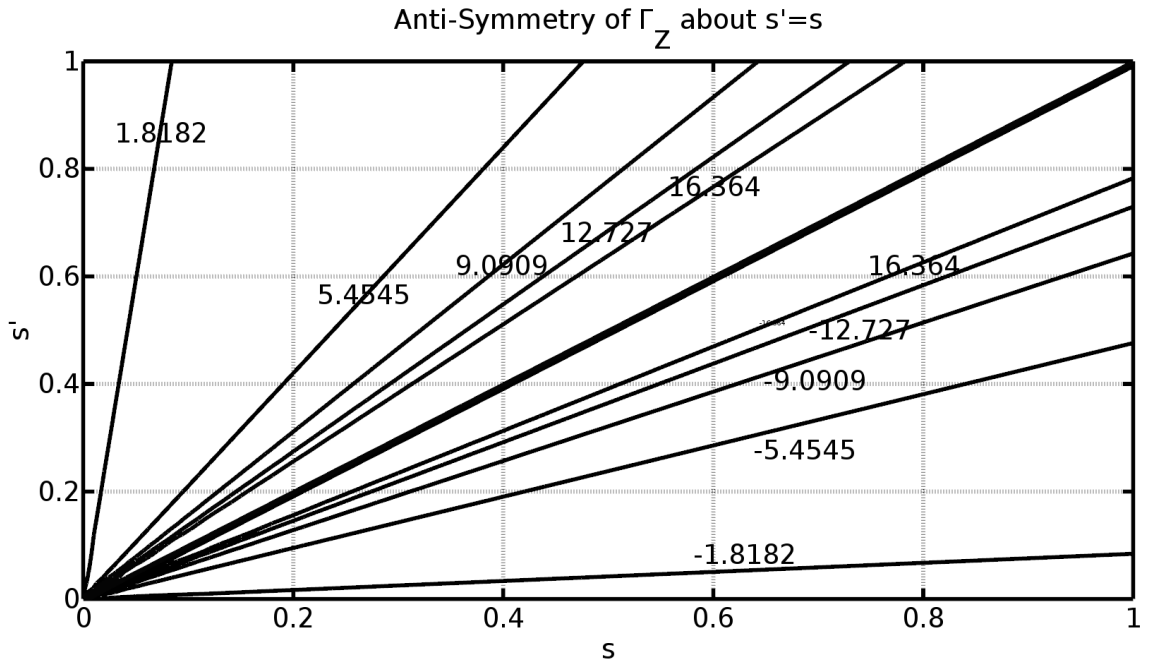


Figure 6.6: Contour plot showing anti-symmetry of  $\frac{s+s'}{s-s'}$  over the process zone.

Figure 6.6 shows a contour plot of

$$F\{s, s'\} = \frac{s + s'}{s - s'} \quad (6.97)$$

from Figure 6.6, the contour plot shows that the function is anti-symmetric about the  $s = s'$  line. Values near the line approach  $\pm\infty$  and taper off to zero when off the centre line. This anti-symmetry can also be seen as

$$\begin{aligned} F\{s', s\} &= \frac{s' + s}{s' - s} \\ &= \frac{s + s'}{(-1)(s - s')} = -F\{s, s'\} \end{aligned} \quad (6.98)$$

since the integrand of  $\Gamma_Z$  is antisymmetric over the process zone (i.e., the limits of integration), then

$$\Gamma_Z = 0 \quad (6.99)$$

and

$$\Gamma_G = \frac{C_\nu\{\tilde{t}_R\}}{4\pi} \left( \int_0^{R_P} \frac{\sigma_f\{s'\}}{\sqrt{s'}} ds' \right) \left( \int_0^{R_P} \frac{\sigma_f\{s\}}{\sqrt{s}} ds \right) \quad (6.100)$$

Using the definition of stress intensity (equation 3.80) into equation 6.100 results in a relationship between the stress intensity and the fracture energy given by

$$\begin{aligned} \Gamma_G &= \frac{C_\nu\{\tilde{t}_R\}}{4\pi} \left( \sqrt{\frac{\pi}{2}} K_I \right) \left( \sqrt{\frac{\pi}{2}} K_I \right) \\ &= \frac{C_\nu\{\tilde{t}_R\}}{8} K_I^2 \end{aligned} \quad (6.101)$$

#### 6.2.4.4 Crack Growth

Under continuous crack growth, the process zone is fully developed. This does not mean it is of a constant size as it will grow with increasing stress intensity, but the zone growth is small so that the apparent crack grows at the same time. During this phase the crack will grow due to the local stress causing the atoms in the ice lattice to break apart, forming the new surfaces of the extended crack. From the previous sections, the crack expands by a distance of  $R_P$  over a time interval of  $t_R$ . Starting with the definition of creep compliance, and using the definitions of fracture energy and effective compliance, an equation for stable continuous crack growth can be formulated.

Expanding the compliance term to include the elastic component, i.e.,

$$C_\nu\{t\} = C_0 + C_1 t^n \quad (6.102)$$

will have no effect on the previous analysis with an addition of a constant elastic component to the displacement terms. Since the displacement in the definition of fracture energy (equation 6.76) takes the spatial derivative of  $v$  (and likewise  $v_R$ ),

then the fracture energy analysis is unchanged since the constant term is dropped. This means equation 6.101 is correct whether the elastic compliance is included or not.

Subbing equation 6.102 into 6.101, and solving for  $\dot{a}$

$$\Gamma_G = \frac{C_0 + C_1 t_R^n}{8} K_I^2 \quad (6.103)$$

and using equation 6.73

$$\begin{aligned} \Gamma_G &= 8^{-1} \left( C_0 + C_1 (\ell_n^{\frac{1}{n}} R_P \dot{a}^{-1})^n \right) K_I^2 \\ 8\Gamma_G K_I^{-2} &= C_0 + C_1 \ell_n R_P^n \dot{a}^{-n} \\ \dot{a}^{-n} &= (8\Gamma_G K_I^{-2} - C_0) (C_1 \ell_n R_P^n)^{-1} \\ \dot{a} &= (8\Gamma_G K_I^{-2} - C_0)^{\frac{-1}{n}} (C_1 \ell_n R_P^n)^{\frac{1}{n}} \\ \dot{a} &= \left( \frac{C_1 K_I^2}{8\Gamma_G - C_0 K_I^2} \right)^{\frac{1}{n}} \ell_n^{\frac{1}{n}} R_P \end{aligned} \quad (6.104)$$

Noting that

$$\dot{a} = \frac{\partial a}{\partial t} \quad (6.105)$$

and defining the fracture toughness (critical stress intensity) as

$$K_G = \sqrt{\frac{C_0}{8\Gamma_G}} \quad (6.106)$$

gives the crack growth rate,

$$\frac{\partial a}{\partial t} = \left( \frac{C_1 K_I^2}{8\Gamma_G \left[ 1 - \left( \frac{K_I}{K_G} \right)^2 \right]} \right)^{\frac{1}{n}} \ell_n^{\frac{1}{n}} R_P \quad (6.107)$$

under constant loading. Applying equation 6.22 expands equation 6.107 to

$$\frac{\partial a}{\partial t} = \frac{\pi}{2} \left( \frac{C_1 K_I^2}{8\Gamma_G \left[ 1 - \left( \frac{K_I}{K_G} \right)^2 \right]} \right)^{\frac{1}{n}} \ell_n^{\frac{1}{n}} \left( \frac{K_I}{\sigma_m I_1} \right)^2 \quad (6.108)$$

#### 6.2.4.5 Time to Failure

For the case of constant loading and assuming self-similar crack growth (i.e., the process zone stress profile always looks the same except translated along the material as the crack grows), then

$$\sigma_m I_1 = \text{Constant} \quad (6.109)$$

In general, the fracture energy,  $\Gamma_G$ , may possibly be a function of loading rate or crack growth rate, but for a constant applied load, it is reasonable to approximate the fracture energy as a constant. By extension, the fracture toughness will also be constant, as seen from equation 6.106.

Using the definition of the stress intensity

$$\begin{aligned} K_I &= Y\{a\} \sigma \sqrt{\pi a} \\ \left( \frac{K_I}{K_G} \right)^2 &= \frac{Y\{a\}^2 \pi a \sigma^2 C_0}{8\Gamma} = \frac{Y\{a\}^2 a}{a_G} \end{aligned} \quad (6.110)$$

where

$$a_G = \frac{8\Gamma}{\pi C_0 \sigma^2} \quad (6.111)$$

and  $Y\{a\}$  is the geometric shape function as a function of crack length. Substituting

back into equation 6.108 yields

$$\frac{da}{dt} = \left(\frac{\pi}{2}\right) \left(\frac{C_1 Y\{a\}^2 \pi a \sigma^2}{8\Gamma \left(1 - Y\{a\}^2 \frac{a}{a_G}\right)}\right)^{\frac{1}{m}} \ell_m^{\frac{1}{m}} \frac{Y\{a\}^2 \pi a \sigma^2}{\sigma_m^2 I_1^2} \quad (6.112)$$

Separation of variables in equation 6.112 leads to

$$(a_G)^{\frac{1}{m}} \left(\frac{1 - Y\{a\}^2 \frac{a}{a_G}}{Y\{a\}^{2(1+\frac{1}{m})} a^{m+1}}\right)^{\frac{1}{m}} da = \left(\frac{\pi^2}{2}\right) \left(\frac{C_1}{C_0}\right)^{\frac{1}{m}} \ell_m^{\frac{1}{m}} \frac{\sigma^2}{\sigma_m^2 I_1^2} dt \quad (6.113)$$

and integrated from the initial ( $a_0$ ) to current ( $a$ ) crack size and from 0 to current time,  $t$

$$\int_{a_0}^a \left(\frac{a_G}{a}\right)^{\frac{1}{m}} \left(\frac{1 - Y\{a\}^2 \frac{a}{a_G}}{Y\{a\}^{2(1+\frac{1}{m})}}\right)^{\frac{1}{m}} \frac{da}{a} = \left(\frac{\pi^2}{2}\right) \left(\frac{C_1}{C_0}\right)^{\frac{1}{m}} \ell_m^{\frac{1}{m}} \int_0^t \frac{\sigma^2}{\sigma_m^2 I_1^2} dt \quad (6.114)$$

making the substitutions  $\gamma = \frac{a}{a_0}$ ,  $d\gamma = \frac{da}{a_0}$ , and  $\frac{d\gamma}{\gamma} = \frac{da}{a}$  gives

$$\int_1^{\frac{a}{a_0}} \left(\frac{\frac{a_G}{a_0\gamma} - Y[a_0\gamma]^2}{Y[a_0\gamma]^{2(1+\frac{1}{m})}}\right)^{\frac{1}{m}} \frac{d\gamma}{\gamma} = \left(\frac{\pi^2}{2}\right) \left(\frac{C_1}{C_0}\right)^{\frac{1}{m}} \ell_m^{\frac{1}{m}} \frac{\sigma^2}{\sigma_m^2 I_1^2} t \quad (6.115)$$

which reduces to the form of Schapery(1975c) when  $Y\{a\} = 1$  for a central crack in an infinite, thin plate.

From equation 6.112, it can be seen that for an infinite, thin plate, the specimen will fail when the crack size reaches the critical crack size (when  $a = a_G$ ). Recasting the limits from equation 6.114

$$\int_{a_0}^{a_G} \left(\frac{a_G}{a}\right)^{\frac{1}{m}} \left(1 - \frac{a}{a_G}\right)^{\frac{1}{m}} \frac{da}{a} = \left(\frac{\pi^2}{2}\right) \left(\frac{C_1}{C_0}\right)^{\frac{1}{m}} \ell_m^{\frac{1}{m}} \int_0^{t_f} \frac{\sigma^2}{\sigma_m^2 I_1^2} dt \quad (6.116)$$

and using the substitutions  $u = \frac{a}{a_G}$  and  $du = \frac{da}{a_G}$  gives

$$\int_{\frac{a_0}{a_G}}^1 \left(\frac{1}{u}\right)^{1+\frac{1}{m}} (1-u)^{\frac{1}{m}} du = \left(\frac{\pi^2}{2}\right) \left(\frac{C_1}{C_0}\right)^{\frac{1}{m}} \ell_m^{\frac{1}{m}} \frac{\sigma^2}{\sigma_m^2 I_1^2} t_f \quad (6.117)$$

where  $t_f$  is the time to failure.

### 6.2.5 Intermittent Crack Growth

The previous section is for a crack that is under continuous crack growth with a fully developed process zone (i.e.,  $R_P$  is constant over time). Under discontinuous loading, this would not particularly hold. For the experiments performed during this project, this is not a concern as the tests either underwent ramp up to failure or held at a constant load. However, assuming the ice is undamaged (aside from the pre-notched crack, of course), then the ice may start without an initial process zone. This means that for the crack to grow, a process zone would have to grow. During this time, the growth of the crack is completely due to the process zone growth. This means that until the process zone is fully developed, the apparent crack does not grow (unless an unstable failure occurs, of course).

#### 6.2.5.1 Crack Opening Displacement

To begin the study of intermittent/initial crack growth, it is best to consider the crack opening width. Starting with the non-simplified displacement

$$v = \frac{1}{2\pi} \int_0^t C_\nu\{t - \tau\} \frac{\partial}{\partial \tau} \left\{ \int_0^{R_P} \sigma_f\{s'\} \left( 2\sqrt{\frac{s}{s'}} - \text{Ln} \left| \frac{\sqrt{s'} + \sqrt{s}}{\sqrt{s'} - \sqrt{s}} \right| ds' \right) \right\} d\tau \quad (6.118)$$

By definition

$$s = a\{t\} - x = R_P\{t\} - 0 \quad (6.119)$$

by setting  $x = 0$  and noting that the crack growth is simply the growth of the process zone initially.

Substituting equation 6.119 into 6.118 gives

$$v = \frac{1}{2\pi} \int_0^t C_\nu\{t - \tau\} \frac{\partial}{\partial \tau} \left\{ \int_0^{R_P} \sigma_f\{s'\} \left( 2\sqrt{\frac{R_P}{s'}} - \text{Ln} \left| \frac{\sqrt{s'} + \sqrt{R_P}}{\sqrt{s'} - \sqrt{R_P}} \right| ds' \right) \right\} d\tau \quad (6.120)$$

Using the following definitions

$$\begin{aligned} u &= \frac{s'}{R_P} \\ ds' &= R_P du \\ \text{Ln} \left| \frac{\sqrt{u} + 1}{\sqrt{u} - 1} \right| &= \text{Ln} \frac{1 + \sqrt{u}}{1 - \sqrt{u}} \end{aligned} \quad (6.121)$$

where the last is true since  $u \leq 1$ , and the limits change

$$\begin{aligned} \text{as } s' \rightarrow 0 \quad u &\rightarrow 0 \\ \text{as } s' \rightarrow R_P \quad u &\rightarrow 1 \end{aligned} \quad (6.122)$$

For a constant process zone stress ( $\sigma_f = \sigma_m$ ), the displacement becomes

$$\begin{aligned} v &= \frac{1}{2\pi} \int_0^t C_\nu\{t - \tau\} \frac{\partial}{\partial \tau} \left\{ \sigma_m R_P \int_0^1 2\sqrt{\frac{1}{u}} - \text{Ln} \frac{1 + \sqrt{u}}{1 - \sqrt{u}} du \right\} d\tau \\ &= \frac{1}{2\pi} \int_0^t C_\nu\{t - \tau\} \frac{\partial}{\partial \tau} \{2\sigma_m R_P\} d\tau \end{aligned} \quad (6.123)$$

Using the definition of the process zone size from equation 6.22, the displacement

becomes

$$\begin{aligned}
 v &= \frac{1}{2\pi} \int_0^t C_\nu\{t-\tau\} \frac{\partial}{\partial\tau} \left\{ 2\sigma_m \left( \frac{\pi}{2} \left( \frac{K_I}{\sigma_m I_1} \right)^2 \right) \right\} d\tau \\
 &= \frac{1}{8\sigma_m} \int_0^t C_\nu\{t-\tau\} \frac{\partial K_I^2}{\partial\tau} d\tau \\
 &= \frac{K_I^2}{8\sigma_m} \int_0^t K_I^{-2} C_\nu\{t-\tau\} \frac{\partial K_I^2}{\partial\tau} d\tau
 \end{aligned} \tag{6.124}$$

where the  $K_I^2$  and  $K_I^{-2}$  are added for reasons that will become evident when discussing the fracture energy.

### 6.2.5.2 Fracture Energy

#### 6.2.5.2.1 Constant Process Zone Stress

Fracture energy is also defined as

$$\Gamma_G = \int_0^{v_m} \sigma_f dv \tag{6.125}$$

where  $v_m$  is the crack opening displacement at failure. For constant process zone stress, and using equation 6.124, this becomes

$$\begin{aligned}
 \Gamma_G &= \sigma_m v_m \\
 &= \frac{K_I^2}{8} \int_0^t K_I^{-2} C_\nu\{t-\tau\} \frac{\partial K_I^2}{\partial\tau} d\tau
 \end{aligned} \tag{6.126}$$

Defining the secant compliance as

$$C_s = \int_0^t K_I^{-2} C_\nu\{t-\tau\} \frac{\partial K_I^2}{\partial\tau} d\tau \tag{6.127}$$

gives the fracture energy as

$$\Gamma_G = \frac{1}{8} K_I^2 C_s\{t\} \tag{6.128}$$



which has a similar form to the continuous crack growth case.

### 6.2.5.2.2 Time-varying Process Zone Stress

As mentioned, during the initial growth of the process zone, the stress inside the zone may not be necessarily constant but may vary over time (such as increasing under increasing applied load).

Consider the approximate crack opening displacement near the crack tip, given by

$$v = -\frac{2}{3\pi} \int_0^{t_i} C_\nu \{t - \tau\} \frac{\partial}{\partial \tau} \left\{ \sigma_m I_2 s^{\frac{3}{2}} R_P^{-\frac{1}{2}} \right\} d\tau \quad (6.129)$$

Multiplying the term inside the braces by  $K_I^2/K_I^2$  results in

$$\begin{aligned} v &= -\frac{2}{3\pi} \int_0^{t_i} C_\nu \{t - \tau\} \frac{\partial}{\partial \tau} \left\{ K_I^2 \frac{\pi \sigma_m I_2 s^{\frac{3}{2}} R_P^{-\frac{1}{2}}}{2 \sigma_m^2 I_1^2 R_P} \right\} d\tau \\ &= -\frac{1}{3} \int_0^{t_i} C_\nu \{t - \tau\} \frac{\partial}{\partial \tau} \left\{ K_I^2 \left( \frac{I_2}{I_1^2} \right) \left( \frac{s}{R_P} \right)^{\frac{3}{2}} \sigma_m^{-1} \right\} d\tau \end{aligned} \quad (6.130)$$

where  $\sigma_m = \sigma_m \{\tau\}$ .

Using equation 6.125, the fracture energy for time-varying  $\sigma_m$  is now

$$\Gamma_G = \int_0^{v_m} \sigma_f dv = \int_0^1 \sigma_f v_m d\rho \quad (6.131)$$

after making the substitution  $\rho = v/v_m$ .

Substituting equation 6.130 in to the above gives

$$\begin{aligned} \Gamma_G &= -\frac{1}{3} \int_0^1 \sigma_f \int_0^{t_i} C_\nu \{t - \tau\} \frac{\partial}{\partial \tau} \left\{ K_I^2 \left( \frac{I_2}{I_1^2} \right) \left( \frac{s}{R_P} \right)^{\frac{3}{2}} \sigma_m^{-1} \right\} d\tau d\rho \\ &= -\frac{1}{3} K_I^2 \int_0^1 \sigma_f \int_0^{t_i} K_I^{-2} C_\nu \{t - \tau\} \frac{\partial}{\partial \tau} \left\{ K_I^2 \left( \frac{I_2}{I_1^2} \right) \left( \frac{s}{R_P} \right)^{\frac{3}{2}} \sigma_m^{-1} \right\} d\tau d\rho \end{aligned} \quad (6.132)$$

Since  $K_I$ ,  $\sigma_f$ , and  $C_\nu\{t\}$  are not dependent on  $v$  (or by extension,  $\rho$ ), the integrals can be switched to give

$$\Gamma_G = -\frac{1}{3}K_I^2 \int_0^{t_i} K_I^{-2} C_\nu\{t - \tau\} \frac{\partial}{\partial \tau} \left\{ \int_0^1 K_I^2 \left( \frac{I_2}{I_1^2} \right) \left( \frac{s}{R_P} \right)^{\frac{3}{2}} \frac{\sigma_f}{\sigma_m} d\rho \right\} d\tau \quad (6.133)$$

From equation 6.130, it can be seen that  $v$  is proportional to  $s^{\frac{3}{2}}$  and  $v_m$  is proportional to  $R_P^{\frac{3}{2}}$ , Thus

$$\begin{aligned} \left( \frac{s}{R_P} \right)^{\frac{3}{2}} &\rightarrow \frac{v}{v_m} = \rho \\ \frac{\sigma_f v}{\sigma_m v_m} &\rightarrow F\{\rho\} \end{aligned} \quad (6.134)$$

resulting in the fracture energy as

$$\Gamma_G = -\frac{1}{3}K_I^2 \int_0^{t_i} K_I^{-2} C_\nu\{t - \tau\} \frac{\partial}{\partial \tau} \left\{ \int_0^1 K_I^2 \left( \frac{I_2}{I_1^2} \right) F\{\rho\} d\rho \right\} d\tau \quad (6.135)$$

Defining  $R\{\rho\}$  as

$$R\{\rho\} = -\frac{8}{3} \left( \frac{I_2}{I_1^2} \right) \int_0^1 F\{\rho\} d\rho \quad (6.136)$$

and rewriting the fracture energy as

$$\begin{aligned} \Gamma_G &= \frac{1}{8}K_I^2 \int_0^{t_i} K_I^{-2} C_\nu\{t - \tau\} \frac{\partial}{\partial \tau} \{K_I^2 R\{\rho\}\} d\tau \\ &= \frac{R\{\rho\}}{8} K_I^2 \int_0^{t_i} K_I^{-2} C_\nu\{t - \tau\} \frac{\partial}{\partial \tau} \{K_I^2\} d\tau \\ &= \frac{R\{\rho\}}{8} K_I^2 C_s\{t\} \end{aligned} \quad (6.137)$$

which has a similar form to the constant stress state, but is multiplied by  $R\{\rho\}$ .

### 6.2.5.3 More on the Secant Compliance

The secant compliance is the compliance of the material during the growth of the process zone to its full size. For a monotonic growth in stress intensity, the secant compliance will always be less than or equal to the creep compliance, i.e.,

$$C_s\{t\} \leq C_\nu\{t\} \quad (6.138)$$

For the case of a power-law growth in stress intensity, denoted by

$$K_I = At^j \quad (6.139)$$

the secant compliance becomes

$$\begin{aligned} C_s &= \int_0^t K_I^{-2} C_\nu\{t - \tau\} \frac{\partial K_I^2}{\partial \tau} d\tau \\ &= \int_0^t (At^j)^{-2} C_\nu\{t - \tau\} \frac{\partial (At^j)^2}{\partial \tau} d\tau \\ &= 2kt^{-2j} C_1 \int_0^{t_i} (t - \tau)^n \tau^{2j-1} d\tau \end{aligned} \quad (6.140)$$

Similar to before, this can be solved to give

$$C_s\{t\} = \ell_{nl} C_1 t^n = C_\nu\{\ell_{nl}^{\frac{1}{n}} t\} \quad (6.141)$$

$$\ell_{nl} = \frac{l}{n+l} \frac{\Gamma\{l\}\Gamma\{n\}}{\Gamma\{n+l\}} \quad (6.142)$$

where  $l = 2j$ .

## 6.3 Nonlinear Viscoelastic Fracture Mechanics

While it is beyond the scope of this thesis, a brief mention of nonlinear viscoelastic fracture mechanics is warranted. The nonlinear theory is an other expansion of the linear viscoelastic theory of Schapery (1975a,b,c). While this theory is quite complex, it borrows a lot of terminology and concepts from the linear theory. Aside from the new geometries and loading scenarios that this project will add to viscoelastic fracture theory, the nonlinear theory is the next important theory that needs to be developed in providing better estimations of ice loads during an interaction.

As mentioned in Section 3.1.4, when a crack grows it releases energy. This energy loss relieves the material of built up stresses. Crack growth is governed by two things related to strain energy. Crack growth initiation occurs when there is a build up of strain energy that ductile processes (e.g., grain boundary sliding and dislocation glide) can no longer relieve which will be related to fracture toughness. Secondly, the path the crack grows in will determine its strain energy release rate (SERR). Often cracks will grow in the direction of maximum SERR (Zou et al., 1996; Taylor, 2010) if the SERR of the crack is greater than the build up from the loads, the crack will grow until the build up of energy is gone, otherwise, the crack will grow to a free surface (i.e, spalling event). Given the importance of the SERR, it becomes important to consider how the energy builds up in the process zone.

Assuming the process zone is small, then it is not important to perfectly model the nonlinear effects in this regime. For fracture mechanics, it is sufficient to only know how the energy is being stored and released as the crack grows, as mentioned. To do this, the energy release rate of crack growth is calculated using the J-Integral.

The original work by Rice (1968) considered a 2-D crack in an elastoplastic mate-

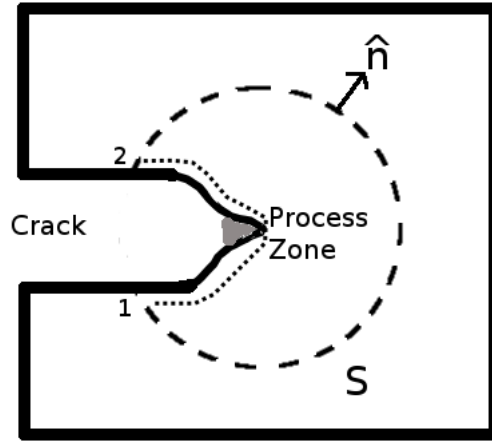


Figure 6.7: The J-integral is defined by a contour around the process zone. The contour has to be inside the material and contain no cracks, so that continuum mechanics applies within the contour.

rial. In this paper, Rice defines the integral

$$d_{Rice} = \int_S \left[ (U \, dy - T_i \frac{\partial u_i}{\partial x_1}) \right] ds \quad (6.143)$$

which is surrounded by the contour,  $S$ , that runs counter-clockwise along the surface of the crack and process zone and clockwise around the loop. The theory considers the Piola stresses and displacements  $\sigma_{ij}^R$  and  $u_i^R$ .  $U$  is the strain energy and  $T_i$  is the traction along the contour given by

$$U = \int_0^{\epsilon_{ij}} \sigma_{ij}^R \, d\epsilon_{ij}^R \quad (6.144)$$

$$T_i^R = \sigma_{ij}^R \hat{n}_j$$

Provided that the contour is within the material and contains no cracks, then continuum mechanics applies within the material. By applying Green's Theorem, Rice (1968) shows that this integral is equal to zero.

The work done by Schapery (1981, 1984a, 1990), modified the Rice's original equations, using the correspondence principle, to provide solutions for viscoelastic materials, based on the solutions for a purely (hyper)elastic material

Using the correspondence principle, Schapery starts with the stresses and strains from the reference elastic solution (i.e., the same stresses and strains used in Rice's theory for an elastoplastic material), which follow the equilibrium equations

$$\frac{\partial \sigma_{ij}^R}{\partial x_j} + F_i^R = 0 \quad (6.145)$$

with body forces  $F_I^R$ . There exists potential functions such that

$$\begin{aligned} \sigma_{ij}^R &= \frac{\partial U}{\partial u_{i,j}^R} \\ F_i^R &= -\frac{\partial U_F}{\partial u_i} \end{aligned} \quad (6.146)$$

where  $U$  would be the strain energy, rewritten here as

$$U = \int_0^{\partial_j u_i^R} \sigma_{ij}^R d\partial_j u_i^R \quad (6.147)$$

and the strain is given by

$$\epsilon_{ij}^R = \frac{1}{2} (\partial_j u_i^R + \partial_i u_j^R + \partial_i u_k^R \partial_j u_k^R) \quad (6.148)$$

By multiplying eqn. 6.145 by  $\partial u_i^R / \partial x_1$ , integrating over the volume, and using the divergence theorem gives

$$d = \int_S [(U + U_F)n_1 - T_i^R \partial_{x_1} u_i^R] ds = 0 \quad (6.149)$$

One form of the J-integral is found by integrating over the part of the contour that

surrounds the crack going counter-clockwise from point 1 to point 2 (where  $dx_2 = 0$ )

$$J_F = \int_o^\alpha \tau_i^R \partial_\xi \Delta u_i^R d\xi \quad (6.150)$$

where  $\xi$  goes from the crack tip out to the failure zone,  $\tau_i$  is the stress (i=2 is normal, i=1,3 are shear stresses), and  $\Delta u$  is the separation between to points that were once together (i.e., the crack opening).

If we consider the rest of the contour going from point 2 clockwise around the continuum material to point 1, then we get

$$\begin{aligned} J_V &= \int_{C_1} [(U + U_F) dx_2 - T_i^R \partial_{x_1} u_i^R dL] \\ J_V &= \frac{1}{L_3} \int_{S_1} [(U + U_F) \hat{n}_1 - T_i^R \partial_{x_1} u_i^R] ds \end{aligned} \quad (6.151)$$

where  $C_1$  is the contour going from point 2 to point 1,  $L_3$  is the thickness of the crack face in the  $x_3$ -direction, and  $S_1$  is the surface that includes  $C_1$ .

Invoking the theory of virtual work, multiplying the equilibrium equations by  $\delta u_i^R$  and integrating over a volume surrounding the crack tip (e.g., with the surface  $S_1$  from above) gives

$$\begin{aligned} \int_V \partial_j \sigma_{ij}^R \delta u_i^R dv + \int_V F_i^R \delta u_i^R dV &= 0 \\ \int_V \nabla \cdot \{ \sigma_{ij}^R \delta u_i^R \} dv - \int_V \sigma_{ij}^R \partial_j \delta u_i^R - \int_V \Phi_F dV &= 0 \end{aligned} \quad (6.152)$$

and using the divergence theorem on the first integral gives

$$\begin{aligned} \int_S (\sigma_{ij}^R \delta u_i^R) \hat{n}_j dS &= \int_V (\Phi + \Phi_F) dv \\ \int_S (T_{ij}^R \delta u_i^R) dS &= \int_V (\Phi + \Phi_F) dv \end{aligned} \quad (6.153)$$

to which the virtual work done as the crack grows is defined as

$$\begin{aligned} W_V^R &= \int_S T_i^R \delta u_i^R \, ds = \int_S [T_i^R \partial_\xi \delta u_i^R \partial_a \xi + \partial_a \delta u_i^R] \delta a \, ds \\ W_V &= -L_3 \delta a \int_0^{\alpha+\delta a} \tau_i^R \partial_\xi \Delta u_i^R \, d\xi = -L_3 \delta a J_F \end{aligned} \quad (6.154)$$

Using the definition of virtual work, the time to crack growth initiation can be found relating the surface energy (plus any viscous effects) to the work done

$$2\Gamma_G = W_V \quad (6.155)$$

to solve for the time that the virtual energy reaches the critical energy of  $2\Gamma_G$ .

When the crack is growing ( $\dot{a} > 0$ ), the virtual work can be defined as

$$W_V = \int_0^\alpha \tau_i \partial_\xi \Delta u_i \, d\xi \quad (6.156)$$

Assuming that  $\alpha$  and  $\dot{a}$  are constant over time steps of  $\alpha/\dot{a}$ ,  $\tau_i$  and  $\Delta u_i$  are independent of  $x_1$ , but not  $\xi$  (self-similar crack growth), and  $D\{t - \tau, t\}$  is unaffected by aging, then the approximation

$$\Delta u_i \approx E_R D\{\tilde{t}, t\} \Delta U_i^R \quad (6.157)$$

can be made, where  $\tilde{t} = k\xi/\dot{a}$ , and  $k \approx 1/3$ . The virtual work can then be approximated by

$$W_V = E_R D\{\tilde{t}_\alpha, t\} \int_0^\alpha \tau_i \partial_\xi \Delta u_i^R \, d\xi \quad (6.158)$$

where  $\tilde{t}_\alpha = k\alpha/\dot{a}$ . From which the crack speed,  $\dot{a}$ , can be found

$$2\Gamma_G = E_R D\{\tilde{t}_\alpha, t\} J_v \quad (6.159)$$



## 6.4 Continuous Crack Growth

The theories of fracture mechanics, including the viscoelastic theory of Schapery (1975a,b,c), consider a crack in an infinite plate under uniaxial loading. This setup is useful in describing and understanding fracture mechanics because it simplifies the mathematics (such as the geometric shape function being equal to 1). Many authors also consider uniaxial creep tests for the same reason of simplifying the mathematics around the applied stress (a step function, but essentially a constant) and its derivatives (zero, aside from the start of the applied load).

The model proposed below expands beyond these limitations without giving rise to overly complicated mathematics that could be prohibitive to implement or too computationally demanding for modern computers. This model will be discussed for the case of 4-point beam bending but can be easily modified to work for other geometries.

The underlying assumptions of the linear viscoelastic model of Schapery will be discussed and validated in Section 7.1 (e.g., a small process zone is required), but will be assumed valid for this chapter. This chapter's discussion can now be focused on developing a new model by modifying the original model of Schapery (1975a,b,c).

In maintaining consistency with Section 6.2, discussion of the model will begin with the continuous crack growth portion of the model. While the model will begin with the intermittent equations, the continuous growth portion will play the bigger role of the model simulation under constant load and ramp loading.

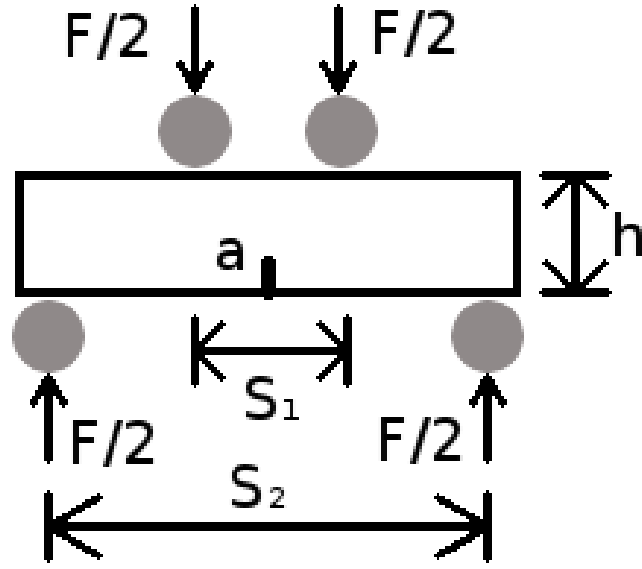


Figure 6.8: Schematic of 4-Point Bending Specimen showing geometry definitions. Depth of the beam into the page is denoted by  $d$ .

#### 6.4.1 Fracture Toughness and Stress Intensity

Starting with Schapery(1975b) formula for crack growth

$$\frac{da}{dt} = \left(\frac{\pi}{2}\right) \left(\frac{C_1}{8\Gamma_G \left(1 - \frac{K_I^2}{K_G^2}\right)}\right)^{\frac{1}{n}} \frac{\ell_n^{\frac{1}{n}} K_I^{2(1+\frac{1}{n})}}{\sigma_m^2 I_1^2} \quad (6.160)$$

This can be written in the form

$$\frac{da}{dt} = \left(\frac{\pi}{2}\right) \left(\frac{C_1 K_I^2}{8\Gamma_G \left(1 - \frac{K_I^2}{K_G^2}\right)}\right)^{\frac{1}{n}} \ell_n^{\frac{1}{n}} \frac{K_I^2}{\sigma_m^2 I_1^2} \quad (6.161)$$

where

$$K_G = \left(\frac{8\Gamma_G}{C_0}\right)^{\frac{1}{2}} \quad (6.162)$$

$$C_0 = \frac{4(1 - \nu^2)}{E} \quad (6.163)$$

as defined in Schapery (1975a,b,c) and  $C_0$  is the elastic compliance under plane strain conditions that would be present near a crack tip. For the case of a pre-notched beam under 4-point bending, the stress intensity is defined as

$$K_I = \left( Y\{a\} \left( \frac{\sqrt{\alpha}}{(1-\alpha)^{\frac{3}{2}}} \right) \right) \frac{3F(S_2 - S_1)}{2dh^{\frac{3}{2}}} \quad (6.164)$$

where the geometric shape function is given by

$$Y\{\alpha\} = 1.9887 - 1.326\alpha - \frac{(3.49 - 0.68\alpha + 1.35\alpha^2)\alpha(1-\alpha)}{(1+\alpha)^2} \quad (6.165)$$

with  $\alpha = a/h$  (Strecker et al., 2005).

### 6.4.2 Process Zone and Crack growth

From Schapery (1975a,b,c), the size of process zone can be approximated as

$$R_p = \frac{\pi}{2} \left( \frac{K_I}{\sigma_m I_1} \right)^2 \quad (6.166)$$

where  $I_1$  defines the stress profile in the process zone.

This can be used in equation 6.161 as

$$\frac{da}{dt} = \left( \frac{C_1 K_I^2}{8\Gamma_G \left( 1 - \frac{K_I^2}{K_G^2} \right)} \right)^{\frac{1}{n}} \ell_n^{\frac{1}{n}} R_P \quad (6.167)$$

or as

$$\frac{da}{dt} = \left( \frac{C_1 K_I^2}{(8\Gamma_G - C_0 K_I^2)} \right)^{\frac{1}{n}} \ell_n^{\frac{1}{n}} R_P \quad (6.168)$$

which masks the unstably that occurs at  $K_I = K_G$ , but shows the dependence on the elastic compliance (equation 6.167 is the version used in the model).

### 6.4.3 Failure Energy and the Process Zone Stress Field

The remaining aspect of the model relates to parameters  $\Gamma_G$ ,  $\sigma_m$ , and  $I_1$ . Due to the unknown nature of the process zone, these parameters are harder (if not impossible) to determine. This section attempts to provide some thoughts on what may be happening inside the zone but is in no way definitive (merely a speculation on the author's part).

$\Gamma_G$  is related to the bonding of the atoms. It can stand to reason that this should be a constant for a constant temperature, as the bonds between atoms/molecules will have a constant bonding energy that would be also affected by temperature.

$\sigma_m$  is the maximum stress found in the process zone. During the initial phase when the process zone is forming, this parameter will change from zero to a maximum. On physical grounds, for a constant temperature  $\sigma_m$  should match the theoretical stress required to break the bonds between atoms and molecules once the crack begins to propagate (as the apparent crack tip advances).

$I_1$  is the area under the shape of the normalized stress curve, but may be simply thought as a way to define the curve (for understanding purposes). The maximum value that  $I_1$  can have is 2, which is achieved for a constant process zone stress field (like a plastic zone of yielding).

The process zone stress is a function of the applied load and the underlying motion of the grains and dislocations, as these act to relieve stress. The ability for grain sliding and dislocation glide will be made easier under higher stress due to the increased energy available. However, these processes require time for them to activate.

Should the grains and dislocations have time to move, the stress field in the process zone should change. The initially high stressed area should decrease, but stress should increase in other areas where the grains and dislocations become stuck. This would have the effect of spreading out the stress field. For constant loading tests that have last a considerable amount of time, the process zone should have a relatively constant

stress field as the grains and dislocations have time to shift around. Thus  $I_1$  should be equal (or nearly so) to 2.

Under faster loading conditions (like the ramp up to failure experiments), the grains and dislocations may not have enough time to shift around. This means that the highest stressed area will be unable to alleviate this stress. This will cause the process zone stress field to be less uniform, meaning that  $I_1 < 2$  (possibly much less than 2).

From elastic considerations, one may expect the highest stress to be near the apparent crack tip (near the mouth). This may not be the case as the process zone may be discontinuous and have other stress concentrations, but it provides a good starting point for discussion. Assuming the process zone is continuous, then one would expect the highest stresses to be near the apparent crack tip and would decrease exponentially further away (in a  $1/\sqrt{r}$  manner from the LEFM theory).

Under slow loading rates (or constant load), the process zone stress is a constant as previously stated. Under fast loading rates, the stress field should be high around the apparent crack tip, but quickly drop off as the stress is unable to be relieved. For medium loading rates, the stress can spread out more than the fast loading test but may be less spread out than the slow loading rates. This results in a trend that

$$\begin{aligned} \text{as } \dot{F} \rightarrow 0 \quad I_1 &\rightarrow 2 \\ \text{as } \dot{F} \rightarrow \infty \quad I_1 &\rightarrow 0 \end{aligned} \tag{6.169}$$

For illustrative purposes, using an exponential decreasing function to describe the process zone stress gives insights into the value of  $I_1$ . Consider the following

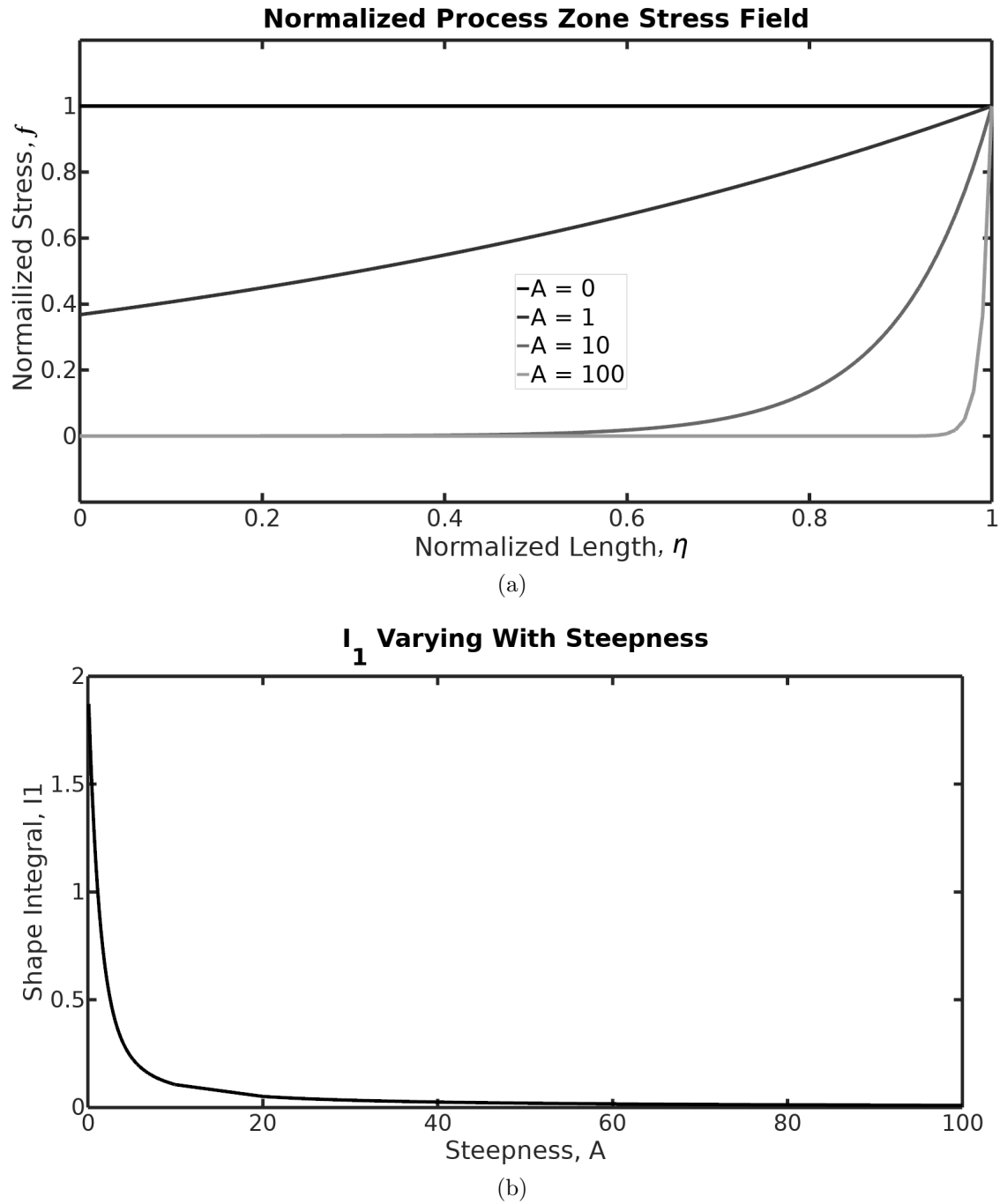


Figure 6.9: a) Exponentially decreasing normalized process zone stress fields with different steepness parameter,  $A$ . b) The value of the  $I_1$  for varying steepness parameter

normalized stress field

$$f = \exp \{-A(1 - \eta)\}$$

$$I_1 = 2 \frac{D_F \{\sqrt{A}\}}{\sqrt{A}} \quad (6.170)$$

where  $A$  defines the steepness of the decay,  $\eta$  is the normalized distance (apparent crack tip at 1, actual crack tip at 0), and  $D_F$  is the Dawson Function defined as

$$D_F \{x\} = \exp \{-x^2\} \int_0^x \exp \{y^2\} dy$$

$$= -i \frac{\pi}{2} \exp \{-x^2\} \operatorname{erf} \{xi\} \quad (6.171)$$

where  $i = \sqrt{-1}$  and the Error Function is defined as

$$\operatorname{erf} \{x\} = \frac{2}{\sqrt{\pi}} \int_0^x \exp \{t^{-2}\} dt \quad (6.172)$$

Figure 6.9a shows various stress fields for different values of the steepness parameter in equation 6.170. For  $A = 0$ , the stress field is constant and becomes more sharply defined for larger  $A$ . One can think of  $A$  being a function of loading rate and that  $A = 0$  for constant loading and increases as the loading rate increases.

Figure 6.170b shows how this hypothetical  $I_1$  varies with  $A$ . As  $A \rightarrow 0$  (slow loading) then  $I_1 \rightarrow 2$  as expected. Under fast loading, the stress field is more concentrated near the apparent crack tip and  $I_1$  tends to zero. The curve in Figure 6.9b suggests that  $I_1$  has an exponential decreasing relationship with  $A$  and possibly with the loading rate, as suggested from Figure 5.4.

Stated briefly, the model will assume that the fracture energy and the maximum process zone are constants (at least for constant temperature) and  $I_1$  will be a function of loading rate. While it may be more prudent to lump these variables as one, there

is no evidence to suggest that the model will be improved by this change. One should also consider that the three variables do not always appear in all equations (such as equation 6.166), and would pose issues for the model.

## 6.5 Intermittent Crack Growth

The model is assumed to start with no process zone, such that the process zone has to grow as suggested in Section 6.2.5. During the initial phase, the length of the crack is simply the initial crack length plus the current length of the process zone defined in equation 6.166.

### 6.5.1 Secant Compliance

Having calculated the stress intensity from equation 6.164 and using equation 7.1, the secant compliance is calculated using

$$C_s = \int_0^t K_I^{-2} C_\nu \{t - \tau\} \frac{\partial K_I^2}{\partial \tau} d\tau \quad (6.173)$$

which is a hereditary integral that requires integration at every time step until failure initiation into the continuous crack growth phase.

### 6.5.2 Fracture Initiation

Continuous crack growth begins once the initial phase ends (i.e., there is a fully-developed process zone). This is determined by the fracture energy defined as

$$\Gamma_G = \frac{1}{8} K_I^2 C_s \{t\} \quad (6.174)$$

Failure initiation is said to occur once  $\Gamma_G$  from equation 6.174 reaches a critical



value (e.g., if the critical value is  $1 \text{ J/m}^2$ , then continuous crack growth commences once equation 6.174 obtains a value of  $1 \text{ J/m}^2$ ).

## 6.6 Numerical Implementation

The following section outlines the numerical implementation of the viscoelastic fracture model discussed. Figure 6.10 provides a flow chart of the numerical implementation. Figure 6.10a outlines the intermittent crack growth phase, referring to reader to the continuous crack growth phase upon completion. Figure 6.10b then outlines the continuous crack growth phase, which will produce the final output upon completion. Details of the various steps in the model are discussed below.

### 6.6.1 Time-Stepping

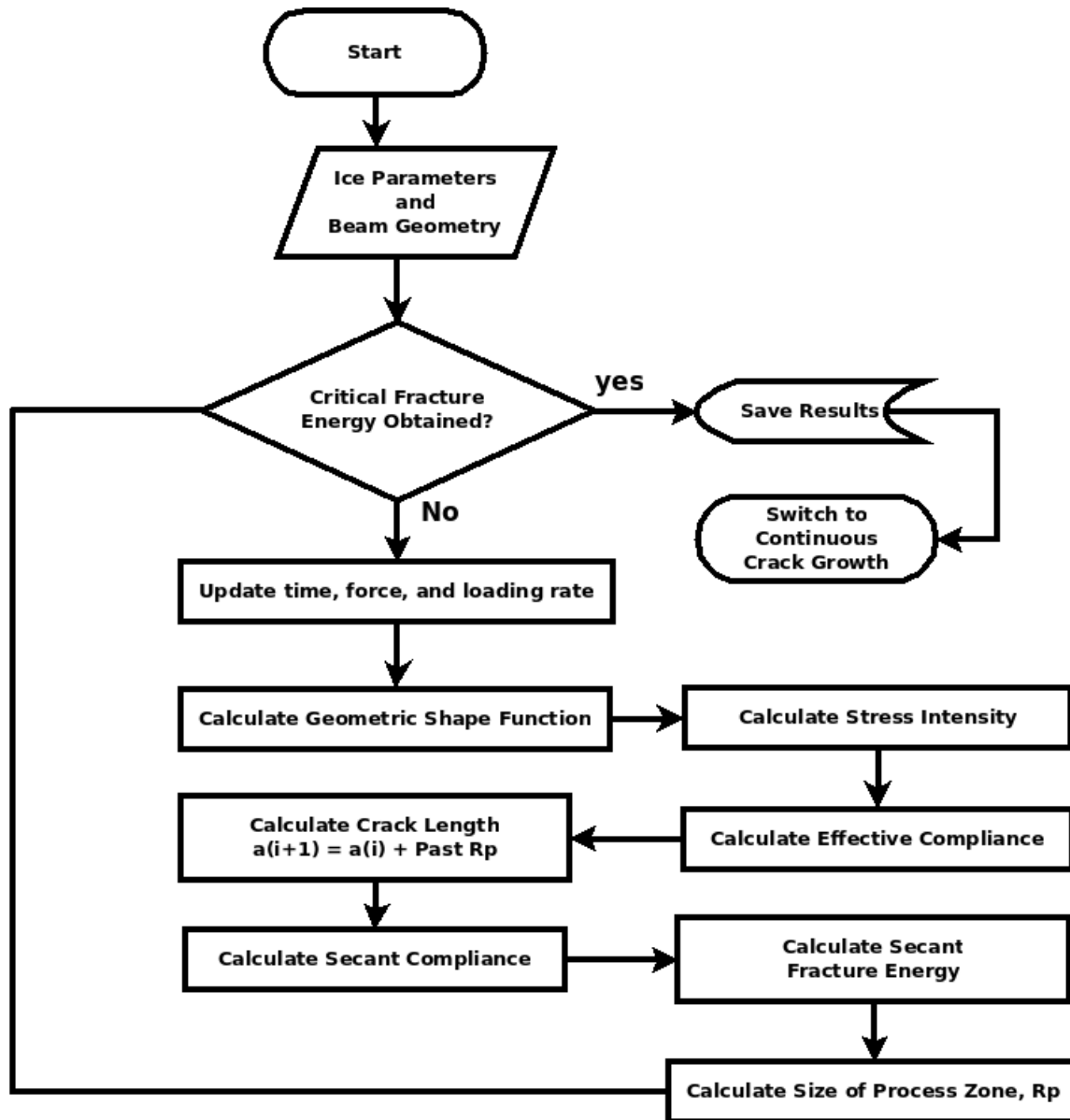
The model is implemented with a Euler forward method. While other numerical schemes are available, such as Heun's Method, that provides more stability and accuracy, the basic Euler's method was chosen to match the numerical scheme used in commercial FEA solvers like Abaqus FEA.

The default time step for continuous crack growth is defined as

$$\Delta t = \frac{0.1}{\dot{F}} \quad (6.175)$$

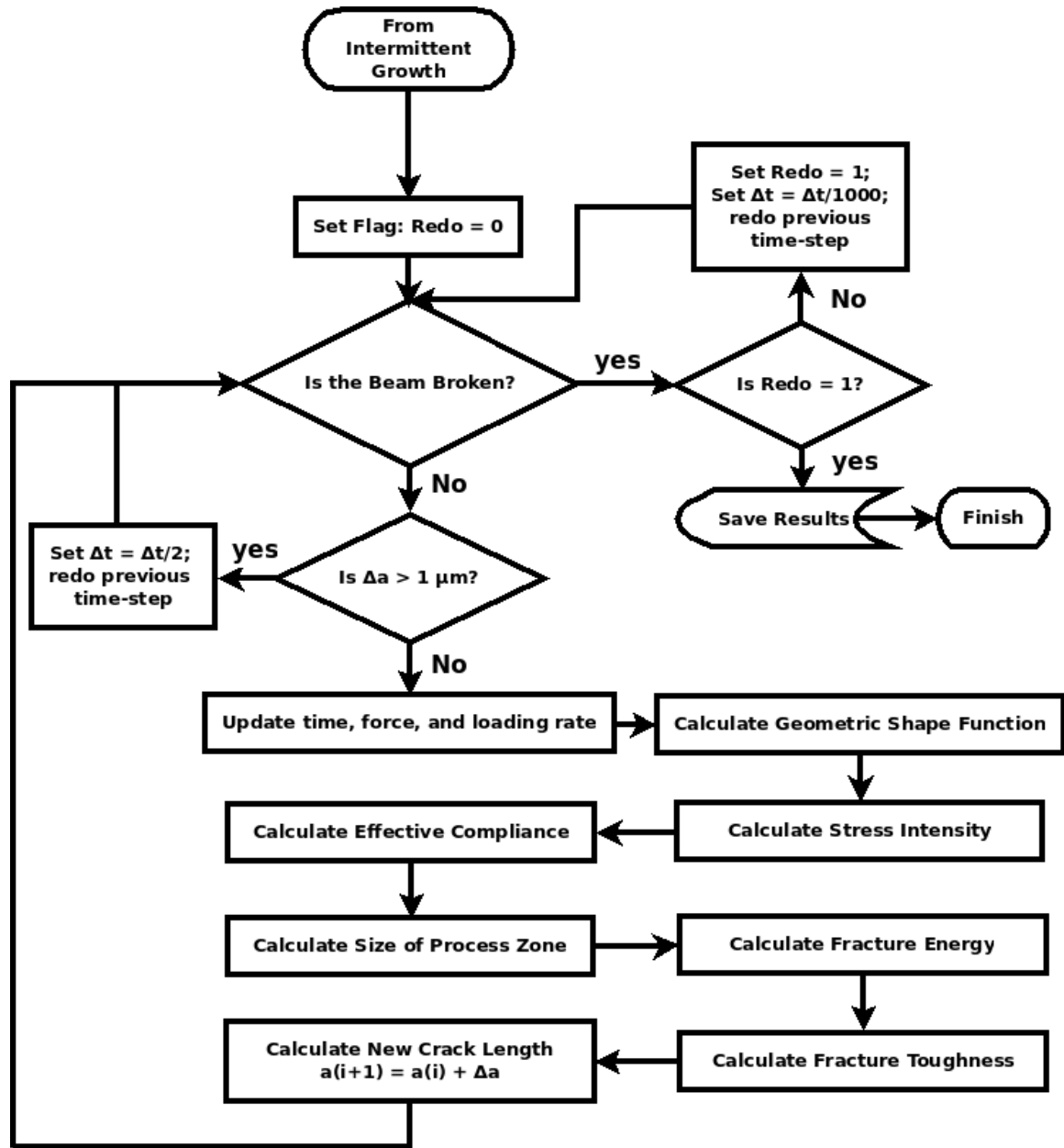
for  $\dot{F}$  of the ramp up phase. This provides a sensible baseline time stepping that typically will not lead to numerical instability, but is not prohibitively small for doing quick model runs. For the intermittent portion of the model, the time step was initially set to  $\Delta t = 1$  millisecond but was allowed to vary as needed.

To prevent large changes, such as numerical instability, in the crack length, the



(a) Intermittent Crack Growth

Figure 6.10



(b) Continuous Crack Growth

Figure 6.10: Flow chart of how the model numerically simulates continuous crack growth.

model checks the difference between  $a_{i+1}$  and  $a_i$ . If that difference is too big (currently defined as a micrometer) then the model will discard the new values and redo the time step with the time step halved and will keep halving  $\Delta t$  until the condition is met or a user-defined minimum value for  $\Delta t$  is met).

Once the crack has reached the value of  $h$  (i.e., the ice breaks), the model will undo the last couple of values (so return to time  $t_{i-1}$ ) and run the model with a default time step of

$$\Delta t = \frac{0.001}{\dot{F}} \quad (6.176)$$

to fine tune the results of when the ice broke, for more accurate results of time to failure and fracture load (it does this “do-over” once, the next time the ice breaks, the model will finish)

### 6.6.2 Updating the Force

The model currently uses a force loading profile of a constant ramp up from zero to a maximum value that it would hold (provided the modelled ice doesn't break during ramping), however, the code can be easily modified to take an input loading.

Under ramp up to hold, the force at time  $t$  is defined as

$$F\{t\} = \min \left\{ \dot{F}t, F_{max} \right\} \quad (6.177)$$

where  $F_{max}$  is the applied load for the constant load tests and set to an unobtainable value for the ramp up to failure model runs.

Numerically, this is written as

$$F_{i+1} = \min \left\{ F_i + \dot{F}_i t, F_{max} \right\} \quad (6.178)$$

though the min function could be removed with a prescribed loading.

### 6.6.3 Updating the Stress Intensity and Geometric Shape Function

The stress intensity is given as

$$K_{i+1} = Y_i^* \{\alpha_i\} \frac{3F_i(S_2 - S_1)}{2dh^{\frac{3}{2}}} \quad (6.179)$$

where

$$Y^* \{\alpha_i\} = Y \{\alpha_i\} \frac{\sqrt{a_i}}{(1 - \alpha_i)^{\frac{3}{2}}} = \left( 1.9887 - 1.326\alpha_i - \frac{(3.49 - 0.68\alpha_i + 1.35\alpha_i^2)\alpha_i(1 - \alpha_i)}{(1 + \alpha_i)^2} \right) \frac{\sqrt{a_i}}{(1 - \alpha_i)^{\frac{3}{2}}} \quad (6.180)$$

with  $\alpha_i = a_i/h$  and the beam dimensions from Figure 6.8.

### 6.6.4 Updating the Size of the Process Zone

The new process zone size can be calculated as

$$R_{p_{i+1}} = \frac{\pi}{2} \left( \frac{K_{i+1}}{\sigma_{m_{i+1}} I_1} \right)^2 \quad (6.181)$$

As discussed above,  $\sigma_m$  is set to a constant that represents the theoretical strength of the bonds in the crystal lattice of ice (the weakest would be along the basal plane).

the value of  $I_1$  is set to depend on the applied loading rate. The function is a

bounded power-law decay given as

$$I_1 = \min \left\{ \max \left\{ \dot{F} - \dot{F}_0, 0 \right\}^m, 2 \right\} \quad (6.182)$$

where  $\dot{F}_0$  and  $m$  are constants, and  $I_1$  has an upper bound of 2, which will occur for slow loading rates and constant loading.  $\sigma_m$ ,  $\dot{F}_0$ , and  $m$  are parameters that have to be found empirically using available data from the beam series.

## 6.6.5 Continuous Crack Growth

### 6.6.5.0.1 Updating the Fracture Toughness

The fracture toughness is a function of the failure energy, elastic compliance, and Poisson's ratio (currently set to 0.33). Fracture toughness is defined as

$$K_{G_{i+1}} = \frac{2\Gamma_{G_{i+1}}}{(1 - \nu^2)C_0} \quad (6.183)$$

### 6.6.5.0.2 Euler Forward Crack growth

$$a_{i+1} = a_i + \Delta t \left( \frac{C_{1_{i+1}} K_{i+1}^2}{8\Gamma_{G_{i+1}} \left( 1 - \frac{K_{i+1}^2}{K_{G_{i+1}}^2} \right)} \right)^{\frac{1}{n}} \ell_n^{\frac{1}{n}} R_{P_{i+1}} \quad (6.184)$$

the model will continue to update and grow the crack until either the ice breaks (defined as  $a_{i+1} = h$ ) or when a user-defined time is reached (when  $t_{i+1} = t_{max}$ ).

## 6.6.6 Intermittent Crack Growth

### 6.6.6.1 Secant Compliance

The secant compliance can be approximated using the trapezoidal rule as

$$C_{s_i} = \sum_{k=1}^i \frac{f\{t_{k+1}\} + f\{t_k\}}{2} \Delta t_k \quad (6.185)$$

$$f\{t_k\} = K_{I_i}^{-2} [C_0 + C_1(t_i - t_k)^n] \frac{K_k^2 - K_{k-1}^2}{t_k - t_{k-1}}$$

which is valid for uniform or non-uniform time steps.

### 6.6.6.2 Fracture Initiation

The fracture initiation energy is numerically determined by

$$\Gamma_{G_i} = \frac{1}{8} K_{I_i}^2 C_{s_i} \quad (6.186)$$

# Chapter 7

## Model Validation and Results

### 7.1 Underlying Assumptions of the Schapery Model

Since the new model developed in Chapter 6 is modified from the works of Schapery (1975a,b,c), this new model will also make use of the assumptions from the earlier model from Schapery.

One assumption that was made is that the primary and secondary creep terms can be combined into a single term in the form of equation 6.61. To show that this assumption is valid, at least for the time scale considered in this project, various datasets are shown to match this form in the following section. For convenience, equation 6.61 is rewritten here as

$$C_\nu = C_1 t^n \tag{7.1}$$

As mentioned in Section 6.2.2, the second underlying assumption of the model is that the process zone is small, which allows for the details of the process zone to be glossed over. Section 7.1.3 will show that, for reasonable considerations of process zone stresses, the process zone is expected to be small.



### 7.1.1 Datasets Used for Validation

To begin the analysis of the validation of the effective compliance, a collection of datasets were used. The datasets are from Schapery (1997), LeClair et al. (1999), Sinha (1978), and Brill and Camp (1961). These experiments performed creep tests on ice samples under various conditions (detailed below). This section will analyse the data to show that the creep curves can be approximated by equation 7.1 (accounting for the elastic compliance).

Schapery (1997) and LeClair et al. (1999) performed uniaxial tension tests on ice samples. Samples were loaded under creep and recovery cycles with three stress levels of 0.13, 0.23, and 0.32 MPa. Each stress level was applied for time periods of 1, 2, and 4 minutes with recovery periods roughly 3 times as long between each successive loading (e.g, load 0.13 MPa for 1 minutes, recover for 3 minutes, load 0.13 MPa for 2 minutes, recover for 6 minutes, load 0.13 MPa for 4 minutes, recover 12 minutes, now load to 0.23 MPa for 1 minutes, recover 3 minutes, and so on...) as shown in Figure 7.1. The type of ice used in these experiments was saline, polycrystalline laboratory-grown ice. The ice was grown from a 26 ppt salt-water mix that was chilled to  $-1^{\circ}\text{C}$  and seeded by spraying a mist on top of the solution (to mimic natural growth). This resulted in the formation of randomly oriented S2-columnar ice with a grain size of 10 mm. While a nonlinear viscoelastic model is required to fit the full dataset, each individual creep load can be modelled using equation 7.1 (discussed in the next section).

Figures 7.2 and 7.3 are experimental results from Sinha (1978). Sinha (1978) grew S2-columnar ice using deaerated water in a plastic container chilled at  $-10^{\circ}\text{C}$ . Finely crushed ice was sprinkled on the top of the water to act as the seed for grain nucleation. Grains near the top had a random c-axis orientation but became elongated and vertically-oriented deeper down in the resulting ice block. Grain diameters

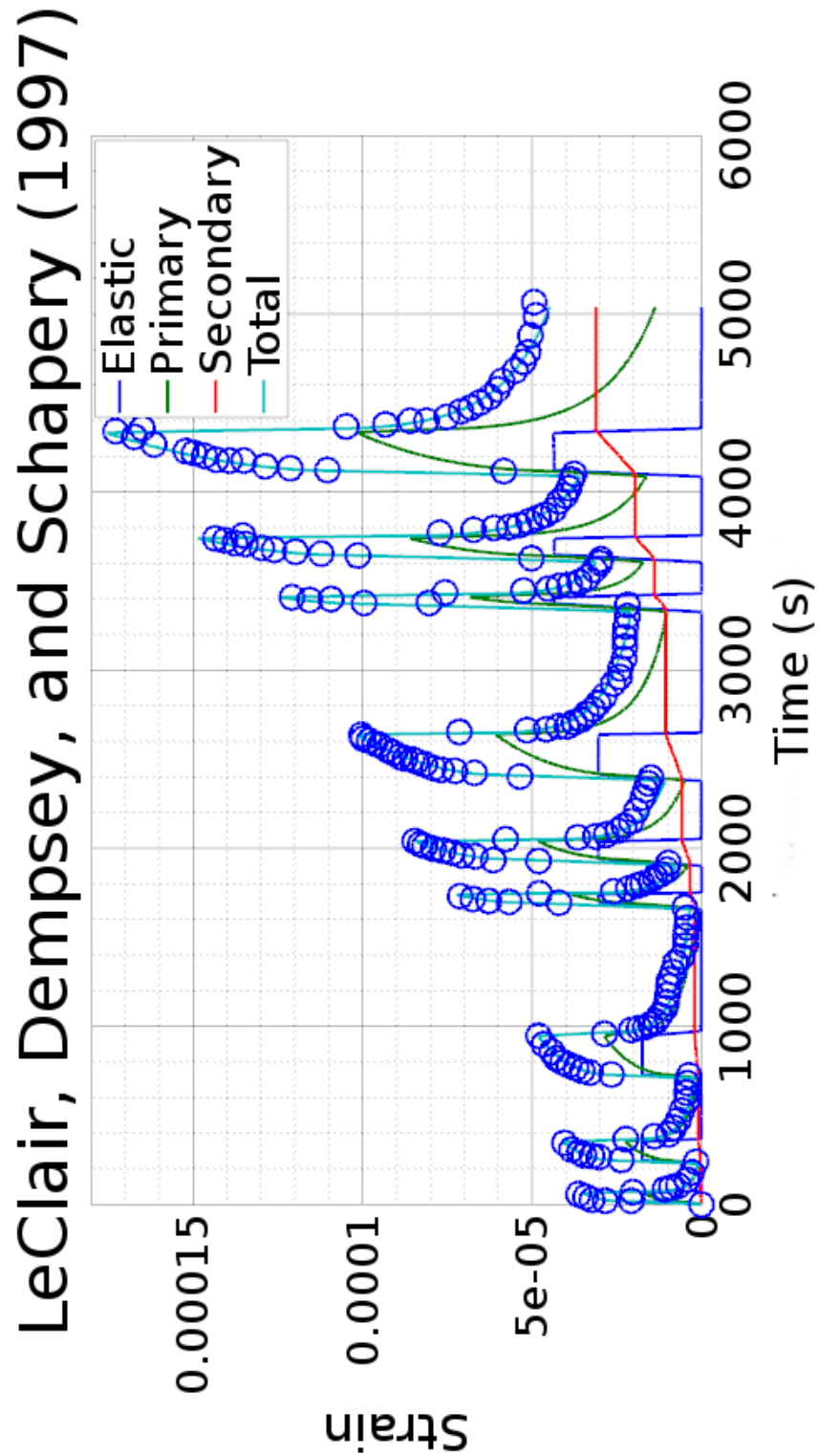


Figure 7.1: Data (represented by circles) of ice specimens under uniaxial tension from Schapery (1997); LeClair et al. (1999). Nonlinear optimization of the parameters from equation 2.45.

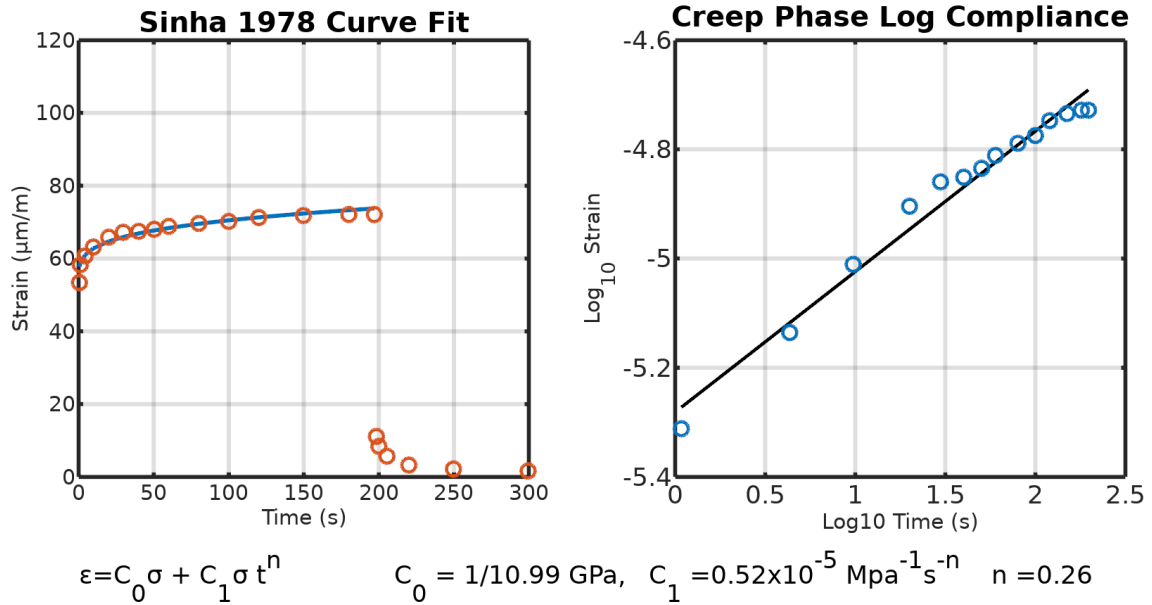


Figure 7.2: Left: Comparison of experimental data Sinha (1978) ( $-41^\circ\text{C}$ , columnar ice) to an effective linear compliance of the form in equation 7.1 by nonlinear optimization of the model parameters.

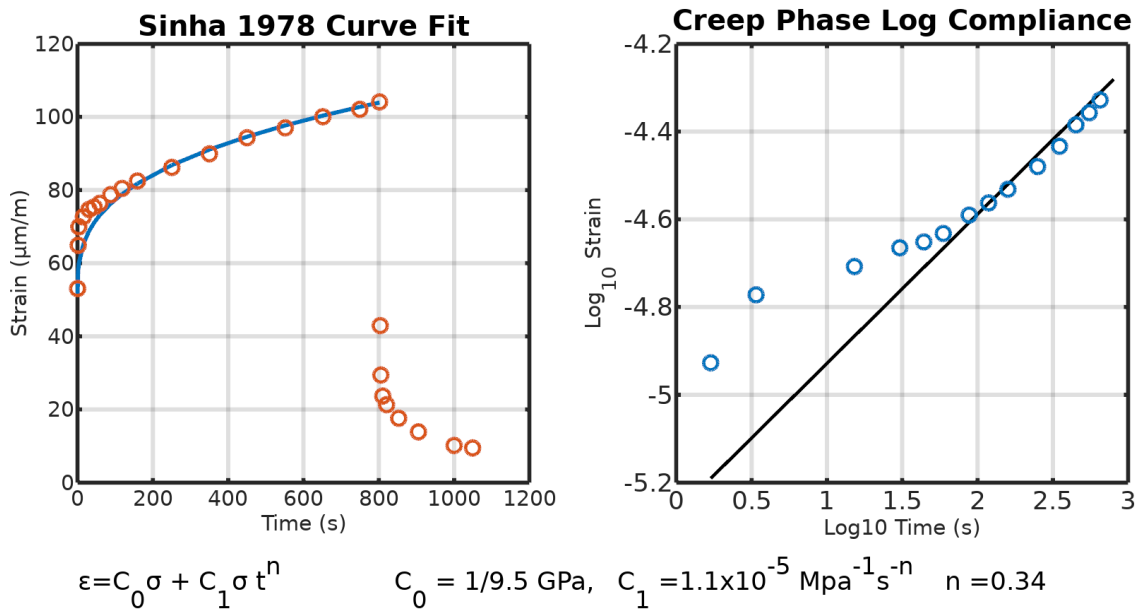


Figure 7.3: Left: Comparison of experimental data Sinha (1978) ( $-30^\circ\text{C}$ , columnar ice) to an effective linear compliance of the form in equation 7.1 by nonlinear optimization of the model parameters.

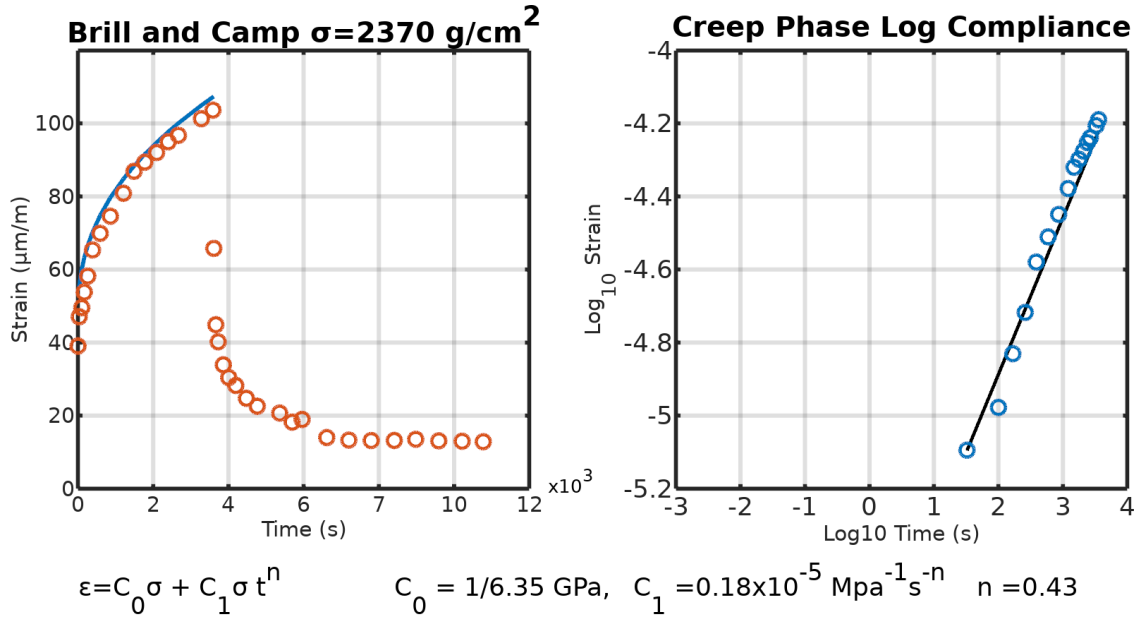


Figure 7.4: Left: Comparison of experimental data Brill and Camp (1961) ( $-5^\circ\text{C}$ , isotropic ice) to an effective linear compliance of the form in equation 7.1 by nonlinear optimization of the model parameters.

were around 3 mm in size. The ice was cut into rectangular blocks and loaded in compression perpendicular to the long side of the grain.

Ice samples used in Brill and Camp (1961) were polycrystalline in nature. The ice was grown from tap water, covered with fine snow particles and chilled at  $-5^\circ\text{C}$ . The resulting ice had a random grain orientation and a grain diameter of 1–2 mm. Figure 7.4 shows a specimen that underwent uniaxial tension at  $-5^\circ\text{C}$ .

Of the datasets considered, the ice grown in Brill and Camp (1961) is the most similar to the ice grown for the beam series. The ice samples of Brill and Camp (1961) are randomly oriented and isotropic, whereas the columnar ice from the other series would have a preferred c-axis. The grain size of Brill and Camp (1961) is slightly smaller than the 2–3.35 mm grain size used in the beam bending series. The other difference is that Brill and Camp (1961) performed their series at  $-5^\circ\text{C}$  instead of  $-10^\circ\text{C}$ .

### 7.1.2 Effective Compliance Validation

For each of the nine loading cycles in Figure 7.1, the beginning of each cycle is zeroed both in time and strain to study the creep properties of the newly applied load. Figure 7.6 displays the log-log plots of the data in these cycles along with a linear fit. From the figure, it is clear that there is a strong linear relationship between the ice compliance and time. This suggests that a power-law type equation should predict the creep behaviour of ice reasonably well. Similarly, Figure 7.2 shows a strong indication of a power-law type compliance. Figure 7.2 shows the data (in circles) plotted against the fits from equation 7.1. The bottom shows the values used in the equation.

Both of these results are for short time periods of ice. Since delayed elastic creep is modelled using a power-law type equation, it is reasonable to expect good approximations to happen during time scales in which it is the dominant form of strain. Over time, the viscous creep will become dominant which should change the shape of the compliance curve towards a more linear path (under creep conditions). This means that other datasets should be checked to confirm that the power-law type equation holds true for longer time periods.

Figure 7.3 shows ice under creep for roughly 800 seconds ( $13\frac{1}{3}$  minutes). Many of the experiments performed in this project fall roughly into this time frame. Even at this time scale, equation 7.1 is capable of providing reasonable fits to the data.

To ensure that equation 7.1 still approximates creep curves for longer time scales, the data from Brill and Camp (1961) can be used. The data shows ice under creep for 1 hour, which exceeds any of the experiments in this project that resulted in broken ice samples. Figure 7.4 shows that equation 7.1 fits the data as well as it did during the shorter experiments.

From this, it is reasonable to assume that the effective compliance method used in the model will provide accurate results for the time scales used in the experiments.

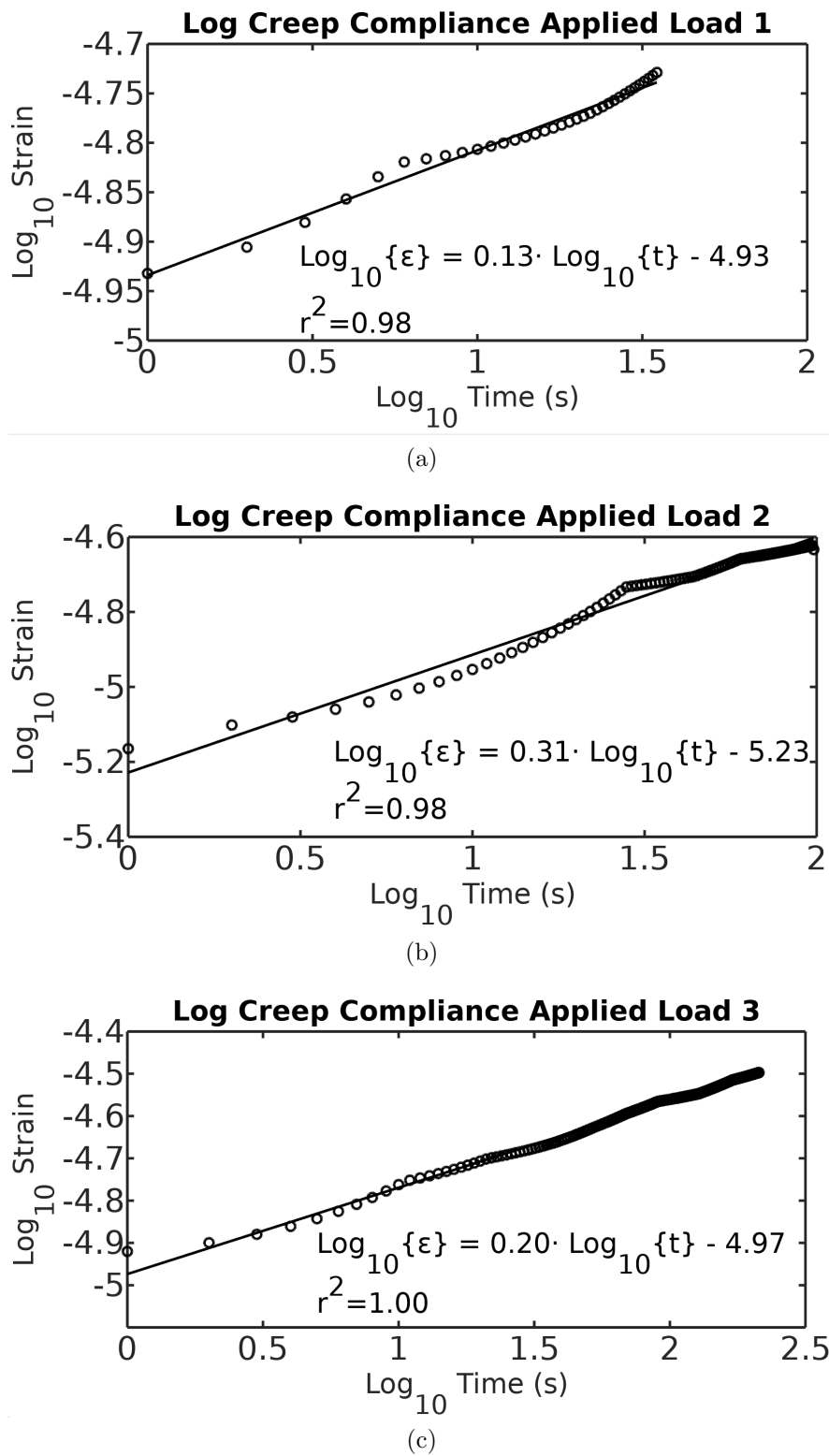
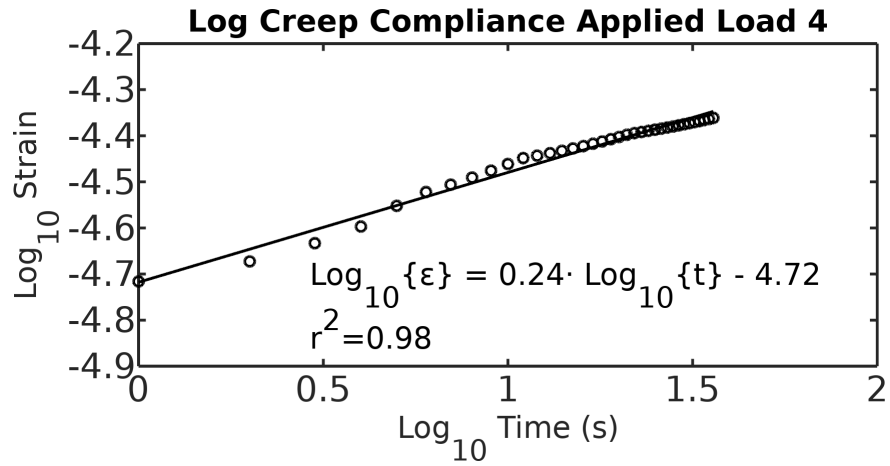
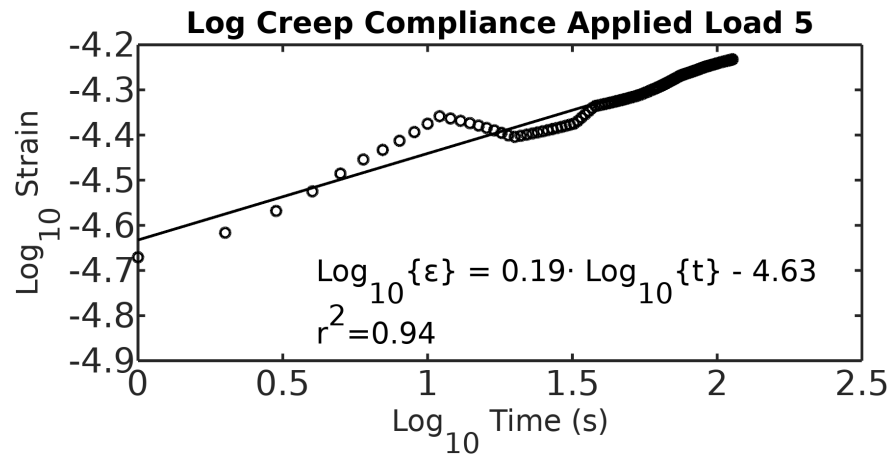


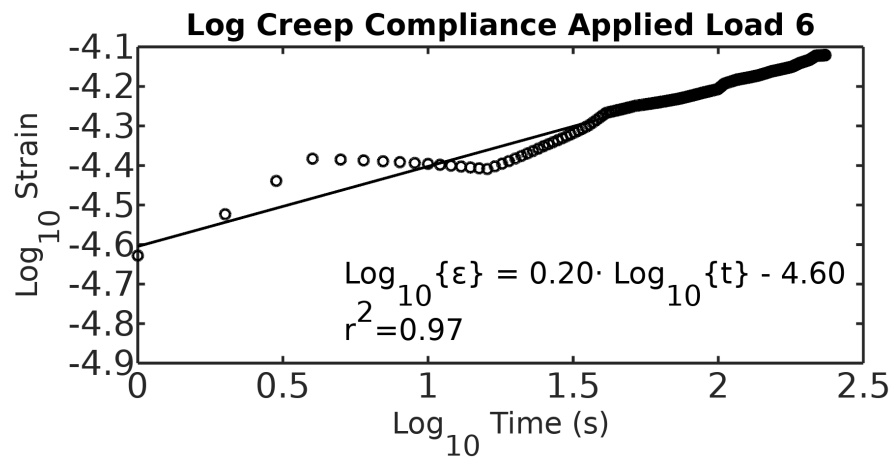
Figure 7.5: Log-log plots showing the creep response of the nine cycles applied to the ice sample from Schapery (1997); LeClair et al. (1999).



(a)



(b)



(c)

Figure 7.6

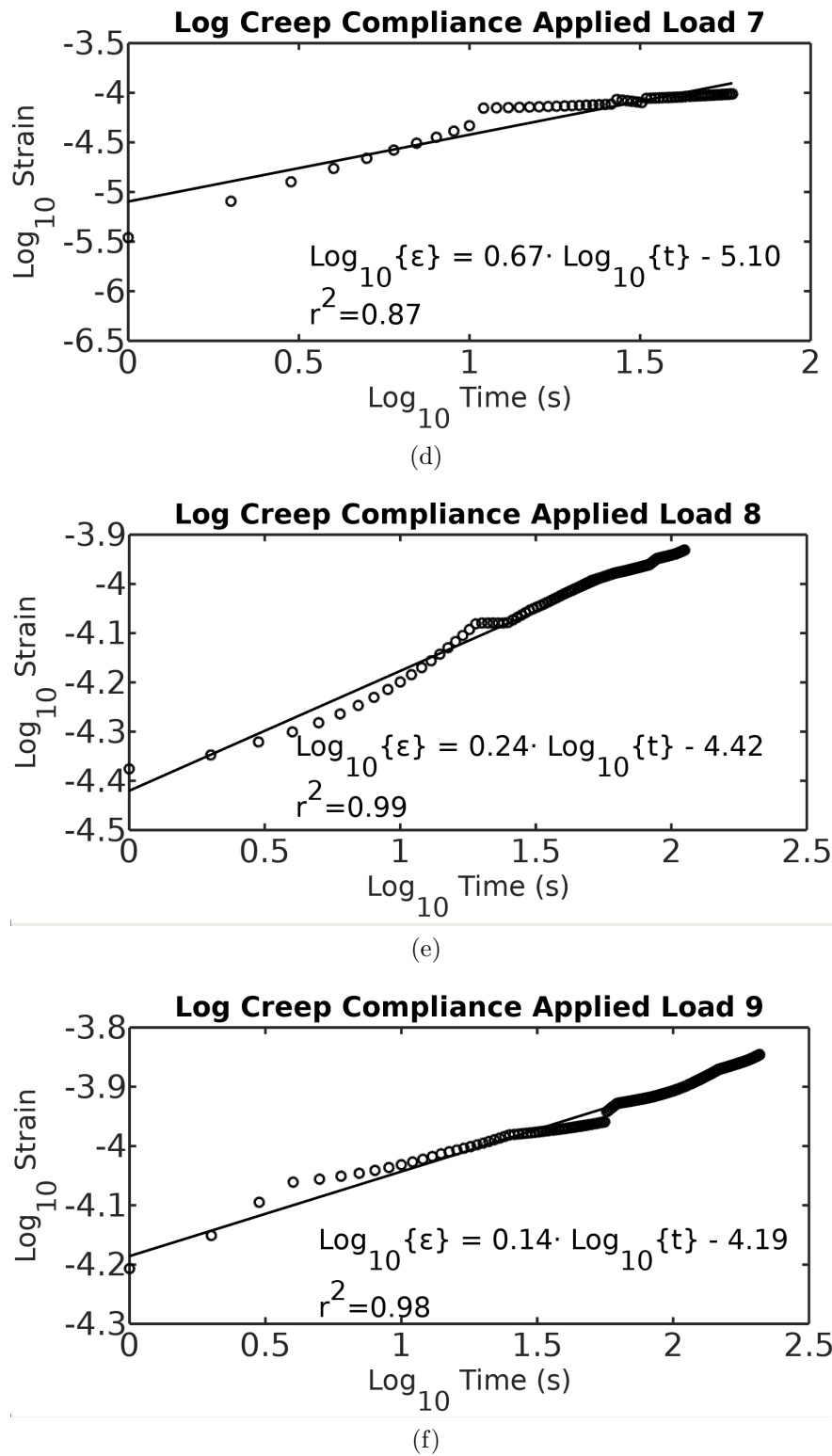


Figure 7.6: Log-log plots showing the creep response of the nine cycles applied to the ice sample from Schapery (1997); LeClair et al. (1999).



Source	$C_0$ ( $10^{-5}$ )	$C_1$ ( $10^{-5}$ )	$n$
Sinha (1978) (-41°C)	9.10	0.52	0.26
Sinha (1978) (-30°C)	10.5	1.10	0.34
Brill and Camp (1961)	15.4	3.00	0.28

Table 7.1: Summary of model coefficients of the compliances from Sinha (1978) and Brill and Camp (1961).

A summary of the compliance parameters can be found in Table 7.1.

### 7.1.3 Validation of Small Process Zone Size

The size of the process zone is defined in Schapery (1975a) as

$$R_p = \left(\frac{\pi}{2}\right) \left(\frac{K_I}{\sigma_m I_1}\right)^2 \quad (7.2)$$

For an estimation of the process zone in ice, consider a linear stress profile that is maximum at the crack tip and decreases towards the apparent crack tip, as shown in Figure 7.7a. Using the following values for ice

$$K_{IC} \approx 0.1 \text{ MPa}\sqrt{m}$$

$$\sigma_f \{\eta\} = \sigma_m(1 - b\eta) \quad (7.3)$$

$$1 \text{ MPa} < \sigma_m < 600 \text{ MPa}$$

produces the results in Figure 7.7c. Figure 7.7c shows the size of the process zone as a function of maximum stress in a linear profile ( $b = 0$  would be a plastic response,  $b = 1$  would have zero stress at the apparent crack tip). The figure shows that unless the maximum stress in the process zone is less than 2 MPa, the size of the zone is

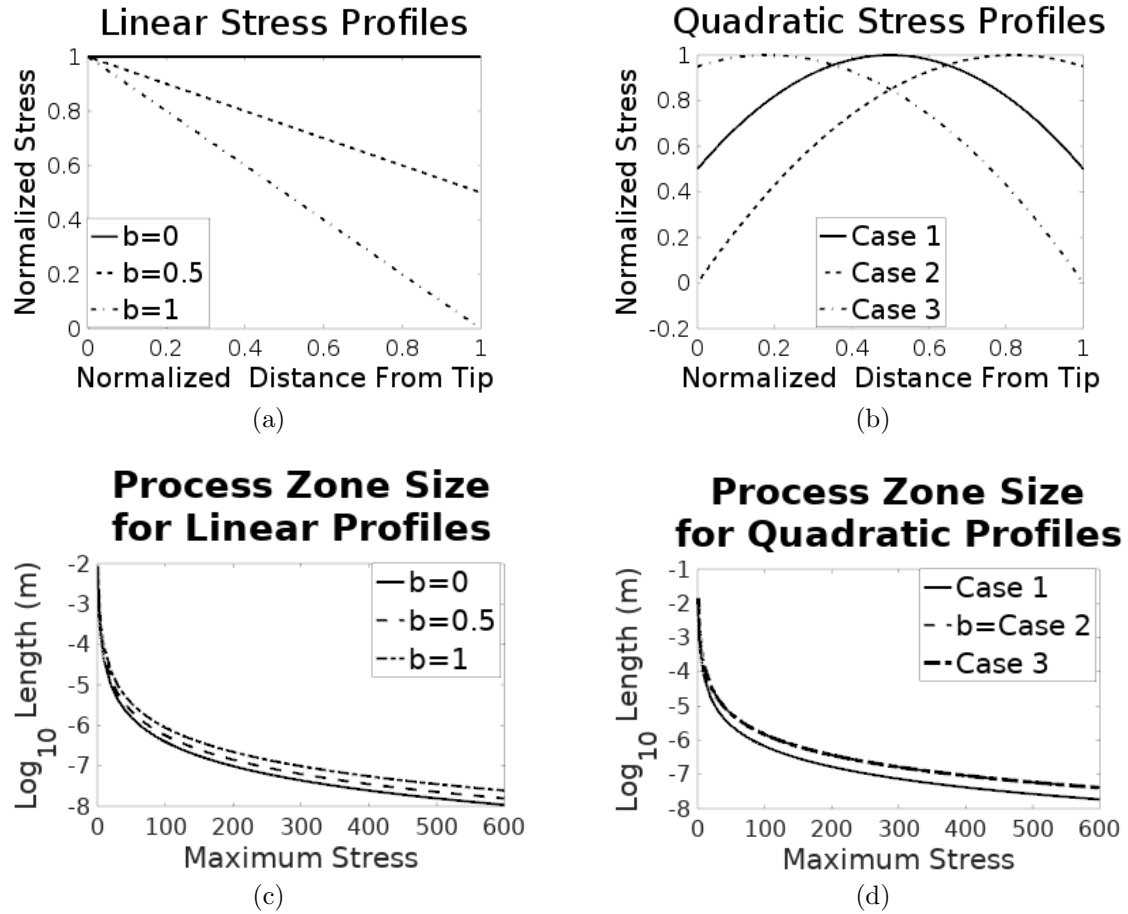


Figure 7.7: a-c) Linear profile and process zone size. b-d) Quadratic profile and process zone size.

certainly negligible. Given that fracture requires breaking the bonds between atoms, it is clear that the stress is magnitudes higher than 2 MPa (probably in the 100–600 MPa range). Similarly, Figure 7.7b and d show the results for parabolic process zone distributions. Case 1 shows a curve where the magnitude at the actual and apparent tips are half the maximum stress, case 2 shows a profile that is more stressed towards the apparent crack tip, and case 3 shows one that is more stressed towards the actual crack tip. While there is some difference between the results, the differences are very small. In either case, provided the stress is above 2 MPa, the process zone should be relatively small, allowing the one to gloss over the specifics of the process zone in favour of a simplified, but acceptable theory.

## 7.2 Validation of Linear Model

Ice is a nonlinear viscoelastic material that is better described by equation 2.45, rewritten here as

$$\epsilon \{t\} = C_0\sigma + C_1^*\sigma^{p^*}t^{n^*} + C_2^*\sigma^{q^*}t \quad (7.4)$$

as opposed to a linear viscoelastic model of

$$\epsilon \{t\} = C_0\sigma + C_1\sigma t^n + C_2\sigma t \quad (7.5)$$

of which the viscous ( $C_2$ ) creep is combined with the primary ( $C_1$ ) creep to form a single creep term in Schapery (1975a,b,c).

This nonlinearity of the ice rheological properties can pose issues for the model, given the the linear model may not accurately represent the nonlinear ice. This means that the model could have trouble modelling the ice if the nonlinearity is too great. However, provided the nonlinearity is small, then the model can provide an accurate

Model Parameters Used to Fit LeClair et al. (1999)			
Linear Parameters		Nonlinear Parameters	
$C_0$	$13.3 \times 10^{-5} \text{MPa}^{-1}$	$C_0$	$13.3 \times 10^{-5} \text{MPa}^{-1}$
$C_1$	$3.82 \times 10^{-5} \text{MPa}^{-1} \text{s}^{-\frac{1}{3}}$	$C_1^*$	$5.65 \times 10^{-5} \text{MPa}^{-1.2} \text{s}^{-\frac{1}{3}}$
$n$	$1/3$	$n^*$	$1/3$
$C_2$	$5.87 \times 10^{-8} \text{MPa}^{-1} \text{s}^{-1}$	$C_2$	$49.7 \times 10^{-8} \text{MPa}^{-2.79} \text{s}^1$
$p$	$1.00$	$p^*$	$1.20$
$q$	$1.00$	$q^*$	$2.79$

Table 7.2: Model parameter used in fitting LeClair et al. (1999) in Figure 7.8.

estimation of time to failures or peak ramp loading. Therefore, a check should be made to ensure that ice can be reasonably approximated by a linear viscoelastic model.

To address this issue, consider the multiple stress loading that was done in LeClair et al. (1999). Table 7.2 shows parameters used in linear (equation 7.5) and nonlinear (equation 7.4) fits of this data. From Table 7.2, it can be seen that the primary creep term is only slightly nonlinear at  $p^* = 1.2$  and the viscous creep has a nonlinearity of  $q^* = 2.79$  which is slightly below the typical value of 3 ( $q^*$  is often called  $n$  in the Glen's flow equation for viscous creep (Glen, 1955)).

Figure 7.8a and b show the linear and nonlinear fits for the parameters in Table 7.2. As expected, Figure 7.8b (the nonlinear fit) provides a better fit to the data than the linear fit in Figure 7.8a. That said, Figure 7.8a provides a rather good fit to the data, suggesting that a linear model does provide a reasonable estimation for the behaviour of the ice for the shorter time lengths. This would suggest that the ramp loading series, often lasting less than a second to complete, should be reasonably simulated by the linear model.

For longer times, and higher stresses, the nonlinearity of the ice could become an issue. Creep in ice is made up of the primary and secondary creep terms that need to be considered.

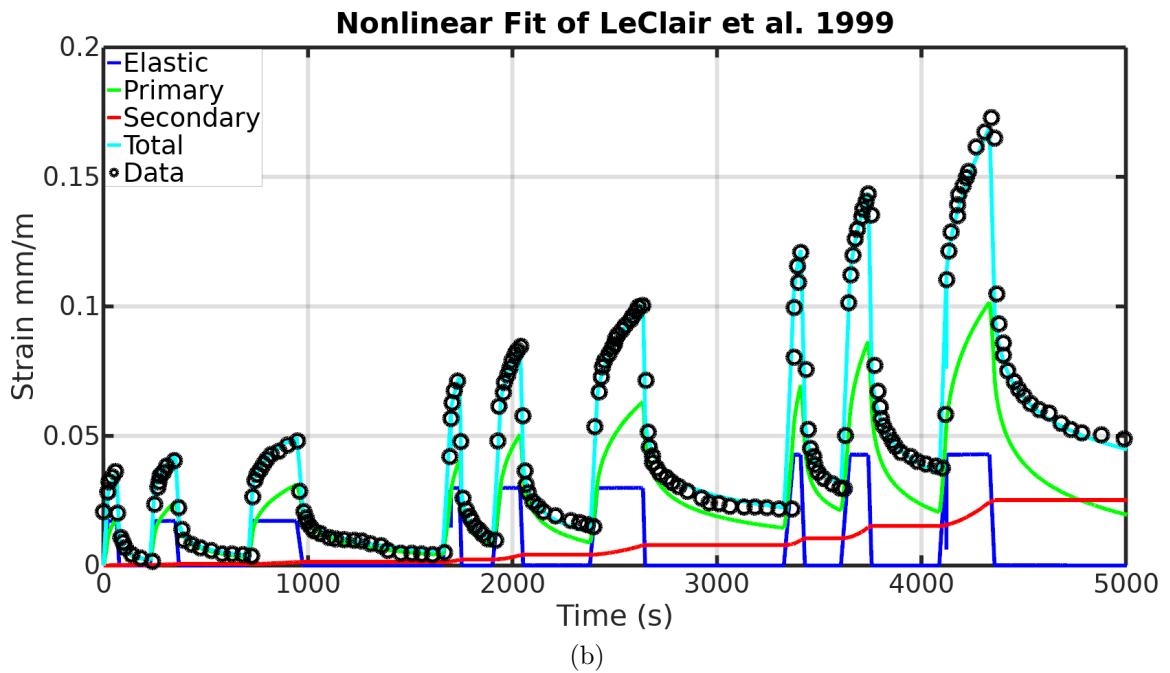
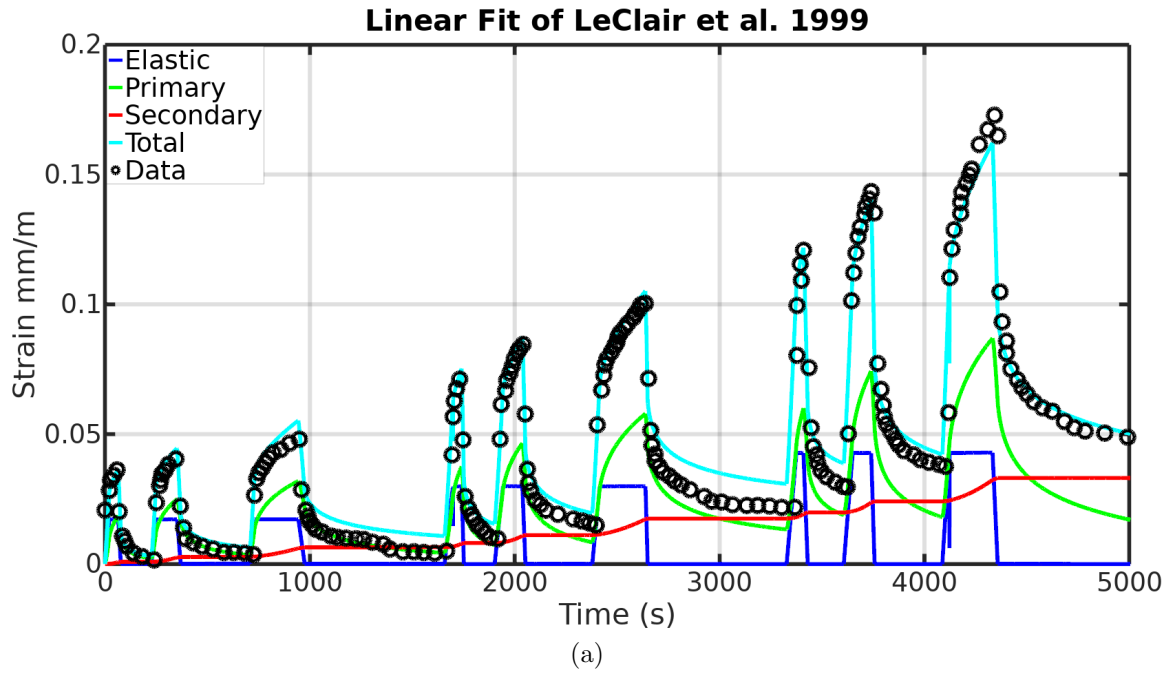


Figure 7.8: Linear and nonlinear parameter optimization fits of LeClair et al. (1999) using equations 7.5 and 7.4.

### 7.2.1 Primary Creep

Primary creep in isotropic, polycrystalline ice is defined in (Sinha, 1983) as

$$\epsilon_d = c_1 \left( \frac{d_1}{d} \right) \left( \frac{\sigma}{E} \right)^p (1 - e^{-(at)^n}) \quad (7.6)$$

considering the last term in equation 7.6

$$\epsilon \{t\} = 1 - e^{-(at)^n} \quad (7.7)$$

and making the substitution  $x = \beta t^n$ , where  $\beta = a^n$ , gives

$$\epsilon \{x\} = 1 - e^{-x} \quad (7.8)$$

The Taylor series expansion around  $x = x_0$  is

$$\begin{aligned} \epsilon \{x\} &\approx \epsilon \{x_0\} + \epsilon' \{x_0\} (x - x_0) + \epsilon'' \{x_0\} \frac{(x - x_0)^2}{2} + \epsilon''' \{x_0\} \frac{(x - x_0)^3}{6} + \dots \\ \epsilon \{x\} &\approx \epsilon \{x_0\} + \epsilon' \{x_0\} (x - x_0) + \mathcal{O}\{(x - x_0)^2\} \end{aligned} \quad (7.9)$$

for early time steps, we can let  $x_0 \approx 0$  since  $t \approx 0$  giving the Maclaurin series

$$\epsilon \{x\} \approx \epsilon \{0\} + \epsilon' \{0\} (x) \quad (7.10)$$

Using

$$\epsilon' \{x\} = e^{-x} \quad (7.11)$$

gives

$$\epsilon \{x\} = (1 - e^{-x}) + e^{-x}(x)$$

$$\epsilon \{x\} = 1 - e^{-x}(1 - x)$$

$$\epsilon \{x\} \approx 1 - (1)(1 - x)$$

$$\epsilon \{x\} \approx x$$

and converting back to  $t$

$$\epsilon \{t\} \approx \beta t^n \quad (7.12)$$

as long as  $\beta t^n$  remains relatively small.

Equation 7.12 suggests that equation 7.6 can be approximated by

$$\epsilon_d = A t^n \quad (7.13)$$

where

$$A = c_1 \left( \frac{d_1}{d} \right) \left( \frac{\sigma}{E} \right)^p \beta = c_1 \left( \frac{d_1}{d} \right) E^{-s} a^n \quad (7.14)$$

Equation 7.13 is of the form by Andrade (1910), which is known to be equivalent (for time frames up to a decade) to the broad-spectrum approach developed in Schapery (1962). In short, the broad-spectrum approach involves approximating the delayed elastic creep by a series of linear Kelvin-Voigt units in a generalized Burgers model of a viscoelastic material.

This suggests that the nonlinearity in the primary creep can be approximated by a linear model, leaving only the viscous creep to be a potential issue in terms of using a linear model to predict ice behaviour.

Symbol	Parameter	Value
E	Young's Modulus	9.5 GPa
$c_1$	Primary Creep Constant	9
$d_1$	Reference Grain Diameter	1 mm
d	Grain Diameter	5 mm
p	Primary Creep Nonlinearity	1
q	Secondary Creep Nonlinearity	3
n	Primary Creep Exponent	0.34
a	Primary creep Coefficient	$1.76 \times 10^{-7} \text{s}^{-1}$
$s_1$	Reference Stress	1 MPa

Table 7.3: Parameter values used to generate creep values from equations 7.6 and 7.15.

### 7.2.2 Secondary Creep

The secondary creep from Sinha (1983) is defined as

$$\epsilon_\nu = c_2 \left( \frac{\sigma}{\sigma_1} \right)^q t \quad (7.15)$$

where  $c_2$  is a constant and  $\sigma_1$  is a reference stress.

Unlike the primary creep, there is no broad-spectrum approach that would allow a linearization of the secondary creep. Following the normalized compliance approach of Sinha (1978), define normalized compliance as  $E\epsilon_t/\sigma$ . From this analysis, one can determine a length of time in which the nonlinear effects can be neglected and a linear model provides an acceptable approximation to the ice behaviour.

For the experiments performed in Sinha (1978) the total strain on the ice is given by

$$\epsilon_t = \frac{\sigma}{E} + c_1 \left( \frac{d_1}{d} \right) \left( \frac{\sigma}{E} \right)^p (1 - e^{-(at)^n}) + c_2 \left( \frac{\sigma}{\sigma_1} \right)^q t \quad (7.16)$$

using the parameters defined in Table 7.3.

The cracks in the beam are under tensile stress and should undergo tensile fracture in the range of 0.7–3.1 MPa for temperatures of -10°C —20°C (Petrovic, 2003). To



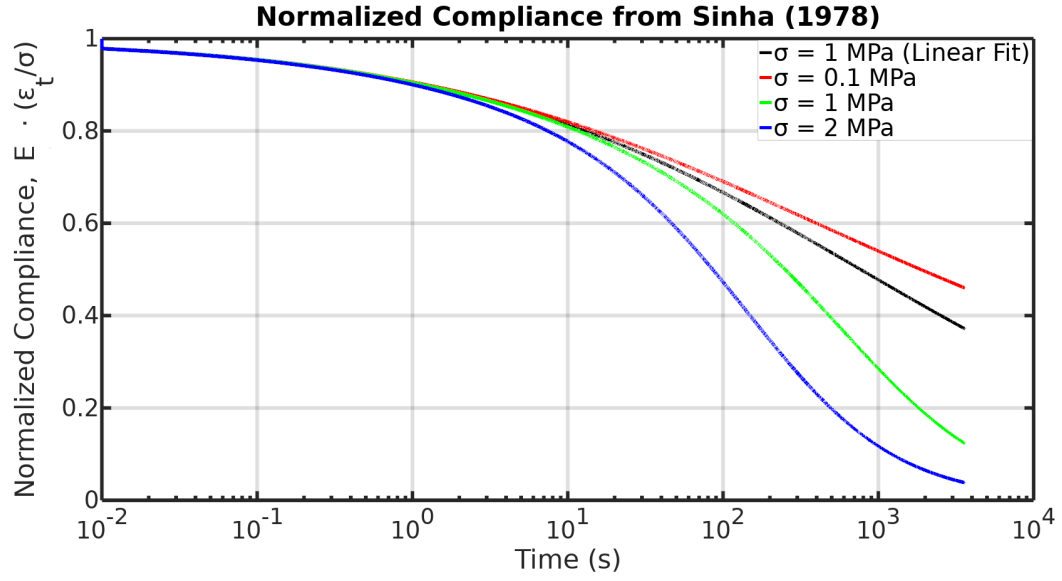


Figure 7.9: Normalized creep for experiments performed by Sinha (1978) presented in Figure 7.3.

test how the nonlinearity affects the ice behaviour, stresses of 0.1, 1.0, and 2.0 MPa were used to calculate three normalized creep compliance curves.

Normalizing the strain in equation 7.16 as  $E(\epsilon_t/\sigma)$  gives the red, green, and blue curves in Figure 7.9 for the three different stress levels chosen. Using the linear model fit shown in Figure 7.3, and normalizing by the elastic term, gives the black curve shown in Figure 7.9.

Figure 7.9 shows that the linear fit, using the equation and parameters from Figure 7.3 (noting that  $C_0 = 1/E$ ), underestimates the normalized creep curves for longer time periods (comparing the black curve to the green curve for same stress). The linear model manages to give reasonable results for times upto 20–30 seconds, but is quickly deviating from the 2 MPa curve. This would suggest that the model should provide reasonable results for the ramp series experiments, as many of them were much shorter than a second in duration, but may have issues fitting the constant load series as these experiments lasted several minutes to almost an hour.

A similar analysis was also performed on the experiments of Brill and Camp (1961),

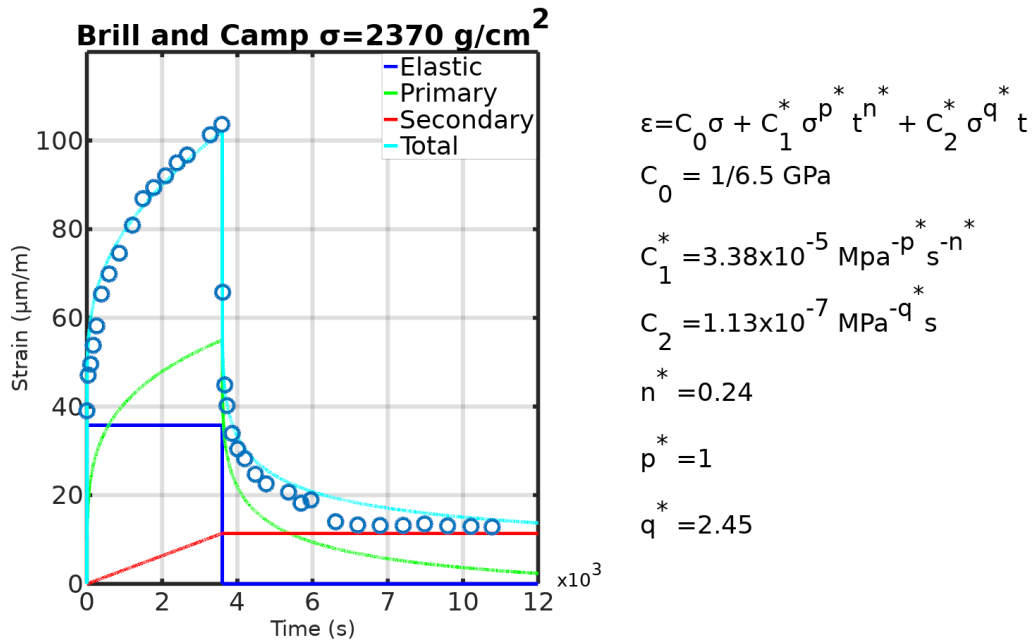


Figure 7.10: Nonlinear parameter optimization fit of the creep curve from Brill and Camp (1961).

as the ice used was polycrystalline like the ice used in the beam bending experiments. Figure 7.10 shows a nonlinear fit of the data using equation 7.4 and the values listed in Figure 7.10.

Normalizing the creep from equation 7.4 and equation 7.5 (using the values from Figure 7.4), generates the normalized compliance curves in Figure 7.11. The linear model curve fares better in this series than it does in Figure 7.9, suggesting that the linear model may even be good for upto 100 seconds. While better than the results of Figure 7.9, these results still suggest that the ramp series should be approximated well by the model, but the constant load series would become less accurate for the longer tests.

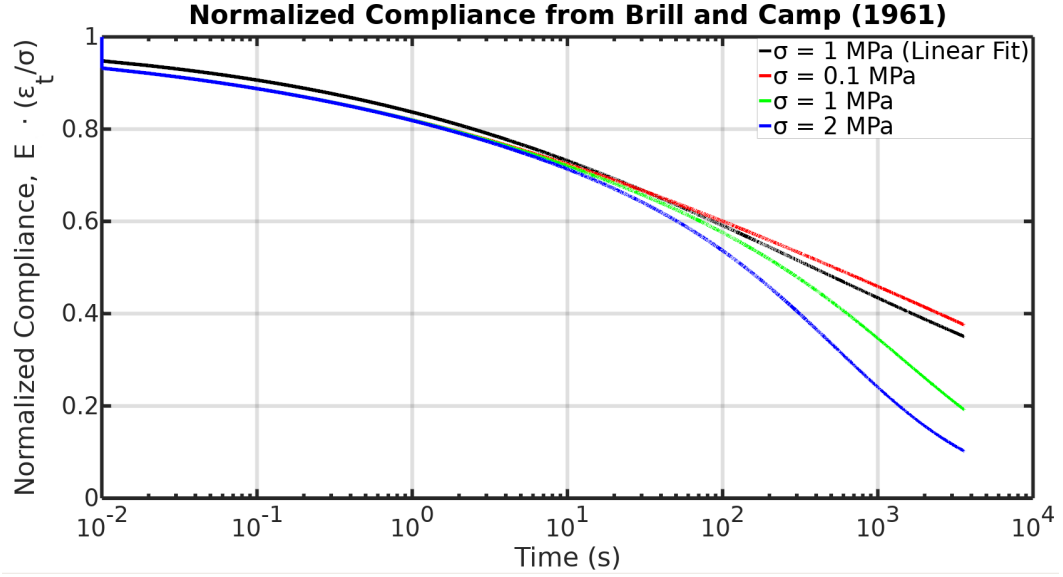


Figure 7.11: Normalized creep curves for the experiments of Brill and Camp (1961).

Dimension	Symbol	Value
Bottom Roller Separation	$S_2$	285.75 mm
Top Roller Separation	$S_1$	100.0 mm
Beam Thickness	$h$	40.0 m
Beam Depth	$d$	60.0 mm
Initial Crack Length	$a_0$	10.0 mm

Table 7.4: Geometric dimensions of the ice beam for the ramp series.

Dimension	Symbol	Value
Bottom Roller Separation	$S_2$	150.0 mm
Top Roller Separation	$S_1$	50.0 mm
Beam Thickness	$h$	20.0 m
Beam Depth	$d$	30.0 mm
Initial Crack Length	$a_0$	5.0 mm

Table 7.5: Geometric dimensions of the ice beam for the constant load series.

Parameter	Value
$C_0$	$1.57 \times 10^{-10} \text{ Pa}^{-1}$
$C_1$	$1.8 \times 10^{-10} \text{ Pa}^{-1} \text{s}^{-0.47}$
$n$	0.470
$\sigma_m$	318 MPa
$\Gamma_G$	$1.60 \text{ J/m}^2$

Table 7.6: Rheological Parameters from uniaxial fit to (Brill and Camp, 1961).

## 7.3 Beam Geometry

Tables 7.4 and 7.5 list the beam geometry for the constant ramp and constant load series. The name of the variables is adapted from the beam bending schematic in Figure 6.8.

## 7.4 Model Fits Using Brill and Camp Parameters

The goal of this chapter is to show how well the model can match the data collected from the two 4-point bending series experiments discussed in Chapter 5. To begin, consider the uniaxial model fits of the creep tests performed by Brill and Camp (1961). This parameter set was chosen because the ice used in Brill and Camp (1961) was polycrystalline ice, with grain size of 1–2mm, and tested at  $-5^\circ\text{C}$ . This is rather similar to ice used in the current experiment, which was polycrystalline, 2–3.35 mm grain diameter, and tested at  $-10^\circ\text{C}$ .

The creep parameters in Table 7.6 are taken from Figure 7.4 from Section 7.1.1.  $\sigma_m$  and  $\Gamma_G$  from Table 7.6 were arbitrarily chosen as reasonable values of these two parameters and used to fit the experimental data from the two bending series.

Figures 7.12 and 7.13 show the numerical results of the model simulations of the constant ramping experiments and the constant applied load bending tests from Chapter 5. From these two figures, the parameters from Table 7.6 provide reasonable

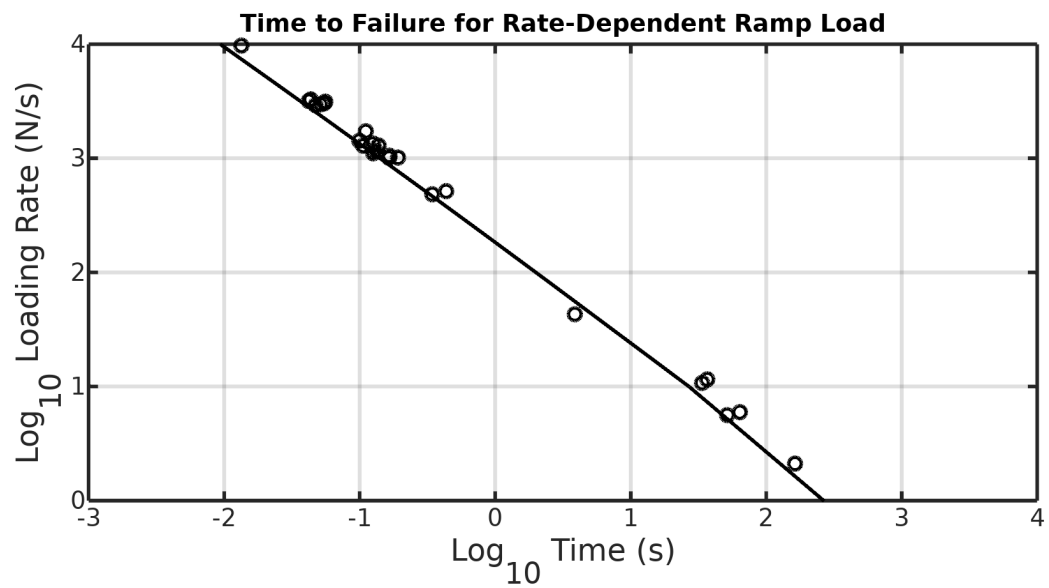
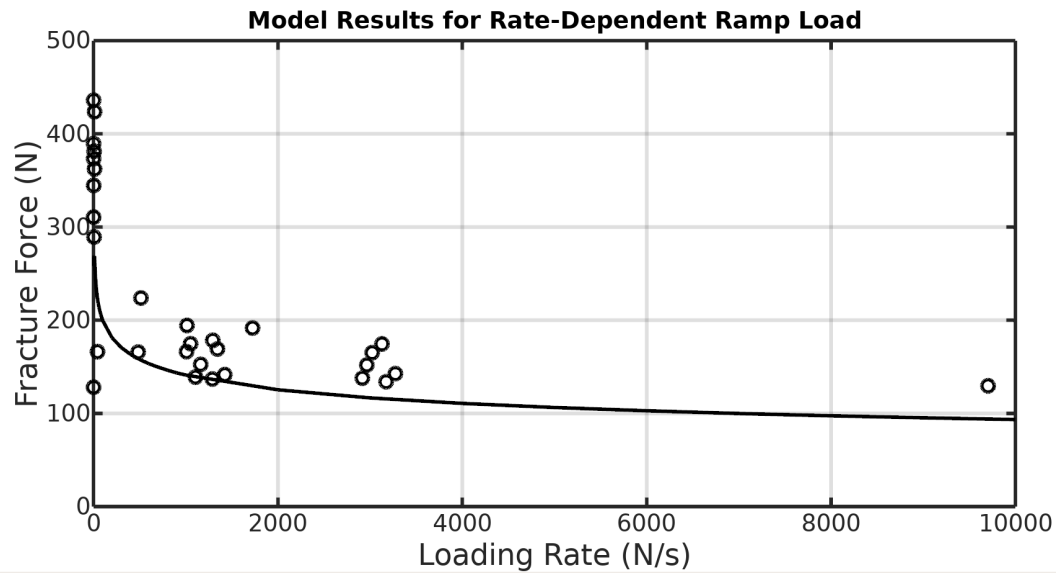
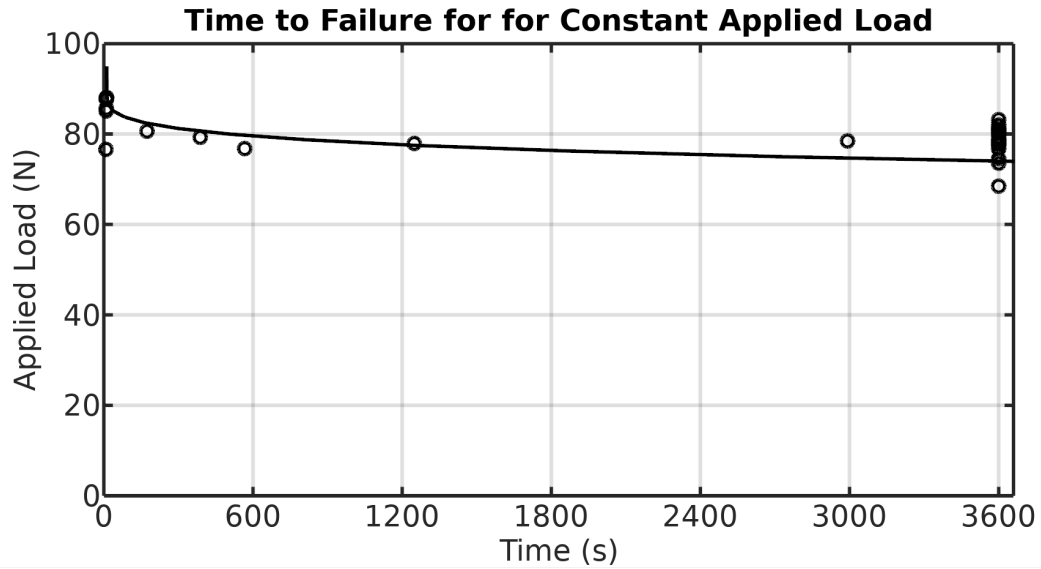
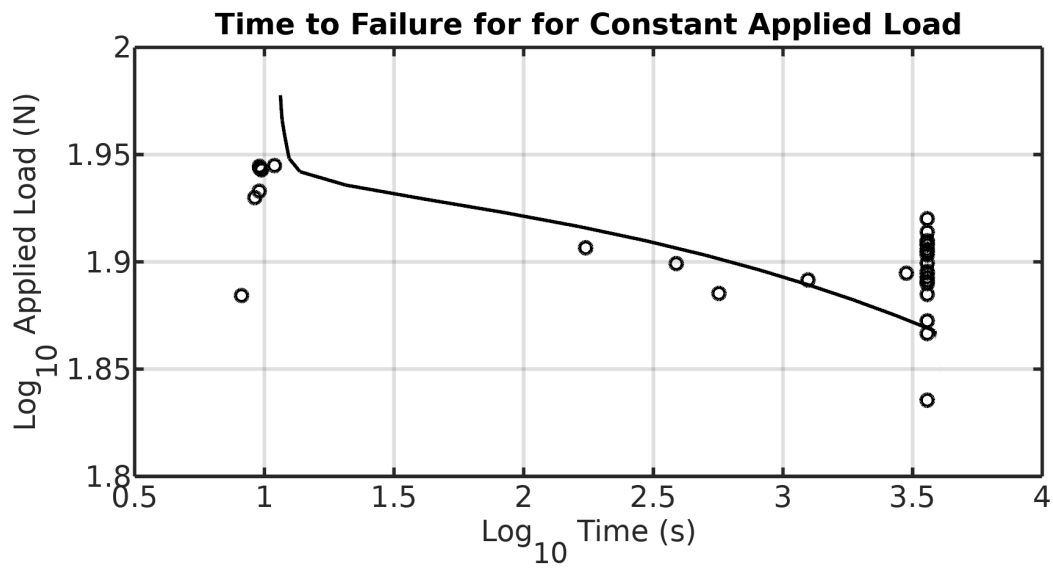


Figure 7.12: Model Results of 4-Point bending under constant ramping using parameters from Table 7.6.



(a)



(b)

Figure 7.13: Model Results of 4-Point bending under constant applied load using parameters from Table 7.6.

Parameter	Value
$C_0$	$1.20 \times 10^{-10} \text{ Pa}^{-1}$
$C_1$	$1.44 \times 10^{-10} \text{ Pa}^{-1} \text{s}^{-0.3134}$
$n$	0.313
$\sigma_m$	318 MPa
$\Gamma_G$	$1.61 \text{ J/m}^2$

Table 7.7: Rheological ice model parameters from experimental fitting.

agreement to the data collected. The parameters used slightly underestimates the strength of the ice in Figure 7.12 for the ramp loading series, and overestimates the strength of the ice (overestimates the time to failure) from the constant applied load series.

Given that the ice and temperature considered in Brill and Camp (1961) is different from that used in Chapter 5, these results are quite promising. Considering the differences, it is reasonable to consider varying the parameters from Table 7.6. The next few sections will explore the effects of changing the parameters of Table 7.6.

## 7.5 Independent Model Fits

In this section, the model is fitted to both of the beam series independently of each other. In other words, even though the ice is the same in both series (i.e., should have the same rheological parameters), no such restriction has been used.

Given that this is an initial run of the model, and there is limited experimental results, the first step is to see how well the model can predict the behaviour of the ice. The results presented here are the best fit the model can give for both series.

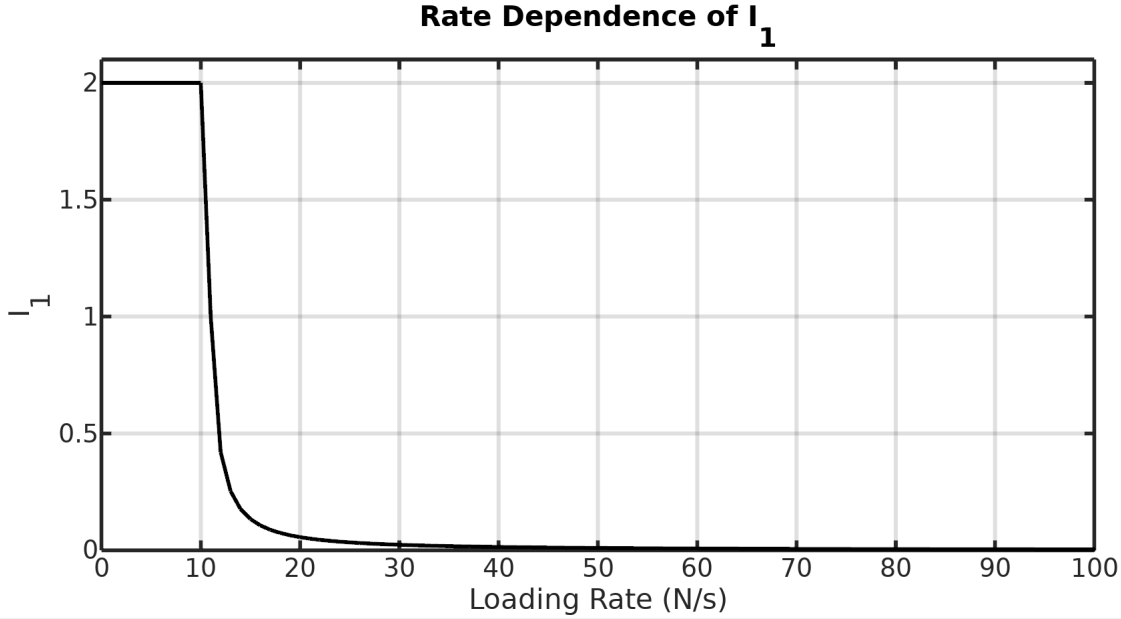


Figure 7.14: Rate dependence of  $I_1$  with loading rate, due to the change in the distribution of the process zone stress field under different loading rates.

### 7.5.1 Rate-Dependent Fracture Results

The model parameters used in this study are listed in Table 7.7. These parameters for ice were determined from a nonlinear optimization of the data to provide the best fits (in a least squares sense) for both of the experimental programs done using 4-point beam bending in ice. Following equation 6.182, and discussed in Sections 6.4.3 and 6.6.4,  $I_1$  was set to be loading rate dependent and is given by

$$I_1 = \min \left\{ \max \left\{ \dot{F} - 10 \frac{N}{s}, 0 \right\}^{-1.25}, 2 \right\} \quad (7.17)$$

and would have a value of 2 when held under constant load, as shown in Figure 7.14.

The model results for the ramp to failure of the first beam series is plotted in Figure 7.15. The figure shows that the model is able to capture the decreasing power-law of the force versus loading rate.



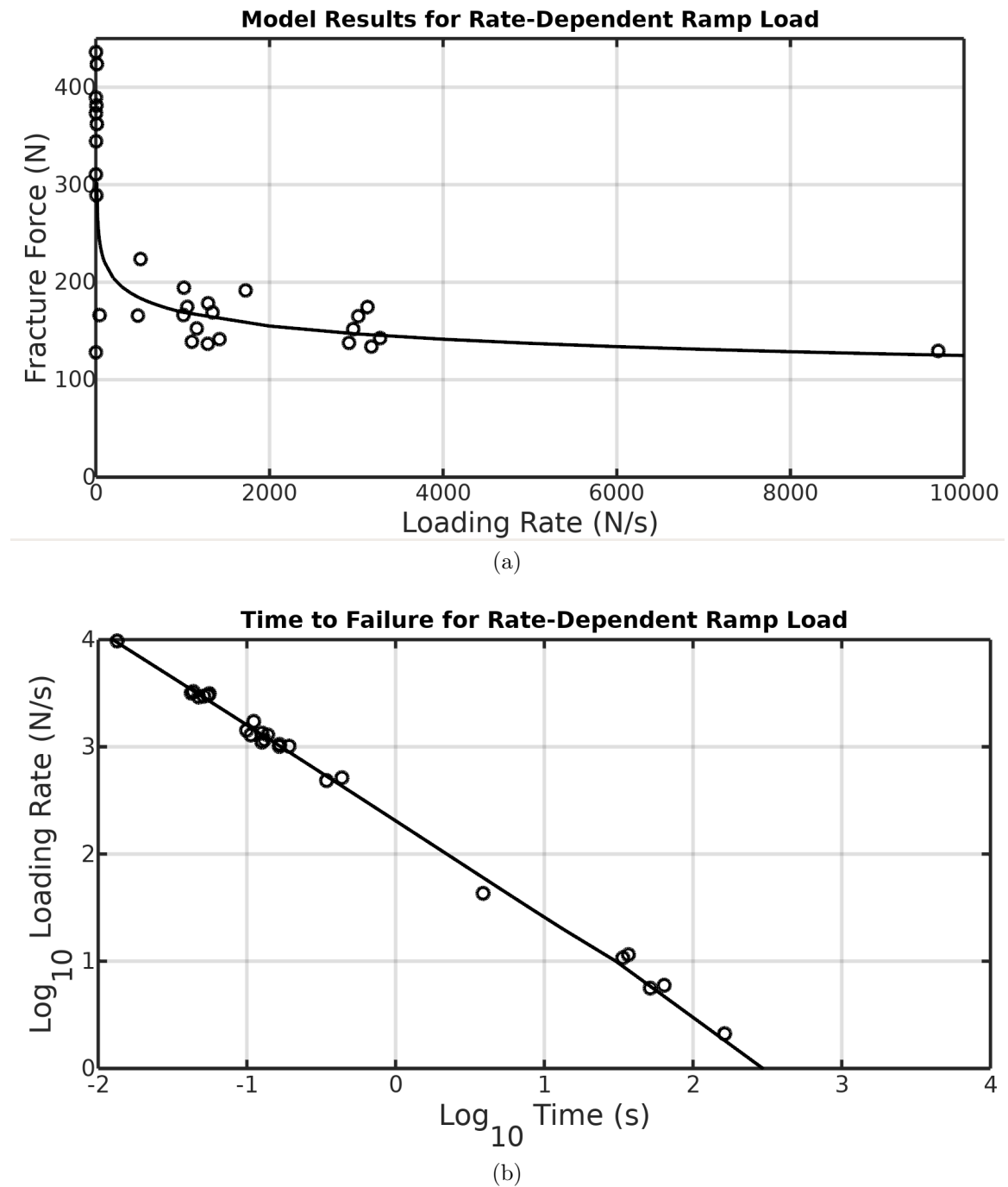


Figure 7.15: Results of model simulation for the ramp up to failure experiments. a) shows the data plot on a normal scale and b) shows the data plotted in the log-log domain.

Parameter	Value
$C_0$	$1.52 \times 10^{-10} \text{ Pa}^{-1}$
$C_1$	$1.71 \times 10^{-10} \text{ Pa}^{-1} \text{ s}^{-0.3134}$
$n$	0.514
$\sigma_m$	349 MPa
$\Gamma_G$	$1.53 \text{ J/m}^2$

Table 7.8: Rheological ice model parameters from experimental fitting.

### 7.5.2 Time to Failure Predictions

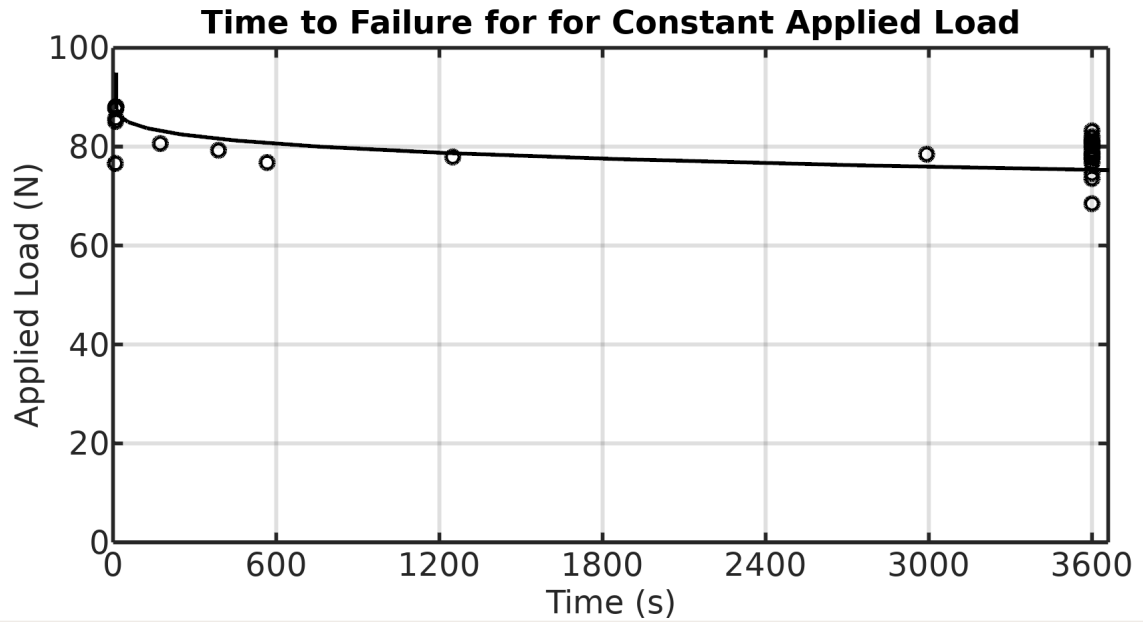
For the second series, the optimized model parameters are listed in Table 7.8. The results of the model simulation are plotted in Figure 7.16.

As before, the model provides excellent fits to the data, with only slightly longer times recorded for the higher loads (the model curve is slightly above the data at lower times). The model is able to replicate the decreasing power-law relationship between applied load and time to failure.

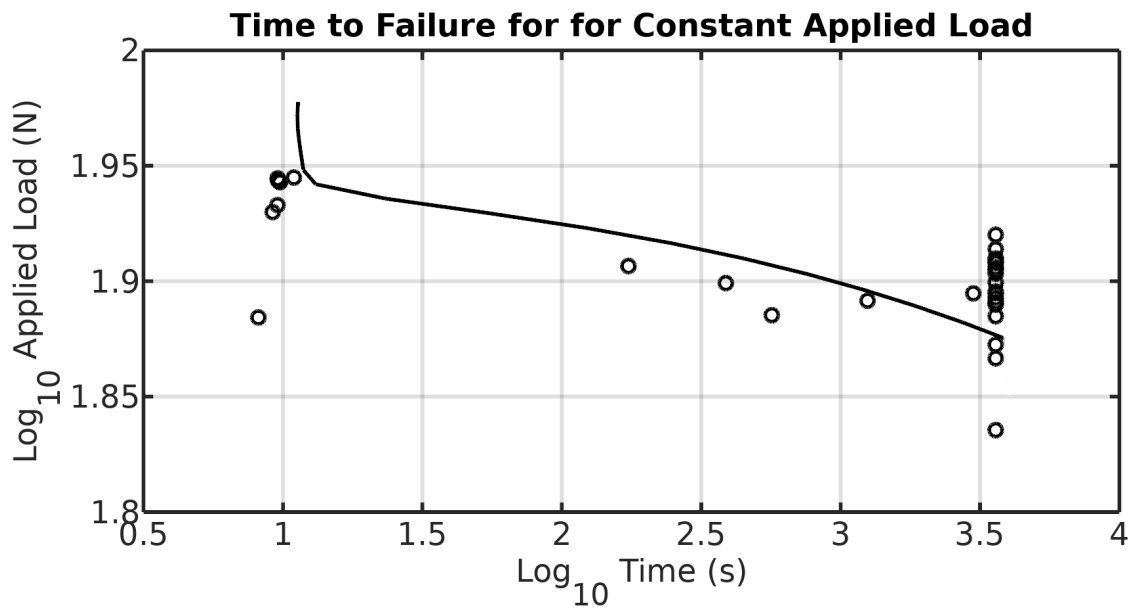
### 7.5.3 Discussion

The goal of this section was to illustrate the model's ability to fit the experimental data. Given the limited data available, the previous fits were individually optimized for each series independent of each other, even though they used ice grown using the same method. Given the natural variability in ice strength (as seen by the scatter in the data), this exercise demonstrated that the model is capable of fitting the data and exhibits behaviour that matches the behaviour of the ice samples.

The two optimization fits use strikingly different values for the parameters. Given the limited data (in particular, the time to failure data for the constant applied loads), this is not unexpected due to the scatter in ice strength. With more data, it is likely that the two optimizations would agree more as the scatter in ice strength can be averaged out more.



(a)



(b)

Figure 7.16: Model results for time to failure for the small ice beams used in the second series. a) shows the results the results using normal space, whereas b) shows the results in log-log space.

Parameter	Value
$C_0$	$1.15 \times 10^{-10} \text{ Pa}^{-1}$
$C_1$	$2.71 \times 10^{-10} \text{ Pa}^{-1} \text{ s}^{-0.3}$
$n$	0.30
$\sigma_m$	318 MPa
$\Gamma_G$	$1.60 \text{ J/m}^2$

Table 7.9: Rheological ice model parameters from experimental fitting of both beam series.

## 7.6 Combined Model Fits

Since the ice for both series was grown under similarly controlled conditions, it is reasonable to assume that they should have the same (if not similar) rheological parameters. In this section, the model was fitted to provide a set of parameters that would result in reasonable fits to both beam bending series. The rheological parameters used in the following sections are given in Table 7.9

### 7.6.1 Rate-Dependent Fracture Results

#### 7.6.1.1 Baseline Model Results

With the new ice parameter set ( $I_1$  is still defined by equation 7.17), the model results (shown in Figure 7.17) provide an excellent fit with the experimental data.

#### 7.6.1.2 Sensitivity Analysis of Model to Rheological Parameters

Given the uncertainty and variance that the properties of ice exhibit, a sensitivity analysis of the model to the ice parameters has been conducted. For each parameter, five other values were tested along with the baseline result.

For each run, a single parameter was changed from the base value to one of the values in Table 7.10. For example, the Medium run in Figure 7.18a replaces the value of  $C_0$  from  $1.154 \times 10^{-10}$  to  $1.3001 \times 10^{-10}$ .

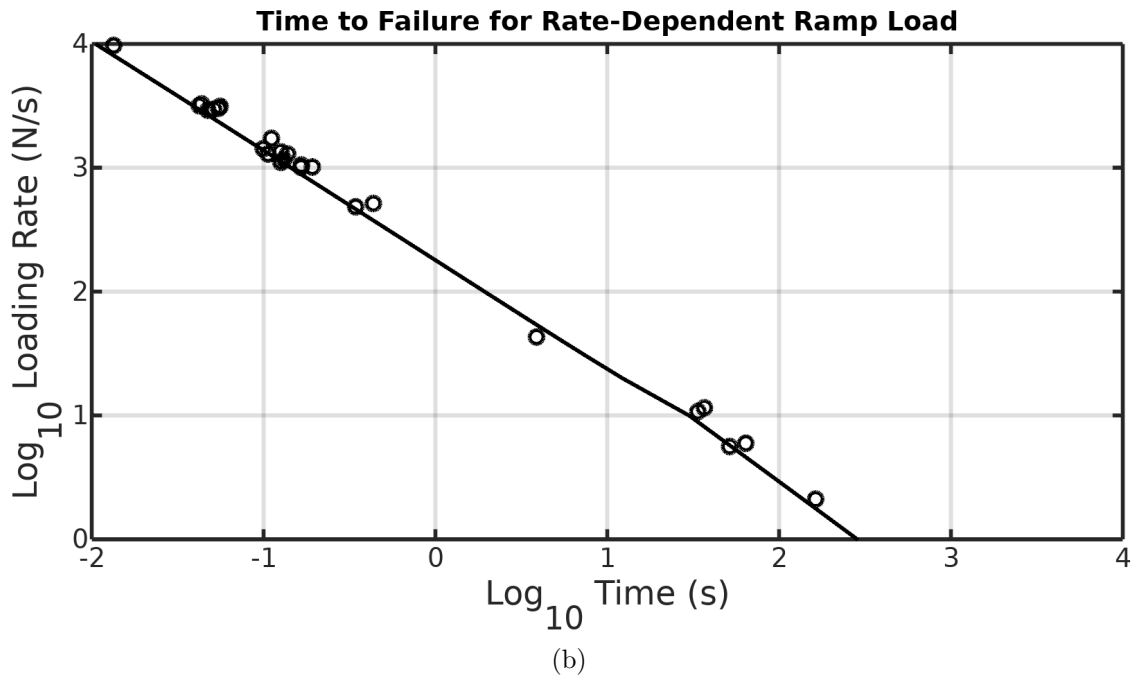
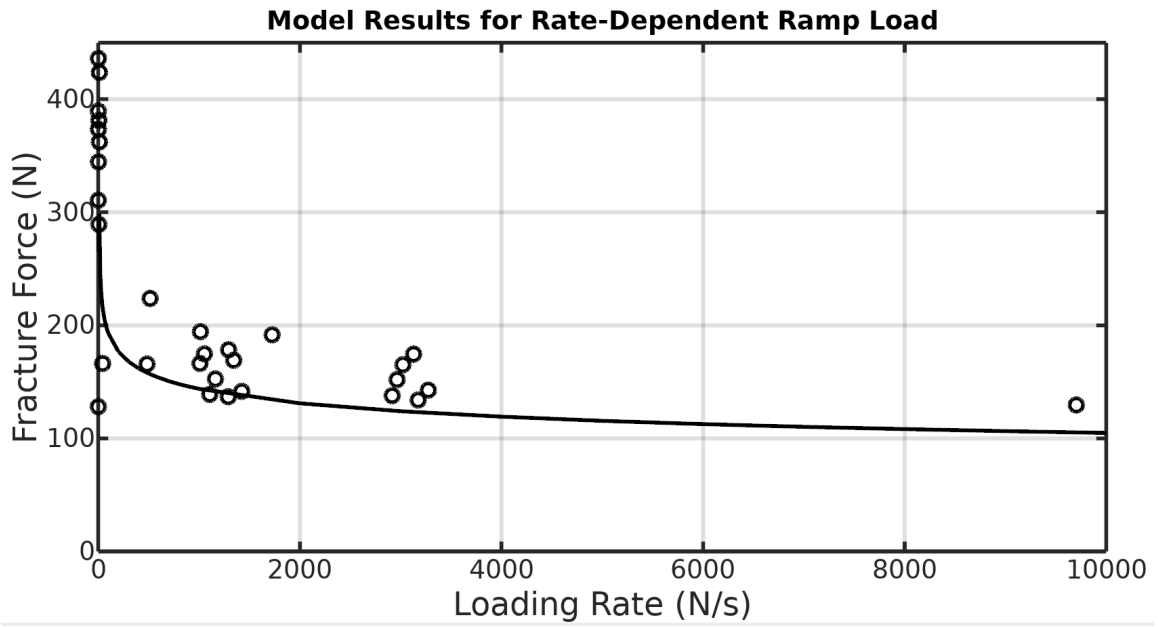


Figure 7.17: Results of model simulation for the ramp up to failure experiments. a) shows the data plot on a normal scale and b) shows the data plotted in the log-log domain. The rheological ice parameters used are in Table 7.9.

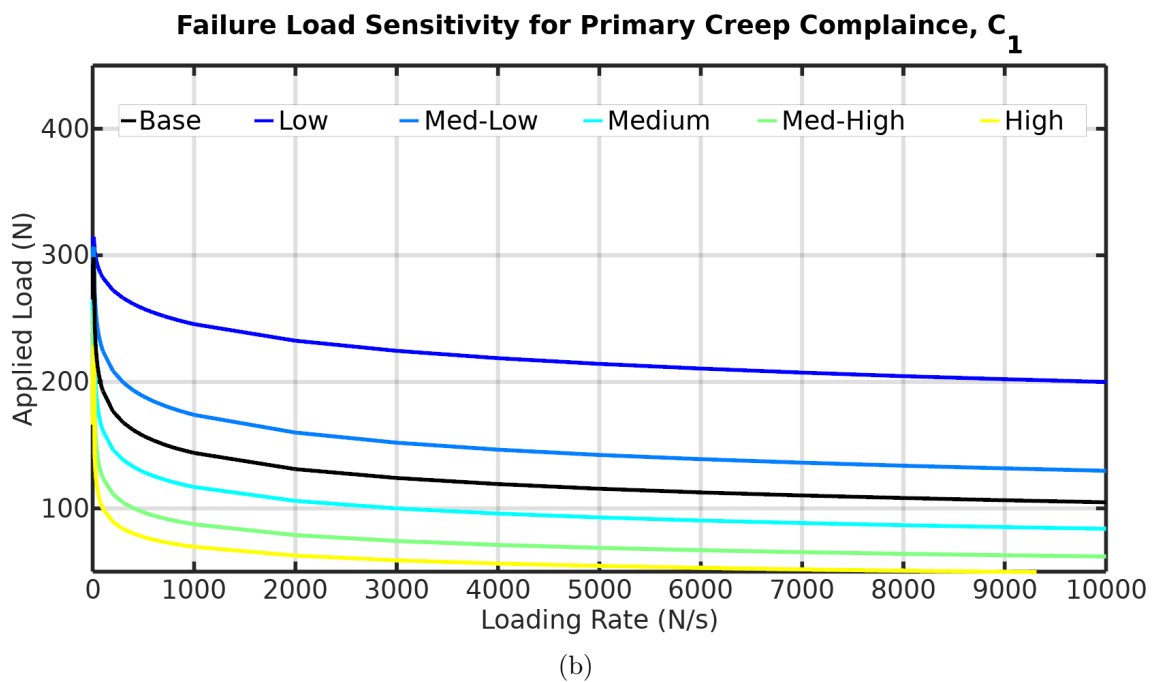
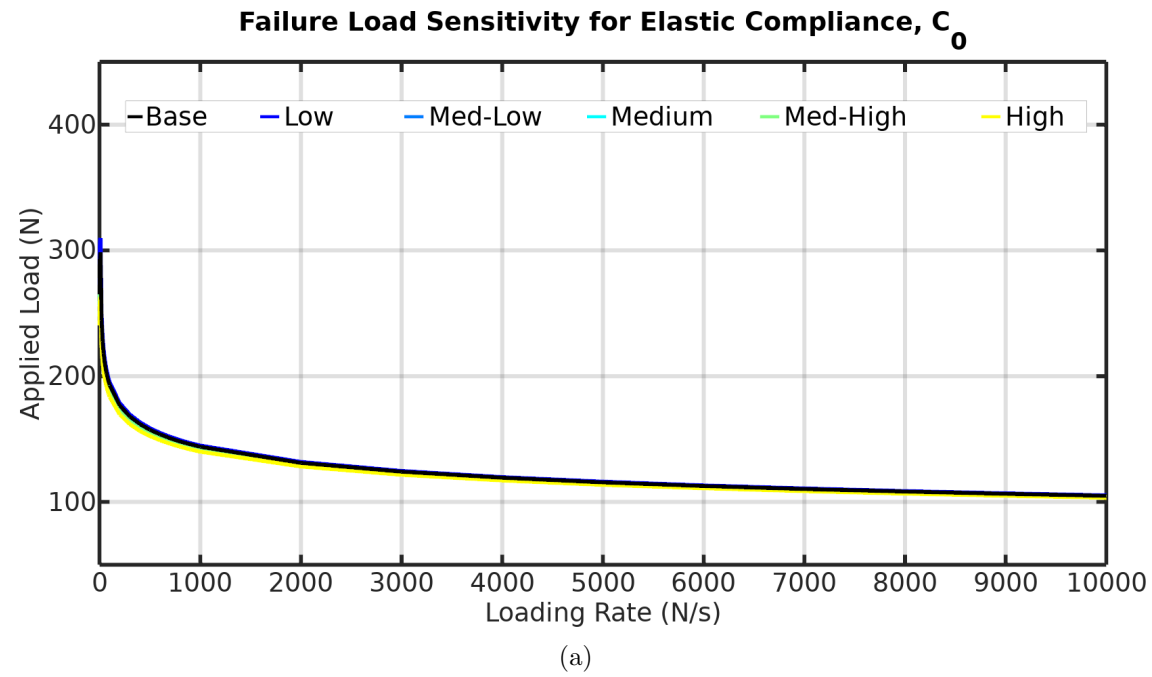
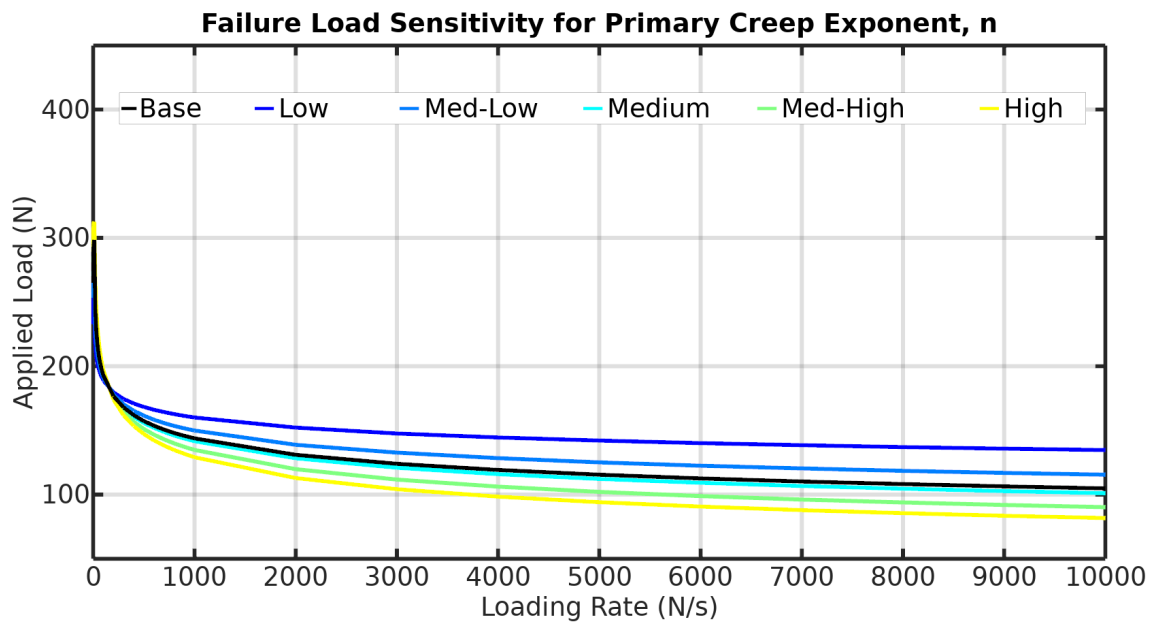
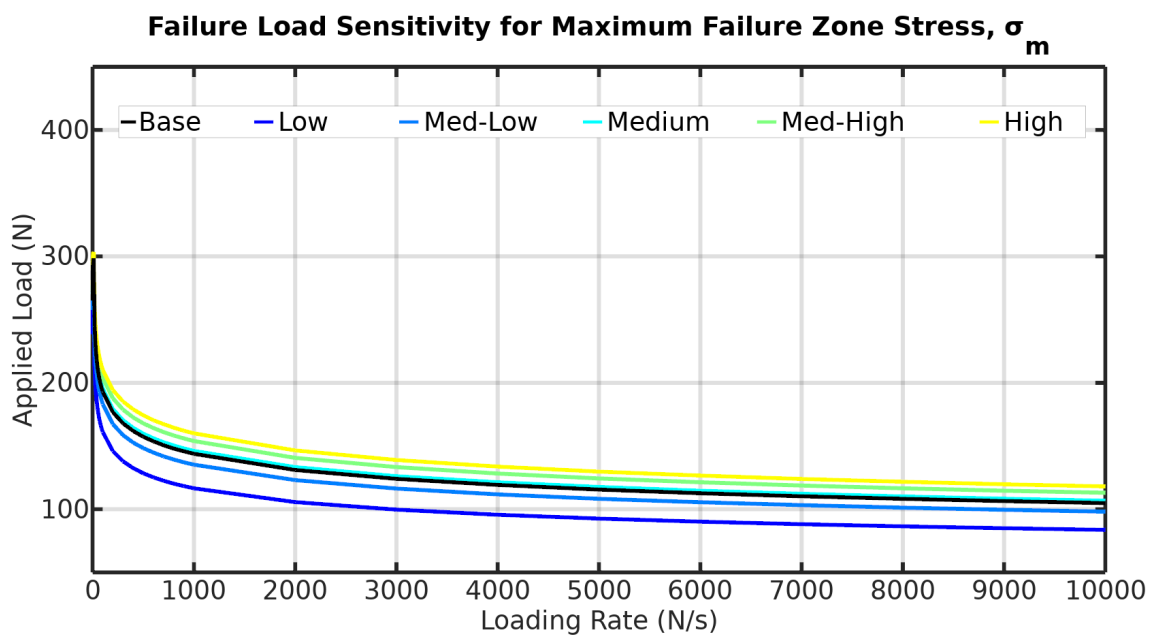


Figure 7.18



(c)



(d)

Figure 7.18

Sensitivity Values For Ramp Loading						
Variable	Base	Low	Med-Low	Medium	Med-High	High
$C_0 \times 10^{-10}$	1.15	1.06	1.18	1.30	1.42	1.54
$C_1 \times 10^{-10}$	2.71	0.271	1.35	5.42	13.5	27.1
$n$	0.300	0.150	0.238	0.325	0.413	0.500
$\sigma_m$	318	100	225	350	475	600
$\Gamma_G$	1.60	1.00	1.25	1.50	1.75	2.00

Table 7.10: Values of the parameters used in the sensitivity analysis for the ramp loading.

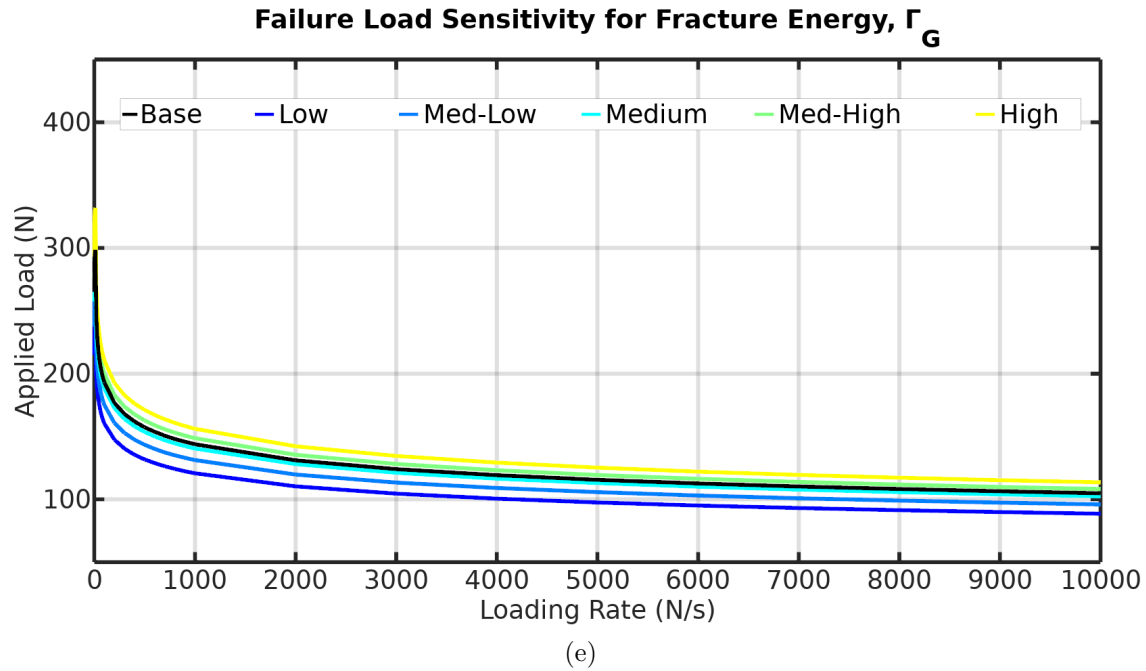


Figure 7.18: Sensitivity analysis of rheological ice parameters for ramp up to failure simulations.



Figure 7.18a shows the sensitivity results of the elastic compliance from  $1.056 \times 10^{-10}$  to  $1.54 \times 10^{-10}$  ( $E = 6.47\text{--}9.47$  GPa). Quite surprisingly, the model results are rather insensitive to the value of elastic compliance for the ramp loading experiments. One effect that the elastic compliance has is to change the peak load seen in the slower loading tests (lower compliance increases the peak ice strength).

Given that the  $C_1$  parameter is less known than  $C_0$  (which could be constrained by reasonable values of elastic modulus), the  $C_1$  parameter was allowed to vary by an order of magnitude in either direction. Figure 7.18b shows that the model is very sensitive to  $C_1$  over this test range. Lower values of  $C_1$  increase the strength of the ice (as expected).

The last creep parameter,  $n$ , was tested over a range of 0.15–0.5, which would cover any expected value of  $n$ . Figure 7.18c shows that the model is rather insensitive to  $n$  for slower rates, but becomes rather sensitive for the faster loading rates. Higher values of  $n$  decrease the strength of the ice as it causes an increase in the ice's ability to undergo creep.

Aside the creep parameters, the model also considers the maximum stress in the process zone, which would be near the required stress to break the bonds in the lattice. The value of  $\sigma_m$  was allowed to vary from 100–600 MPa, consistent with an expected fracture stress of the bonds. Figure 7.18d shows that the model is rather sensitive to the value of  $\sigma_m$ , with increasing  $\sigma_m$  leading to stronger ice, as expected.

Lastly, Figure 7.18e shows the model's sensitivity to the fracture energy,  $\Gamma_G$ . Similar to  $\sigma_m$ , increasing  $\Gamma_G$  increases the strength of the ice as this parameter is directly related to the strength of the ice.

Sensitivity Values For Constant Applied Loading						
Variable	Base	Low	Med-Low	Medium	Med-High	High
$C_0 \times 10^{-10}$	1.15	1.05	1.18	1.30	1.42	1.54
$C_1 \times 10^{-10}$	2.71	1.35	2.03	3.39	4.06	4.74
$n$	0.300	0.150	0.238	0.325	0.413	0.500
$\sigma_m$	318	100	225	350	475	600
$\Gamma_G$	1.60	1.00	1.25	1.50	1.75	2.00

Table 7.11: Values of the parameters used in the sensitivity analysis for the constant applied load tests.

## 7.6.2 Time to Failure Predictions

### 7.6.2.1 Baseline Model Results

Figure 7.19 shows the model results for the parameters from Table 7.9. This is clearly not a plot that best fits the experimental data, as was done in Section 7.5.2.

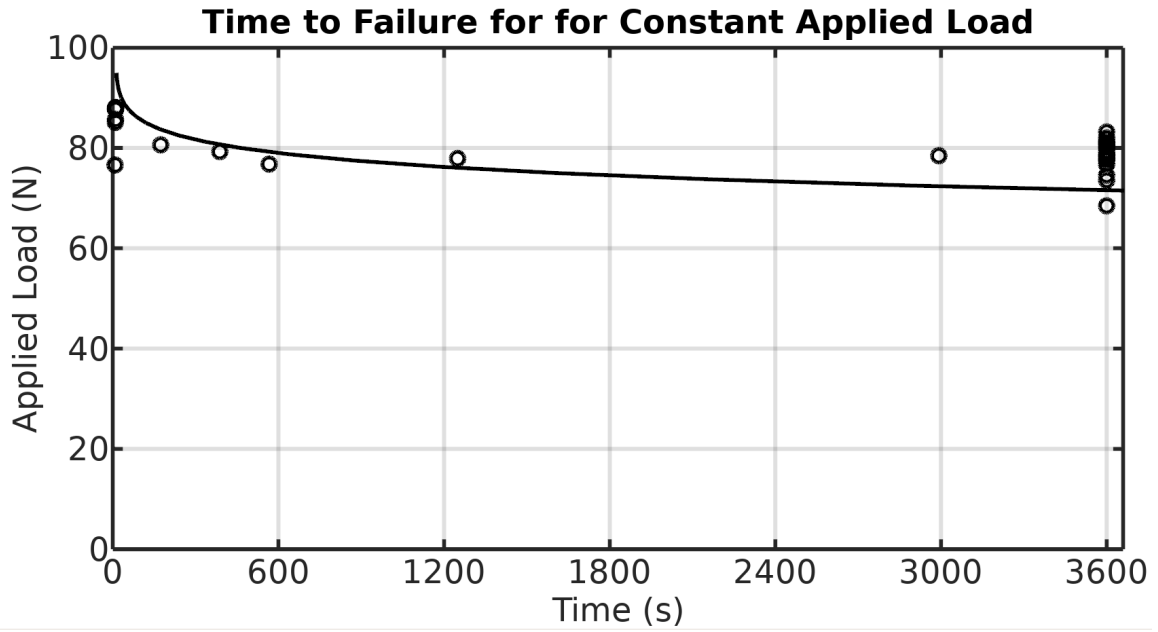
While not a best fit, the model still behaves similarly to the data. Given the variability of ice fracture strength and the limited data available, it is not unreasonable to assume that there would be many data points that could exist on the plot between the model curve and the available data points. This can be seen in the amount of scatter in Figure 5.7 from the experiments that never broke (those plotted at the one hour mark).

Clearly, more data is needed to truly determine how well the model predicts the time to failure. However, the results are promising in that more data would likely show that the model prediction here is closer than it seems and that a better fit could be obtained with more data.

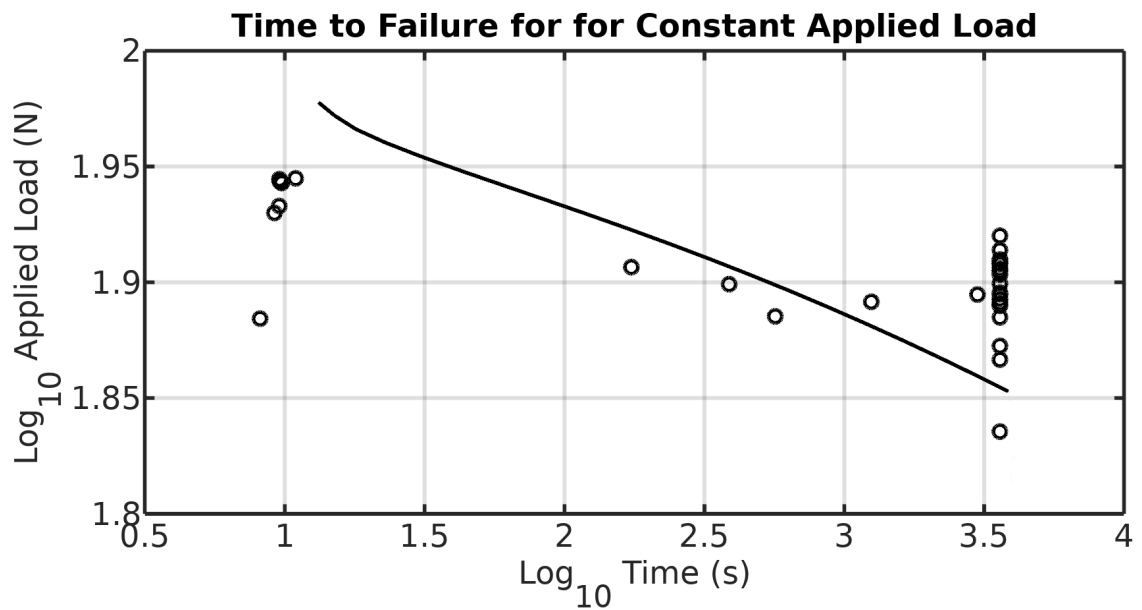
### 7.6.2.2 Sensitivity Analysis

Similar to the ramp loading case, a sensitivity analysis was performed for the constant applied load tests. The values of the parameters are listed in Table 7.11.

Figure 7.20a shows that the time to failure series is much more sensitive to the



(a)



(b)

Figure 7.19: Model Results for time to failure for the small ice beams used in the second series. a) shows the results the results using normal space, whereas b) shows the results in log-log space. These results use the parameter set from Table 7.9.

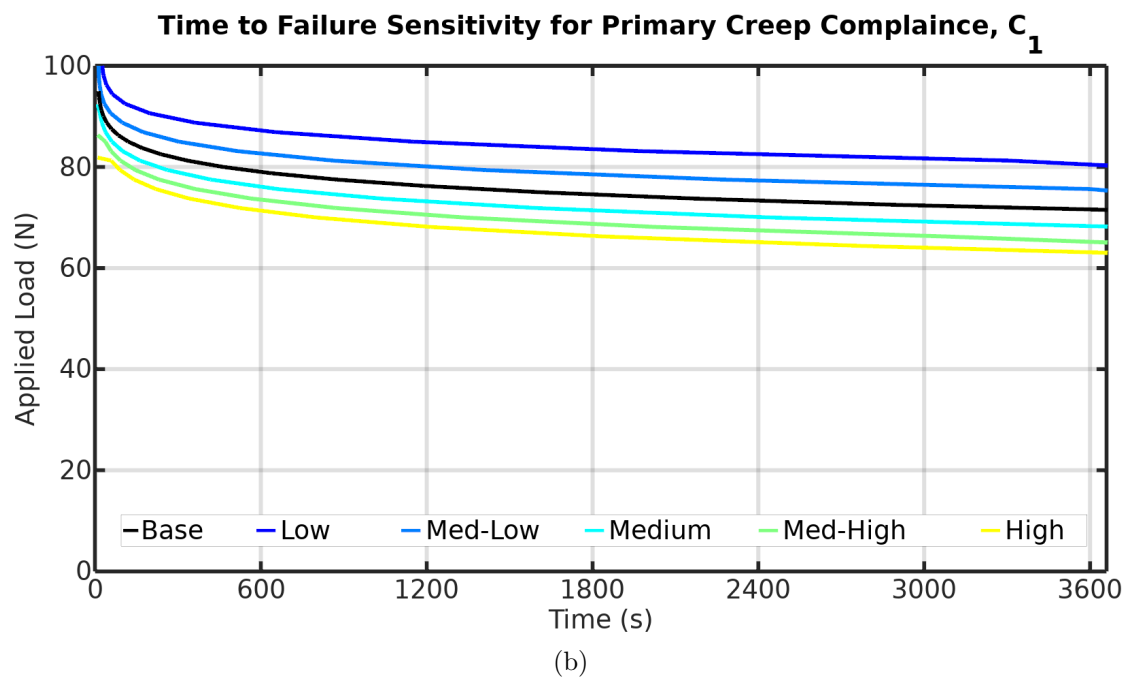
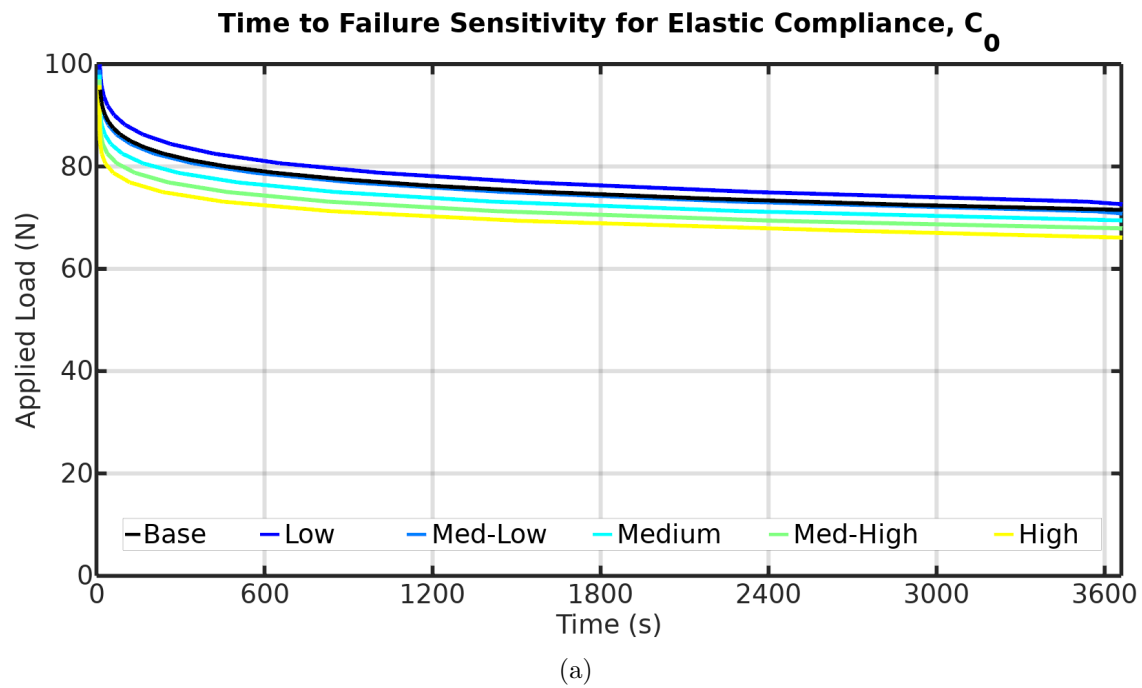


Figure 7.20

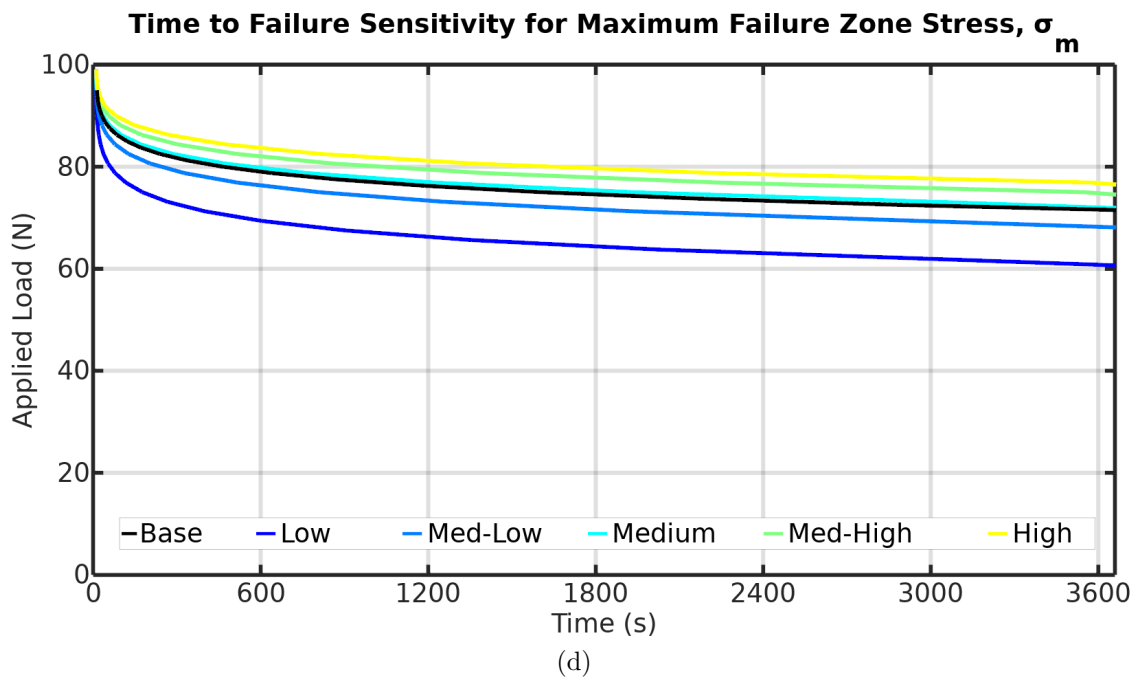
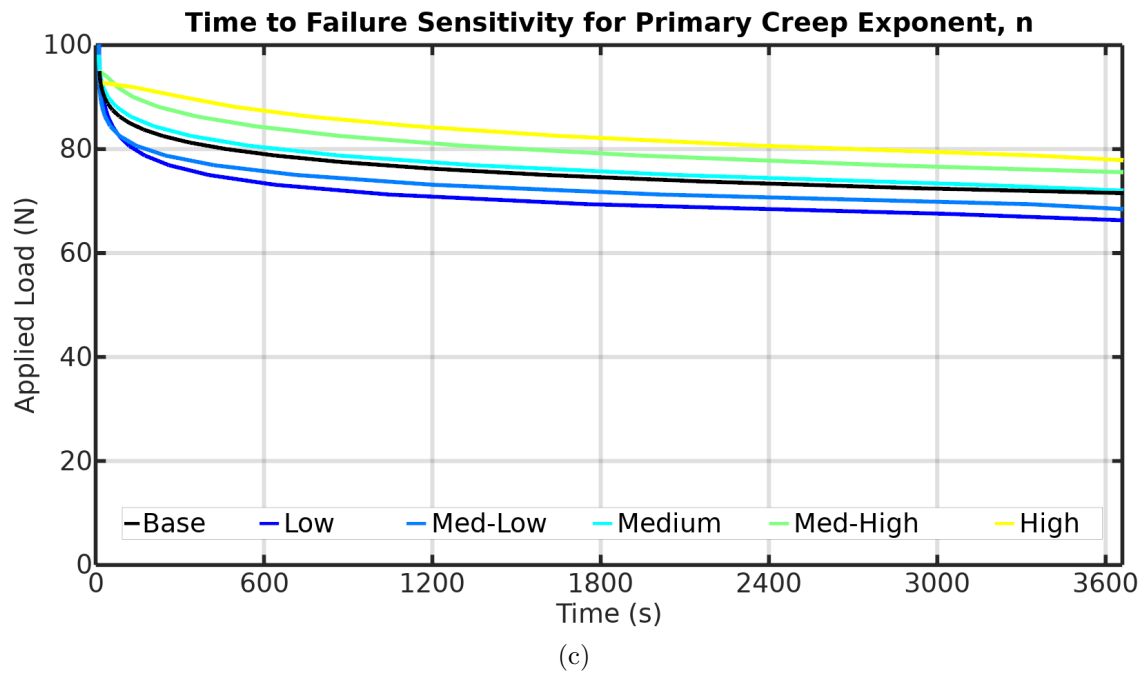


Figure 7.20

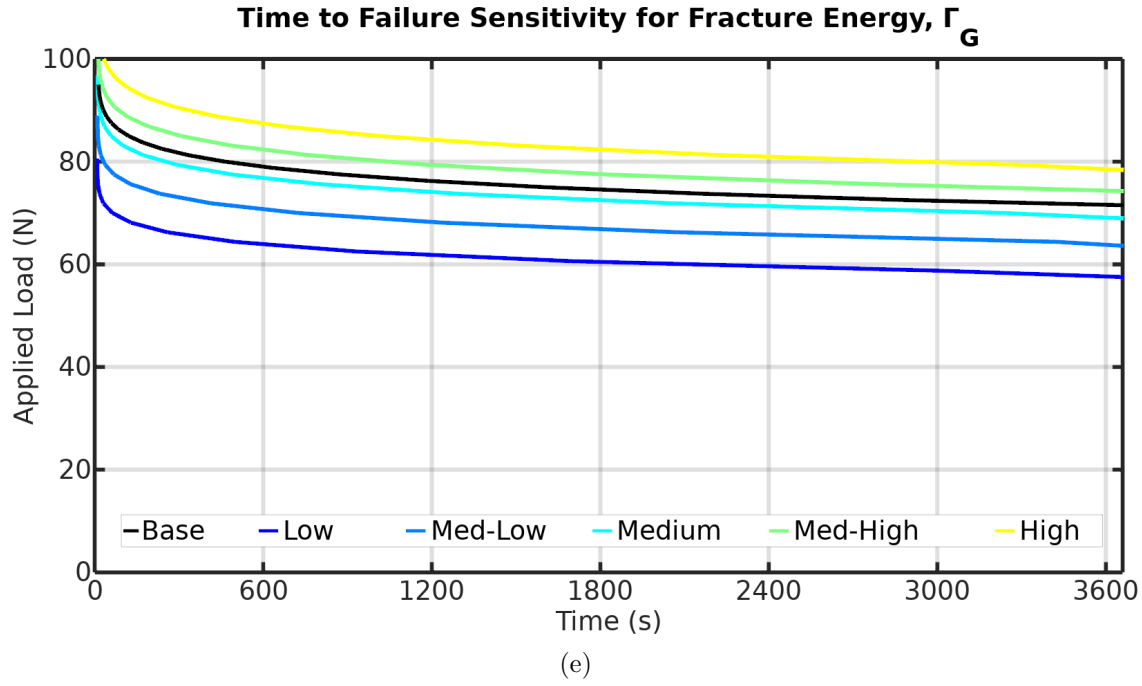


Figure 7.20: Sensitivity analysis of rheological ice parameters for time to failure simulations.

value of elastic compliance than the ramp series was. As expected, increasing  $C_0$  causes the ice to be weaker, leading to shorter time to failure under equal loading (the model curve is lowered).

The time to failure series is highly sensitive to the value of  $C_1$ . For the ramp series, the value of  $C_1$  as varied from 0.1–10 times the base value, but this was changed to 0.5–1.75 for the time to failure series due to the high sensitivity. For the values tested in this range, Figure 7.20b shows that the model is still rather sensitive to  $C_1$ , with increased compliance leading to weaker ice, just like  $C_0$ .

Figure 7.20c shows the model sensitivity to the creep exponent,  $n$ . Quite counter-intuitively, the model shows that the ice is stronger with increasing  $n$ . The reason for this can be seen in equation 6.161. Equation 6.161 shows that the crack growth rate has an exponent of  $1/n$  around the terms in parentheses (i.e., it is the  $n$ -th root). Larger values of  $n$  actually suppress crack growth. Unlike the ramp loading tests,

where an excessive force was used to break the ice samples, the constant load tests were designed so that the increasing crack size was the reason for failure instead of the applied load. Since  $n$  tends to suppress crack growth, this leads to longer times to failure as  $n$  is increased.

Figures 7.20d and e show the sensitivity of the model to the process zone parameters,  $\sigma_m$  and  $\Gamma_G$ . The model is rather sensitive to both of these parameters, with more sensitivity to  $\Gamma_G$ . Increasing either leads to stronger ice that requires longer times to fail under similar constant loads, which is an expected result.

### 7.6.3 Discussion and Summary

The results of combined model fits are shown in figures 7.17 and 7.19. For a single set of parameters, the model was able to provide reasonable fits to both experimental series. The combined parameters underestimate the strength of the ice of the ramp loading series in comparison to the optimized values, and overestimates the strength of the ice of the constant load series in comparison to the optimized parameter set.

As suggested in Section 7.6.2.1, more data could be collected for the constant load series. It is not unreasonable to suggest that new data would likely include stronger ice samples. In other words, it is possible that new data would suggest that the ice is stronger than the constant load series data would indicate from the limited data available. Should this be the case, then a new parameter set could be fitted that would match this stronger ice as well as provide a better fit for the ramp loading series.

Sensitivity analysis of the model suggests that the model is highly sensitive to all the parameters within a reasonable range of values for each. The model results were not sensitive to the elastic compliance for the ramp loading series, but were for the constant load series. In both cases, the elastic compliance did affect the peak strength

of the ice.

The model was really sensitive to the primary creep compliance coefficient,  $C_1$ , with increasing values leading to weaker ice. Given that the primary creep of the ice is directly proportional to this value, it is no surprise that this term is rather important. The constant load series was more sensitive to the value of  $C_1$  than the ramp load series. This can be explained by the constant load series tests requiring longer times, allowing for more creep to occur.

The model results behave striking different under ramp loading versus constant loading for changes in the primary creep exponent,  $n$ . Under ramp loading, increases in the value of  $n$  lead to weaker ice, whereas increasing  $n$  leads to stronger ice under constant loading. This has to do with the dual nature of  $n$ . On one hand, increasing  $n$  would lead to increased creep compliance, which would result in weaker ice (similar to how larger  $C_1$  leads to weaker ice). On the other hand, as mentioned in Section 7.6.2.1,  $n$  also acts to suppress the growth of cracks. Under ramp loading, the ever-increasing applied load is what causes the ice to fail and there is little stable crack growth before catastrophic failure, suggesting that  $n$  mainly acts to cause weaker ice due to increased compliance. For the constant load series, the main reason the ice fails is due to the stable growth of the crack that leads to catastrophic failure. Since the constant load series relies on crack growth,  $n$ 's effect of suppressing the crack growth dominates over its weakening of the ice due to increased compliance.

The last two parameters,  $\sigma_m$  (maximum process zone stress) and  $\Gamma_G$  (fracture energy), detail the processes occurring in the process zone ahead of the apparent crack tip. These two parameters are related to the discrete fracture processes (such as bond breaking or dislocation glide) occurring in the zone. As such, increases in these values lead to increased ice strength for both series, as expected.

The sensitivity analysis also alludes to reasons that ice exhibits so much scatter



in its strength. For example, ice is known to exhibit Young's modulus values from 5 – 11 GPA which the sensitivity analysis shows can have a significant impact on the strength of ice. This is likewise true for other parameters as well. Considering the works of Sinha (Sinha, 1978, 1979, 1983, 1988), the primary creep component is shown to be related to the size of the grains in the ice. While all attempts to create uniform grain sizes were taken into consideration, the thin sections of ice samples shows that there is some variance in the sizes (and orientations) that will have a clear effect on the primary creep coefficient. These will also likely have an effect on other parameters as well. Given the importance of how the local stress ( $\sigma_m$ ) affects the results, depending on the exact location of the crack in terms of other defects (like dislocations, grain boundaries, triple points, etc...) will have a significant effect on the local stress value, which will affect the strength of ice. While not explored in this project, the parameters will also be temperature dependent, which will affect the strength of ice.

Both the model fits and the sensitivity analysis suggests that the model can adequately describe the fracture properties of the ice samples under 4-point bending for constant applied loads and constant ramp loading. Sensitivity analysis shows that the model parameters behave in a manner that is consistent with the underlying physics that they describe.

The model has an advantage over a fully-developed finite analysis in that is fast to run, requiring 2–3 minutes of runtime for a single run using 6 threads in parallel (using the OpenMP library with Fortran) on a personally-owned laptop running a quad-core 2.3 GHz processor and 8 Gb of ram. The main drawback of the model is that it is designed for specific geometries and would not work for generalized loading scenarios that an finite element analysis would be required for (this could be a future implementation, as this model was designed to work for the experiments performed

Parameter	Value
$C_0$	$1.224 \times 10^{-10} \text{ Pa}^{-1}$
$C_1$	$7.929 \times 10^{-15} \text{ Pa}^{-1.499} \text{ s}^{-0.20}$
$n$	0.351
$\sigma_m$	95.1 MPa
$\Gamma_G$	$2.173 \text{ J/m}^2$

Table 7.12: Rheological ice model parameters from experimental fitting CT-specimens from Liu and Miller (1979).

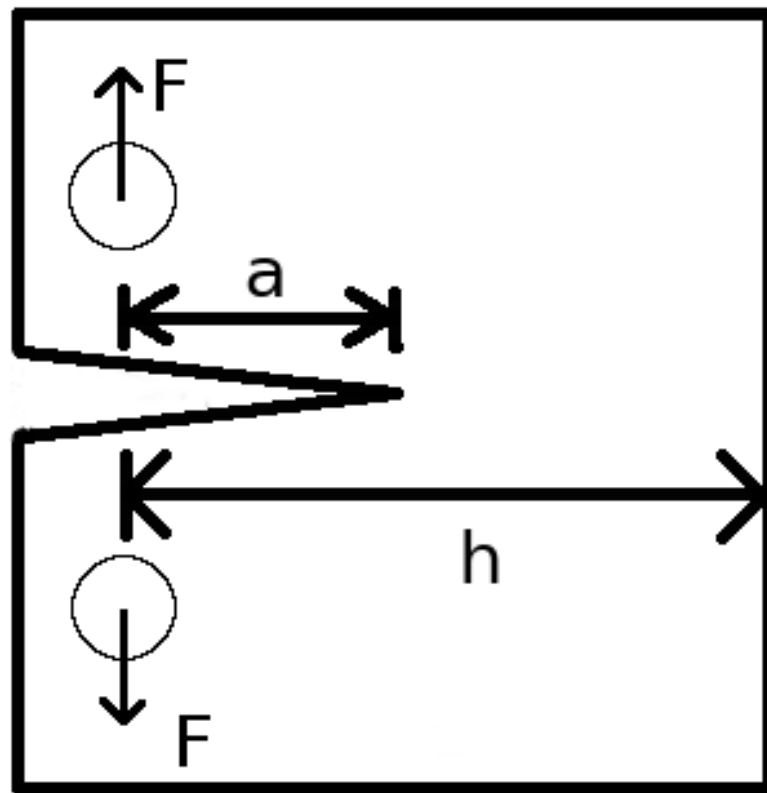
in-house).

## 7.7 Model Fits of Liu and Miller (1979)

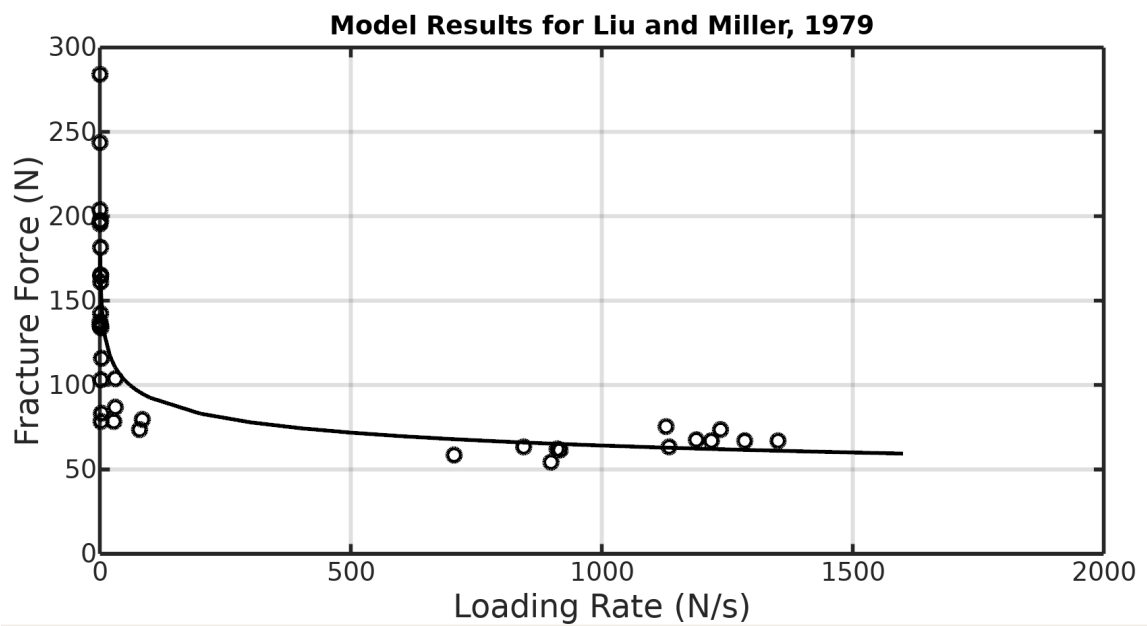
So far, the model has been used to fit the data from two 4-point bending series performed in-house. It is also reasonable to assume the model would work for a central crack in thin plates, as it is developed from Schapery (1975a,b,c) who developed his model for that case.

In this section, the model will be shown to be flexible enough to work for other geometries with a few modifications to the model described in Chapter 6. To show how this can be done, consider the specimens tested in Liu and Miller (1979). As discussed in Section 3.1.7, Liu and Miller (1979) performed ramp loading tests on CT-specimens, as shown in Figure 7.21a.

Table 7.12 and Figure 7.21b show the model fit of the experimental data from Liu and Miller (1979). The data from Liu and Miller (1979) list the results in terms of fracture toughness and rate of fracture toughness. It is assumed that these are the



(a)



(b)

Figure 7.21: Comparison of results from Liu and Miller (1979) (dots) to viscoelastic model with parameters used in Table 7.12

apparent fracture toughness calculated (i.e., assuming no crack growth) using

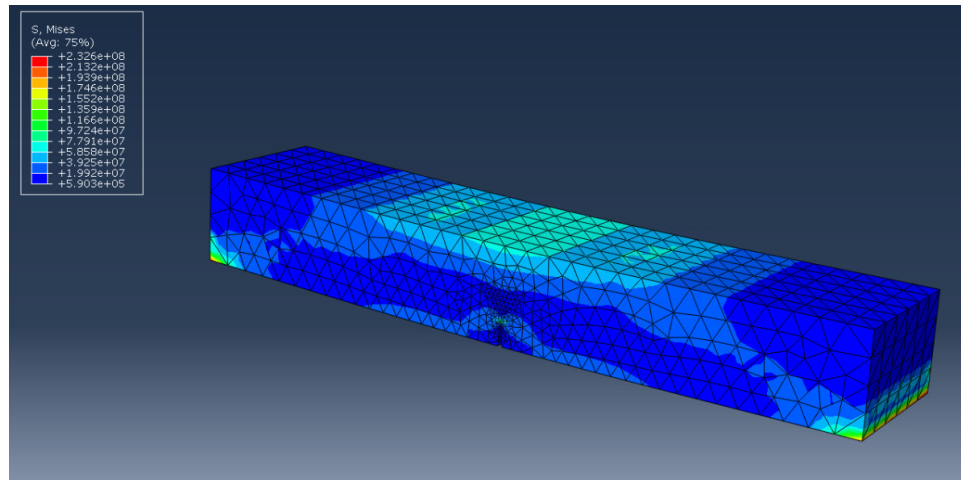
$$\begin{aligned}
 K_I &= \frac{Y \{\alpha\} F}{B \sqrt{h}} \\
 \dot{K}_I &= \frac{Y \sqrt{a} \dot{F}}{BL} \\
 Y &= 29.6 - 185.5\alpha + 655.7\alpha^2 - 1017\alpha^3 + 638.9\alpha^4
 \end{aligned} \tag{7.18}$$

where  $B$  is the thickness of the CT-specimen and  $h$  is its length (see figure 7.21a). The force and loading rates were derived from equation 7.18 using the  $K_I$  and  $\dot{K}_I$  from Liu and Miller (1979).

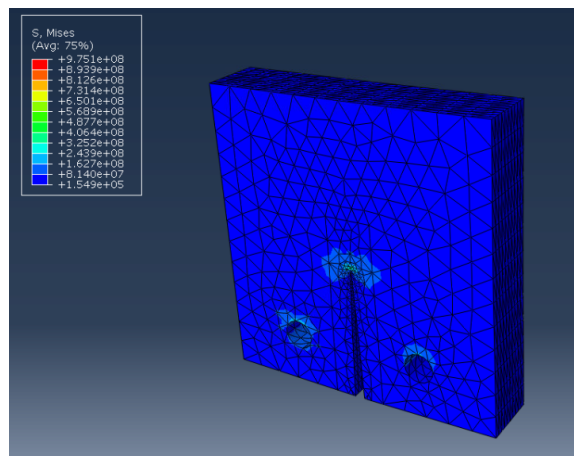
The model for the beam series was modified to use the 1<sup>st</sup> and 3<sup>rd</sup> of equation 7.18 for the stress intensity and geometric shape functions. The model parameters were fitted to match the force and loading rate derived from the data. The results of this fit can be seen in Figure 7.21b, with the parameter values defined in Table 7.12.

Much like the ramp to failure beam bending tests, the data for the ramp to failure CT-specimens display a decreasing power-law type relationship, which is matched by the model. It is expected that the parameters of the ice from Liu and Miller (1979) would be different due to

- The type of ice used – in-house experiments used isotropic ice with grain size of 2 3.35 mm while Liu and Miller (1979) grew columnar ice.
- The orientation of the c-axis. The beams would have a random distribution of c-axis orientations, while the CT-specimens had c-axis perpendicular to the long axis of the grains.
- The bubble density of the ice samples.
- Temperature – All the in-house experiments Were done at -10°C, whereas the tests from Liu and Miller (1979) varied from -1°C to -46°C.



(a)



(b)

Figure 7.22: Static loading finite element analysis of a) In-house 4-point beam bending and b) compact tension specimen of Liu and Miller (1979).

Aside from the different ice types, different failure loads in the ice may be due to the geometry of the specimens. Finite element analysis of the two geometries was performed. For the beam in Figure 7.22a, the bottom rollers remained stationary and the top rollers were displaced 2 mm into the ice. For the compact tension specimen in Figure 7.22b, one grip hole remained stationary while the other was displaced vertically by 2 mm.

The analysis showed that for these same displacements (as the respective authors would have measured), the stresses near the crack in the compact specimen were roughly four times greater than those of the beam. This would suggest that the cracks in Liu and Miller (1979) were subject to greater stresses and failed under lower loads than the ice beams from Chapter 5.

With a few quick changes to the definitions of stress intensity and the geometric shape function, the model was quickly converted from a 4-point bending simulation to a CT-specimen simulation. While not done here, it is easy to see how the model can be quickly changed to work with a variety of specimen types.

## 7.8 Time to Failure Approximation

As discussed in Section 6.2.4.5, equation 6.117 is an approximation of the time to failure for a crack in a thin plate. For the case of thin plate, equation 6.117 could be used to approximate the time to failure without the need of a fully developed model (though this equation would ignore the effects of the initial growth of the process zone as it only considers the continuous crack growth stage).

More generally, it has been suggested in Jordaan and Xiao (1992), with a physical basis discussed in Schapery (1984b) and Schapery (1991), that the crack growth rate

for any crack can be represented by

$$\dot{a} = c_1 J^k \quad (7.19)$$

where  $J$  is the energy release rate and  $c_1$  and  $k$  are constants.

Using the elastic approximation

$$\begin{aligned} \dot{a} &= c_1 G^k \\ \dot{a} &= c_1 \left( \frac{(1 - \nu^2) K^2}{E} \right)^k \end{aligned} \quad (7.20)$$

where  $G$  is the elastic energy release rate for plain strain from equation 3.24.

Substituting equation 6.164 into equation 7.20 gives

$$\dot{a} = c_1 c_2 \left( Y \{ \alpha \} \frac{\sqrt{\alpha}}{(1 - \alpha)^{\frac{3}{2}}} \right)^{2k} \quad (7.21)$$

with  $\alpha = a/h$  and

$$c_2 = (1 - \nu^2) E^{-k} \left( \frac{3F(S_2 - S_1)}{2dh^{\frac{3}{2}}} \right)^{2k} \quad (7.22)$$

where the beam geometry terms are as shown in Figure 6.8 and are listed in Table 7.5 for the constant load series.

Rearranging equation 7.21 leads to

$$\int_{a_0}^a \left( Y \{ \alpha \} \frac{\sqrt{\alpha}}{(1 - \alpha)^{\frac{3}{2}}} \right)^{-2k} da = \int_0^t c_1 c_2 dt \quad (7.23)$$

Equation 7.23 can be solved numerically for any given values of  $c_1$ ,  $k$ , and the applied load ( $F$ , which will affect  $c_2$ ). Numerical optimization of equation 7.23 results

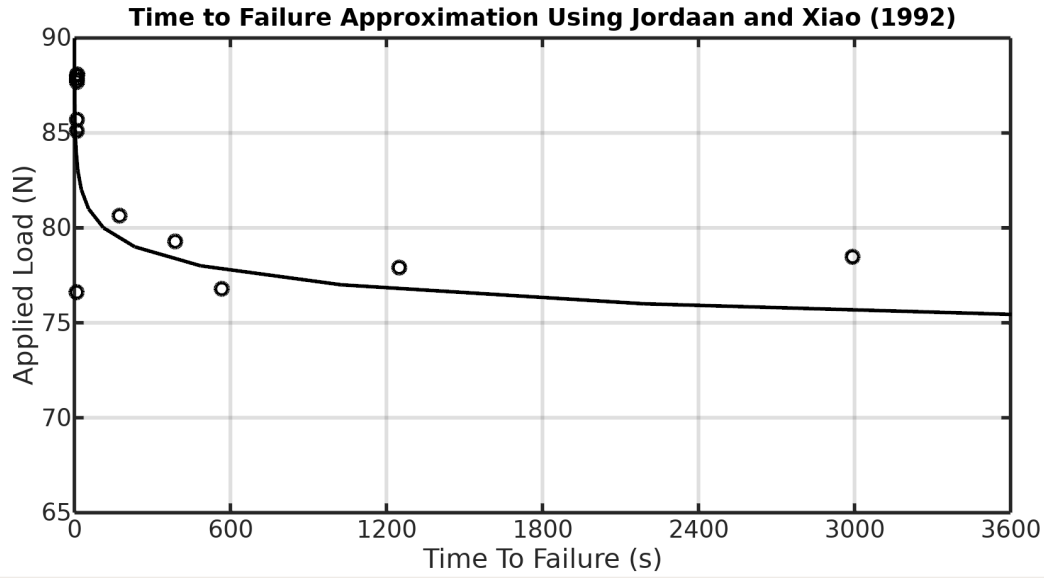


Figure 7.23: Optimized fit of constant load series using the crack growth approximation from Jordaan and Xiao (1992).

in

$$\begin{aligned} c_1 &= 3.0 \times 10^{-18} \\ k &= 29 \end{aligned} \tag{7.24}$$

and results in the fit shown in Figure 7.23. Figure 7.23 shows that this empirical approximation behaves similarly to the linear viscoelastic model and displays the decreasing power-law curve fit to the data.



# Chapter 8

## Conclusion

### 8.1 Summary

#### 8.1.1 A Brief overview

Before going into details of the conclusions, the following list will highlight some of the main features and results of the model and experiments performed in this project.

The indentation experimental program:

- Showed that with a proper scaling of velocity for different sized indentors would result in similar beviour in ice.
- Proper scaling of the velocity aims to keep the strains and strain rates the same. This can be used to scale experiments from laboratory to larger scales.
- Ice exhibits damage-enhanced creep under slow loading.
- Medium rate tests provided a transition towards brittle behaviour. These experiments also exhibited delayed failure.

- Fast loading experiments exhibited more brittle-like behaviour, resulting in many small, localized spalling events.
- a decreasing power-law between pressure and area was observed (known as the scale effect), that was similar to results from field experiments.

The ramp loading 4-point bending experiments:

- Allowed for simplified analysis of a single crack.
- Showed a clear decreasing power-law relationship between ice strength (fracture toughness) and increasing loading rate.
- Alluded to that ice was a strongly time-dependent material with ice strength ranging from about 450 N down to about 150 N.

The constant load 4-point bending experiments:

- Used a gravity-based system to provide a constant load for an extended period of time.
- Ice was shown to undergo stable crack growth, leading to delayed failure in ice.
- The time to failure increased exponentially as the the applied load was lowered.

Sensitivity analysis of both 4-point bending series:

- showed that the strength of ice was strongly related to all of the viscoelastic parameters.
- This strong dependence on the parameters suggests that the scatter in ice strength is related to the local conditions near a crack tip.

The viscoelastic fracture model:

- Expanded on the earlier model of Schapery (1975a,b,c).
- Schapery's model was designed for a central crack in a thin, infinite plate under biaxial stress (though uniaxial would work for a slight change in values).
- This project expanded Schapery's theory to new geometries, particularly 4-point bending and compact tension specimens.
- Schapery's theory was also expanded to include ramp up to failure loading.
- Validation of the model assumptions showed the assumptions were reasonable for the given experiments.
- While not a generalized model that can be used in finite element analysis, the model will work for geometries that have a defined fracture toughness equation.
- The model was shown to give reasonable results in comparison to the experimental data for the two 4-point bending series in predicting ice strength and time to failure.
- The model also provided reasonable fits to the compact tension specimen data from Liu and Miller (1979).

### 8.1.2 Time-Dependent Properties of Ice

Chapters 4 and 5 summarize the results of the experimental programs completed during this project. The first of these series involved cylindrical ice samples surrounded by steel moulds under indentation by spherical-capped indentors.

When considering the velocity-to-indentor-size ratio (the “normalized velocity”), the ice samples displayed markedly different behaviours under different loading rates.

For slower normalized velocities, the ice behaved in a creep-like behaviour and ice was ejected from the contact area as a fine particulate (much like toothpaste), in what is known as extrusion. At the fastest normalized velocities, the ice would break off in discrete, localized pieces referred to as spalls. For medium-rate normalized velocities, the behaviour of the ice was a mix of the previous two cases, with spalling events being less frequent but with larger pieces than under fast loading. The medium-rate tests also exhibited delayed failure as a crack grew stably under load, until reaching a critical length.

To study the process of ice fracture, ice beams with a pre-notched crack were subjected to 4-point bending. The first series of experiments placed the ice under a ramp up to failure at various loading rates. This series showed that the failure load of the ice was time-dependent. Ice that was subjected to slower loading rates were able to withstand greater loads than the ice that underwent faster loading rates. This behaviour exhibited a decreasing power-law type curve. This behaviour was also seen in experiments on other specimen geometries (Liu and Miller, 1979; Hamza and Muggeridge, 1980; Urabe et al., 1980).

The constant-rate ramp up to fracture series exhibited a 3-fold increase in apparent fracture toughness, similar to the experiments of Dempsey (1996), but for ice samples of the same size. While the experiments (and the model) considered the loading rate as the time-dependent aspect that affects ice properties, it is likely that the strain rate is the fundamental factor behind the changes in the apparent fracture toughness. This would suggest that the size effect observed in Dempsey (1996) was simply due to the change in strain rate caused by the different sized samples. This can also be seen in the indenter series using the “normalized velocities” for the indenter. The use of “normalized velocities” was a means to scale the experiments such that they have similar strain rates, leading to similar results, even though the indenter sizes

and velocities were changing.

The second set of 4-point bending experiments placed the ice samples under a constant load. The aim of this series was to apply a load to the ice such that stable crack growth would occur that would lead to delayed failure. Experiments were able to capture delayed failure in the ice samples for various loads. A plot of load versus time to failure indicate that there is a decreasing power-law relationship between them.

The goal of the theory and model developed in this project was to provide a physics-based explanation of the time-dependent observations from the in-house experimental program, as well as observations from other laboratory experiments and from field data.

### 8.1.3 The Underlying Theory

Chapter 3 details the development of the linear elastic fracture theory that underlies the model developed in this thesis. The theory is first developed from linear elastic fracture mechanics discussed in Westergaard (1939), Williams (1957), and Alturi et al. (1975). These theories, which are related, describe the elastic stress field around a crack in an infinite plate under biaxial tension, but are effectively the same for uniaxial tension with a change in coefficients. For an elastic crack, it would not undergo any growth before the unstable fracture when the fracture toughness of the ice has been met. These theories predicted an infinite stress singularity at the stress tip. The work of (Barenblatt, 1962), introduced the idea of cohesive molecular forces that resisted crack growth. With this additional process, (Barenblatt, 1962) was able to remove this infinite stress singularity.

The theory of linear viscoelastic fracture mechanics were expanded from the linear elastic theory in Chapter 6. The two theories are linked through the correspondence principle discussed in Graham (1968) and Schapery (1975a,b,c). The works of

Schapery (1975a,b,c) detail the process by which a crack can grow stably in a linear viscoelastic material for stress fields less than what would cause unstable fracture, as in the elastic case. By use of the correspondence principle, Schapery develops an effective compliance that replaces the elastic compliance in describing material behaviour. This effective compliance can be used to calculate the stress and displacement fields of the viscoelastic material at various times from the elastic stress field solution under the same conditions.

As with the previous authors, Schapery (1975a,b,c) considers the case of a thin plate under biaxial tension of a constant applied load. From his theory, he was able to predict the time to failure for a thin plate specimen under load. The theory developed in this thesis was derived to expand on the theory of Schapery (1975a,b,c). The theory was expanded to include predictions for other geometries. In particular, the theory was expanded to predict the time to failure for ice beams held under constant load in a 4-point bending apparatus. The new theory also considered 4-point bending beams and CT specimens (Liu and Miller, 1979) under a constant ramping load.

These two new additions to the linear viscoelastic theory greatly expand the applicability of Schapery's theory to new loading conditions and to new specimens. This new theory was the basis for the model that was developed and tested with 4-point bending experiments completed in-house, as well as comparisons to the CT-specimen data from Liu and Miller (1979).

#### 8.1.4 The Viscoelastic Fracture Model

The model was built (and expanded) upon the linear viscoelastic model developed in Schapery (1975a,b,c). The model uses an Explicit Euler time-stepping to simulate the growth of a crack in an ice beam under 4-point bending, but other geometries can be incorporated.

To condition the model, two sets of 4-point beam bending experiments were done. They used ice samples grown in a similar fashion and were pre-notched with a crack  $1/4$  of the thickness of the beam. The first series provided data on the failure strength of ice under various applied loading rates, that showed a decreasing power-law in ice strength with increasing loading rate. The second series of beam bending tests focused on capturing delayed failure in ice under a constant applied load. The second series exhibited a decreasing power-law curve between the applied load and time to failure when the time to failure is plotted on the x-axis (conversely one can say that the time to failure increased exponentially with decreased applied load). Having these two data sets, the model was able to provide an excellent agreement to both data sets using a single set of parameters that define the properties of the ice used.

The model used several assumptions that included a small process zone and that a nonlinear viscoelastic rheological ice model could be converted to a linear viscoelastic ice model. The process zone was indeed found to be small for reasonable estimation of the stress field inside the process zone. While somewhat limited in the types of loading used, the linear viscoelastic compliance was found to provide reasonable fits to the nonlinear viscoelastic compliance for the types of loading used in this project.

The model was able to provide excellent agreement to the experiments performed in-house, as well as the data Liu and Miller (1979). The results can be found in Chapter 7. This model was able to predict the decreasing power-law relationship between the failure load and the loading rate for both the 4-point bending and CT-specimens. The model also predicted the relationship between the time to failure for the beam bending specimens under various constant load (exhibiting a decreasing power-law when plotted as force vs time to failure).

One of the outcomes of this new model is to provide insights into the rheological and fracture properties of ice as a viscoelastic material. These insights can aid in

the design process of ships and other structures that are to be deployed in ice-prone regions, such as the Canadian Arctic. With improved (and more efficient) designs, there could be increased activity in the Canadian Arctic that could provide better mineral extraction, transportation routes, and a better local economy for the people who call the Arctic home.

## 8.2 Practical Implications

The purpose of this model is to provide insights into the fracture properties of ice. Due to the need to develop the Canadian Arctic, for both the residents and for mineral exploration, ice is going to play a major role in how engineers and designers build infrastructure and vessels to withstand the Arctic environment.

Fracture mechanics plays an important role during interactions with ice, as it limits the strength of the ice. Cracks, grains, and other flaws in the ice drastically weaken it from its theoretical strength (which is true for every solid material, in general). These flaws greatly increase the local stresses, such as those near the tip of a crack, so that the local stresses are at the theoretical limit, but the applied loads are much less. For example, the theoretical strength of ice is likely on the order of 100 MPa (or more), but tensile strength of ice is on the order of 1 MPa (Petrovic, 2003).

Many of the applications of ice fracture mechanics, and the accompanying viscoelastic theory, will be related to building infrastructure (such as wharves) that can withstand the interactions with ice. Similar to infrastructure would be any ocean-bound structures like drilling platforms that operate in areas prone to sea ice. In both cases, the structures have to be built to withstand the interaction. Additionally, engineers and designers would like to build these objects as efficiently as possible to minimize the required materials and cost of maintenance, without compromising the



integrity of the structure. Improved models of ice fracture mechanics (and viscoelastic theory) will aid in the design process by providing better estimations on the strength of ice under various conditions.

Secondly is the use of ships in the Arctic. Development of the local infrastructure will require ships to carry resources to and from the Arctic, as well as the necessities for the local populace. The development of Arctic infrastructure would also allow for the use of the Northwest Passage through the Canadian Arctic, allowing for better and quicker trade with Asian Markets, as well as developing northern tourist attractions. Similar to stationary structures, ships will have to interact with the ice in the case that they are ice breakers meant to collide with ice, or in the case that there is no way to avoid the ice (such as ice floes than span the ocean). Depending on the type and thickness of the ice, the ships may be able to break through with ease, provided that they are durable enough to withstand the impact. Alternatively, a common technique for breaking stronger ice is to ram up onto the ice. Over time, the weight of the ship will break the ice due to the stable crack growth predicted by viscoelastic fracture mechanics.

While often a burden to overcome, the ice present in the Arctic can also be exploited to aid in exploration and development. As explored in Masterson et al. (1980) and Ekelund and Masterson (1980), ice can be used as landing strips for aircraft and as temporary roads/bridges for transportation. Drilling rigs can also be built on ice islands (Masterson et al., 1980). Analysis of this is done using the theory of an elastic plate (the ice) on an elastic foundation (the ocean). The highest stress concentration occurs at the hole that the drilling equipment pass through. The stress concentration is estimated from the theory of Westergaard (1939). As suggested in this thesis, the theory of linear elastic fracture mechanics, of which the work of Masterson et al. (1980) is based upon, can be improved upon by incorporating a viscoelastic fracture

mechanics model, such as the one developed in this thesis. Improved stress analysis from a viscoelastic fracture model would help assess the requirements of designing an ice platform that is both economical and safe for the lifetime of its use.

## 8.3 Future Work

The model presented in this project is a new application of the theory presented in Schapery (1975a,b,c), expanded to incorporate new geometries and loading scenarios. As such, there are many ways the model could be expanded upon.

### 8.3.1 New Geometries

Currently, the model is applied to 4-point beam bending as it relates to the experiments performed in this project. The model was also modified for CT-specimens. The model can be easily modified to be used for other common test specimens, such as 3-point beam bending specimens. Performing experiments using other specimens would provide a good test to see how the model performs under different geometries.

### 8.3.2 The Process Zone

The process zone is an important part of the fracture process, but little is known about it. The theories and model presented in this project aim to minimize the need to have detailed knowledge of the process zone. However, given the importance of the process zone, it seems that further exploration of its inner workings could be a worthwhile endeavour. It is hard to say much of its practical use in terms of present models, but new insights into its workings could lead to even better models that are less restricted by some of the assumptions about the process zone.

### 8.3.3 Combining with Finite Analysis

Currently, the model is a 1-D model of the growth of a crack under plane strain (and subject to having a small process zone). While this is useful for common geometries like the 4-point beam bending where there are equations for the stress intensity, many interactions with ice will have no such equations readily available. Currently, the concepts and equations in the model are used in specialized geometries, but there is no reason that they could not be expanded upon to be used in a more generalized fashion as a part of a finite analysis of a complex loading scenario.

The use finite element analysis could open up a suite of new scenarios such as multiple cracks in a specimen, such as the indentation series. The incorporation of concepts like strain energy release rate could affect a crack's trajectory under various loading and confinement conditions, providing more insights to phenomena such as wing cracks.

### 8.3.4 Converting to a Nonlinear Viscoelastic Fracture Model

Later works by Schapery (Schapery, 1984a, 1990) advanced into developing a nonlinear viscoelastic model based on the (elastoplastic) J-Integral technique developed in Rice (1968). While this new theory is more complex than the theory presented in this project (as would be expected of a nonlinear fracture theory), many of the concepts from the linear theory present here are present in the nonlinear theory. Some of key equations and concepts for this theory are outlined in Section 6.3.

The creation of a nonlinear viscoelastic fracture model would likely lead to better estimations of the fracture strength of ice and its time to failure under an applied load. This could provide even further advancements in the design process.

Schapery's nonlinear theory lends itself more to the development of a finite element

approach and may address the previous issues from Section 8.3.3.

### **8.3.5 More Experimental Data**

Due to the limited amount of data, particularly delayed failure data, the model parameters may not be as accurate as they should be. This would pose issues should the model be used as a predictive tool. With the collection of more data, the model can be tested for its ability to provide predictions/estimations of ice loads for new experiments. As the model is in its initial stages, the fact that it displays the proper behaviour for reasonable rheological ice parameters is promising, but further testing is needed confirm the validity of the model before it can be used with confidence.

# Bibliography

- Alturi, S. N., Kobayashi, A. S., and Nakagaki, M. (1975). An assumed displacement hybrid finite element model for linear fracture mechanics. *International Journal for Fracture*, 11:257–271.
- Anderson, T. L. (2005). *Fracture Mechanics: Fundamentals and Applications*. CRC Press., Boca Raton, FL, 3 edition.
- Andrade, E. N. d. C. (1910). On the viscous flow in metals, and allied phenomena. *Proceedings of the Royal Society of London A: Mathematical, Physical and Engineering Sciences*, 84(567):1–12.
- Barenblatt, G. I. (1962). The mathematical theory of equilibrium cracks in brittle fracture. *Advances in Applied Mechanics*, VII:55–129.
- Barrette, P., Pond, J., Li, C., and Jordaan, I. (2003). Laboratory-scale indentation of ice. Technical report, National Research Council Program on Energy Research and Development.
- Batto, R. A. and Schulson, E. M. (1993). On the ductile-to-brittle transition in ice under compression. *Acta metallurgica et materialia*, 41(7).
- Bjerrum, N. (1952). Structure and properties of ice. *Science*, 115(2989):385–390.

- Born, M. and Green, H. S. (1946). A general kinetic theory of liquids. i. the molecular distribution functions. *Proceedings of the Royal Society of London A: Mathematical, Physical and Engineering Sciences*, 188(1012):10–18.
- Brill, R. and Camp, P. R. (1961). Properties of ice. Technical report, U.S. Army Cold Regions Research and Engineering Laboratory.
- Cannon, N., Schulson, E., Smith, T., and Frost, H. (1990). Wing cracks and brittle compressive fracture. *Acta Metallurgica et Materialia*, 38(10):1955 – 1962.
- Croasdale, K., Cammaert, A. B., and Metge, M. (1994). A method for the calculation of sheet ice loads on sloping structures. In *Proceedings IAHR Symposium on Ice*, volume 2, pages 874–885, Trondheim.
- Croasdale, K., Jordaan, I., Frederking, R., and Noble, P. (2016). Engineering in canada’s northern oceans research and strategies for development. Technical report, Canadian Academy of Engineering.
- Croasdale, K. R. (1980). Ice forces on fixed rigid structures. In *1st IAHR State-of-the-Art Report on Ice Forces on Structures. CRREL Special Report 80-26*, pages 34–106, Hanover, N.H.
- Danielewicz, B. W. and Metge, M. (1981). Ice forces on hans island. Technical report, Canadian Marine Drilling, Ltd.
- DeFranco, S. J. and Dempsey, J. P. (1990). Crack growth stability in S2 ice. In *International Symposium on Ice*, volume 1, pages 168–182. Proceedings of the 10th International Symposium on Ice, Helsinki University of Technology, Espoo, Finland.
- Dempsey, J., Adamson, R., and Mulmule, S. (1995). Large-scale in-situ fracture of ice. In *Proceedings of FRAMCOS*, volume 2.

- Dempsey, J. P. (1996). Scale effects on the fracture of ice. In Arsenault, R. J., Cole, D., Gross, T., Kostroz, G., Liaw, P. K., Parameswaran, S., and Sizek, H., editors, *The Johannes Weertman Symposium*, pages 351–361. The Minerals, Metals and Materials Society.
- Dempsey, J. P., Adamson, R. M., and Mulmule, S. V. (1999). Scale effects on the in-situ tensile strength and fracture of ice. part ii: First-year sea ice at resolute, n.w.t. *International Journal of Fracture*, 95:347–366.
- Dugdale, D. S. (1959). Yielding of steel sheets containing slits. *Journal of the Mechanics and Physics of Solids*, 8:100–104.
- Ekelund, M. and Masterson, D. (1980). Floating ice platforms for oil exploration in the arctic islands. *ARCTIC*, 33(1).
- Fanourgakis, G. S. and Xantheas, S. S. (2006). The bend angle of water in ice ih and liquid water: The significance of implementing the nonlinear monomer dipole moment surface in classical interaction potentials. *Journal of Chemical Physics*, 124(17):174504.
- Frederking, R. M. W., Jordaan, I. J., and McCallum, J. S. (1990). Field tests of ice indentation at medium scale: Hobson’s Choice ice island, 1989. In *In Proceedings of the 10th International Symposium on Ice*, volume 2, pages 931–944, Espoo, Finland. IAHR.
- Frost, H. and Ashby, M. (1982). *Deformation-mechanism maps: the plasticity and creep of metals and ceramics*. Pergamon Press.
- Gagnon, R. E. and Gammon, P. H. (1995). Characterization and flexural strength of iceberg and glacier ice. *Journal of Glaciology*, 41(137):103–11.

- Glen, J. W. (1955). The creep of polycrystalline ice. *Proceedings of the Royal Society of London. Series A. Mathematical and Physical Sciences*, 228(1175):519–538.
- Goodman, D. J. and Tabor, D. (1978). Fracture toughness of ice: A preliminary account of some new experiments. *Journal of Glaciology*, 21(85):651–660.
- Graham, G. A. (1968). The correspondence principle of linear viscoelasticity theory for mixed boundary value problems involving time-dependent boundary regions. *Quarterly of Applied Mathematics*, 26:167–174.
- Griffith, A. A. (1921). The phenomena of rupture and flow in solids. *Philosophical Transactions of the Royal Society of London A: Mathematical, Physical and Engineering Sciences*, 221(582-593):163–198.
- Hamza, H. and Muggeridge, D. B. (1980). Plane strain fracture toughness  $K_{IC}$  of fresh water ice. In *Int Port and Ocean Eng Upper Arctic Cond Conf 79*, volume 1.
- Hardy, M., Jefferies, M., Rogers, B., and Wright, B. (1996). Dynamac: Molikpaq ice loading experience. Technical report, National Research Council.
- Hobbs, P. (1974). *Ice Physics*. Clarendon Press.
- Hoek, E. and Bieniawski, Z. T. (1965). Brittle rock fracture propagation in rock under compression. *International Journal of Fracture Mechanics*, 1(3):137–155.
- Hunt, R. A. and McCartney, L. N. (1979). A new approach to weibull’s statistical theory of brittle failure. *International Journal of Fracture*, 15(4).
- Inglis, C. E. (1913). Stresses in a plate due to the presence of cracks and sharp corners. *Trans. Inst. Nav. Arch.*, 55:219–230.



- Jordaan, I., Li, C., Sudom, D. Stuckey, P., , and Ralph, F. (2005). Principles for local and global ice design using pressure- area relationships. In *18th International Conference on Port and Ocean Engineering under Arctic Conditions (POAC'05)*, Potsdam New York, United States.
- Jordaan, I. J. (2001). Mechanics of ice-structure interaction. *Engineering Fracture Mechanics*, 68:1923–1960.
- Jordaan, I. J. and Xiao, J. (1992). Interplay between damage and fracture in ice-structure interaction. In *Proceedings of the 11th International Symposium on Ice (IAHR/92)*, volume 3, pages 1448–1467, Banff, Canada.
- Kachanov, M. L. (1982a). A mircocrack model of rock inelasticity part i: frictional sliding on microcracks. *Mechanics of Materials*, 1:19–27.
- Kachanov, M. L. (1982b). A mircocrack model of rock inelasticity part ii: propagation of microcracks. *Mechanics of Materials*, 1:29–41.
- Kavanagh, M., O'Rourke, B., Jordaan, I., and Taylor, R. (2015). Observations on the time-dependent fracture of ice. In *Ian Jordaan Honoring Symposium on Ice Engineering*, volume 8 of *International Conference on Offshore Mechanics and Arctic Engineering*, St. John's, Newfoundland, Canada. ASME.
- Kendall, K. (1978). Complexities of compression failure. *Proceedings of the Royal Society of London. A. Mathematical and Physical Sciences*, 361(1705):245–263.
- Knauss, W. G. (1970). Delayed failure - the griffith problem for linearly viscoelastic materials. *International Journal of Fracture*, 6(1).
- Langdon, T. G. (1973). Creep mechanisms in ice. In Whalley, E., Jones, J. J., and

- Gold, L. W., editors, *Physics and Chemistry of Ice*, pages 344–349, Ottawa. Royal Society of Canada.
- LeClair, E. S., Schapery, R. A., and Dempsey, J. P. (1999). A broad-spectrum constitutive modeling technique applied to saline ice. *International Journal of Fracture*, 97:209–226.
- Liu, H. W. and Miller, K. J. (1979). Fracture toughness of fresh-water ice. *Journal of Glaciology*, 22(86):135–143.
- Lu, W., Lubbad, R., Lset, S., and Kashafutdinov, M. (2016). Fracture of an ice floe: Local out-of-plane flexural failures versus global in-plane splitting failure. *Cold Regions Science and Technology*, pages 1–13.
- Mackay, J. R. (1993). The sound and speed of ice-wedge cracking, arctic canada. *Canadian Journal of Earth Sciences*, 30:509–518.
- Masterson, D., Nevel, D., Johnson, R., Kenny, J., and Spencer, P. (1992). The medium scale iceberg impact test program. In *Proceedings of the International Association of Hydraulic Engineering and Research (IAHR) Symposium on Ice*.
- Masterson, D. M., Anderson, K. G., and Stranbe, A. G. (1980). Strain measurements in floating ice platforms and their application to platform design: Reply. *Canadian Journal of Civil Engineering*, 7:565–568.
- Masterson, D. M., Jordaan, I. J., Frederking, R. M. W., and Spencer, P. A. (1993). Description of multi-year ice indentation tests at hobson’s choice ice island- 1990. In *the 12<sup>th</sup> International Conference on Offshore Mechanics and Arctic Engineering 1993(OMAE93)*, pages 145–155, Glasgow, England. ASME.

- Masterson, D. M., Spencer, P. A., Nevel, D. E., and Nordgen, R. P. (1999). Velocity effects from multi-year ice tests. In *18<sup>th</sup> International Conference on Offshore Mechanics and Arctic Engineering (OMAE99)*, St. John's, Canada. ASME.
- Mulmule, S. and Dempsey, J. (1998). A viscoelastic fictitious crack model for the fracture of sea ice. *Mechanics of Time-Dependent Materials*, 1:331–356.
- Muskhelishvili, N. I. (1953a). *Singular Integral Equations*. P. Noordhoff, Ltd., Netherlands.
- Muskhelishvili, N. I. (1953b). *Some Basic Problems of the Mathematical Theory of Elasticity*. Noordhoff International Publishing, Netherlands, 2 edition.
- Nabarro, F. R. N. (1947). Dislocations in a simple cubic lattice. *Proceedings of the Physical Society*, 59(2):256.
- Nakazawa, N., Akagawa, S., and Kawamura, M. (1999). Medium-scale indentation test (msfit). In *Proceedings of the 9<sup>th</sup> International Offshore and Polar Engineering Conference*, page 498.
- O'Rourke, B. J., Jordaan, I. J., Taylor, R. S., and Gürtner, A. (2015). A spherical indentation tests on confined ice specimens at small scales. In *Ian Jordaan Honoring Symposium on Ice Engineering*, volume 8. ASME.
- Parsons, B. L., Snellen, J. B., and Hill, B. (1987). Preliminary measurements of terminal crack velocity in ice. *Cold Regions Science and Technology*, 13:233–238.
- Peierls, R. (1940). The size of a dislocation. *Proceedings of the Physical Society*, 52(1):34.
- Petrenko, V. and Whitworth, R. (1999). *Physics of Ice*. OUP Oxford.

- Petrovic, J. J. (2003). Review mechanical properties of ice and snow. *Journal of Materials Science*, 38(1):1–6.
- Raj, R. and Ashby, M. F. (1971). On grain boundary sliding and diffusional creep. *Metallurgical Transactions*, 2:1113–1127.
- Read, W. T. (1953). *Dislocations in crystals*. New York : McGraw-Hill.
- Rice, J. R. (1968). A path independent integral and the approximate analysis of strain concentration by notches and cracks. *Journal of Applied Mechanics*, 35:379–386.
- Sanderson, T. (1988). *Ice mechanics: risks to offshore structures*. Cold Region Engineering Studies. Graham & Trotman.
- Schapery, R. A. (1962). A simple collocation method for fitting viscoelastic models to experimental data. Technical report, California Institute of Technology.
- Schapery, R. A. (1964). Application of thermodynamics to thermomechanical, fracture, and birefringent phenomena in viscoelastic media. *Journal of Applied Physics*, 35:1451–1465.
- Schapery, R. A. (1975a). A theory of crack initiation and growth in viscoelastic media I. Theoretical development. *International Journal of Fracture*, 11(1):141–158.
- Schapery, R. A. (1975b). A theory of crack initiation and growth in viscoelastic media II. Approximate methods of analysis. *International Journal of Fracture*, 11(3):369–387.
- Schapery, R. A. (1975c). A theory of crack initiation and growth in viscoelastic media III. Analysis of continuous growth. *International Journal of Fracture*, 11(4):549–562.

- Schapery, R. A. (1981). On viscoelastic deformation and failure behavior of composite materials with distributed flaws. In Wang, S. S. and Renton, W. J., editors, *Advances in Aerospace Structures and Materials – AD-01*, New York, USA. The American Society of Mechanical Engineers.
- Schapery, R. A. (1984a). Correspondence principles and a generalized  $J$  integral for large deformation and fracture analysis of viscoelastic media. *International Journal of Fracture*, 25:195–233.
- Schapery, R. A. (1984b). Time-dependent fracture: Continuum aspects of crack growth. *Encyclopedia of Materials Science and Engineering*, pages 5043–5053.
- Schapery, R. A. (1990). On some path independent integrals and their use in fracture of nonlinear viscoelastic media. *International Journal of Fracture*, 42:189–207.
- Schapery, R. A. (1991). *Simplifications in the Behavior of Viscoelastic Composites with Growing Damage*, pages 193–214. Springer New York, New York, NY.
- Schapery, R. A. (1997). Thermoviscoelastic constitutive equations for polycrystalline ice. *Journal of Cold Regions Engineering*, 11(2):146–157.
- Schulson, E. M. (1997). The brittle failure of ice under compression. *The Journal of Physical Chemistry B*, 101:6254–6258.
- Sinha, N. (1983). Creep model of ice for monotonically increasing stress. *Cold Regions Science and Technology*, 8(1):25 – 33.
- Sinha, N. K. (1977). Technique for studying the structure of sea ice. *Journal of Glaciology*, 18:315–323.
- Sinha, N. K. (1978). Rheology of columnar-grained ice. *Experimental Mechanics*, 18(12):464–470.

- Sinha, N. K. (1979). Grain boundary sliding in polycrystalline materials. *Philosophical Magazine*, 40(6):825–842.
- Sinha, N. K. (1988). Crack-enhanced creep in polycrystalline material: strain-rate sensitive strength and deformation of ice. *Journal of Materials Science*, 23:4415–4428.
- Strecker, K., Ribeiro, S., and Hoffmann, M.-J. (2005). Fracture toughness measurements of lps-sic: A comparison of the indentation technique and the sevn method. *Materials Research*, 8(2):121–124.
- Taylor, G. I. (1934). The mechanism of plastic deformation of crystals. part i. theoretical. *Proceedings of the Royal Society of London A: Mathematical, Physical and Engineering Sciences*, 145(855):362–387.
- Taylor, R. S. (2010). *Analysis of scale effect in compressive ice failure and implications for design*. PhD thesis, Memorial University of Newfoundland, St. John’s, Canada.
- Taylor, R. S., Frederking, R., and Jordaan, I. J. (2008). The nature of high pressure zones in compressive ice failure. In Jasek, M., editor, *19<sup>th</sup> IAHR International Symposium On Ice*.
- Taylor, R. S. and Jordaan, I. J. (2015). Probabilistic fracture mechanics analysis of spalling during edge indentation in ice. *Engineering Fracture Mechanics*, 134:242–266. Accepted.
- Timco, G. and Frederking, R. (1983). Flexural strength and fracture toughness of sea ice. *Cold Regions Science and Technology*, 8(1):35 – 41.
- Timco, G., Wright, B., Barker, A., and Poplin, J. (2006). Ice damage zone around the

- molikpaq: Implications for evacuation systems. *Cold Regions Science and Technology*, 44(1):67 – 85.
- Timco, G. W. (2011). Isolated ice floe impacts. *Cold Regions Science and Technology*, 68:35–48.
- Timco, G. W. and Cornett, A. M. (1997). The influence of variable-thickness ice on the loads exerted on sloping structures. *Cold Regions Science and Technology*, 26:39–53.
- Turner, J. (2018). *Constitutive Behaviour of Ice Under Compressive States of Stress and its Application to Ice-Structure Interactions*. PhD thesis, Memorial University of Newfoundland, St. John's, Canada.
- Urabe, N., Iwassaki, T., and Yoshitake, A. (1980). Fracture toughness of sea ice. *Cold Regions Science and Technology*, 3:29–37.
- Weibull, W. (1951). A statistical distribution function of wide applicability. *Journal of Applied Mechanics*.
- Weiss, J. and Schulson, E. M. (1994). The failure of fresh-water granular ice under multiaxial compressive loading. *Acta metallurgica et materiali*, 43(6):2303–2315.
- Wells, J., Jordaan, I., Derradji, A., and Taylor, R. (2011). Small-scale laboratory experiments on the indentation failure of polycrystalline ice in compression: Main results and pressure distribution. *Cold Regions Science and Technology*, 65.
- Westergaard, H. M. (1939). Bearing pressures and cracks. *Journal of Applied Mechanics*, 6(2):A49–A53.
- Williams, M. L. (1952). Stress singularities resulting from various boundary conditions

in angular corners of plates in extension. *Journal Of Applied Mechanics, Trans. ASME*, 74:526.

Williams, M. L. (1957). On the stress distribution at the base of a stationary crack. *Journal of Applied Mechanics*, 24:109–114.

Zhu, X.-K. and Joyce, J. A. (2012). Review of fracture toughness (G, K, J, CTOD, CTOA) testing and standardization. *Engineering Fracture Mechanics*, 85:1–46.

Zou, B., Xiao, J., and Jordaan, I. J. (1996). Ice fracture and spalling in ice-structure interaction. *Cold Regions Science and Technology*, 24:213–220.



## Appendix A

### CAD Specification Sheets for Dead Weight Apparatus

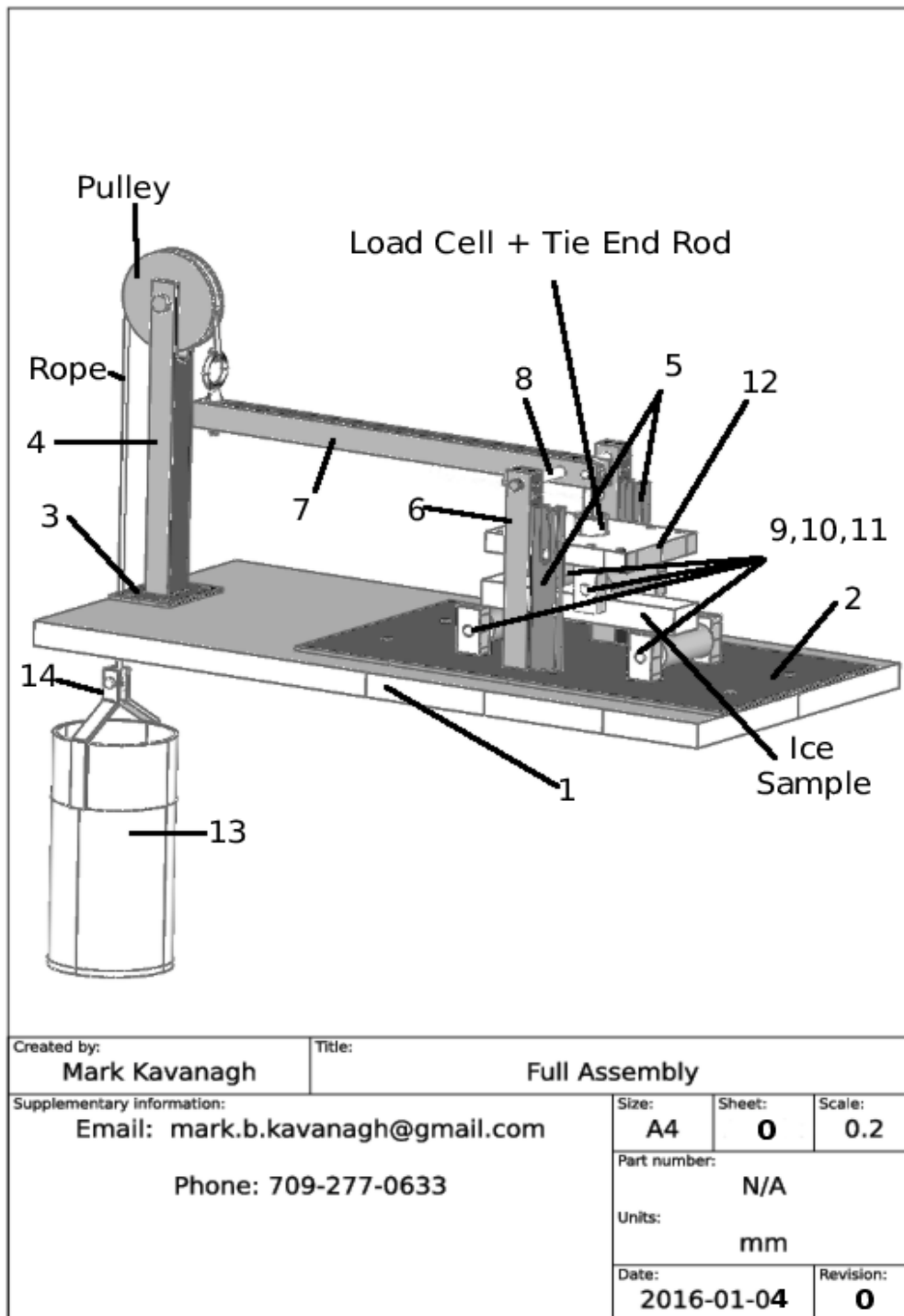


Figure A.1: Complete Assembly with component labels.

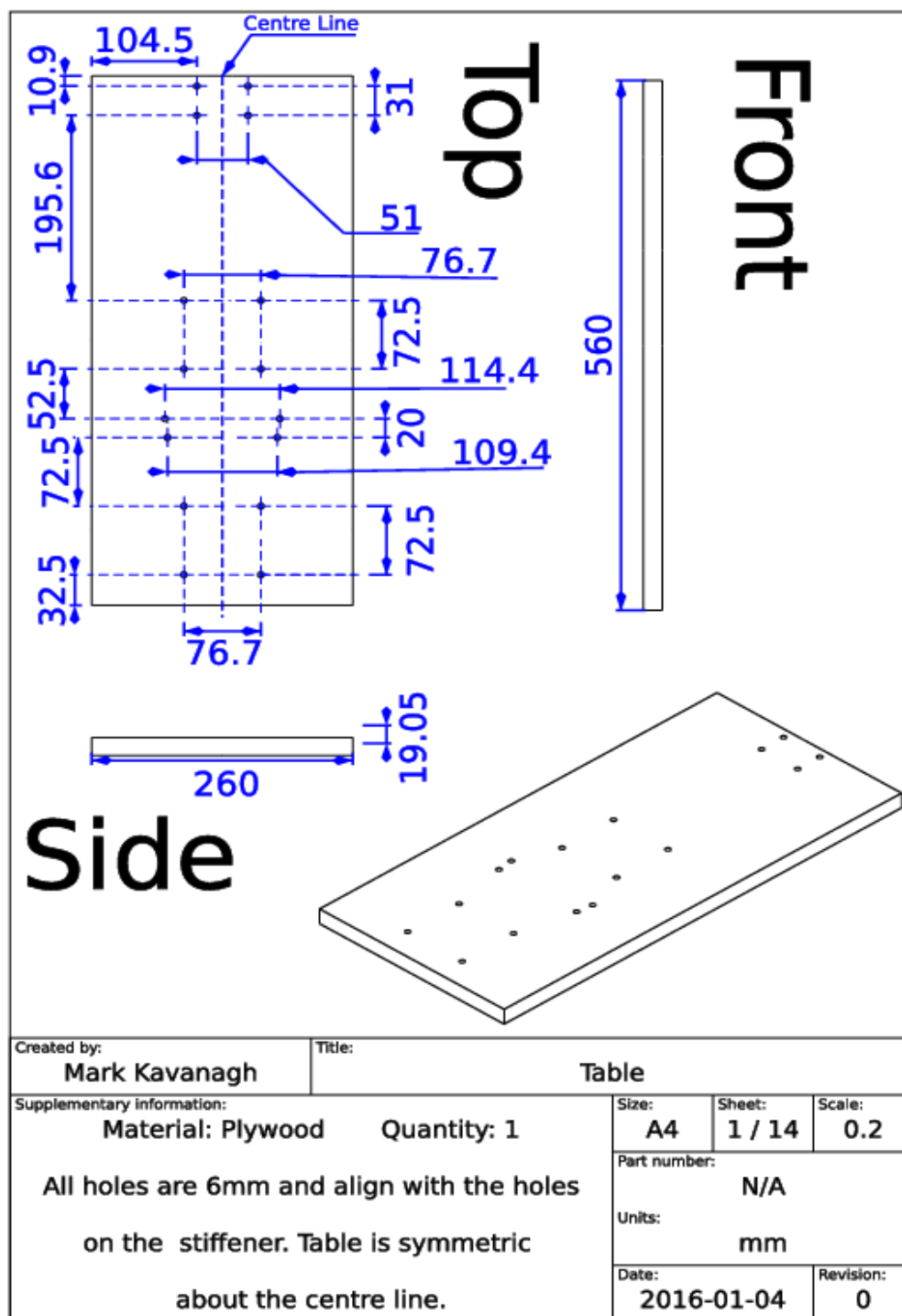


Figure A.2: Specifications for wooden table at the base of the apparatus.

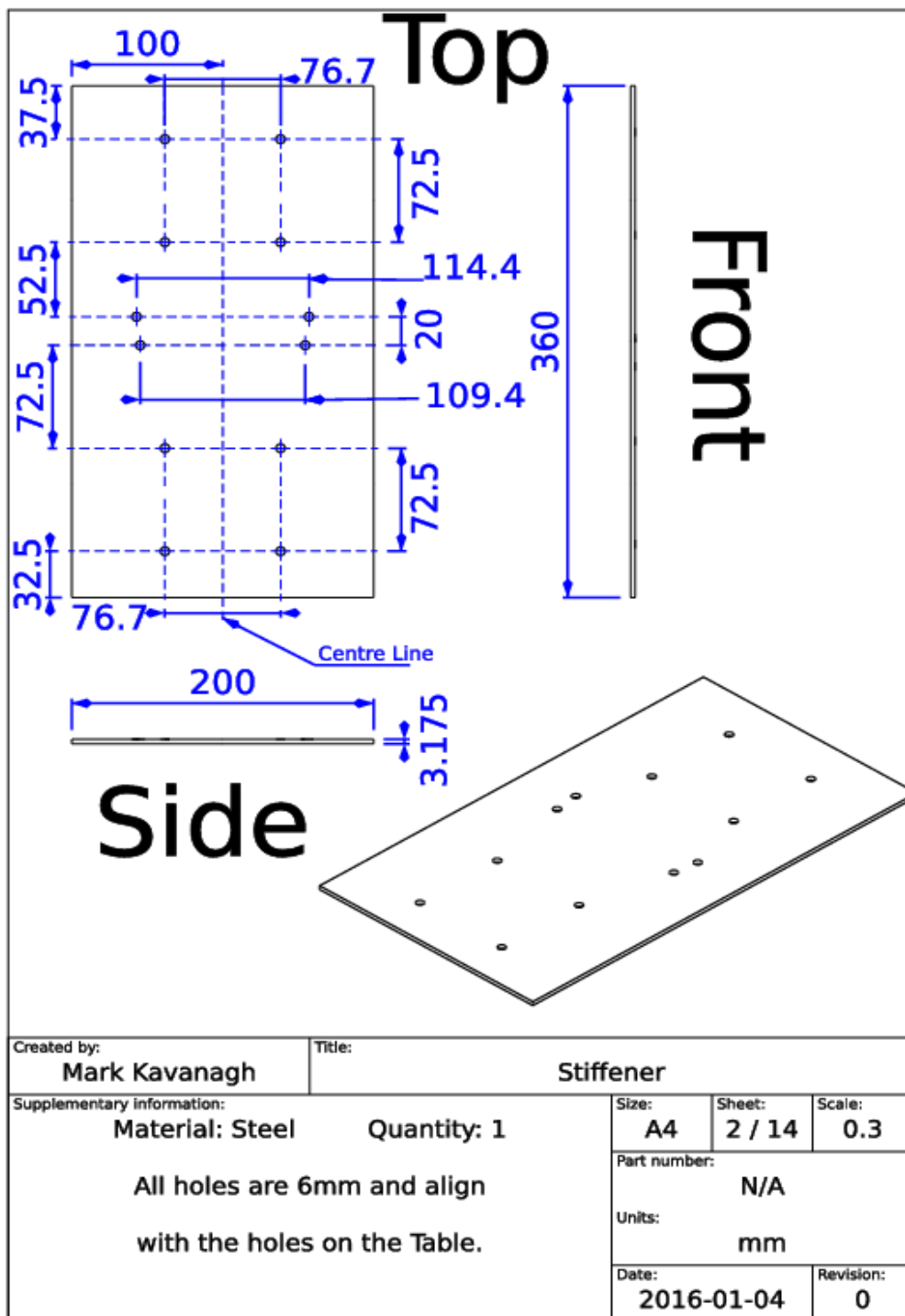


Figure A.3: Specifications for table stiffener

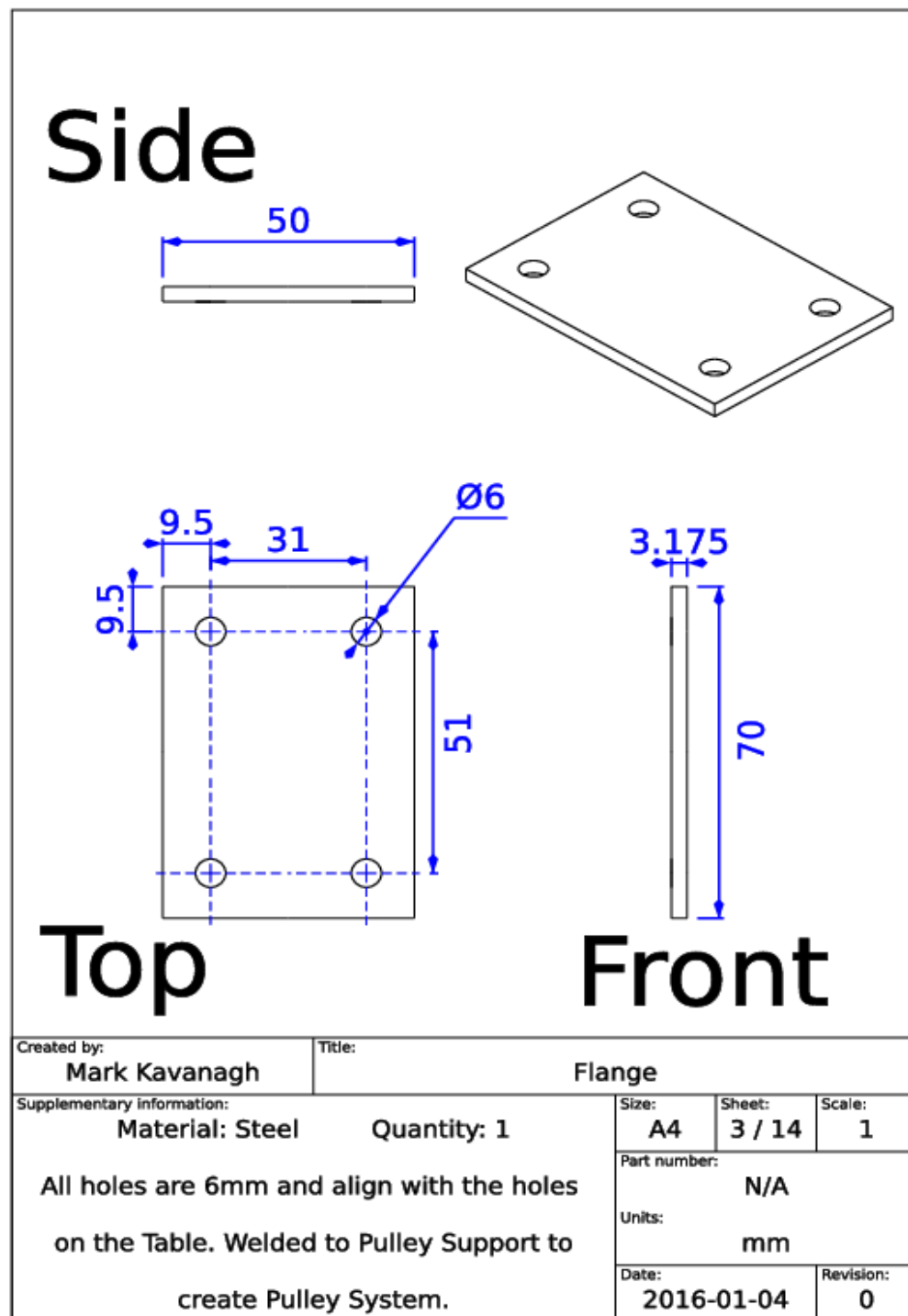


Figure A.4: Specifications for flange at the base of the pulley system.

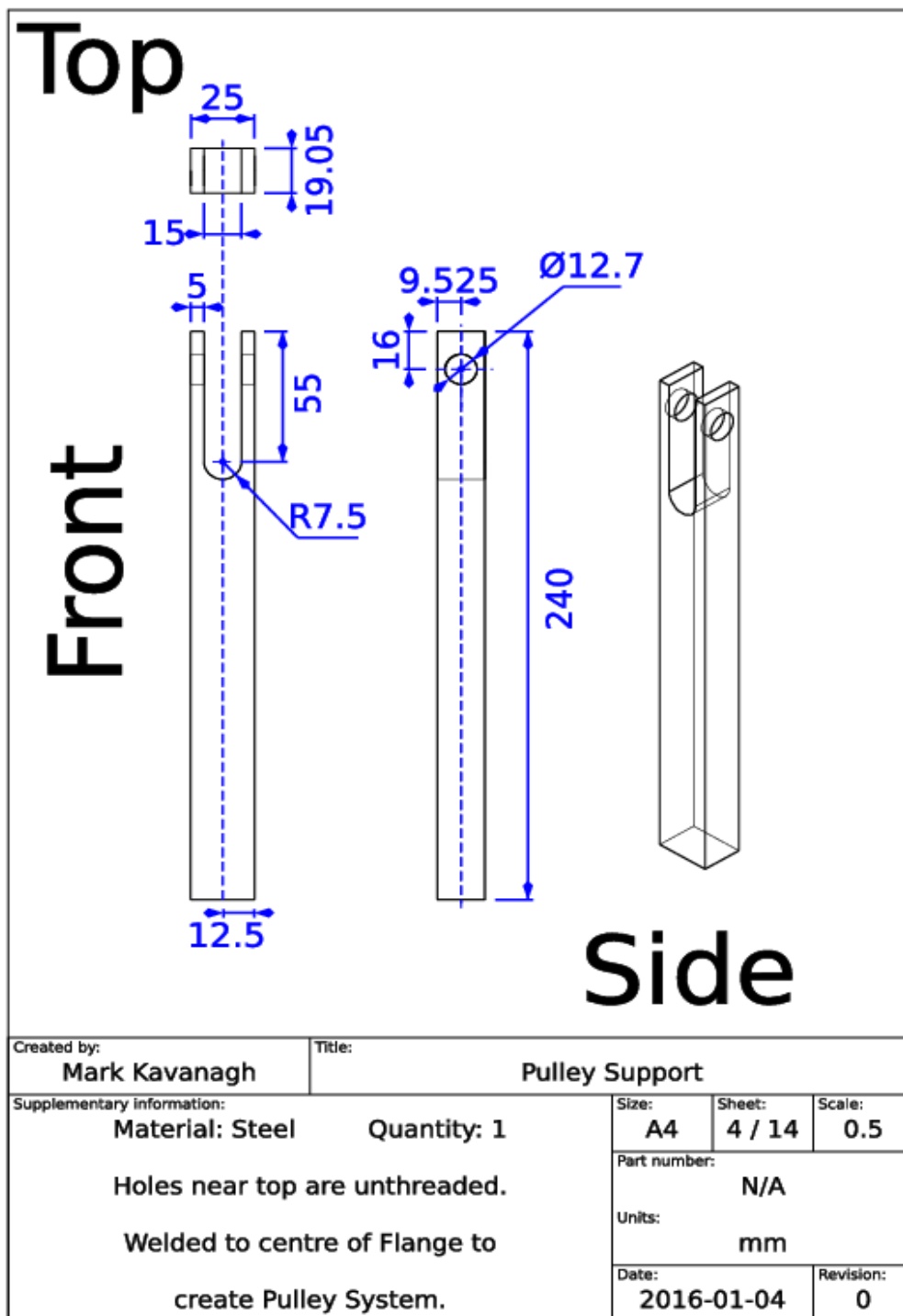


Figure A.5: Specifications for the bar that holds up the pulley.

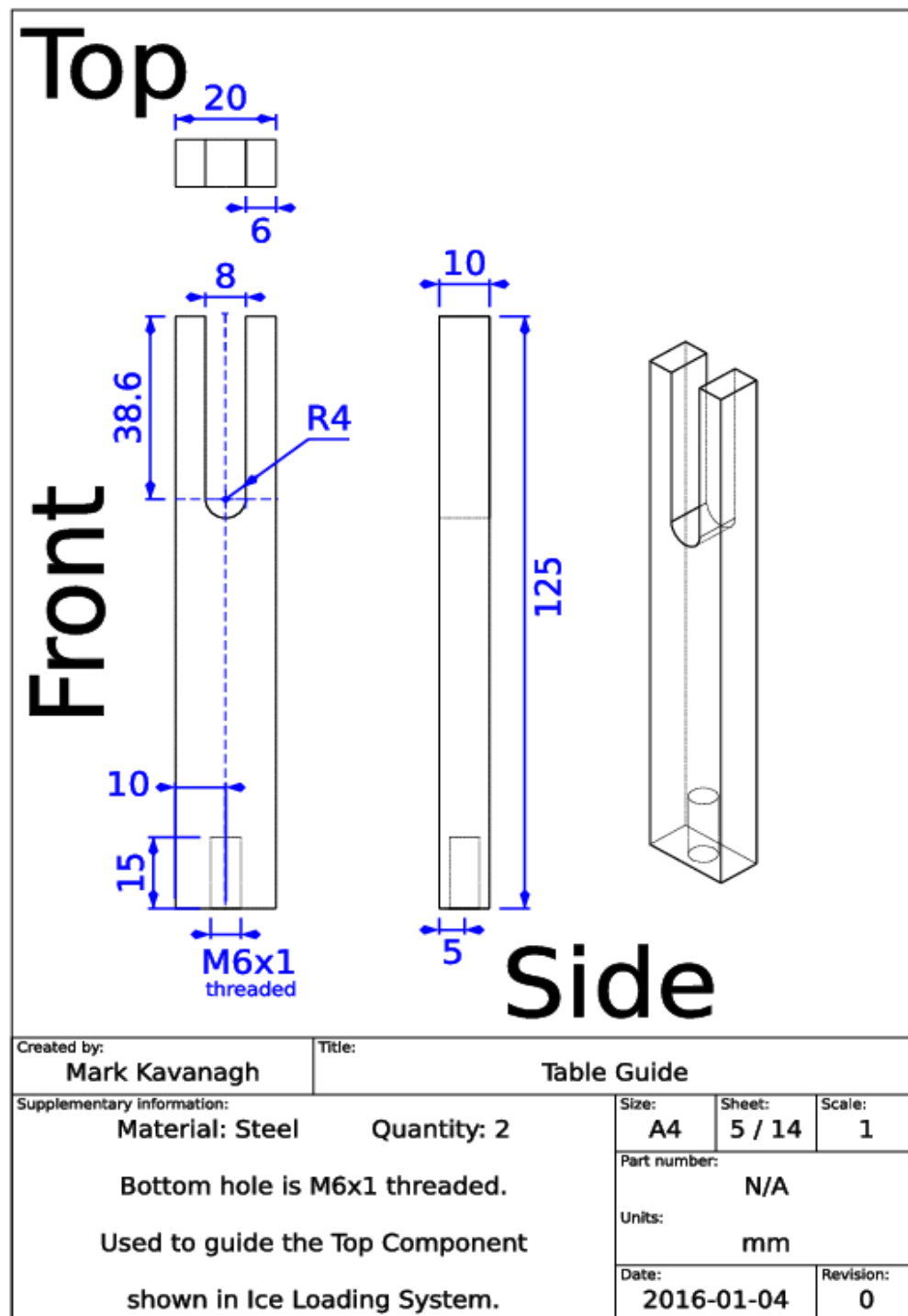


Figure A.6: Specifications for the table guide that aligns the top plate.

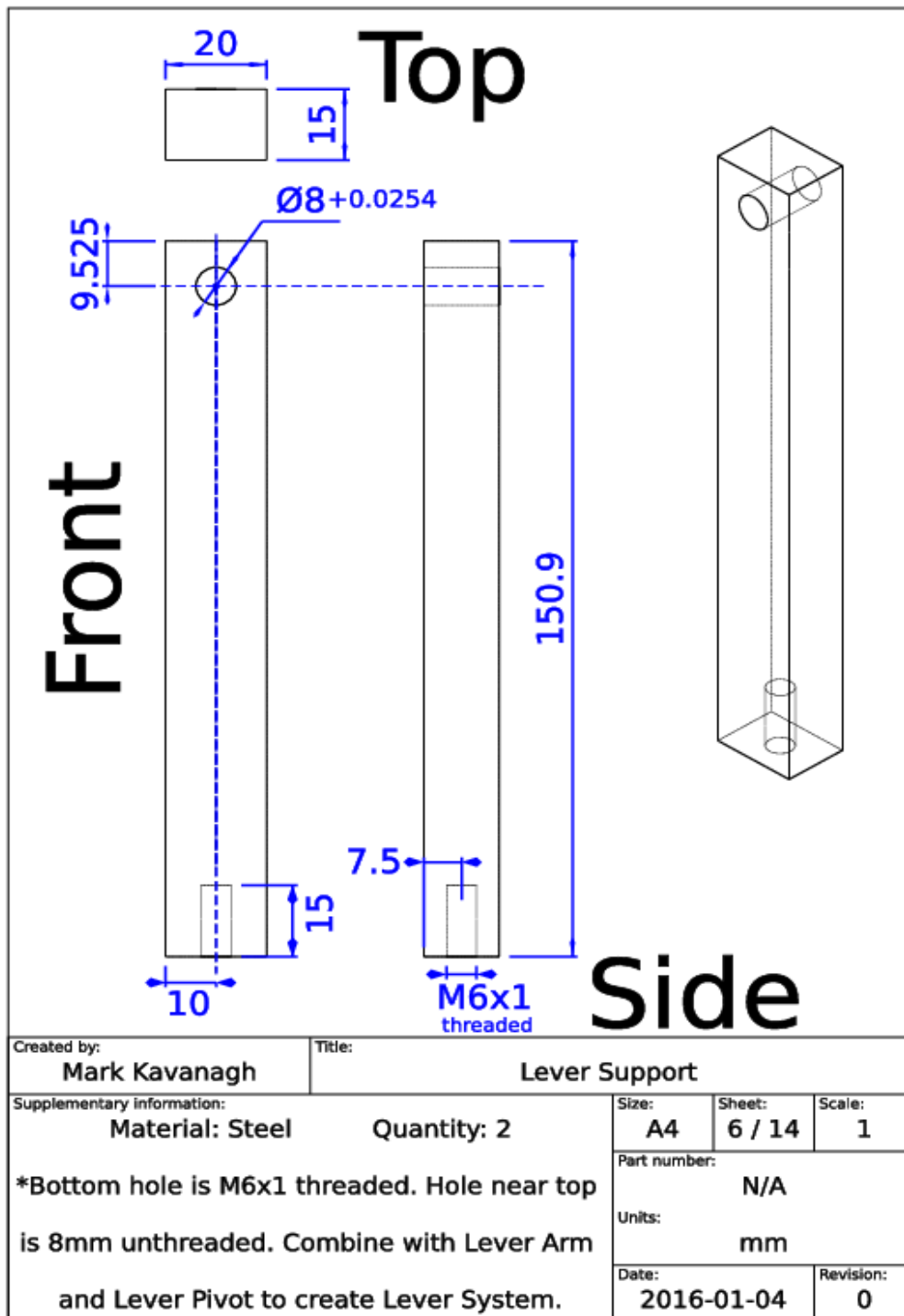


Figure A.7: Specifications for the supports that hold up the lever.



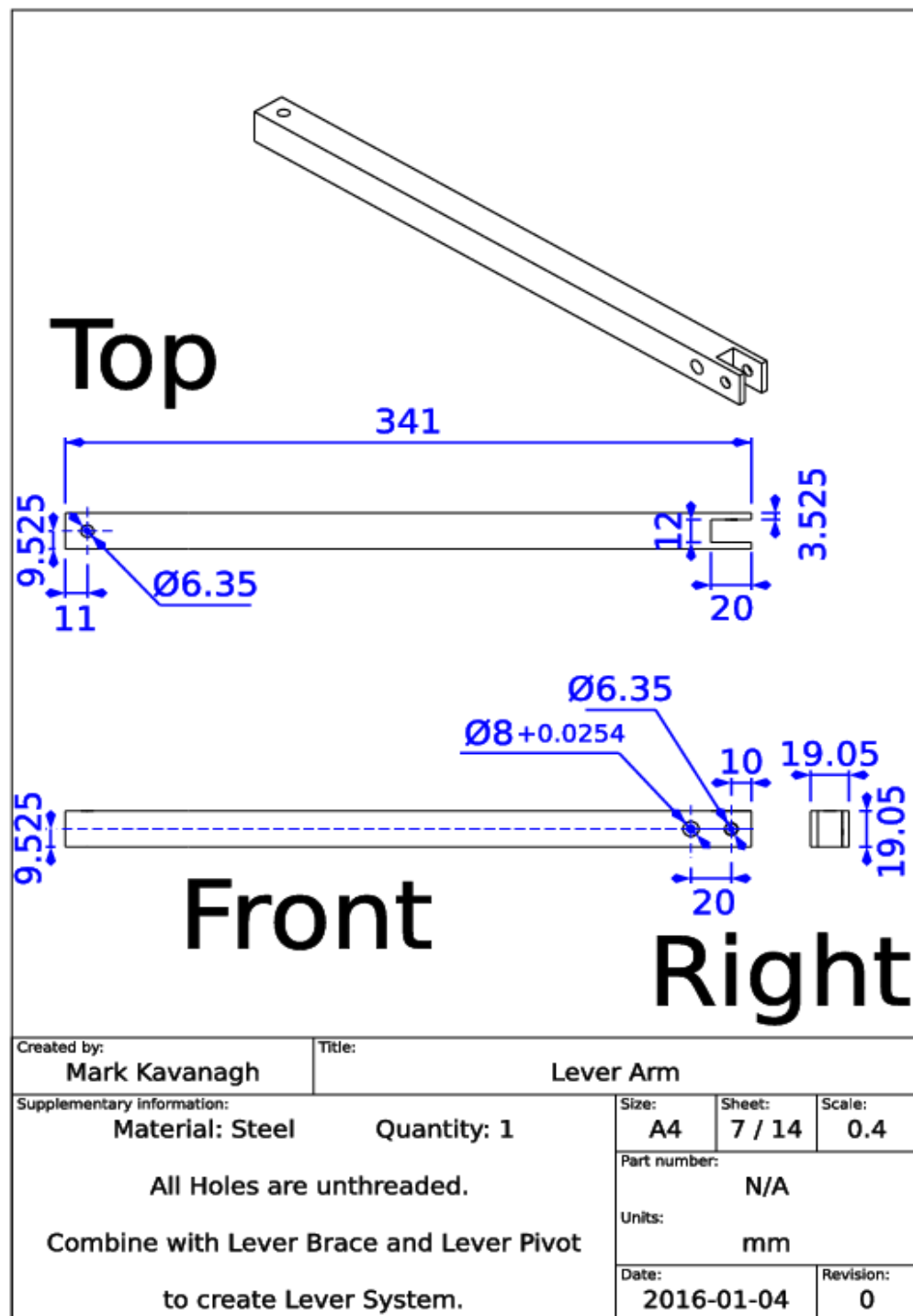


Figure A.8: Specification for the lever arm.

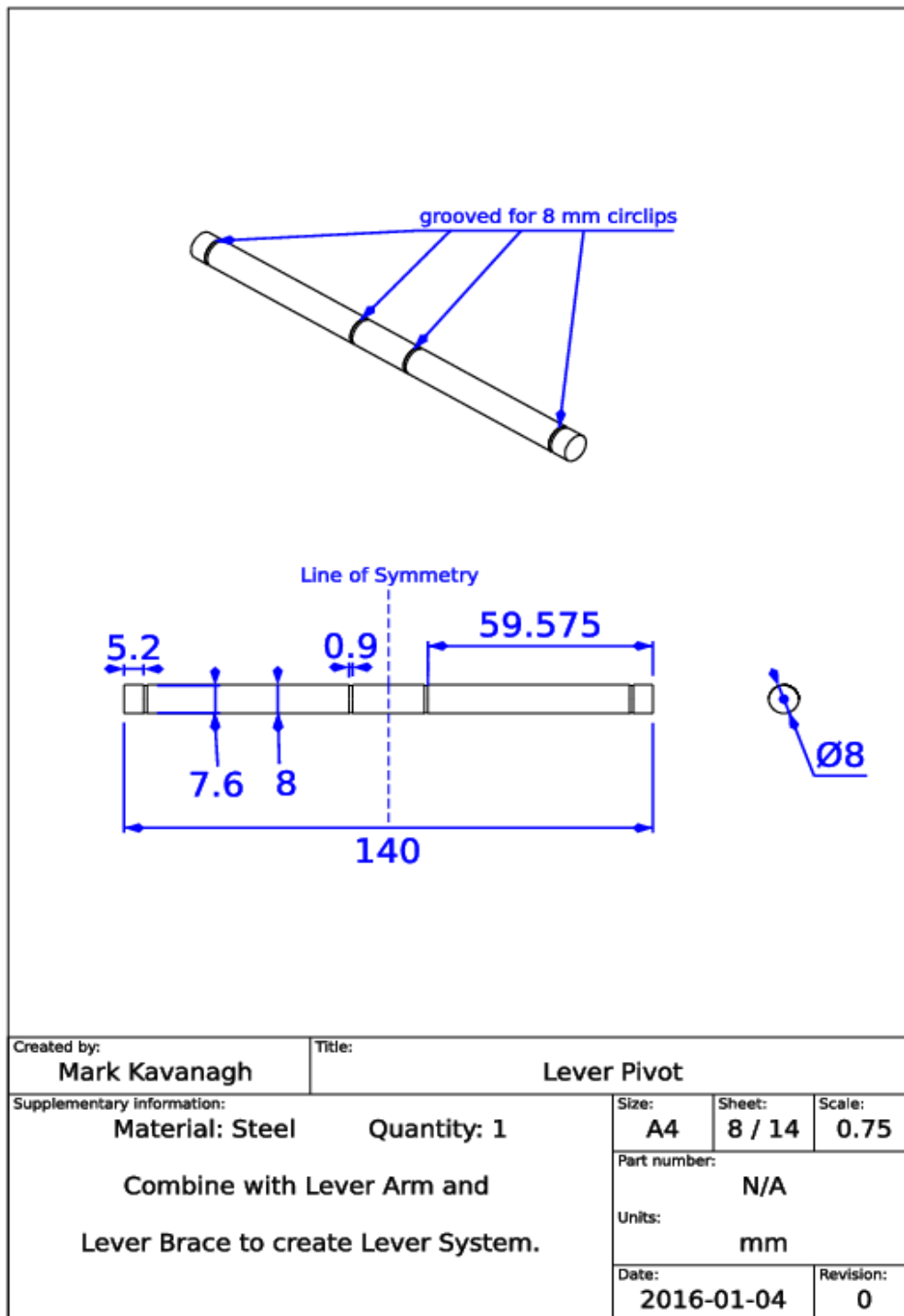


Figure A.9: Specifications for the rod that the lever pivots about.

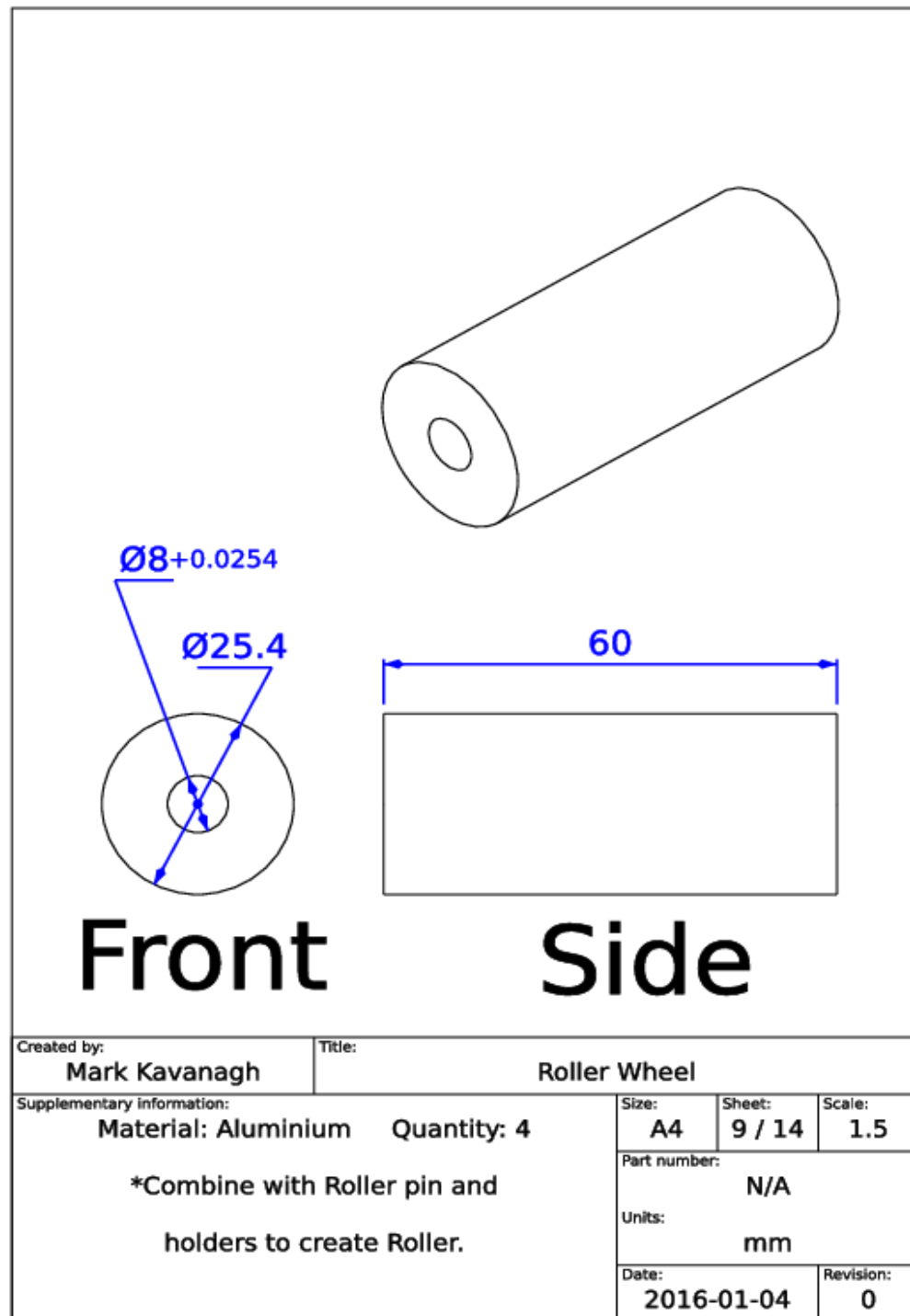


Figure A.10: Specifications for the hollowed cylinder part of the rollers.

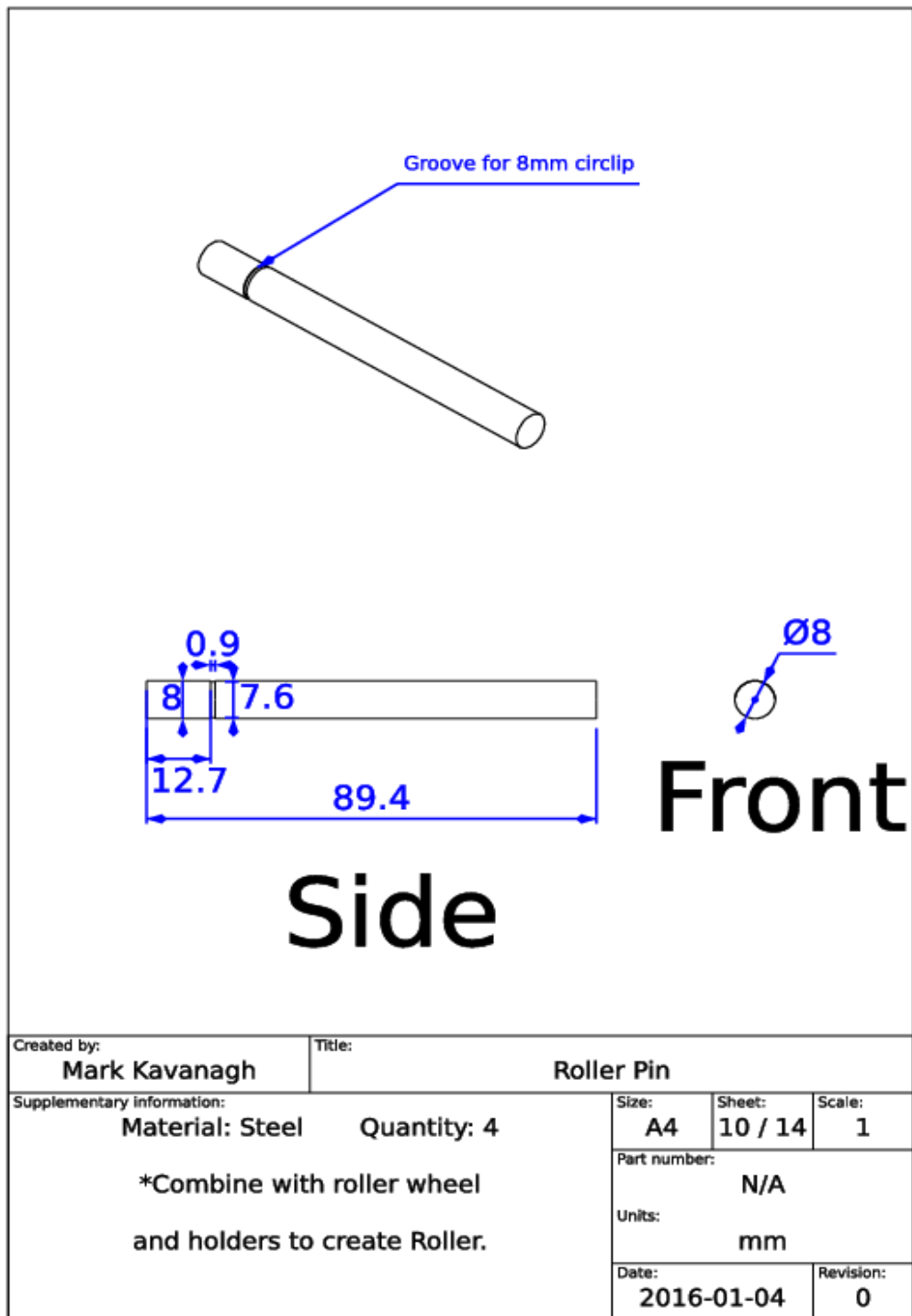


Figure A.11: Specifications for the steel core of the rollers.

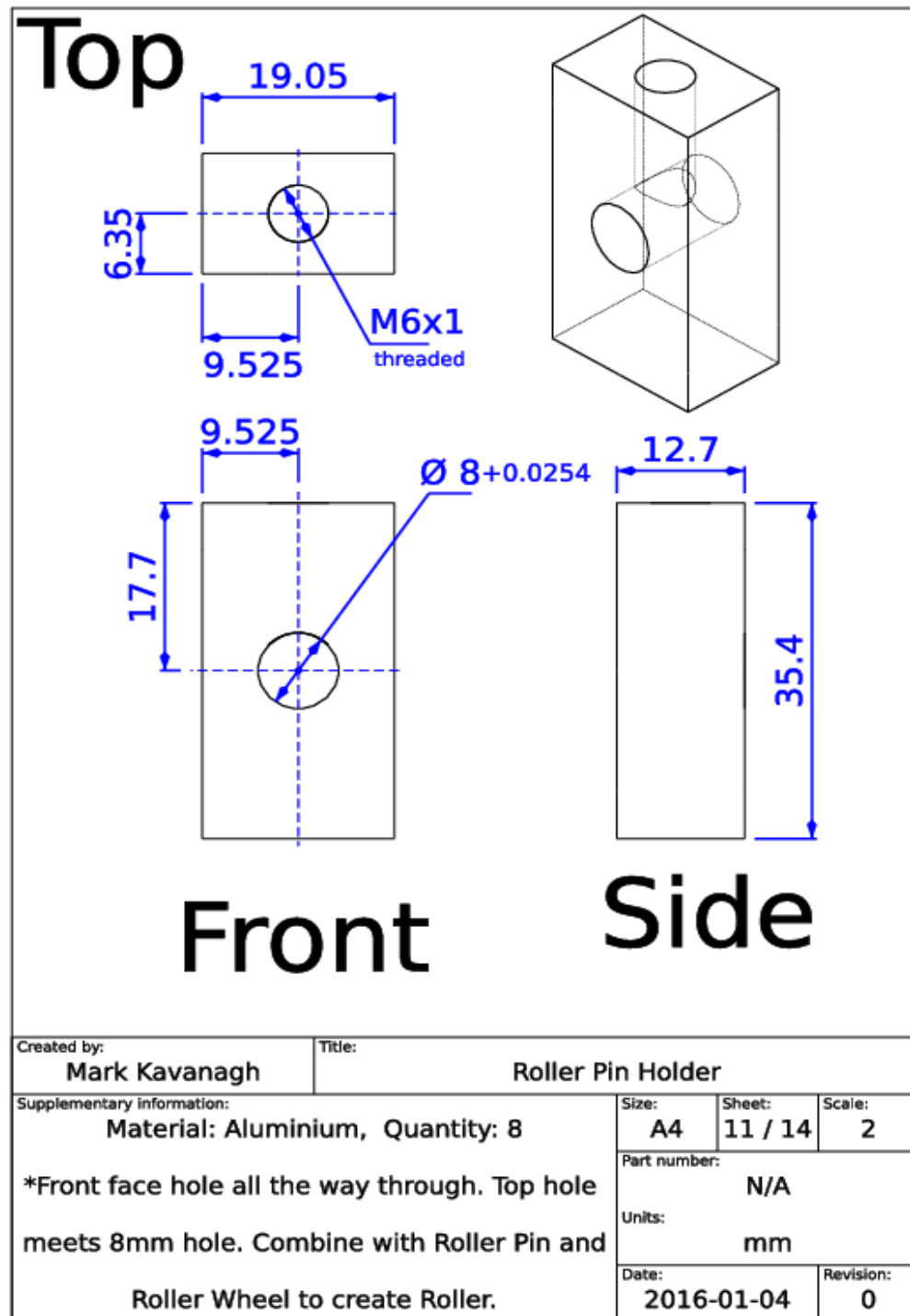


Figure A.12: Specifications for the holders that connect the rollers to the table or top plate.

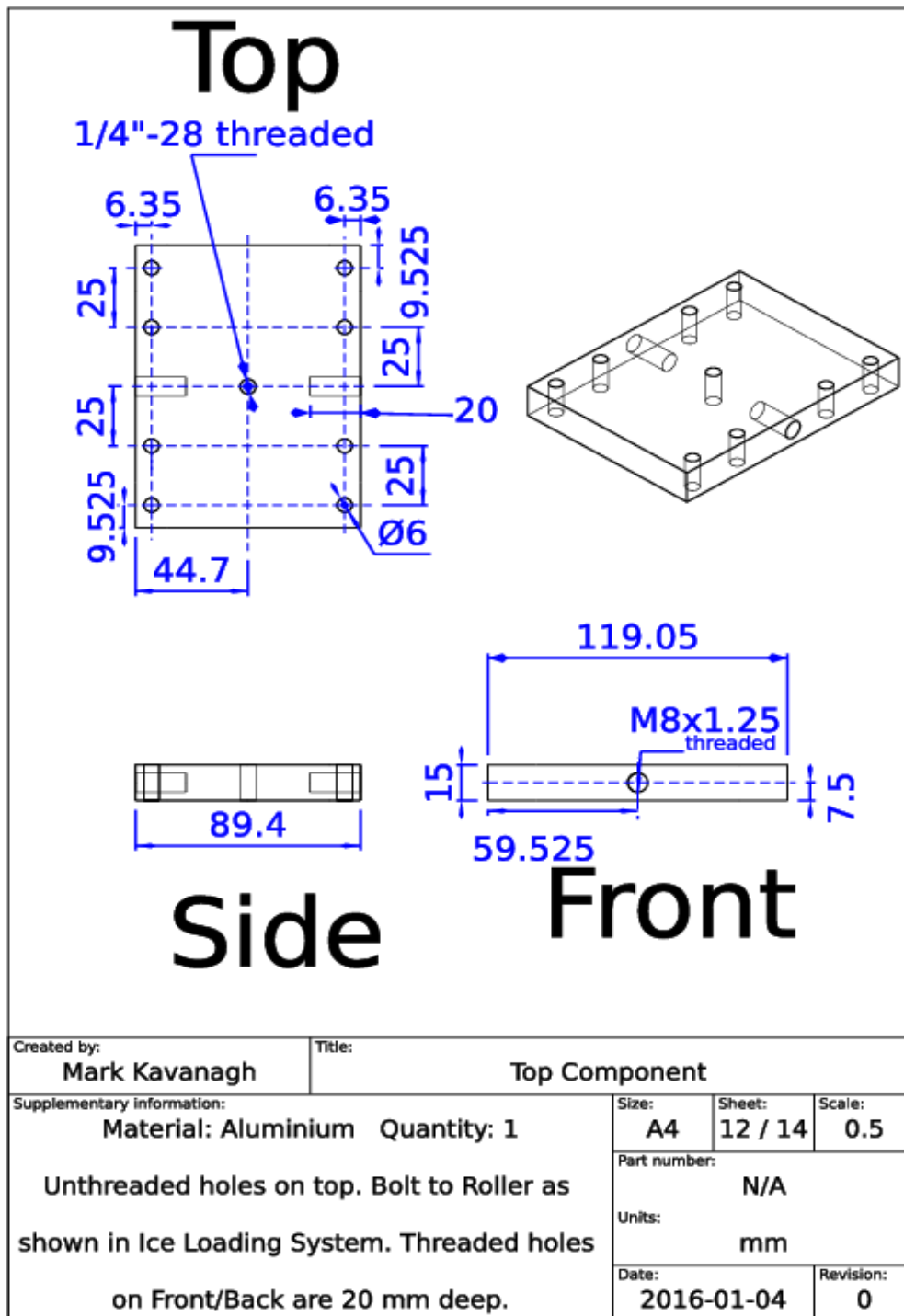


Figure A.13: Specifications for the top plate.

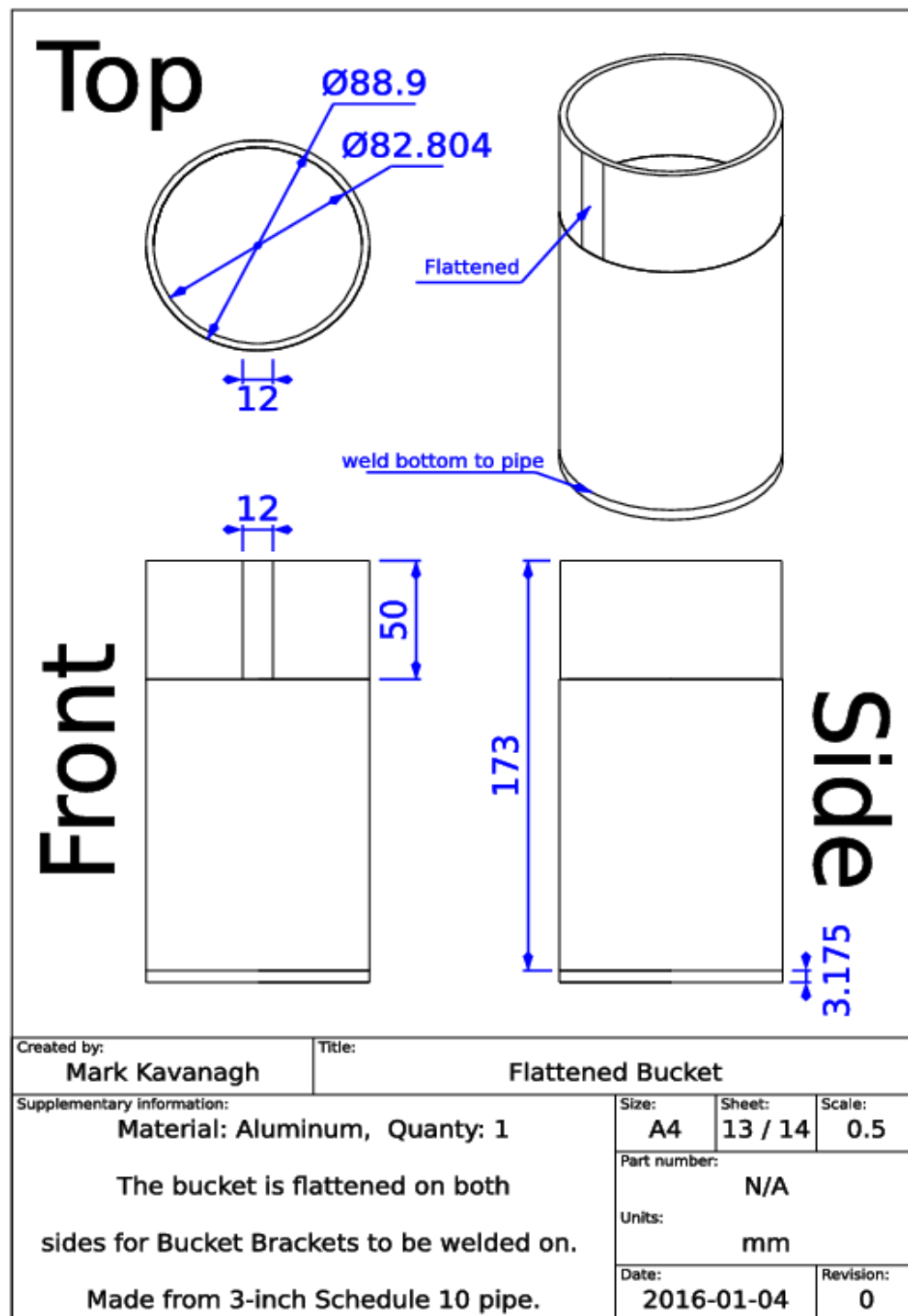


Figure A.14: Specifications for the bucket portion of the hanging mass.

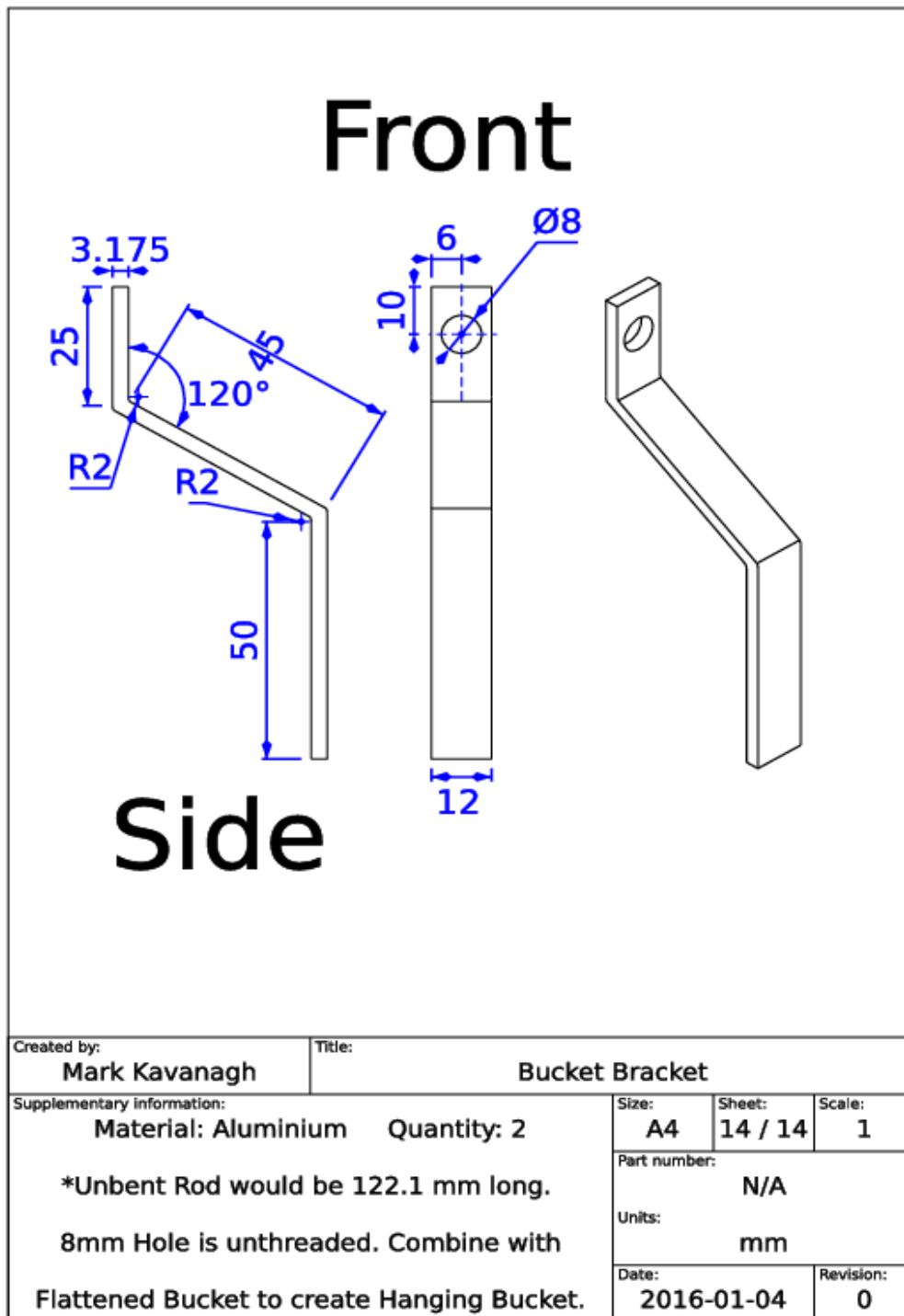


Figure A.15: Specifications for the brackets that connect the bucket to the pulley (via string).



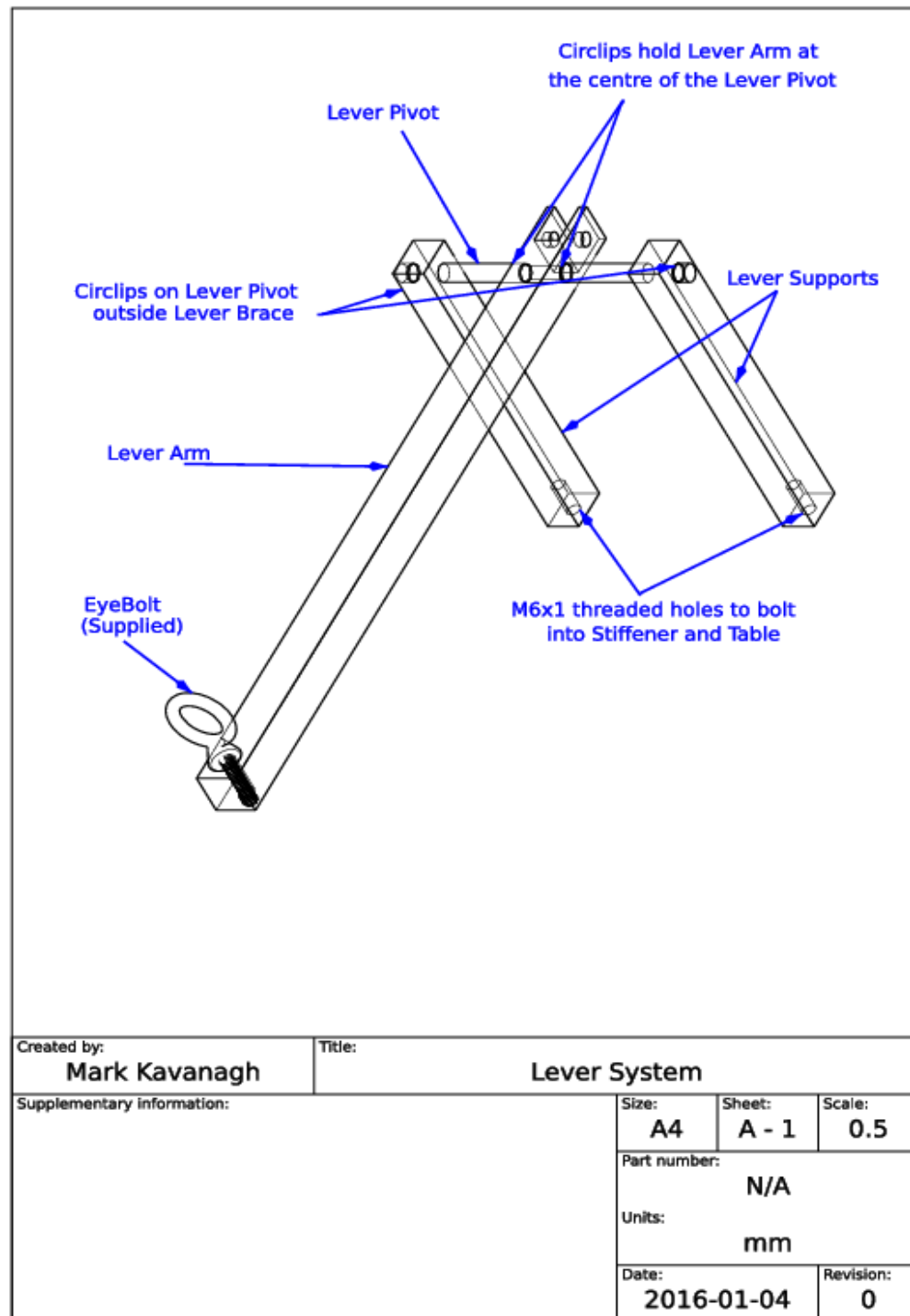


Figure A.16: Diagram illustrating the construction of the lever arm and its supports.

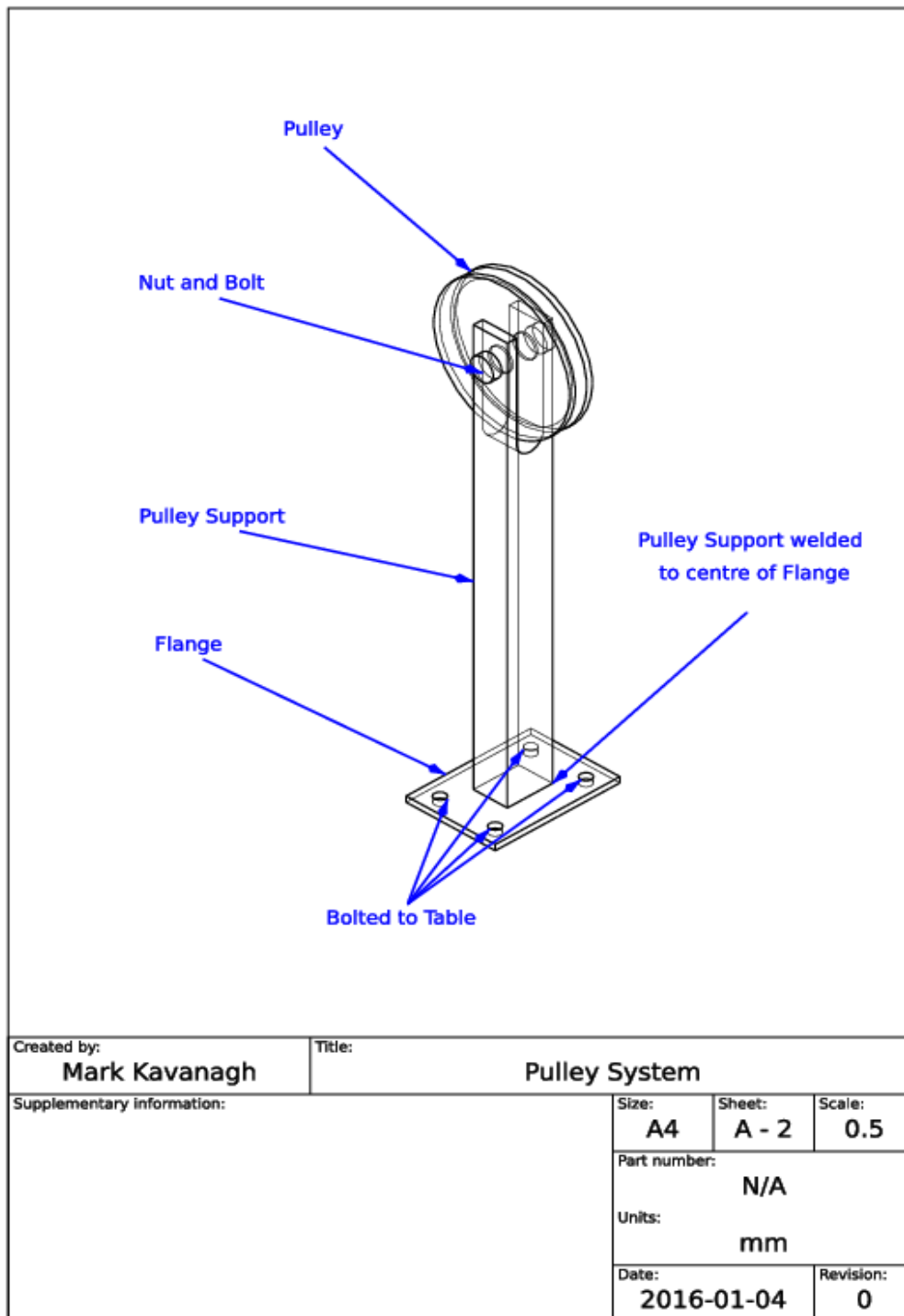


Figure A.17: Diagram illustrating the construction of the pulley, its support, and the stiffening flange.

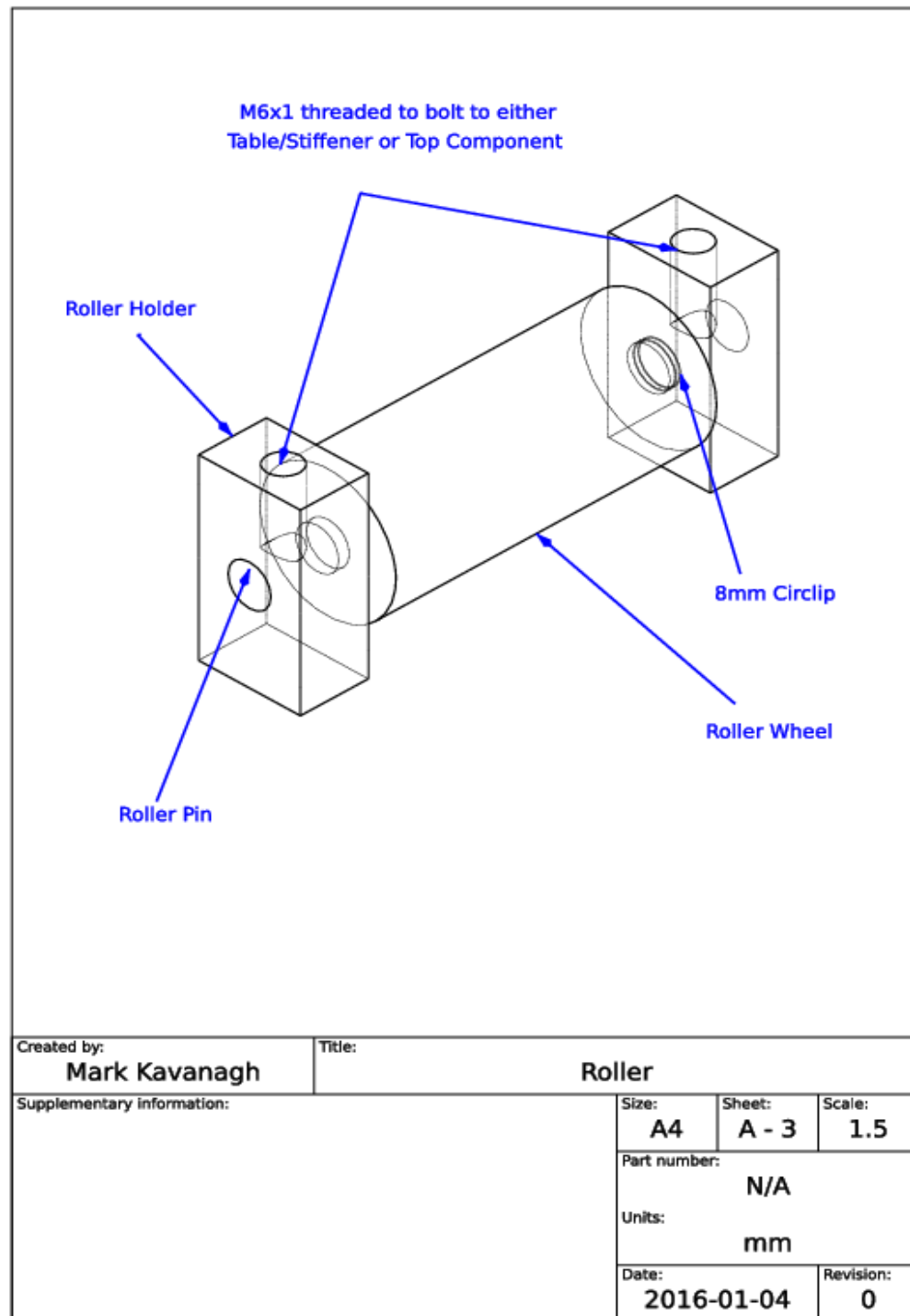


Figure A.18: Diagram illustrating the assembly of a roller from its constituent parts.

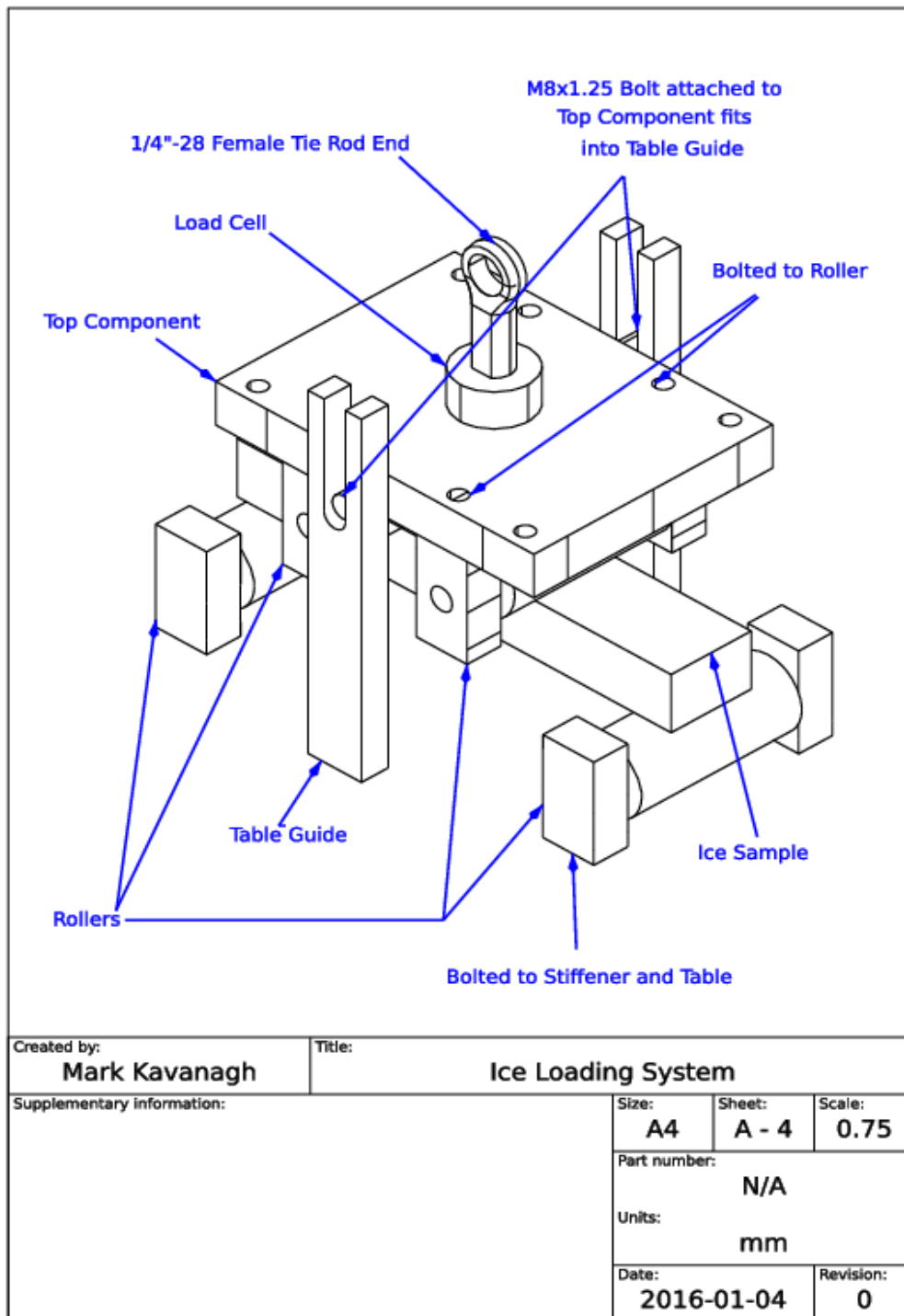


Figure A.19: Diagram illustrating the assembly of the components that apply and measure the load on the ice sample.

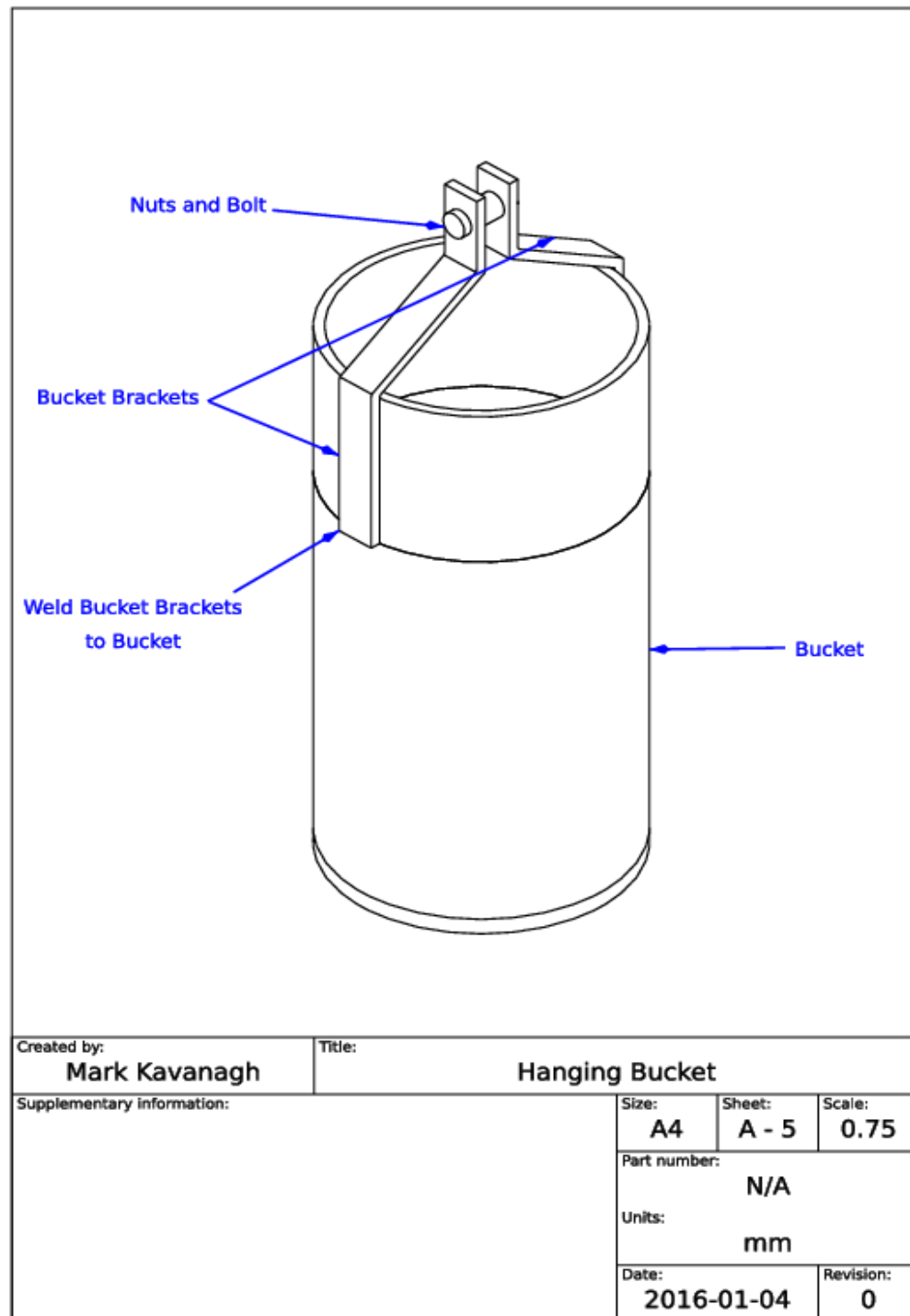


Figure A.20: Diagram of the hanging mass assembled from the bucket and its brackets.